

Washington University in St. Louis

Washington University Open Scholarship

Arts & Sciences Electronic Theses and
Dissertations

Arts & Sciences

Spring 5-15-2023

Hydrolysis-directed Vapor-phase Synthesis and Solution Processing of Nanostructured Conducting Polymers

Haoru Yang

Follow this and additional works at: https://openscholarship.wustl.edu/art_sci_etds

Recommended Citation

Yang, Haoru, "Hydrolysis-directed Vapor-phase Synthesis and Solution Processing of Nanostructured Conducting Polymers" (2023). *Arts & Sciences Electronic Theses and Dissertations*. 2924.
https://openscholarship.wustl.edu/art_sci_etds/2924

This Dissertation is brought to you for free and open access by the Arts & Sciences at Washington University Open Scholarship. It has been accepted for inclusion in Arts & Sciences Electronic Theses and Dissertations by an authorized administrator of Washington University Open Scholarship. For more information, please contact digital@wumail.wustl.edu.

WASHINGTON UNIVERSITY IN ST. LOUIS

Department of Chemistry

Dissertation Examination Committee:

Bryce Sadtler, Chair

Jonathan Barnes

Julio D'Arcy

Young-Shin Jun

Vijay Ramani

Hydrolysis-directed Vapor-phase Synthesis and Solution Processing of Nanostructured
Conducting Polymers

by

Haoru Yang

A dissertation presented to
Washington University in St. Louis
in partial fulfillment of the
requirements for the degree
of Doctor of Philosophy

May 2023

St. Louis, Missouri

© 2023, Haoru Yang

Table of Contents

List of Figures	iv
List of Tables	viii
Acknowledgments.....	ix
Abstract.....	xii
Chapter 1: Introduction to Nanostructured Conducting Polymer Synthesis.....	13
1.1 Brief History of Conducting Polymer Synthesis.....	13
1.2 Applications of Conducting Polymers and Their Composites	16
1.2.1 Conducting Polymer-based Energy Storage Devices	16
1.2.2 Conducting Polymer-based Sensors.....	17
1.2.3 Photothermal Application of Conducting Polymers	18
1.2.4 Electromagnetic Interference (EMI) Shielding Application of Conducting Polymers	19
1.3 Common Synthetic Strategies	20
1.3.1 Electrochemical Synthesis of Conducting Polymers	20
1.3.2 Solution-phase Synthesis of Conducting Polymers	22
1.3.3 Vapor-phase Synthesis of Conducting Polymers.....	23
1.3.4 Current Research in Conducting Polymer Synthesis	26
1.4 Oxidative Polymerization Mechanism	27
1.5 Synthesis of Nanostructured Conducting Polymers and Composites	30
1.5.1 Templated Synthesis of Nanostructured Conducting Polymers.....	31
1.5.2 Template-free Synthesis of Nanostructured Conducting Polymers	32
1.6 Iron Corrosion Product (Rust) and Rust-based Vapor-phase Polymerization (RVPP)..	33
1.6.1 Brief Introduction to Iron Corrosion Product.....	34
1.6.2 Hydrolysis of Ferric Ions	35
1.6.3 Dissolution of Iron Corrosion Product.....	37
1.6.4 Proposed Mechanism for Rust-based Vapor-phase Polymerization (RVPP)	39
1.7 References	41
Chapter 2: Rust-based Vapor-phase Polymerization of Nanofibrillar Poly(3,4-ethylenedioxythiophene)/Polypyrrole Composite on Flexible Substrates.....	58
2.1 Introduction	58
2.2 Materials and Methods	60

2.3	Results and Discussion.....	63
2.4	Conclusions	82
2.5	References	84
Chapter 3: Covalently Bonding Nanostructured Poly(3,4-ethylenedioxythiophene) to Functionalized Glass		90
3.1	Introduction	90
3.2	Materials and Methods	91
3.3	Results and Discussion.....	95
3.4	Conclusions	112
3.5	References	114
Chapter 4: Poly(3,4-ethylenedioxythiophene)-integrated Masonry Material via Vapor-phase Polymerization		120
4.1	Introduction	120
4.2	Materials and Methods	122
4.3	Results and Discussions	123
4.4	Conclusions	134
4.5	References	135
Chapter 5: Solution Processing of Sub-micron Poly(3,4-ethylenedioxythiophene) Particles		139
5.1	Introduction	139
5.2	Materials and Methods	140
5.3	Results and Discussion.....	144
5.4	Conclusions	159
5.5	References	160
Chapter 6: One Eye on the Past, the Other on the Future		166
6.1	Effect of Relative Humidity and Additional Organic Solvents in Rust-based Vapor-phase Polymerization	166
6.2	Spectroelectrochemical Characterization of Reaction Intermediates.....	168
6.3	Conducting Polymer-filled 3D Printing Filaments	168
6.4	Enhancing the Energy Density of Conducting Polymer-based Supercapacitors	170
6.5	References	171
Appendix.....		173
Curriculum Vitae		174

List of Figures

Figure 1.1 Photo of Dr. Henry Letheby by W. & D. Downy.....	13
Figure 1.2 Colors of polyaniline under different pH and oxidation states.....	14
Figure 1.3 Polymerization of polyacetylene	15
Figure 1.4 Structures of common parent conducting polymers in current research	16
Figure 1.5 Schematic diagram of a three-electrode electrochemical cell	20
Figure 1.6 Jaroslav Heyrovský invented the first polarograph in 1922.....	22
Figure 1.7 Four stages of vapor-phase synthesis	26
Figure 1.8 Polymerization mechanism of five-membered heterocycles.....	28
Figure 1.9 Oxidative doping of polypyrrole and polythiophene.....	28
Figure 1.10 Polymerization scheme of aniline	30
Figure 1.11 Nanostructured conducting polymers.....	31
Figure 1.12 Chemical formulas and names of all naturally occurring phases of iron corrosion product	35
Figure 1.13 Hydrolysis scheme of octahedral iron(III) complexes	36
Figure 1.14 Oriented attachment and Ostwald ripening during crystallization	37
Figure 1.15 Splitting growth during crystallization.....	37
Figure 1.16 Dissolution scheme of iron(III) oxides/hydroxides/oxyhydroxides	38
Figure 1.17 Experimental variables that alter the kinetics of dissolution.....	39
Figure 1.18 The mixed reaction pathways in rust-based vapor-phase polymerization.....	40
Figure 1.19 PEDOT nanofibers produced via RVPP consists of a core/shell structure	40
Figure 2.1 Schematic diagram for vapor-phase deposition of conducting polymer nanofibers on Kirigami sheets	64
Figure 2.2 Optical micrographs of polypyrrole synthesized under various HCl concentrations..	64
Figure 2.3 SEM images of β -FeOOH crystals and granular morphology of PEDOT	65
Figure 2.4 Acid-catalyzed polymerization of EDOT and pyrrole	67

Figure 2.5 Spectroscopic and mechanical characterization of conducting polymer coatings	68
Figure 2.6 Raman spectrum of a HCl-doped PPy film	69
Figure 2.7 UV-Vis-NIR characterization of conducting polymers.....	70
Figure 2.8 Nanofibrillar PEDOT/PPy composite as Kirigami electrodes	71
Figure 2.9 Electrochemical characterizations of PEDOT and PPy films	73
Figure 2.10 Adhesion tests of PEDOT to a PET substrate	75
Figure 2.11 PPy film delaminates from a PET substrate after scotch tape test	75
Figure 2.12 Nanofibrillar PEDOT Kirigami sheets with increasing numbers of unit cells.....	76
Figure 2.13 Conductivity measurement via a four-point probe.....	76
Figure 2.14 Nanofibrillar PEDOT/PPy Kirigami supercapacitors	78
Figure 2.15 Cyclic voltammograms of PEDOT in 1 M LiClO ₄ electrolyte under various scan rates	79
Figure 2.16 The supercapacitor withstands various modes of deformation	80
Figure 2.17 Nanofibrillar PEDOT Kirigami electrodes for wearable humidity dosimeters.....	82
Figure 3.1 Glass silanization and polymer synthesis	96
Figure 3.2 Mechanisms in rust-based vapor-phase polymerization.....	97
Figure 3.3 Scanning electron micrographs of washed and unwashed PEDOT nanofibers.	99
Figure 3.4 Rust-based vapor-phase polymerization of PEDOT on silanized glass is quenched at various times	99
Figure 3.5 Characterization of a PEDOT-coated silanized glass electrode	101
Figure 3.6 Additional characterization of PEDOT on silanized glass and untreated glass	102
Figure 3.7 Proposed mechanism of a PEDOT chain covalently bonding to the phenyl group ..	103
Figure 3.8 Scotch tape test of PEDOT coating on silanized glass.....	103
Figure 3.9 Proposed structures of PEDOT polymer chains on silanized glass and untreated glass	106
Figure 3.10 Fabrication and performance of a planar supercapacitor	107

Figure 3.11 Sequential removal of PEDOT coating and characterization.....	108
Figure 3.12 Stability test of a planar supercapacitor.....	109
Figure 3.13 Optical micrographs of silanized glass after hematite deposition and corresponding cross-sectional electron micrographs of PEDOT coating	110
Figure 3.14 Characterization of an edge-coated electrode and fabrication of a transparent supercapacitor	111
Figure 3.15 Assembly procedure of a sandwich-type supercapacitor	112
Figure 4.1 Schematic diagrams of synthetic approach and temperature sensing device	125
Figure 4.2 Dissolution of ferric oxyhydroxide in hydrochloric acid	125
Figure 4.3 Oxidative radical polymerization of EDOT	125
Figure 4.4 Olation and oxolation of ferric ions.....	126
Figure 4.5 Back-scattering electron micrographs of PEDOT-coated tiles	127
Figure 4.6 Characterization of PEDOT synthesized with organic solvents.....	128
Figure 4.7 Friedel-Crafts alkylation between alcohol and chlorobenzene catalyzed by PEDOT	129
Figure 4.8 Reaction between alcohol and concentrated HCl.....	129
Figure 4.9 Current vs. voltage curves of PEDOT show linear behavior even when exposed to various pH.....	132
Figure 4.10 Performance of a PEDOT tile temperature sensor	133
Figure 4.11 Performance of a PEDOT brick temperature sensor and a concept of integrated sensing in masonry construction	134
Figure 5.1 Thermogravimetric analysis of PEDOT particle electrode	143
Figure 5.2 Schematic diagram of aerosol synthesis and particle characterization	145
Figure 5.3 An optical micrograph of PEDOT particles	145
Figure 5.4 Schematic diagram of a 3D-printed gap electrode for measuring electrical resistance	146
Figure 5.5 Photos of collected liquid dispersion from various EDOT: Fe ³⁺ ratios during synthesis	148

Figure 5.6 Morphology evolution of PEDOT particles with different EDOT to Fe ³⁺ ratios.....	148
Figure 5.7 Spectroscopic characterizations and electrical resistance measurements of PEDOT particles	149
Figure 5.8 Characterizations of PEDOT particle-loaded carbon electrodes.....	151
Figure 5.9 Electrochemical performance comparison between a drop-casted electrode and an electrophoretic deposited electrode.....	152
Figure 5.10 PEDOT particle-based paint and proof-of-concept sensors fabricated from particle-coated 3D-printed objects	155
Figure 5.11 Photos of PEDOT:PSS paint on 3D-printed thermoplastics	155
Figure 5.12 Optical micrographs of PEDOT particle coated TPU strain sensor	157
Figure 5.13 Proof-of-concept light-induced sanitation of a PEDOT particle coating	158
Figure 6.1 2D PEDOT nanoflower synthesized under high concentration of ethanol	167
Figure 6.2 Schematic diagram of a modified 3D printing extruder that combines extrusion and polymerization.	169
Figure A1 Graphical abstract of publication, “Nanostructured Poly(3,4-Ethylenedioxythiophene) (PEDOT) Coatings on Functionalized Glass for Energy Storage.”	173
Figure A2 Graphical abstract of publication, “Solution Processable Poly(3,4-Ethylenedioxythiophene) Nanoparticles.”	173
Figure A3 Model of a 3D-printed pellet press for measuring electrical conductivity of powders. The dimensions are measured in millimeters.....	173

List of Tables

Table 4.1 Average two-point electrical resistance of PEDOT from RVPP with organic solvents.	127
--	-----

Acknowledgments

I have many mentors, role models, and friends I am grateful for during my journey for knowledge in the US that has spanned a third of my life. To my professional mentors, Prof. Beth Martin and Prof. Julio D’Arcy, I am thankful for the support and advice you provided in my career, and I am also thankful for your guidance when I lacked a goal or motivation. To my thesis advisory committee, Prof. Bryce Sadtler and Prof. Jonathan Barnes, I am thankful for your advice and constructive criticism because you helped me grow and honed my skills as a chemist. I am also grateful to Dr. Huafang Li, Mr. James Linders, and Mr. James Graflage for your help in designing and building the reactors I used throughout my research, as well as the microscopy techniques I used to characterize my samples. I would like to thank the staffs in the chemistry department, Mr. Christopher Thuet and Mr. Gerry Kohring, for their help with computer software troubleshooting and purchasing the necessary chemicals for my research. To the previous graduate students of D’Arcy lab, Dr. Luciano Santino, Dr. Yang Lu, Dr. Yifan Diao, and Dr. Hongmin Wang, you are both my role models and treasured friends. I will make sure to pass on what I learned from you to new students in the D’Arcy group. To the Norlin family, I am so glad Josh became my roommate during my first year at WashU. You are always so kind to me and make me feel welcome, especially during the tough times between 2020 and 2022 when my family could not come to visit due to COVID restrictions. To my close friends in the chemistry department, Liangyi Chen, Lin Lin, Jiang Luo, and Jinping Yang, and to all the other friends I made during my time in the US (whether through golf, boardgames, or other social events). Thank you for your company, I would not have made it this far without you.

I want to express my special gratitude to my family, especially my parents and grandparents. You always love and support me unconditionally. I hope my accomplishments so far have made you proud, and I will keep trying my best in the future.

Haoru Yang

Washington University in St. Louis

May 2023

Dedicated to both of my grandfathers and my great-grandmother who are in heaven.

ABSTRACT OF THE DISSERTATION

Hydrolysis-directed Vapor-phase Synthesis and Solution Processing of Nanostructured Conducting Polymers

by

Haoru Yang

Doctor of Philosophy in Chemistry

Washington University in St. Louis, 2023

Professor Bryce Sadtler, Chair

Conducting polymers are a class of organic material that possesses semiconducting properties. Their unique molecular structure facilitates charge transport via delocalized π -electron network in the polymer backbone. Creating nanostructures in a conducting polymer increases its surface area to volume ratio and promotes molecular interaction at the surface of the polymer, resulting in enhanced physical and chemical properties, such as ion transfer, adsorption/desorption efficiency, and electrical conductivity. This dissertation focuses on synthesizing nanostructured conducting polymers and their composites from the vapor phase. The mechanisms in a novel synthetic strategy that utilizes iron corrosion products to initiate polymerization and template nanostructure formation is examined. Vapor-phase synthesis is carried out on both organic and inorganic substrates, and varying reaction conditions, such as temperature, reaction time, or anions in the iron(III) salt, creates a spectrum of morphologies (0D particles, 1D fibers, and amorphous films). This dissertation also presents methods for overcoming challenges in conducting polymer processing. Vapor-phase synthesized conducting polymers are fabricated into electrodes for state-of-art supercapacitors, humidity and temperature sensors, and proof-of-concept functional 3D-printed objects.

Chapter 1: Introduction to Nanostructured

Conducting Polymer Synthesis

1.1 Brief History of Conducting Polymer Synthesis

One of the earliest accounts of conducting polymer dates back to the 19th century. In 1862, Dr. Henry Letheby obtained a “blue substance” that was likely polyaniline while investigating the anodic oxidation product of aniline in sulfuric acid (Figure 1.1). Letheby also described the material changed color (to blue and violet) when exposed to ammonia and concentrated sulfuric acid.^{1–3} We now know these color changes originated from the molecular structure change in polyaniline at different doping levels and oxidation states—blue as emeraldine base in alkaline pH and violet as pernigraniline when over-oxidized in concentrated sulfuric acid (Figure 1.2).⁴ Another early account was from Dr. Angelo Angeli in 1915. He oxidized pyrrole in a mixture of hydrogen peroxide and acetic acid and named the conductive dark brown-black product “pyrrole black,” which we now know as polypyrrole.⁵



Figure 1.1 Photo of Dr. Henry Letheby by W. & D. Downey. Used with permission. Copyright 2023, National Portrait Gallery, London, United Kingdom.

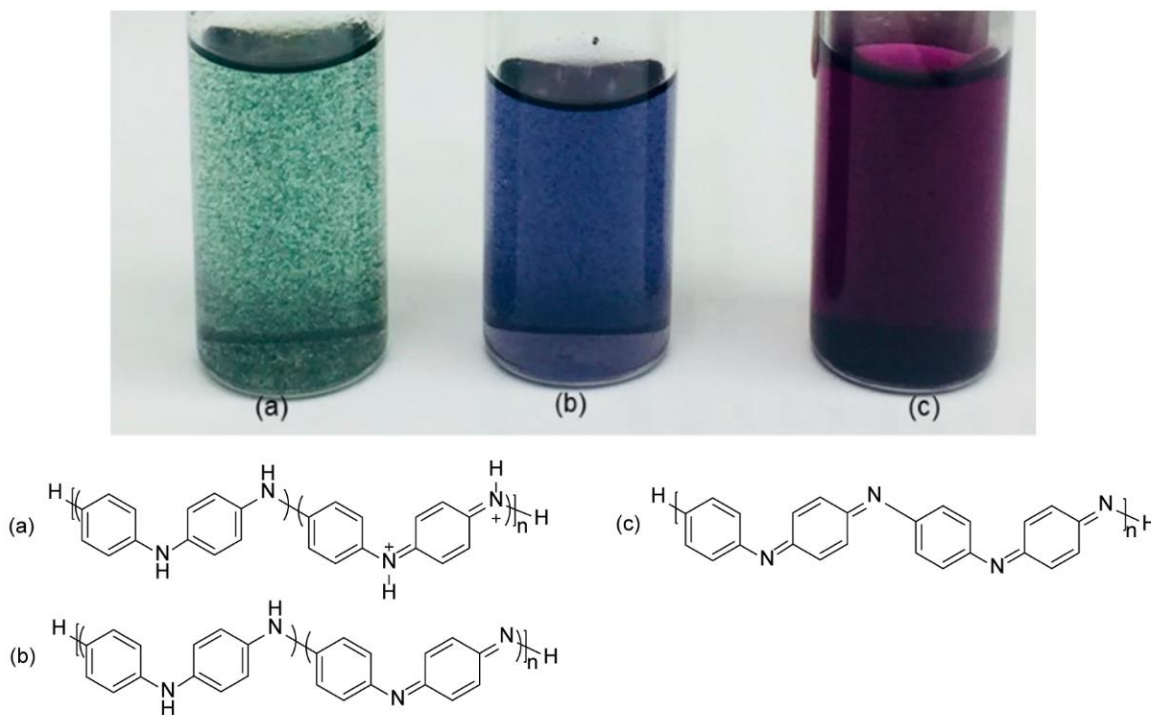


Figure 1.2 Colors of polyaniline under different pH and oxidation states. a) emeraldine salt, b) emeraldine base, and c) pernigraniline base. Adapted with permission from Reference 4. Copyright MDPI 2019.

Decades later, the research on synthesis and processing of polyacetylene launched the field of conducting polymer research (Figure 1.3).² In 1958, Natta et al. were the first to report a method for preparing high molecular weight, highly crystalline, and regularly structured polyacetylene from polymerization in hexane with $\text{Al}(\text{Et})_3/\text{Ti}(\text{OPr})_4$ as initiator.^{2,6} In the following decades various alternative routes were developed for polyacetylene synthesis, including the Luttinger route (1960) and the Shirakawa route (1971).⁷ In 1977, Dr. Hideki Shirakawa, Dr. Alan MacDiarmid, and Dr. Alan Heeger reported an electrical conductivity of 38 S/cm in iodine-vapor-treated polyacetylene film at room temperature (eleven orders of magnitude increase compared to an untreated sample).⁸ In a following study, they observed an even higher electrical conductivity of 560 S/cm at room temperature from AsF_5 -treated polyacetylene. According to

their paper, the conductivity adjusted for density of treated polyacetylene was almost metallic, and the polyacetylene samples were sufficient substitutes to metal wires in simple electrical circuits.⁹ Heeger, MacDiarmid, and Shirakawa are the first to demonstrate tunable electrical conductivity in an organic material that were traditionally considered to be insulating. Their papers became the foundation and inspired further research in the synthesis, processing, and application of conducting polymers. Heeger, MacDiarmid, and Shirakawa were awarded the Nobel Prize in Chemistry in 2000 due to the significance of their discovery.²

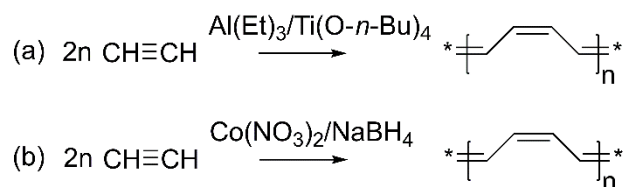


Figure 1.3 Polymerization of polyacetylene. a) Natta route and Shirakawa route. b) Luttinger route.

Despite possessing close to metallic electrical conductivity, polyacetylene is not stable in air and is sensitive to humidity. Other less conductive polymers with higher stability under ambient conditions have gained much interest since the early 1980s, including polyaniline, polypyrrole, polythiophene, and their derivatives (Figure 1.4).² Some polymers and their composites, such as poly(3,4-ethylenedioxythiophene) polystyrene sulfonate (PEDOT:PSS) are commercialized and widely researched because it is easy to synthesize and stable under ambient conditions. In the past two decades, nanostructured conducting polymers attracted much interest due to their enhanced electrochemical properties. Structural features at sub-micron scales increases the surface area to volume ratio, facilitates molecular interactions at the interface, and improves charge carrier mobility of conducting polymers.^{10–18} Understanding and controlling the process in nanostructured conducting polymer synthesis is crucial and leads to improvements in

performance of conducting polymer-based energy storage devices, sensors (chemoresistive, pressure, and temperature), photovoltaics, catalysts (photo- and electro-), photothermal agents, and coatings for electromagnetic interference shielding.^{19–32}

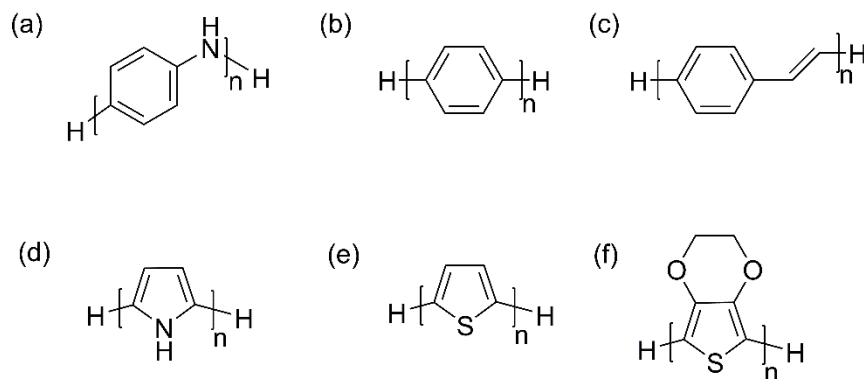


Figure 1.4 Structures of common parent conducting polymers (a-e) in current research. a) polyaniline, b) polyphenylene, c) poly(phenylene vinylene), d) polypyrrole, e) polythiophene. f) Poly(3,4-ethylenedioxythiophene), a polythiophene derivative.

1.2 Applications of Conducting Polymers and Their Composites

In the 1970s and 1980s, research in conducting polymers mainly utilized the electrical conductivity of this material to disperse charges for antistatic coating.^{5,33,34} Research in the following decades focused on utilizing the semiconducting properties of conducting polymers, which leads to fabrication of state-of-the-art energy storage devices and electromagnetic interference shielding coatings. Additionally, research on the biocompatibility of conducting polymers demonstrate the material's potential for wearable temperature and chemoresistive sensors, as well as photothermal agents.

1.2.1 Conducting Polymer-based Energy Storage Devices

Conducting polymers such as PEDOT and polypyrrole are mainly used in electrodes for electrochemical capacitors (supercapacitors). This type of energy storage device possesses a

higher charge/discharge rate (power density) than batteries and stores more charge (energy density) than electrolytic capacitors. The charge storage mechanisms of a supercapacitor consists of electric double layer capacitance (EDLC) and pseudocapacitance. EDLC stores charges via adsorption of ions on the electrode surface, and pseudocapacitance stores charges via redox reaction on the electrode.³⁵

Current research in conducting polymer-based supercapacitor often involves synthesis of polymer composites with carbon or metal oxides. Porous carbon enhances the electrical conductivity of the electrode and facilitates facile charge transfer during charging/discharging. Additionally, the porous structure templates nanostructure formation during conducting polymer synthesis, increasing the surface area of the electrode and enhances charge storage via EDLC.¹⁴ Metal oxides, such as nickel oxide and cobalt oxide, undergo redox reaction and are ideal materials for a supercapacitor that utilizes pseudocapacitance. However, these oxides often lack electrical conductivity, resulting in low charge/discharge rate. Conducting polymer/metal oxide composite combines the electrical conductivity of conducting polymers with the redox reaction of metal oxides. The synergy in the composite results in state-of-the-art energy storage performance in a supercapacitor electrode.¹⁵

1.2.2 Conducting Polymer-based Sensors

The electrical conductivity of a conducting polymer changes as a function of doping level and temperature. Dopants are mobile charge carriers inside the polymer, and high dopant concentration results in high electrical conductivity.^{36,37} The electrical conductivity in semiconductors such as conducting polymer originates from the promotion of charge carriers from the valence band to the conduction band. When heated, the valence band charge carriers

possess high internal energy and are readily promoted to conduction band, therefore as temperature increases the electrical resistance of semiconductor decreases.³⁸ Conducting polymer-based sensors utilize this tunable electrical conductivity for temperature sensing and chemoresistive sensing.

Wearable temperature sensors are fabricated by coating conducting polymer on textile or other flexible and stretchable substrate. Research on wearable sensors focuses on increasing the sensitivity and response time of the sensor. High sensitivity and short response time are achieved by creating nanostructures in the conducting polymer coating during or after synthesis.^{39,40} Additionally, conducting polymers are also utilized in chemoresistive sensors for detecting ammonia, nitrogen dioxide, or changes in relative humidity (water).⁴¹

1.2.3 Photothermal Application of Conducting Polymers

Photothermal effect is produced when the electrons inside a material are excited by photons then undergo nonradiative decay and release phonons, resulting in the production of heat. Conducting polymers such as PEDOT and polypyrrole exhibit strong absorption of light in the near infrared wavelength and high efficiency in photothermal conversion. Therefore, these polymers are widely studied as photothermal therapy and photoacoustic imaging agents, as well as photothermal anti-icing/deicing coatings.^{27–30}

Conducting polymer nanoparticles with sizes between 40 and 70 nm are biocompatible and absorbable by cells via endocytosis. Past research on photothermal therapy demonstrate that cancer cells often possesses a higher concentration of polymer nanoparticles than normal cells due to their enhanced metabolism. When exposed to an infrared laser (typically 808 nm), the

high concentration of conducting polymer nanoparticles in cancer cells lead to rapid heating, resulting in death of cancer cells with minimal damage to adjacent normal cells.^{27,28}

1.2.4 Electromagnetic Interference (EMI) Shielding Application of Conducting Polymers

The rapid development of electronic and wireless devices have overcrowded communication channels with different frequencies of electromagnetic waves. Electromagnetic interference shielding is of great importance in medical, communications, and military applications for filtering out unwanted frequencies and avoiding interference between components in electronic devices.⁴² EMI shielding is traditionally achieved via metal casing; however, metals are prone to corrosion, and their densities results substantial weight when applied at large scale. In recent years, conducting polymers rise as promising alternatives to metals in EMI shielding due to their high shielding efficiency, light weight, and stability in environment that is usually corrosive to metals.⁴²

EMI shielding is achieved through three mechanisms: reflection, absorption, and multiple internal reflection. Reflection is the surface of a material rejecting part of an incident EM wave, similar to light reflecting on the surface of glass. Absorption takes place when the incident EM wave induces alignment of electrical or magnetic dipoles in a material. The alignment of dipoles generates an EM wave that is out of phase to the incident wave, resulting in destructive interference that reduces the amplitude of the incident wave. Multiple internal reflection utilizes the structure and thickness to reflect an incident EM wave within a material repeatedly. These reflections consumes the energy of an incident wave, resulting in reduced amplitude.⁴³ Conducting polymer-based coating typically utilizes absorption mechanism for EMI shielding.

Improving the electrical conductivity of the polymer enhances the electric dipole moment in the material, resulting in state-of-the-art shielding performance.³²

1.3 Common Synthetic Strategies

Conducting polymers are typically synthesized through three routes: electrochemical, solution-phase, and vapor-phase. Both solution- and vapor-phase syntheses require an oxidant to initiate the polymerization, whereas electrochemical polymerization utilizes an oxidative potential to initiate polymerization and obviates the need of an oxidant.

1.3.1 Electrochemical Synthesis of Conducting Polymers

Electrochemical polymerization typically utilizes cyclic voltammetry in a three-electrode electrochemical cell that consists of a working, a counter, and a reference electrode (Figure 1.5). Polymer synthesized via this method is usually deposited on the working electrode as a film. Thickness, conjugation length, and doping level of the synthesized polymer film are controlled via altering parameters of the electrochemical cell, such as voltage, scan rate, pulsed or constant current, polymerization time, electrolyte concentration, types of solvent, and pH.^{44–47}

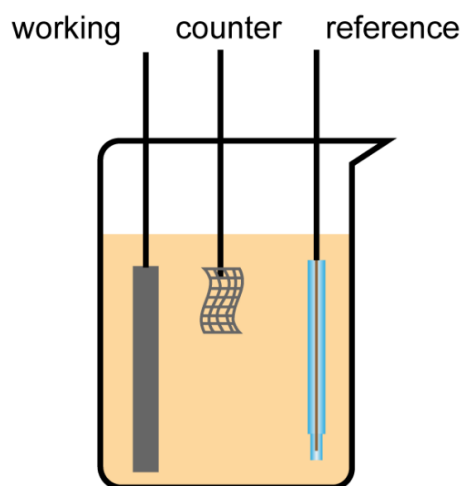


Figure 1.5 Schematic diagram of a three-electrode electrochemical cell.

An essential equipment for electrochemical polymerization is the potentiostat (developed from polarograph, Figure 1.6), and it is used for controlling parameters of a three-electrode cell and recording data.⁴⁸ As such, some seminal works of electrochemical polymerization were published in the 1980s and 1990s with the development of digital potentiostats.^{49–52} The coupling of voltammetry, spectroscopy, and spectroelectrochemistry assisted the understanding of polymerization mechanisms and intermediate species during synthesis. In 1987, Geniès et al. demonstrated an oxidized aniline formed both cationic radical and nitrenium cation. The formation of nitrenium ion resulted in two non-equivalent polyaniline structures due to coupling at both *para* and *ortho* positions.⁴⁹ This discovery supplemented the aniline polymerization mechanism previously proposed by solution-phase studies.⁵³ In 1990, Łapkowski electrochemically polymerized aniline in various acids, including hydrochloric, sulfuric, perchloric, and tetrafluoric acids, and observed the nitrenium cation during the initial stage of polymerization via spectroelectrochemical measurements.⁵⁰ Łapkowski's experiments confirmed the mechanism of aniline polymerization proposed by Geniès et al. Additionally, he demonstrated excess nitrenium ions created defects in polyaniline backbone and disrupted the formation of linear polyaniline structure.⁵⁰ Aside from deconvoluting polymerization mechanisms, early research in electrochemical polymerization also revealed that electrical conductivity of polymers is due to redox reaction in the π -conjugated backbone instead of electroactive pendant groups. In 1981, Diaz et al. electrochemically polymerized pyrrole and demonstrated the polymer film was capable of repeated switching between insulating and conductive states.⁵¹ Their analysis suggested that polypyrrole was cationic during synthesis and contained anionic dopants (one anion per four pyrrole units). Diaz et al. were one of the first to

electrochemically characterize highly conductive organic polymer films. They also demonstrated that polymers similar to polypyrrole were redox active and electrically conductive due to the delocalization in their π -conjugated backbones.⁵¹

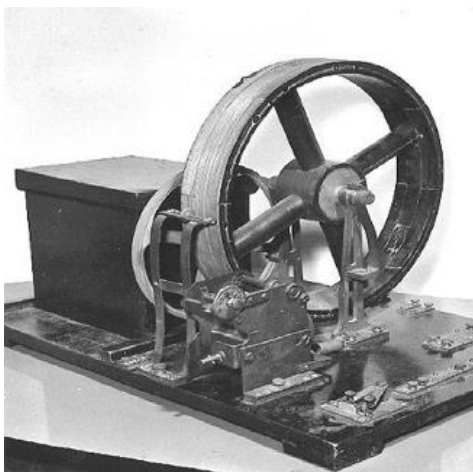


Figure 1.6 Jaroslav Heyrovský invented the first polarograph in 1922. Adapted from Reference 48 and is in the public domain.

1.3.2 Solution-phase Synthesis of Conducting Polymers

In solution-phase synthesis, both oxidant and monomer are mixed in a solvent; the polymer product nucleates and precipitates out of the solution via either homogeneous or heterogeneous nucleation. Nucleation of polymer product is controlled via experimental parameters, such as the interface between solution and nucleation sites, surface tension of the solvent, reaction temperature, and mechanical agitation.^{54–59}

The history of solution-phase synthesis traces back to 1958 with Natta's publication on polyacetylene.⁶ This polymer was systematically studied over the next decades, specifically its synthetic routes and methods of enhancing electric conductivity.⁷ However, polyacetylene is not stable in air, and doping the polymer often involves toxic compounds such as AsF_5 .⁵² Thus, research interest gradually shifted to chemical synthesis of conducting polymers that are stable

under ambient conditions and do not require toxic dopants, such as polyaniline, polypyrrole, and polythiophene. These polymers can be synthesized in bulk quantities while their syntheses only require solutions of ammonium persulfate (APS) or iron(III) salts as oxidants.^{60–62} In 1988, scientists from Bayer AG developed a polythiophene derivative, poly(3,4-ethylenedioxythiophene) (PEDOT), and the polymer soon gained much research interest due to its high electrical conductivity and stability under ambient conditions.^{33,34,63} In 1995, Yamato et al. reported a synthesis incorporating a polyanion polystyrene sulfonate (PSS) into polypyrrole and PEDOT that enhanced the polymers' water solubility.⁶⁴ This breakthrough greatly enhanced processability and resulted in PEDOT:PSS becoming one of the most widely used commercialized conducting polymers.

1.3.3 Vapor-phase Synthesis of Conducting Polymers

Vapor-phase synthesis is typically achieved through two different techniques: chemical vapor deposition (CVD) and vapor-phase polymerization (VPP). VPP is a conventional technique that flows monomer vapor onto a substrate pretreated with oxidant, and the polymerization often occurs at an interface (vapor/liquid or vapor/solid). CVD is a newer synthetic technique that utilizes both oxidant and monomer in the vapor phase for polymerization.^{65–69} Vapor-phase synthesis excels at creating a homogeneous coating of polymer film on the substrate, and the thickness is controlled via reaction time and stoichiometry of reactants. Additionally, the concentration of proton scavengers (water and anions from the oxidant) are crucial for the formation of highly conjugated polymer backbone because they remove excess charges and stabilize a newly formed polymer backbone. Past research has demonstrated precise tuning of

electrochemical properties of a conducting polymer via adjusting the humidity during the reaction.^{70–73}

The earliest account of conducting polymer vapor-phase synthesis was in 1986 by Ojio and Miyata. They dissolved FeCl_3 in a poly(vinyl alcohol)/water mixture and cast the gel onto plastic substrates, such as poly(ethylene terephthalate) and poly(methyl methacrylate). Polymerization was carried out by exposing the oxidant-impregnated substrate to pyrrole and water vapors, and transparent polymer composite films with electrical conductivity were obtained.⁶⁶ Subsequent publications from other researchers reported deposition on other types of polymer substrates including polyolefins, and the effect of altering anions in the oxidants on electrical conductivity of polypyrrole films.⁶⁹

Vapor-phase synthesis often produces a continuous film with high crystallinity that possesses high electrical conductivity due to its unique kinetics.⁷⁵ Monomers such as pyrrole and thiophene polymerize via a step-growth mechanism; both monomer and oligomer are reactive during polymerization and form longer chains via coupling, resulting in a wide distribution of molecular weight and conjugation length.⁷⁶ During the initial stage of polymerization, monomers are depleted rapidly, resulting in the formation of dimers, trimers, and other oligomers. When the stoichiometry of reactants is uncontrolled, synthesis is often accompanied with polymer branching and short conjugation length in the polymer backbone.⁷⁶ In comparison, chain-growth polymerization controls the regioregularity of a synthesized product, and polymers synthesized through this mechanism usually have more uniform distribution of molecular weight than polymers that undergo step-growth mechanism.^{76,77} The reaction conditions of a vapor-phase synthesis alters polymerization by mimicking a chain-growth mechanism and induces the

formation of highly conjugated polymer backbones. Hence this synthetic strategy often produces conducting polymer films that possesses enhanced electrical conductivity.^{71,72,78,79} In 2010, Fabretto et al. used PEDOT as an example to explore the correlation between film growth mechanism in vapor-phase synthesis and electrical conductivity of PEDOT films.⁸⁰ The growth of a PEDOT film during vapor-phase is divided into four stages based on changes in mass (Figure 1.7). During the first stage, limited mass transport leads to monomer molecules scarcely arriving at the oxidant-rich substrate surface (rate-limiting step), resulting in the oxidant immediately reacting with any monomer that arrives. The second stage occurs when polymerization forms a confluent polymer film on the substrate and covers the unreacted oxidant. During this stage, the rate-limiting step is electron transfer during the oxidation of monomers or oligomers due to limited availability of conductive pathways on the nascent polymer film. The availability of conductive pathway increases and reaches a percolation threshold (stage three) as more polymers are produced, and the reaction rate sharply increases. During the last stage of polymerization, the rate limiting step switches back to the diffusion of monomer vapor, and the reaction rate plateaus as limited mass transport stifles polymerization. The largest conductivity increase is observed during and at the end of stage two. This is due to the limited conductive pathways restricting polymerization to only selected sites, resulting in the formation of highly conjugated polymer backbones that possess enhanced electrical conductivity.⁸⁰

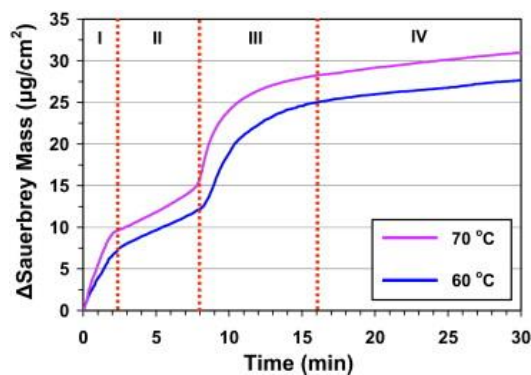


Figure 1.7 Four stages of vapor-phase synthesis. Adapted with permission from Reference 80. Copyright 2010, Elsevier.

1.3.4 Current Research in Conducting Polymer Synthesis

Research in conducting polymer synthesis has developed rapidly and is much more diverse than the 1970s. The advancement in microscopy, especially electron microscopes (scanning, transmission, and scanning tunneling) and atomic force microscope, assisted research in conducting polymer synthesis and nanostructure characterization.⁸¹ Characterization at sub-micron scale facilitates the understanding of structure-property relationship in nanostructured conducting polymers, and most publications in current research involves controlling and characterizing the polymer's nanostructure. Recent publications demonstrate that chemically modifying the polymer chains enhance electrochemical performance and processability of nanostructured polymers and their composites. For example, electrochemically depositing polypyrrole on carbon foam and polydopamine promotes ion transfer while reducing the stacking density of polypyrrole, resulting in a supercapacitor electrode with outstanding areal capacitance.⁴⁷ Post-synthetic chemical treatment alters the electrical conductivity and sorption properties, and opens up potential for tailoring conducting polymers to various applications including electrochemical desalination, cation selective membranes, and electrodialysis.⁴⁴

Development of alternative synthetic routes to the commonly used oxidative polymerization is another focus in current research.^{54–56,82–85} The most notable among these is transition-metal-catalyzed polycondensation. The mechanisms involved in this strategy are also step-growth polymerization, therefore developing catalysts or finding reaction conditions that allow more control over molecular weight, dispersity, and regioregularity is crucial.^{77,85} Since most catalysts require palladium and nickel, another emphasis in the research of transition-metal-catalyzed synthesis is developing cheaper catalysts (without palladium or nickel) and solvent-free methods to lower the cost of production.^{55,77} Studies that utilizes the more conventional oxidative polymerization concentrate on controlling nanostructures and synthesizing composites of conducting polymers. Many groups demonstrate significant progress in improving conducting polymers' performance in application such as energy storage, heavy metal ion removal, bioelectronics, and oxygen evolution catalysts.^{54–56,83} Additionally, enhancing the interactions between a nanostructured conducting polymer film and its substrate is also crucial. Enhanced polymer/substrate interaction promotes charge transfers in conducting polymers and improves the stability of the material, which is beneficial for electrodes fabricated for energy storage devices and wearable electronics.^{86–89}

1.4 Oxidative Polymerization Mechanism

Polyaniline, polypyrrole, polythiophene, and their derivatives are among the most widely studied conducting polymers in current research.⁷⁷ Both pyrrole and thiophene are five-membered heterocycles and share a similar oxidative polymerization mechanism (Figure 1.8). The initiator (typically ferric salts, persulfates, or peroxides) oxidizes the monomer into a cationic radical. This radical possesses several resonance structures and is most stable when the positive charge is

on the hetero atom with the radical in the α position.⁹⁰⁻⁹² Two cationic radicals undergo coupling and deprotonation to form a neutral dimer. The oxidation, coupling, and deprotonation steps are cyclic, yielding a π -conjugated polymer chain. When the polymer is further oxidized, anions (dopants) are incorporated via oxidative doping to balance the overall charge of the material (Figure 1.9). Oxidative doping takes place concomitantly with polymerization, delocalizes π electrons on the polymer backbone, and introduces mobile charge carriers, resulting in an electrically conductive material.

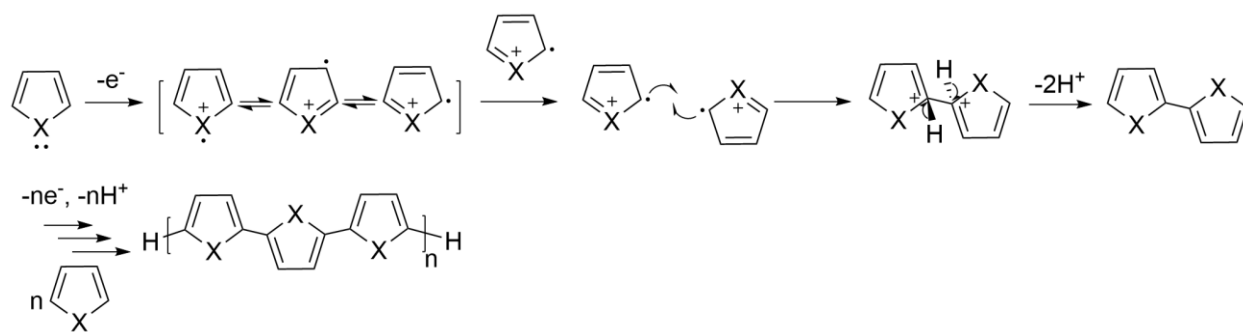


Figure 1.8 Polymerization mechanism of five-membered heterocycles.

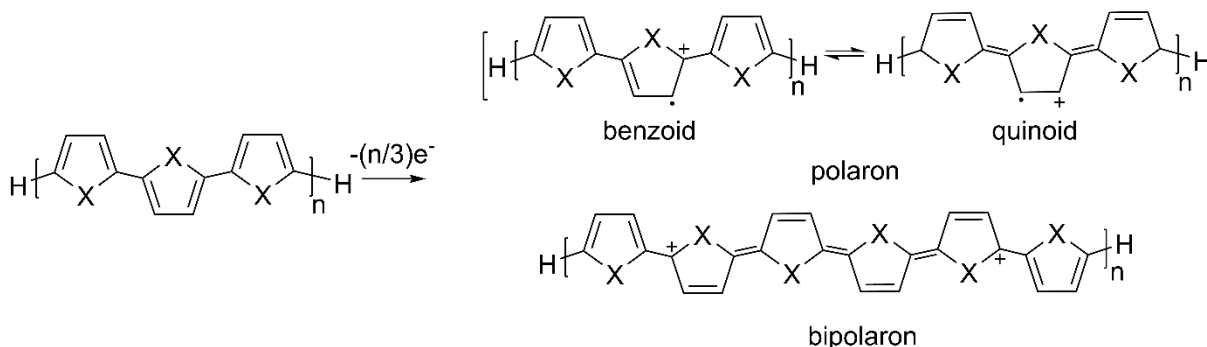


Figure 1.9 Oxidative doping of polypyrrole and polythiophene.

Oxidative polymerization of aniline is slightly different from the mechanism of pyrrole and thiophene (Figure 1.10). Spin density studies of the cationic radical's resonance structures suggest that the unpaired electron residing on the nitrogen atom and the *para*-carbon are both

favorable.⁹³ This gives rise to three possible coupling scenarios during polymerization: nitrogen-nitrogen coupling (head-to-head), nitrogen-arene coupling (head-to-tail), and arene-arene coupling (tail-to-tail). Head-to-head coupling is unlikely because its product is unstable under the acidic environment during polymerization. Additionally, previous study demonstrates that tail-to-tail coupling is more favorable than head-to-tail coupling.⁹²⁻⁹⁵ Thus, two aniline cationic radicals undergo arene-arene coupling and deprotonation to form a dimer. The cationic radical of aniline dimer undergoes head-to-tail coupling with other aniline radicals and forms a trimer after deprotonation. Similar to mechanism for five-membered heterocycles, polymerization of aniline consists of repeated oxidation, coupling, and deprotonation. Polyaniline possesses three oxidation states, leucoemeraldine base, pernigraniline base, and emeraldine base, with its conductive form as a salt of emeraldine base. Additionally, polyaniline undergoes both oxidatively and protonically doped in its emeraldine base form.⁹⁶ The polymerization of aniline, pyrrole, and thiophene are step-growth mechanisms, which means ideally both monomeric and oligomeric radicals will undergo coupling. The step-growth nature of these polymers also enables in-situ self-assembly of nanostructures and have attracted much research interest in developing novel synthetic strategies for nanostructured conducting polymers.^{76,97-99}

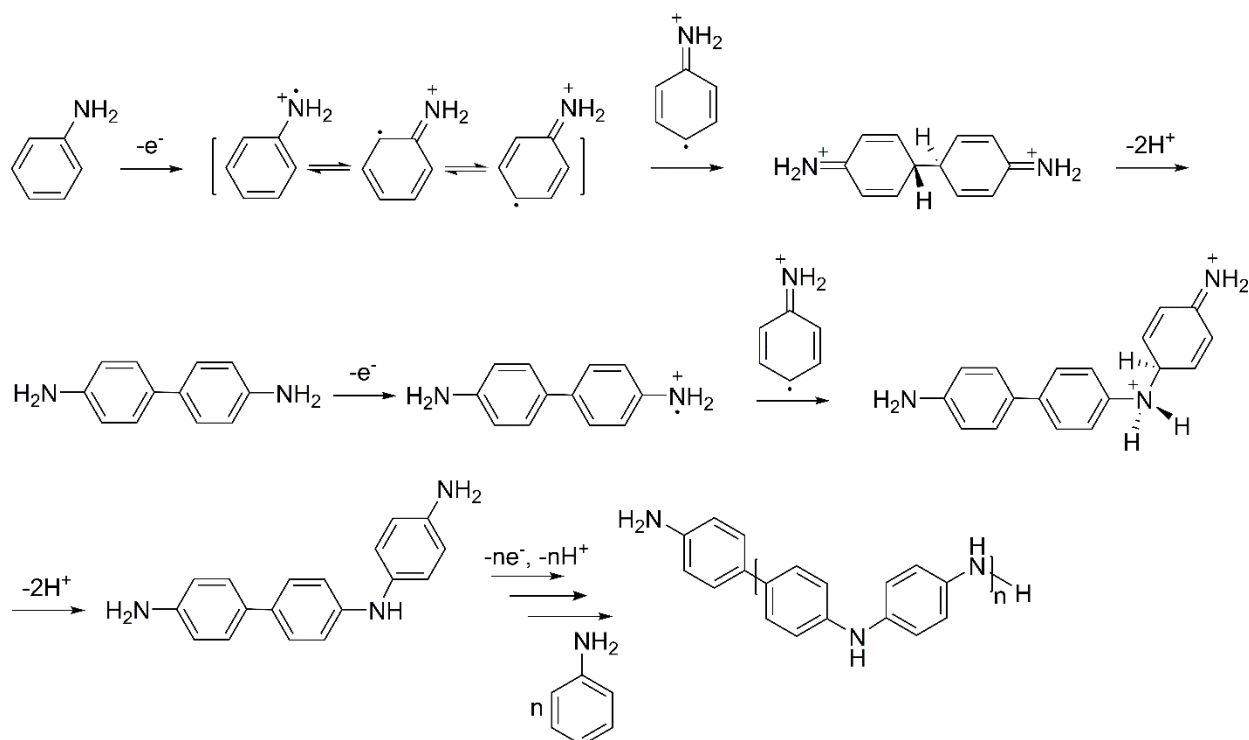


Figure 1.10 Polymerization scheme of aniline.

1.5 Synthesis of Nanostructured Conducting Polymers and Composites

Nanostructured materials are defined as materials with structural features on the scale between 1 and 100 nm.¹⁰⁰ Creating nanostructures in a conducting polymer increases its surface area to volume ratio, resulting in enhanced physical and chemical properties, such as ion transfer, adsorption/desorption efficiency, and electrical conductivity.^{101–107} Therefore, tailoring nanostructures offers a handle to control the electrochemical properties of conducting polymers.¹⁰³ Nanostructured conducting polymers are categorized into 0D spheres, 1D fibers/rods/wires/tubes, 2D sheets/flakes, and 3D structures (spatial ensemble of 1D/2D structures, nanoporous structures, or hierarchical structures) (Figure 1.11).^{79,108–111} These structures are produced via templated synthesis and template-free synthesis.¹⁰³

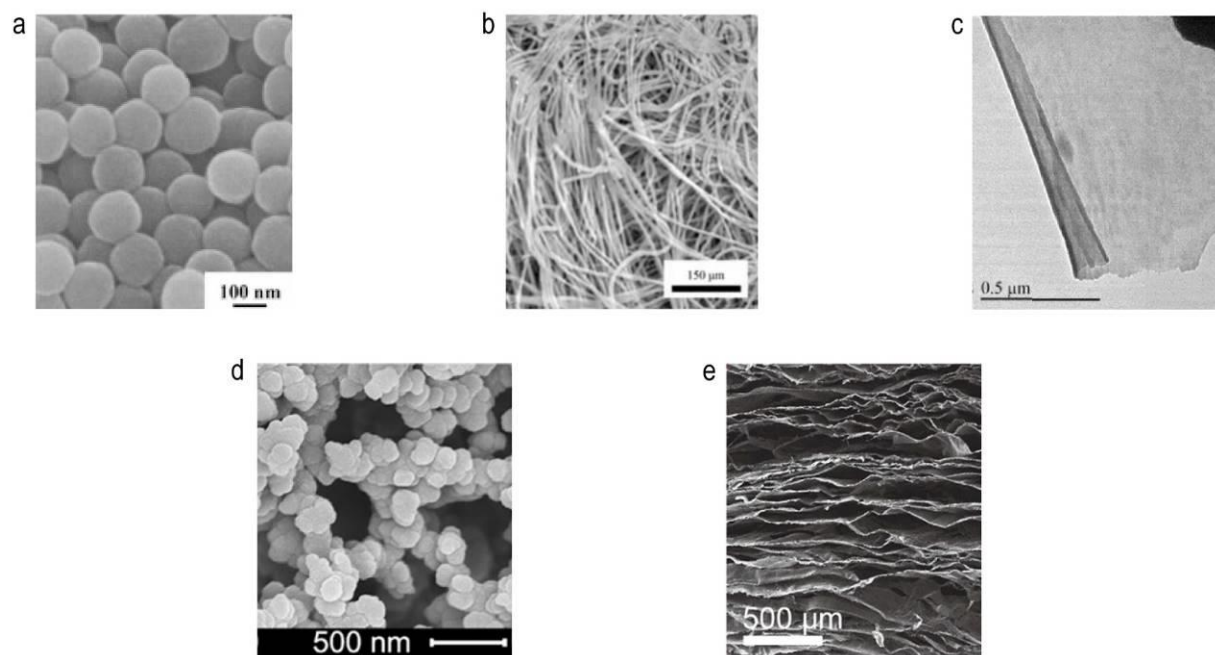


Figure 1.11 Nanostructured conducting polymers. a) 0D particle, b) 1D fiber, c) 2D sheet, d) and e) 3D structures (ensemble of lower dimensional features and hierarchical structures). Adapted with permission from References 79, 109, 110. Copyright 2022, American Chemical Society. Adapted with permission from Reference 108. Copyright 2016, Elsevier. Adapted with permission from Reference 111. Copyright 2022, MDPI.

1.5.1 Templated Synthesis of Nanostructured Conducting Polymers

Templated synthesis is an efficient route for controlling morphology and size of nanostructured conducting polymers.¹⁰³ Depending on the nature of a template, the synthesis is either a hard-template synthesis (e.g., polymer or oxide-based templates) or a soft-template synthesis (e.g., droplet or micelle templates). The structure of a product is dictated by the template used, hence controlling the dimensions and shapes of a template is crucial.

Hard-template synthesis utilizes the structure of solid-state materials to guide the formation of conducting polymer nanostructures. Inorganic materials such as porous silica (SiO_2), alumina (Al_2O_3), and carbon (graphite oxide, activated carbon) are all ideal templates because they are inert and processable in bulk quantities. Additionally, these templates possess large surface area that enhances the electrochemical properties of conducting polymers.^{21,31,112,113} Polymer

materials such as polyurethane, polystyrene, polyester, and polycarbonate are also popular choices because they are both templates and flexible/stretchable substrates.^{114,115} Other templates include oxidative compounds such as vanadium oxide (V_2O_5) and manganese dioxide (MnO_2). They are both templates for nanostructure formation and oxidants for initiating polymerization, resulting in composites that possess synergy between the inorganic oxide and the organic polymer components.^{116–124}

Soft-template synthesis utilizes fluid-like state dispersions, such as emulsion, reverse emulsion, and clusters of organic small molecules for nanostructure formation. This type of template is easier to remove after synthesis than hard templates but more difficult to control in shapes and sizes.¹⁰³ In emulsion synthesis, the more polar oxidant resides in the dispersed water phase and the less polar monomer dissolves in the oil phase. Typical emulsifiers include sodium dodecyl sulfate (SDS), sorbitan monooleate (Span 80) and poly(oxyethylene) sorbitan monooleate (Tween 80). The emulsifier stabilizes the dispersed phase, and the polymer nucleates at the interface between oil and water.^{125–128}

1.5.2 Template-free Synthesis of Nanostructured Conducting Polymers

Template-free synthesis does not require preparation or removal of templates and is usually more cost-effective compared to templated synthesis.¹⁰³ This technique exploits external electric fields, molecular interactions (van der Waals force and hydrogen bonding), and interfaces to guide the formation of nanostructures.

Electrospinning is one of the most efficient techniques in creating 1D nanofibrillar conducting polymers. This technique utilizes an electrostatic field and creates a jet of a charged solution that forms fibrillar structured polymer.¹⁰³ Oxidative polymerization and the spinning process are

concomitant. Electrospinning often produces long continuous nanofibers; however, it also requires other non-conductive polymers as additives to assist the fiber formation, resulting in decreased electrical conductivity.^{111,129,130}

Self-assembly techniques takes advantage of interfaces and molecular interactions to arrange conducting polymers into an organized structure.^{98,103,131} Although self-assembly often favors a thermodynamically stable structure, controlling variables such as temperature, surface tension, and pH, alters the preference of a self-assembly process and enables trapping of kinetically-driven states. For example, polymerizing aniline at a water/chloroform interface under controlled temperature range (between 5 and 60 °C) results in uniform nanofibrillar polyaniline. Aniline molecules are hydrophobic and prefers the organic phase, while the polymer is hydrophilic and prefers the aqueous phase. Therefore, the polymer backbone continuously float to the lighter aqueous phase, leading to linear addition of aniline units during coupling and a fibrillar structure.^{132,133}

1.6 Iron Corrosion Product (Rust) and Rust-based Vapor-phase Polymerization (RVPP)

Current research lacks in synthesizing nanostructured conducting polymers from the vapor phase. This dissertation focuses on addressing this issue and presents novel synthetic strategies that utilize iron corrosion product and iron(III) salts for vapor-phase synthesis of nanostructured conducting polymers and their composites. Iron(III) salts, oxides, and oxyhydroxides are utilized as oxidants for initiating oxidative polymerization. Forced hydrolysis of ferric ions results in crystallization of iron(III) oxides, hydroxides, and oxyhydroxides that are responsible for directing nanostructure formation during polymer synthesis. Varying reaction conditions, such as

temperature, reaction time, or anions in the iron(III) salts, create a spectrum of morphologies (0D particles, 1D fibers, and amorphous films). The following chapters will focus on how to utilize iron corrosion product and iron salts in nanostructured conducting polymer synthesis by creating synergy between three mechanisms: dissolution, hydrolysis, and oxidative polymerization. Additionally, strategies for overcoming challenges in solution processing of conducting polymers are also presented.

1.6.1 Brief Introduction to Iron Corrosion Product

Iron corrosion product, colloquially known as rust, is a collective name for the oxides, hydroxides, and oxyhydroxides produced from hydrolysis of ferric ions in water. Sixteen distinct phases of iron corrosion product exist naturally under different temperature, pH, and pressure (Figure 1.12).^{134–153} Currently, the value of an iron corrosion product such as hematite (α -Fe₂O₃) originates from its stability, low cost, catalytic property,^{154,155} and multi-state redox activity.¹⁵⁶ Hematite nanoparticles serve as catalyst for organic synthesis,¹⁵⁷ photocatalyst for dye degradation,^{158,159} hydrogen evolution,¹⁶⁰ and redox-active electrodes for batteries.^{156,161} Iron corrosion product is also an ideal oxidant for conducting polymer synthesis due to the oxidative nature of ferric ions, and various papers reported using size-controlled iron oxyhydroxide nanoparticles for templated conducting polymer composite synthesis in the past decade.^{162–165} For example, akageneite (β -FeOOH) contains chloride-filled channels in its crystal structure, making it an ideal component in a nanocomposite with polyaniline for chromium ion removal.¹⁶⁴ Other phases such as lepidocrocite (γ -FeOOH) consists of two-dimensional layered structure, and its interlayer distance is useful for ion transport. A composite between polypyrrole and lepidocrocite results in a supercapacitor electrode with high capacitance and cycle stability.¹⁶⁵

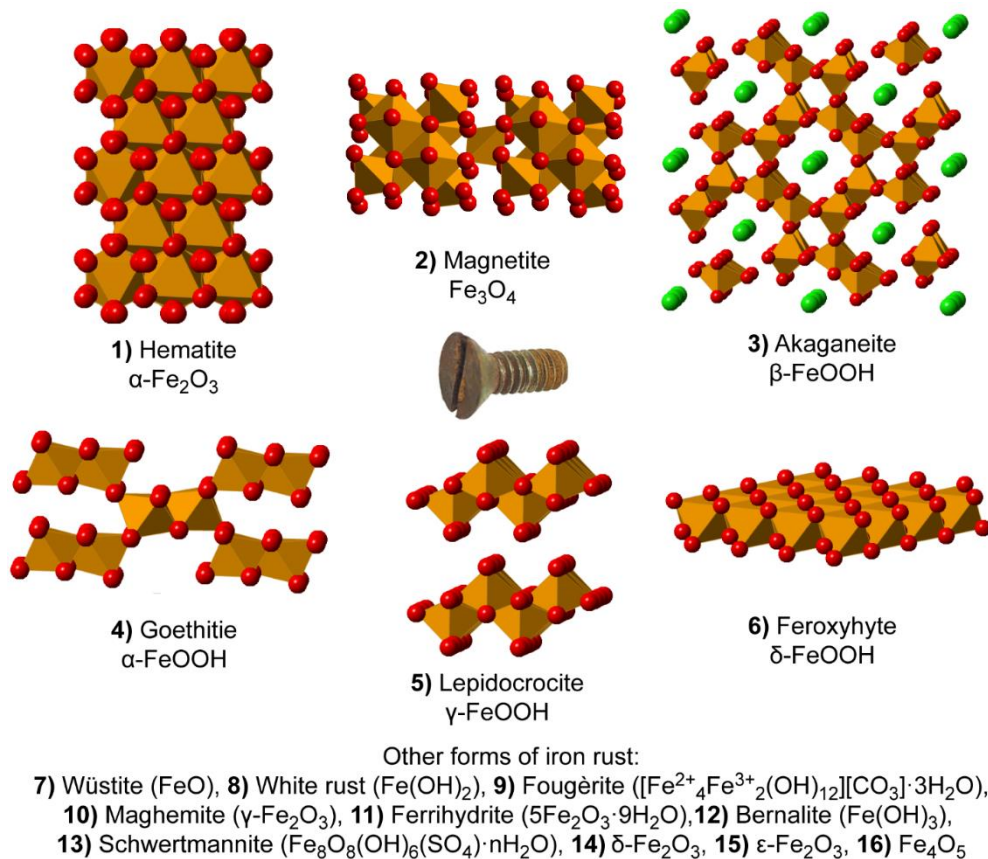


Figure 1.12 Chemical formulas and names of all naturally occurring phases of iron corrosion product. Crystal structures represent the six most common phases.

1.6.2 Hydrolysis of Ferric Ions

Hydrolysis is a solution phase reaction of water (solvent) molecules breaking chemical bonds in solute molecules.^{166,167} If the solute is organic, a water molecule functions as a nucleophile and participates in a substitution reaction where hydroxyl groups ($-\text{OH}$) replaces leaving groups ($-\text{X}$) of a solute molecule. For an inorganic solute, two water molecules form a hydronium (H_3O^+) and a hydroxide (OH^-) ion. The negatively charged hydroxide ions replace the original anions of the solute and form a hydroxide via bonding with the cation (Figure 1.13). Ferric ion hydrolysis produces metastable products that precipitate from the solution as oxides, hydroxides, and oxyhydroxides (iron corrosion product). Various experimental factors, including temperature,

pH, polarity of the solvent, spectator ion, and concentration of Fe^{3+} , influence the final composition and structure of a hydrolysis product. Hydrolysis is favored in basic pH and is driven by elevated temperature. Spectator ions do not participate in hydrolysis; however, they influence the overall pH of the reaction and the formation of iron oxide/hydroxide/oxyhydroxide crystal structures.^{134,168,169} During crystallization, Ostwald ripening, oriented attachment, and splitting growth collectively affect the structure of crystals.^{170–174} In Ostwald ripening, smaller crystals re-dissolve and merge with larger crystals. This process is energetically favored because it reduces the amount of iron species exposed at the surface of crystals and increases the amount of iron atoms that are coordinated in octahedral form. Oriented attachment directs the crystallization by alignment of crystallographic orientations through Coulombic interactions and Lewis acid-base interactions (Figure 1.14). Splitting growth occurs when Fe^{3+} is oversaturated and results in formation of spindle-like crystals (Figure 1.15).^{173,174} Ostwald ripening and oriented attachment are competing mechanisms during crystallization, and the occurrence of one over the other is determined by the local curvature of the crystal.¹⁷⁰

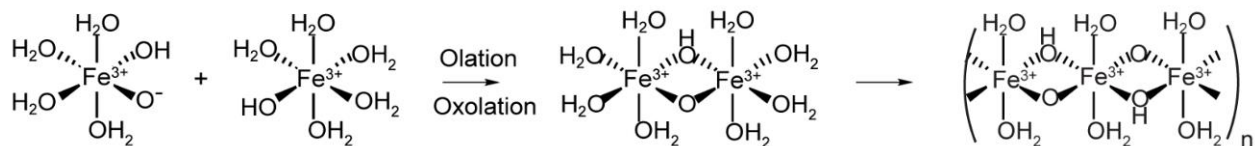


Figure 1.13 Hydrolysis scheme of octahedral iron(III) complexes.

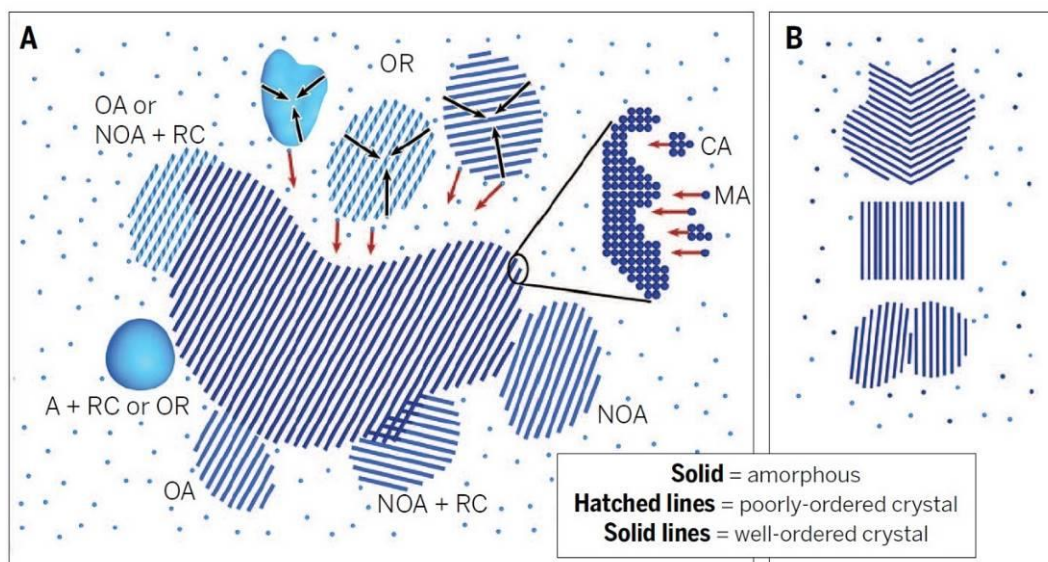


Figure 1.14 Oriented attachment and Ostwald ripening during crystallization. (A) The arrows indicate the direction of motion of monomers, clusters, or surfaces, and the dashed lines give the crystallographic orientations of nanocrystals. The expanded oval shows molecular-scale processes. OR, Ostwald ripening; MA, molecular attachment; CA, cluster attachment; A, amorphous addition; OA, oriented attachment; NOA, non- or semi-oriented attachment; RC, recrystallization. (B) Twins, stacking faults, and dislocations can result from the attachment of crystalline particles. Adapted with permission from Reference 170. Copyright 2015, American Association for the Advancement of Science.

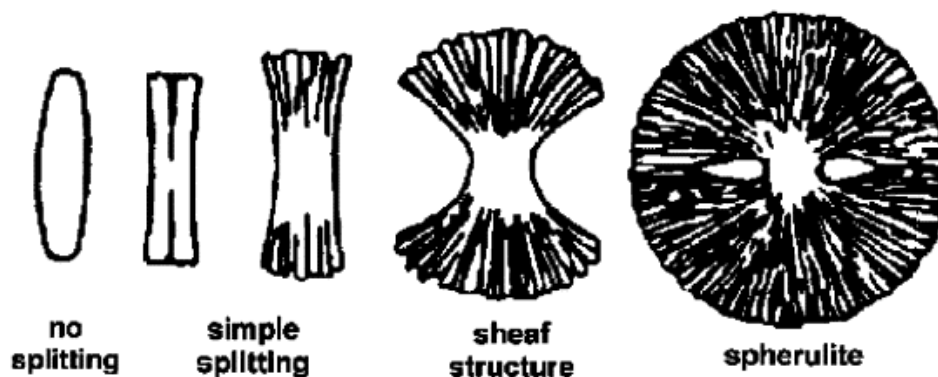


Figure 1.15 Splitting growth during crystallization. Adapted with permission from Reference 173. Copyright 2006, American Chemical Society.

1.6.3 Dissolution of Iron Corrosion Product

Dissolution releases ferric ions (oxidant for polymerization) from an iron corrosion product and consists of three separate mechanisms that take place simultaneously. Figure 1.16 explains these mechanisms using dissolution of an iron(III) oxyhydroxide in oxalic acid as example. The first

mechanism is dissolution via protonation, where the bonding between oxo/hydroxo groups and a surface iron(III) is broken by protons. The iron atom retains its oxidation state and is dissolved as an aqueous ferric ion (Figure 1.16a). Figure 1.16b is dissolution via ligand complexing, where complex formation weakens the oxo and hydroxo bonds between surface iron species and facilitates dissolution. The last mechanism is reductive dissolution, where the surface iron(III) leaves the bulk oxyhydroxide as an iron(II) complex. Iron(II) complex in the solution acts as a catalyst and reduces iron(III) on the surface of oxyhydroxide to iron(II), then both ferrous and ferric ions dissociate from the bulk material in aqueous form. The rate-limiting step during reductive dissolution is the reduction and release of ferrous ions, so depending on whether Fe^{2+} is present in the solution, the rate of this mechanism varies drastically (Figure 1.16c).¹⁷⁵

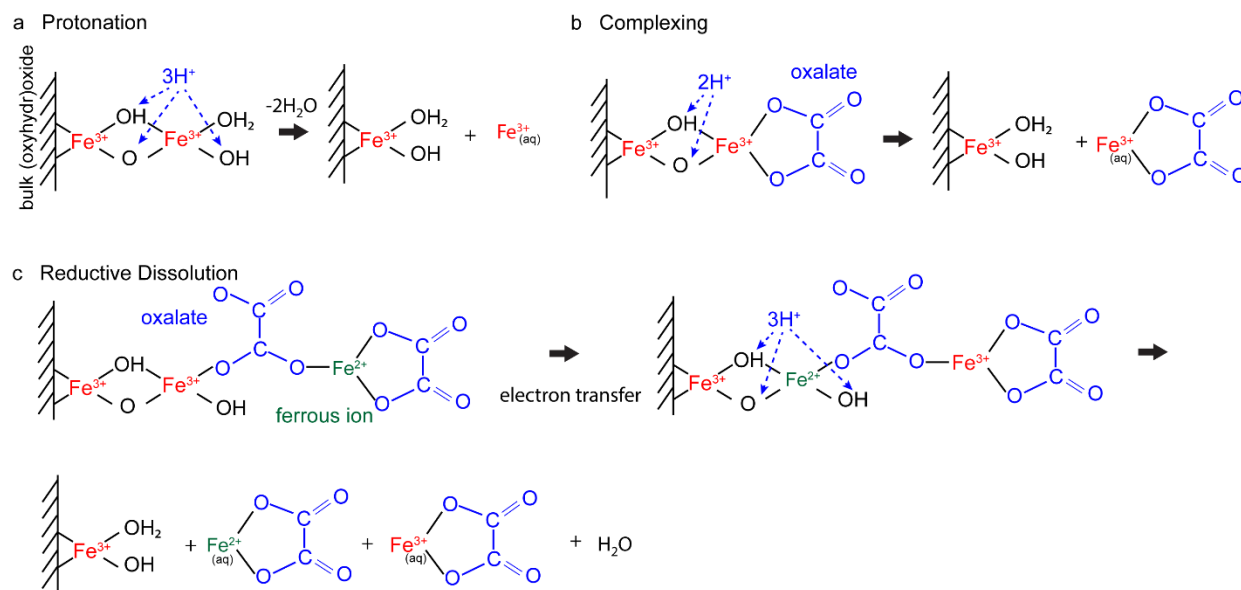


Figure 1.16 Dissolution scheme of iron(III) oxides/hydroxides/oxyhydroxides include: a) dissolution via protonation, b) dissolution via complexing, and c) reductive dissolution.

Various experimental parameters, such as phase of iron corrosion product, pH, temperature, type of ligand present in solution, and concentration of Fe^{2+} , alter the rate of dissolution (Figure

1.17).^{167–172} Previous studies demonstrate that when all the variables are equal, reductive dissolution mechanism is the most facile pathway, followed by ligand adsorption, and dissolution by protonation has the slowest reaction rate.^{177,179}

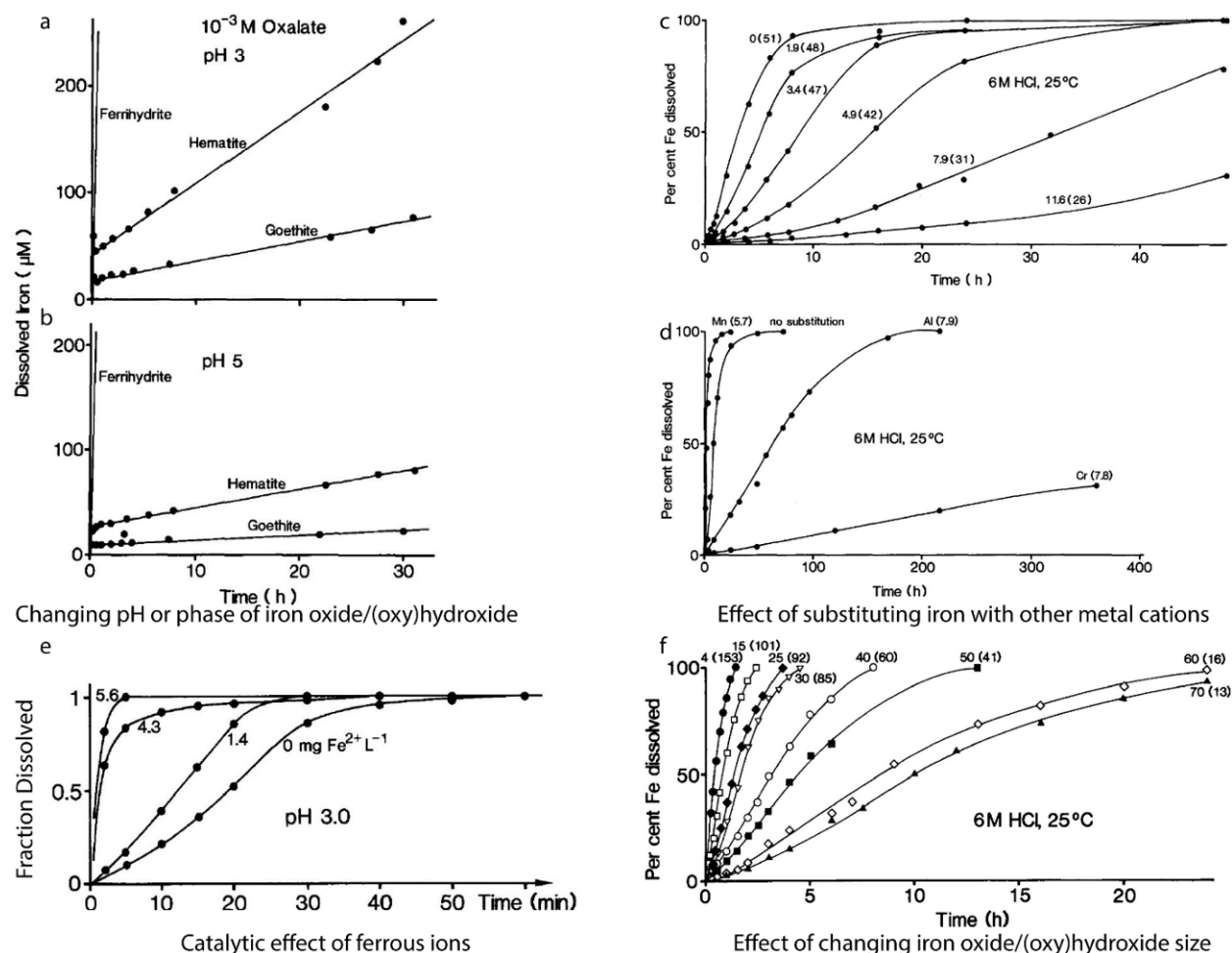


Figure 1.17 Experimental variables that alter the kinetics of dissolution. Adapted with permission from Reference 179. Copyright 1991, Springer Nature.

1.6.4 Proposed Mechanism for Rust-based Vapor-phase Polymerization (RVPP)

The proposed mechanism of rust-based vapor phase polymerization (RVPP) starts with the dissolution of iron corrosion product in the presence of hydrochloric acid (HCl) vapor. A liberated ferric ion either undergoes hydrolysis or initiates oxidative polymerization. Hydrolyzed

Fe^{3+} complexes form nanoparticles through homogenous nucleation, and these nanoparticles then serve as nuclei for heterogenous nucleation of polymers. The reaction continues as more polymer deposits on top of the oxidant layer, and the hydrolyzed nanoparticles merge and grow through Ostwald ripening, oriented attachment, and splitting growth. The growth of crystals directs the formation of polymer nanostructures (Figure 1.18). A core/shell-structured nanofibrillar composite with iron oxide/iron chloride core and polymer shell is produced via the mix-mechanistic pathway of dissolution, hydrolysis, and oxidative polymerization (Figure 1.19).^{162,181}

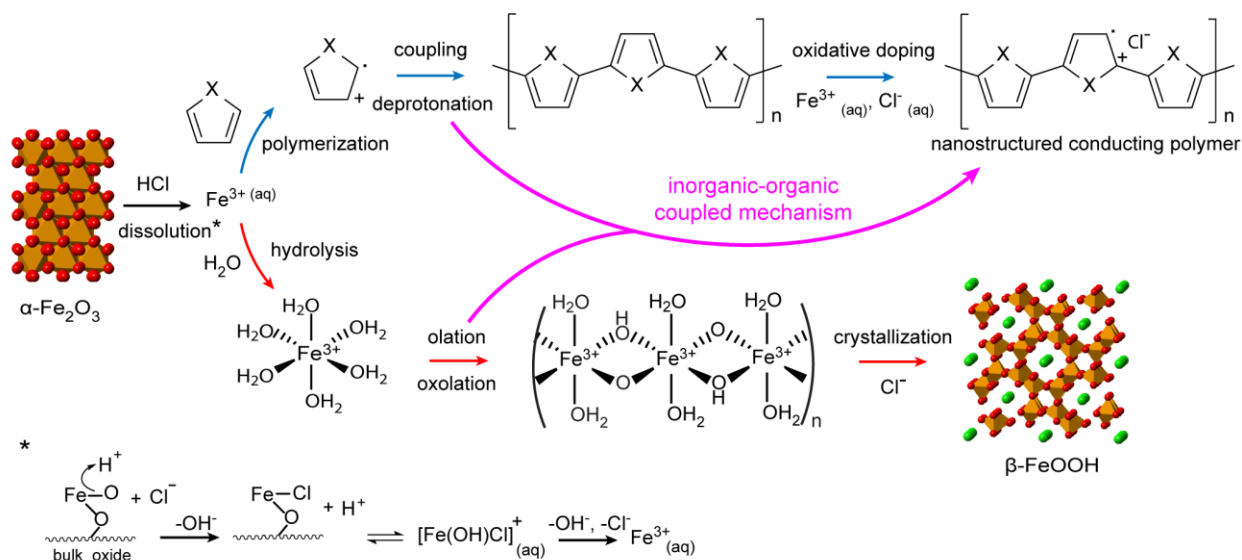


Figure 1.18 The mixed reaction pathways in rust-based vapor-phase polymerization.

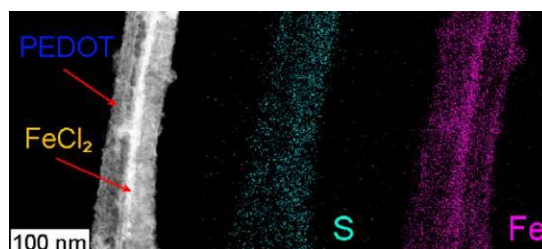


Figure 1.19 PEDOT nanofibers produced via RVPP consists of a core/shell structure. Adapted with permission from Reference 181. Copyright 2019, American Chemical Society.

1.7 References

- (1) Letheby, H. XXIX.—On the Production of a Blue Substance by the Electrolysis of Sulphate of Aniline. *J. Chem. Soc.* **1862**, 15 (0), 161–163. <https://doi.org/10.1039/JS8621500161>.
- (2) Nordén, B.; Krutmeijer, E. Advanced Information - The Nobel Prize in Chemistry 2000. 2000. <https://www.nobelprize.org/prizes/chemistry/2000/press-release/> (accessed 2023-02-15).
- (3) Inzelt, G. Conducting Polymers; Monographs in Electrochemistry; Springer Berlin Heidelberg: Berlin, Heidelberg, 2008; pp 265–269. <https://doi.org/10.1007/978-3-540-75930-0>.
- (4) Mota, M. L.; Carrillo, A.; Verdugo, A. J.; Olivas, A.; Guerrero, J. M.; de la Cruz, E. C.; Noriega Ramírez, N. Synthesis and Novel Purification Process of PANI and PANI/AgNPs Composite. *Molecules* **2019**, 24 (8), 1621. <https://doi.org/10.3390/molecules24081621>.
- (5) Rasmussen, S. C. Conductive Polymers; Zhang, Z., Rouabhia, M., Moulton, S. E., Eds.; CRC Press: Boca Raton, FL : CRC Press, Taylor & Francis Group, 2017., 2018; pp 1–22. <https://doi.org/10.1201/9781315119007>.
- (6) Ito, T.; Shirakawa, H.; Ikeda, S. Simultaneous Polymerization and Formation of Polyacetylene Film on the Surface of Concentrated Soluble Ziegler-Type Catalyst Solution. *J. Polym. Sci. A Polym. Chem.* **1996**, 34 (13), 2533–2542. <https://doi.org/10.1002/pola.1996.854>.
- (7) Feast, W. J.; Tsibouklis, J.; Pouwer, K. L.; Groenendaal, L.; Meijer, E. W. Synthesis, Processing and Material Properties of Conjugated Polymers. *Polymer (Guildf)* **1996**, 37 (22), 5017–5047. [https://doi.org/10.1016/0032-3861\(96\)00439-9](https://doi.org/10.1016/0032-3861(96)00439-9).
- (8) Shirakawa, H.; Louis, E. J.; MacDiarmid, A. G.; Chiang, C. K.; Heeger, A. J. Synthesis of Electrically Conducting Organic Polymers: Halogen Derivatives of Polyacetylene, (CH)_x. *J. Chem. Soc. Chem. Commun.* **1977**, No. 16, 578. <https://doi.org/10.1039/c39770000578>.
- (9) Chiang, C. K.; Druy, M. A.; Gau, S. C.; Heeger, A. J.; Louis, E. J.; MacDiarmid, A. G.; Park, Y. W.; Shirakawa, H. Synthesis of Highly Conducting Films of Derivatives of Polyacetylene, (CH)_x. *J. Am. Chem. Soc.* **1978**, 100 (3), 1013–1015. <https://doi.org/10.1021/ja00471a081>.
- (10) Dongmin Kang, S.; Jeffrey Snyder, G. Charge-Transport Model for Conducting Polymers. *Nat. Mater.* **2017**, 16 (2), 252–257. <https://doi.org/10.1038/nmat4784>.
- (11) Zhang, L.; Andrew, T. L. Deposition Dependent Ion Transport in Doped Conjugated Polymer Films: Insights for Creating High-Performance Electrochemical Devices. *Adv. Mater. Interfaces* **2017**, 4 (23), 1700873. <https://doi.org/10.1002/admi.201700873>.
- (12) Cao, G.; Cai, S.; Chen, Y.; Zhou, D.; Zhang, H.; Tian, Y. Facile Synthesis of Highly Conductive and Dispersible PEDOT Particles. *Polymer (Guildf)* **2022**, 252. <https://doi.org/10.1016/j.polymer.2022.124952>.

- (13) Loh, D. M.; Nava, M.; Nocera, D. G. Polypyrrole-Silicon Nanowire Arrays for Controlled Intracellular Cargo Delivery. *Nano Lett.* **2022**, 22 (1), 366–371. <https://doi.org/10.1021/acs.nanolett.1c04033>.
- (14) Hong, S. H.; Shi, H. H.; Naguib, H. E. Polypyrrole Nanofoam/Carbon Nanotube Multilayered Electrode for Flexible Electrochemical Capacitors. *ACS Appl. Energy Mater.* **2022**, 5 (4), 4059–4069. <https://doi.org/10.1021/acs.aem.1c02333>.
- (15) Shen, Z.-M.; Luo, X.-J.; Zhu, Y.-Y.; Liu, Y.-S. Facile Co-Deposition of NiO-CoO-PPy Composite for Asymmetric Supercapacitors. *J. Energy Storage* **2022**, 51 (December 2021), 104475. <https://doi.org/10.1016/j.est.2022.104475>.
- (16) Evans, D. R. Understanding PEDOT Doped with Tosylate. *Chemical Communications* **2022**, 58 (29), 4553–4560. <https://doi.org/10.1039/d2cc01100j>.
- (17) Sardana, S.; Gupta, A.; Singh, K.; Maan, A. S.; Ohlan, A. Conducting Polymer Hydrogel Based Electrode Materials for Supercapacitor Applications. *J. Energy Storage* **2022**, 45 (November 2021), 103510. <https://doi.org/10.1016/j.est.2021.103510>.
- (18) Nayak, P. D.; Ohayon, D.; Wustoni, S.; Inal, S. Tailoring Electropolymerized Poly(3,4-Ethylenedioxythiophene) Films for Oxygen Reduction Reaction. *Adv. Mater. Technol.* **2022**, 7 (2), 1–8. <https://doi.org/10.1002/admt.202100277>.
- (19) Xia, Y.; Ouyang, J. PEDOT:PSS Films with Significantly Enhanced Conductivities Induced by Preferential Solvation with Cosolvents and Their Application in Polymer Photovoltaic Cells. *J. Mater. Chem.* **2011**, 21 (13), 4927–4936. <https://doi.org/10.1039/c0jm04177g>.
- (20) Diao, Y.; Jung, S.; Kouhnavard, M.; Woon, R.; Yang, H.; Biswas, P.; D'Arcy, J. M. Single PEDOT Catalyst Boosts CO₂ Photoreduction Efficiency. *ACS Cent. Sci.* **2021**, 7 (10), 1668–1675. <https://doi.org/10.1021/acscentsci.1c00712>.
- (21) Fard, L. A.; Ojani, R.; Raoof, J. B.; Zare, E. N.; Lakouraj, M. M. PdCo Porous Nanostructures Decorated on Polypyrrole @ MWCNTs Conductive Nanocomposite—Modified Glassy Carbon Electrode as a Powerful Catalyst for Ethanol Electrooxidation. *Appl. Surf. Sci.* **2017**, 401, 40–48. <https://doi.org/10.1016/j.apsusc.2016.12.240>.
- (22) Guan, Y. S.; Li, H.; Ren, F.; Ren, S. Kirigami-Inspired Conducting Polymer Thermoelectrics from Electrostatic Recognition Driven Assembly. *ACS Nano* **2018**, 12 (8), 7967–7973. <https://doi.org/10.1021/acs.nano.8b02489>.
- (23) Han, S.; Jiao, F.; Khan, Z. U.; Edberg, J.; Fabiano, S.; Crispin, X. Thermoelectric Polymer Aerogels for Pressure–Temperature Sensing Applications. *Adv. Funct. Mater.* **2017**, 27 (44), 1–7. <https://doi.org/10.1002/adfm.201703549>.

- (24) Park, H.; Lee, S. H.; Kim, F. S.; Choi, H. H.; Cheong, I. W.; Kim, J. H. Enhanced Thermoelectric Properties of PEDOT:PSS Nanofilms by a Chemical Dedoping Process. *J. Mater. Chem. A Mater.* **2014**, 2 (18), 6532–6539. <https://doi.org/10.1039/C3TA14960A>.
- (25) Debnath, A.; Deb, K.; Bhowmik, K. L.; Saha, B. Reduced Hopping Barrier Potential in NiO Nanoparticle-Incorporated, Polypyrrole-Coated Graphene with Enhanced Thermoelectric Properties. *ACS Appl. Energy Mater.* **2020**, 3 (8), 7772–7781. <https://doi.org/10.1021/acsaem.0c01174>.
- (26) Al-Asbahi, B. A.; Abdelkader, M.; Alkashef, I. M.; Ahmed, A. A. A.; Ragab, H. S.; El-Shamy, A. G. Embedding of Zinc Peroxide (ZnO₂) Nano-Particles into PEDOT:PSS for Fabricating a New PEDOT:PSS/ZnO₂ System with Promising Thermoelectric Functions. *Mater. Sci. Semicond. Process.* **2022**, 146. <https://doi.org/10.1016/j.mssp.2022.106678>.
- (27) Phan, T. T. V.; Bui, N. Q.; Cho, S. W.; Bharathiraja, S.; Manivasagan, P.; Moorthy, M. S.; Mondal, S.; Kim, C. S.; Oh, J. Photoacoustic Imaging-Guided Photothermal Therapy with Tumor-Targeting HA-FeOOH@PPy Nanorods. *Sci. Rep.* **2018**, 8 (1), 1–13. <https://doi.org/10.1038/s41598-018-27204-8>.
- (28) Zhou, Y.; Hu, Y.; Sun, W.; Lu, S.; Cai, C.; Peng, C.; Yu, J.; Popovtzer, R.; Shen, M.; Shi, X. Radiotherapy-Sensitized Tumor Photothermal Ablation Using γ -Polyglutamic Acid Nanogels Loaded with Polypyrrole. *Biomacromolecules* **2018**, 19 (6), 2034–2042. <https://doi.org/10.1021/acs.biomac.8b00184>.
- (29) Li, W.; Wang, X.; Wang, J.; Guo, Y.; Lu, S. Y.; Li, C. M.; Kang, Y.; Wang, Z. G.; Ran, H. T.; Cao, Y.; Liu, H. Enhanced Photoacoustic and Photothermal Effect of Functionalized Polypyrrole Nanoparticles for Near-Infrared Theranostic Treatment of Tumor. *Biomacromolecules* **2019**, 20 (1), 401–411. <https://doi.org/10.1021/acs.biomac.8b01453>.
- (30) Xie, H.; Wei, J.; Duan, S.; Zhu, Q.; Yang, Y.; Chen, K.; Zhang, J.; Li, L.; Zhang, J. Non-Fluorinated and Durable Photothermal Superhydrophobic Coatings Based on Attapulgite Nanorods for Efficient Anti-Icing and Deicing. *Chemical Engineering Journal* **2022**, 428, 132585. <https://doi.org/10.1016/j.cej.2021.132585>.
- (31) Dar, M. A.; Majid, K.; Hanief Najar, M.; Kotnala, R. K.; Shah, J.; Dhawan, S. K.; Farukh, M. Surfactant-Assisted Synthesis of Polythiophene/Ni_{0.5}Zn_{0.5}Fe₂-: XCe_xO₄ Ferrite Composites: Study of Structural, Dielectric and Magnetic Properties for EMI-Shielding Applications. *Physical Chemistry Chemical Physics* **2017**, 19 (16), 10629–10643. <https://doi.org/10.1039/c7cp00414a>.
- (32) Bora, P. J.; Anil, A. G.; Vinoy, K. J.; Ramamurthy, P. C. Outstanding Absolute Electromagnetic Interference Shielding Effectiveness of Cross-Linked PEDOT:PSS Film. *Adv. Mater. Interfaces* **2019**, 6 (22), 1–5. <https://doi.org/10.1002/admi.201901353>.
- (33) Jonas, F.; Heywang, G.; Schmidtberg, W.; Heinze, J.; Dietrich, M. Polythiophenes, Process for Their Preparation and Their Use.

- (34) Groenendaal, L.; Jonas, F.; Freitag, D.; Pielartzik, H.; Reynolds, J. R. Poly(3,4-Ethylenedioxythiophene) and Its Derivatives: Past, Present, and Future. *Advanced Materials* **2000**, *12* (7), 481–494. [https://doi.org/10.1002/\(SICI\)1521-4095\(200004\)12:7<481::AID-ADMA481>3.0.CO;2-C](https://doi.org/10.1002/(SICI)1521-4095(200004)12:7<481::AID-ADMA481>3.0.CO;2-C).
- (35) Meng, Q.; Cai, K.; Chen, Y.; Chen, L. Research Progress on Conducting Polymer Based Supercapacitor Electrode Materials. *Nano Energy* **2017**, *36*, 268–285. <https://doi.org/10.1016/j.nanoen.2017.04.040>.
- (36) Kim, D.; Zozoulenko, I. Why Is Pristine PEDOT Oxidized to 33%? A Density Functional Theory Study of Oxidative Polymerization Mechanism. *Journal of Physical Chemistry B* **2019**, *123* (24), 5160–5167. <https://doi.org/10.1021/acs.jpcc.9b01745>.
- (37) Yi, C.; Wilhite, A.; Zhang, L.; Hu, R.; Chuang, S. S. C.; Zheng, J.; Gong, X. Enhanced Thermoelectric Properties of Poly(3,4-Ethylenedioxythiophene):Poly(Styrenesulfonate) by Binary Secondary Dopants. *ACS Appl. Mater. Interfaces* **2015**, *7* (17), 8984–8989. <https://doi.org/10.1021/acsami.5b01960>.
- (38) Kittel, C.; Holcomb, D. F. *Introduction to Solid State Physics*, 8th ed.; Johnson, S., Ed.; John Wiley & Sons, Inc.: New York, 1967; Vol. 35. <https://doi.org/10.1119/1.1974177>.
- (39) Yu, Y.; Peng, S.; Blanloeuil, P.; Wu, S.; Wang, C. H. Wearable Temperature Sensors with Enhanced Sensitivity by Engineering Microcrack Morphology in PEDOT:PSS-PDMS Sensors. *ACS Appl. Mater. Interfaces* **2020**, *12* (32), 36578–36588. <https://doi.org/10.1021/acsami.0c07649>.
- (40) Jung, M.; Kim, K.; Kim, B.; Cheong, H.; Shin, K.; Kwon, O. S.; Park, J. J.; Jeon, S. Paper-Based Bimodal Sensor for Electronic Skin Applications. *ACS Appl. Mater. Interfaces* **2017**, *9* (32), 26974–26982. <https://doi.org/10.1021/acsami.7b05672>.
- (41) Kaushik, A.; Kumar, R.; Arya, S. K.; Nair, M.; Malhotra, B. D.; Bhansali, S. Organic-Inorganic Hybrid Nanocomposite-Based Gas Sensors for Environmental Monitoring. *Chem. Rev.* **2015**, *115* (11), 4571–4606. <https://doi.org/10.1021/cr400659h>.
- (42) Kumar, P.; Narayan Maiti, U.; Sikdar, A.; Kumar Das, T.; Kumar, A.; Sudarsan, V. Recent Advances in Polymer and Polymer Composites for Electromagnetic Interference Shielding: Review and Future Prospects. *Polymer Reviews* **2019**, *59* (4), 687–738. <https://doi.org/10.1080/15583724.2019.1625058>.
- (43) Jiang, D.; Murugadoss, V.; Wang, Y.; Lin, J.; Ding, T.; Wang, Z.; Shao, Q.; Wang, C.; Liu, H.; Lu, N.; Wei, R.; Subramania, A.; Guo, Z. Electromagnetic Interference Shielding Polymers and Nanocomposites - A Review. *Polymer Reviews* **2019**, *59* (2), 280–337. <https://doi.org/10.1080/15583724.2018.1546737>.
- (44) Gettler, R. C.; Alaal, N.; Brorsen, K. R.; Young, M. J. Effects of Interchain Crosslinking by Alkyl Dihalides on the Electrochemical Performance of Nanoscale Polypyrrole Films.

(45) Mabrouk, S.; Gurung, A.; Bahrami, B.; Baniya, A.; Bobba, R. S.; Wu, F.; Pathak, R.; Qiao, Q. Electrochemically Prepared Polyaniline as an Alternative to Poly(3,4-Ethylenedioxythiophene)-Poly(Styrenesulfonate) for Inverted Perovskite Solar Cells. *ACS Appl. Energy Mater.* **2022**, *5* (8), 9351–9360. <https://doi.org/10.1021/acsaem.2c00621>.

(46) Li, X.; Wang, X.; Liu, G.; Sui, X.; Wu, Q.; Wang, X.; Lv, X.; Xie, E.; Zhang, Z. 2.5 V “Water in Salt” Aqueous Micro-Supercapacitors Based on Polypyrrole-Coated NiCo Layered Double Hydroxides. *Chemical Engineering Journal* **2023**, *452*, 139140. <https://doi.org/10.1016/j.cej.2022.139140>.

(47) Liu, J.; Wang, Z.; Liu, Q.; Li, S.; Wang, D.; Zheng, Z. Rational Design of Freestanding and High-Performance Thick Electrode from Carbon Foam Modified with Polypyrrole/Polydopamine for Supercapacitors. *Chemical Engineering Journal* **2022**, *447*, 137562. <https://doi.org/10.1016/j.cej.2022.137562>.

(48) *History of the potentiostat.* <https://www.palmsens.com/knowledgebase-article/potentiostat/history-of-the-potentiostat/> (accessed 2023-02-15).

(49) Genies, E. M.; Lapkowski, M. Spectroelectrochemical Evidence for an Intermediate in the Electropolymerization of Aniline. *J. Electroanal. Chem. Interfacial Electrochem.* **1987**, *236* (1–2), 189–197. [https://doi.org/10.1016/0022-0728\(87\)88026-9](https://doi.org/10.1016/0022-0728(87)88026-9).

(50) Łapkowski, M. Electrochemical Synthesis of Linear Polyaniline in Aqueous Solutions. *Synth. Met.* **1990**, *35* (1–2), 169–182. [https://doi.org/10.1016/0379-6779\(90\)90041-I](https://doi.org/10.1016/0379-6779(90)90041-I).

(51) Diaz, A. F.; Castillo, J. I.; Logan, J. A.; Lee, W.-Y. Electrochemistry of Conducting Polypyrrole Films. *J. Electroanal. Chem. Interfacial Electrochem.* **1981**, *129* (1–2), 115–132. [https://doi.org/10.1016/S0022-0728\(81\)80008-3](https://doi.org/10.1016/S0022-0728(81)80008-3).

(52) Keiji Kanazawa, K.; Diaz, A. F.; Gill, W. D.; Grant, P. M.; Street, G. B.; Piero Gardini, G.; Kwak, J. F. Polypyrrole: An Electrochemically Synthesized Conducting Organic Polymer. *Synth. Met.* **1980**, *1* (3), 329–336. [https://doi.org/10.1016/0379-6779\(80\)90022-3](https://doi.org/10.1016/0379-6779(80)90022-3).

(53) Adams, R. N. Anodic Oxidation Pathways of Aromatic Hydrocarbons and Amines. *Acc. Chem. Res.* **1969**, *2* (6), 175–180. <https://doi.org/10.1021/ar50018a003>.

(54) Ren, X.; Yang, M.; Yang, T.; Xu, C.; Ye, Y.; Wu, X.; Zheng, X.; Wang, B.; Wan, Y.; Luo, Z. Highly Conductive PPy–PEDOT:PSS Hybrid Hydrogel with Superior Biocompatibility for Bioelectronics Application. *ACS Appl. Mater. Interfaces* **2021**, *13* (21), 25374–25382. <https://doi.org/10.1021/acsami.1c04432>.

(55) Kim, J.; Moisanu, C. M.; Gannett, C. N.; Halder, A.; Fuentes-Rivera, J. J.; Majer, S. H.; Lancaster, K. M.; Forse, A. C.; Abruña, H. D.; Milner, P. J. Conjugated Microporous Polymers

via Solvent-Free Ionothermal Cyclotrimerization of Methyl Ketones. *Chemistry of Materials* **2021**, 33 (21), 8334–8342. <https://doi.org/10.1021/acs.chemmater.1c02622>.

(56) Tang, C.; Thomas, B.; Ramírez-Hernández, M.; Mikmeková, E. M.; Asefa, T. Metal-Functionalized Hydrogels as Efficient Oxygen Evolution Electrocatalysts. *ACS Appl. Mater. Interfaces* **2022**, 14 (18), 20919–20929. <https://doi.org/10.1021/acsami.2c01667>.

(57) Zhang, W.; Ou, J.; Wang, B.; Wang, H.; He, Q.; Song, J.; Zhang, H.; Tang, M.; Zhou, L.; Gao, Y.; Sun, S. Efficient Heavy Metal Removal from Water by Alginate-Based Porous Nanocomposite Hydrogels: The Enhanced Removal Mechanism and Influencing Factor Insight. *J. Hazard Mater.* **2021**, 418, 126358. <https://doi.org/10.1016/j.jhazmat.2021.126358>.

(58) Ohring, M. KINETICS OF MASS TRANSPORT AND PHASE TRANSFORMATIONS. In *Engineering Materials Science*; Elsevier, 1995; pp 249–297. <https://doi.org/10.1016/B978-012524995-9/50030-1>.

(59) Li, D.; Kaner, R. B. How Nucleation Affects the Aggregation of Nanoparticles. *J. Mater. Chem.* **2007**, 17 (22), 2279. <https://doi.org/10.1039/b700699c>.

(60) Sun, Y.; MacDiarmid, A. G.; Epstein, A. J. Polyaniline: Synthesis and Characterization of Pernigraniline Base. *J. Chem. Soc. Chem. Commun.* **1990**, No. 7, 529. <https://doi.org/10.1039/c39900000529>.

(61) Rapi, S.; Bocchi, V.; Gardini, G. P. Conducting Polypyrrole by Chemical Synthesis in Water. *Synth. Met.* **1988**, 24 (3), 217–221. [https://doi.org/10.1016/0379-6779\(88\)90259-7](https://doi.org/10.1016/0379-6779(88)90259-7).

(62) Corradi, R.; Armes, S. P. Chemical Synthesis of Poly(3,4-Ethylenedioxythiophene). *Synth. Met.* **1997**, 84 (1–3), 453–454. [https://doi.org/10.1016/S0379-6779\(97\)80828-4](https://doi.org/10.1016/S0379-6779(97)80828-4).

(63) Lefebvre, M.; Qi, Z.; Rana, D.; Pickup, P. G. Chemical Synthesis, Characterization, and Electrochemical Studies of Poly(3,4-Ethylenedioxythiophene)/Poly(Styrene-4-Sulfonate) Composites. *Chemistry of Materials* **1999**, 11 (2), 262–268. <https://doi.org/10.1021/cm9804618>.

(64) Yamato, H.; Ohwa, M.; Wernet, W. Stability of Polypyrrole and Poly(3,4-Ethylenedioxythiophene) for Biosensor Application. *Journal of Electroanalytical Chemistry* **1995**, 397 (1–2), 163–170. [https://doi.org/10.1016/0022-0728\(95\)04156-8](https://doi.org/10.1016/0022-0728(95)04156-8).

(65) Lock, J. P.; Im, S. G.; Gleason, K. K. Oxidative Chemical Vapor Deposition of Electrically Conducting Poly(3,4-Ethylenedioxythiophene) Films. *Macromolecules* **2006**, 39 (16), 5326–5329. <https://doi.org/10.1021/ma060113o>.

(66) Bilger, D.; Homayounfar, S. Z.; Andrew, T. L. A Critical Review of Reactive Vapor Deposition for Conjugated Polymer Synthesis. *J. Mater. Chem. C Mater.* **2019**, 7 (24), 7159–7174. <https://doi.org/10.1039/c9tc01388a>.

(67) D’Arcy, J. M.; El-Kady, M. F.; Khine, P. P.; Zhang, L.; Lee, S. H.; Davis, N. R.; Liu, D. S.; Yeung, M. T.; Kim, S. Y.; Turner, C. L.; Lech, A. T.; Hammond, P. T.; Kaner, R. B. Vapor-

Phase Polymerization of Nanofibrillar Poly(3,4- Ethylenedioxythiophene) for Supercapacitors. *ACS Nano* **2014**, 8 (2), 1500–1510. <https://doi.org/10.1021/nn405595r>.

(68) Robinson, M. T.; Simons, C. E.; Cliffel, D. E.; Jennings, G. K. Photocatalytic Photosystem I/PEDOT Composite Films Prepared by Vapor-Phase Polymerization. *Nanoscale* **2017**, 9 (18), 6158–6166. <https://doi.org/10.1039/c7nr01158j>.

(69) Kurachi, K.; Kise, H. Preparation of Polypyrrole/Polyethylene Composite Films by the Vapor-Phase Oxidative Polymerization of Pyrrole. *Polym. J.* **1994**, 26 (12), 1325–1331. <https://doi.org/10.1295/polymj.26.1325>.

(70) Fabretto, M.; Zuber, K.; Hall, C.; Murphy, P.; Griesser, H. J. The Role of Water in the Synthesis and Performance of Vapour Phase Polymerised PEDOT Electrochromic Devices. *J. Mater. Chem.* **2009**, 19 (42), 7871–7878. <https://doi.org/10.1039/b912324e>.

(71) Mueller, M.; Fabretto, M.; Evans, D.; Hojati-Talemi, P.; Gruber, C.; Murphy, P. Vacuum Vapour Phase Polymerization of High Conductivity PEDOT: Role of PEG-PPG-PEG, the Origin of Water, and Choice of Oxidant. *Polymer (Guildf)* **2012**, 53 (11), 2146–2151. <https://doi.org/10.1016/j.polymer.2012.03.028>.

(72) Im, S. G.; Gleason, K. K. Systematic Control of the Electrical Conductivity of Poly(3,4-Ethylenedioxythiophene) via Oxidative Chemical Vapor Deposition. *Macromolecules* **2007**, 40 (18), 6552–6556. <https://doi.org/10.1021/ma0628477>.

(73) Goktas, H.; Wang, X.; Ugur, A.; Gleason, K. K. Water-Assisted Vapor Deposition of PEDOT Thin Film. *Macromol. Rapid Commun.* **2015**, 36 (13), 1283–1289. <https://doi.org/10.1002/marc.201500069>.

(74) Ojio, T.; Miyata, S. Highly Transparent and Conducting Polypyrrole–Poly(Vinyl Alcohol) Composite Films Prepared by Gas State Polymerization. *Polym. J.* **1986**, 18 (1), 95–98. <https://doi.org/10.1295/polymj.18.95>.

(75) Xue, Y.; Chen, S.; Yu, J.; Bunes, B. R.; Xue, Z.; Xu, J.; Lu, B.; Zang, L. Nanostructured Conducting Polymers and Their Composites: Synthesis Methodologies, Morphologies and Applications. *J. Mater. Chem. C Mater.* **2020**, 8 (30), 10136–10159. <https://doi.org/10.1039/D0TC02152K>.

(76) Flory, P. J. *Principles of Polymer Chemistry*; Ithaca : Cornell University Press, 1954.

(77) *Handbook of Conducting Polymers, Fourth Edition - 2 Volume Set*, 4th ed.; Reynolds, J. R., Thompson, B. C., Skotheim, T. A., Eds.; CRC Press, 2019. <https://doi.org/10.1201/b22233>.

(78) Cho, B.; Park, K. S.; Baek, J.; Oh, H. S.; Koo Lee, Y. E.; Sung, M. M. Single-Crystal Poly(3,4-Ethylenedioxythiophene) Nanowires with Ultrahigh Conductivity. *Nano Lett.* **2014**, 14 (6), 3321–3327. <https://doi.org/10.1021/nl500748y>.

- (79) Barpuzary, D.; Kim, K.; Park, M. J. Two-Dimensional Growth of Large-Area Conjugated Polymers on Ice Surfaces: High Conductivity and Photoelectrochemical Applications. *ACS Nano* **2019**, *13* (4), 3953–3963. <https://doi.org/10.1021/acsnano.8b07294>.
- (80) Fabretto, M.; Müller, M.; Hall, C.; Murphy, P.; Short, R. D.; Griesser, H. J. In-Situ QCM-D Analysis Reveals Four Distinct Stages during Vapour Phase Polymerisation of PEDOT Thin Films. *Polymer (Guildf)* **2010**, *51* (8), 1737–1743. <https://doi.org/10.1016/j.polymer.2010.02.019>.
- (81) NobelPrize.org. *Nobel Prize in Physics* 1986. <https://www.nobelprize.org/prizes/physics/1986/press-release/> (accessed 2023-03-14).
- (82) Zhao, J.; Tian, S.; Huang, Q.; Fan, L.; Xiao, C. Ultra-Highly Photocatalytic Removal of Pollutants by Polypyrrole/Cadmium Sulfide/Polyether Sulfone Hybrid Porous Membrane in Single-Pass Mode. *Chemical Engineering Journal* **2022**, *432*, 134300. <https://doi.org/10.1016/j.cej.2021.134300>.
- (83) Zhang, W.; Ou, J.; Tang, M.; He, Q.; Long, A.; Luo, S.; Sun, S.; Wan, J.; Gao, Y.; Zhou, L.; Wang, B.; Wang, H. Physically-Crosslinked Activated CaCO₃/Polyaniline-Polypyrrole-Modified GO/Alginate Hydrogel Sorbent with Highly Efficient Removal of Copper(II) from Aqueous Solution. *Chemical Engineering Journal* **2022**, *431*, 133375. <https://doi.org/10.1016/j.cej.2021.133375>.
- (84) Wu, L.; Guo, Y.; Kuang, G.; Wang, Y.; Liu, H.; Kang, Y.; Ma, T.; Tao, Y.; Huang, K.; Zhang, S. Synthesis and Electrochromic Properties of All Donor Polymers Containing Fused Thienothiophene Derivatives with High Contrast and Color Efficiency. *Polymer (Guildf)* **2022**, *261*, 125404. <https://doi.org/10.1016/j.polymer.2022.125404>.
- (85) King, A. J.; Zhukhovitskiy, A. v. A Chain-Growth Mechanism for Conjugated Polymer Synthesis Facilitated by Dinuclear Complexes with Redox-Active Ligands. *Angewandte Chemie International Edition* **2022**, *61* (29). <https://doi.org/10.1002/anie.202206044>.
- (86) Zheng, X.; Shen, J.; Hu, Q.; Nie, W.; Wang, Z.; Zou, L.; Li, C. Vapor Phase Polymerized Conducting Polymer/MXene Textiles for Wearable Electronics. *Nanoscale* **2021**, *13* (3), 1832–1841. <https://doi.org/10.1039/d0nr07433k>.
- (87) Santino, L. M.; Diao, Y.; Yang, H.; Lu, Y.; Wang, H.; Hwang, E.; D’Arcy, J. M. Vapor/Liquid Polymerization of Ultraporous Transparent and Capacitive Polypyrrole Nanonets. *Nanoscale* **2019**, *11* (25), 12358–12369. <https://doi.org/10.1039/c9nr02771h>.
- (88) Tang, H.; You, L.; Liu, J.; Wang, S.; Wang, P.; Feng, C.; Guo, Z. Integrated Polypyrrole@Sulfur@Graphene Aerogel 3D Architecture via Advanced Vapor Polymerization for High-Performance Lithium-Sulfur Batteries. *ACS Appl. Mater. Interfaces* **2019**, *11* (20), 18448–18455. <https://doi.org/10.1021/acsami.9b04167>.
- (89) Diao, Y.; Woon, R.; Yang, H.; Chow, A.; Wang, H.; Lu, Y.; D’Arcy, J. M. Kirigami Electrodes of Conducting Polymer Nanofibers for Wearable Humidity Dosimeters and

Stretchable Supercapacitors. *J. Mater. Chem. A Mater.* **2021**, *9* (15), 9849–9857. <https://doi.org/10.1039/d0ta11335b>.

(90) Waltman, R. J.; Bargon, J. Electrically Conducting Polymers: A Review of the Electropolymerization Reaction, of the Effects of Chemical Structure on Polymer Film Properties, and of Applications towards Technology. *Can. J. Chem.* **1986**, *64* (1), 76–95. <https://doi.org/10.1139/v86-015>.

(91) Smith, J. R.; Cox, P. A.; Campbell, S. A.; Ratcliffe, N. M. Application of Density Functional Theory in the Synthesis of Electroactive Polymers. *Journal of the Chemical Society, Faraday Transactions* **1995**, *91* (15), 2331. <https://doi.org/10.1039/ft9959102331>.

(92) Heth, C. L.; Tallman, D. E.; Rasmussen, S. C. Electrochemical Study of 3-(N-Alkylamino)Thiophenes: Experimental and Theoretical Insights into a Unique Mechanism of Oxidative Polymerization. *J. Phys. Chem. B* **2010**, *114* (16), 5275–5282. <https://doi.org/10.1021/jp912287s>.

(93) D'Aprano, G.; Proynov, E.; Lebœuf, M.; Leclerc, M.; Salahub, D. R. Spin Densities and Polymerizabilities of Aniline Derivatives Deduced from Density Functional Calculations. *J. Am. Chem. Soc.* **1996**, *118* (40), 9736–9742. <https://doi.org/10.1021/ja953819z>.

(94) Hand, R. L.; Nelson, R. F. Anodic Oxidation Pathways of N-Alkylanilines. *J. Am. Chem. Soc.* **1974**, *96* (3), 850–860. <https://doi.org/10.1021/ja00810a034>.

(95) Wei, D.; Kvarnström, C.; Lindfors, T.; Kronberg, L.; Sjöholm, R.; Ivaska, A. Electropolymerization Mechanism of N-Methylaniline. *Synth. Met.* **2006**, *156* (7–8), 541–548. <https://doi.org/10.1016/j.synthmet.2006.02.009>.

(96) Chiang, J.-C.; MacDiarmid, A. G. ‘Polyaniline’: Protonic Acid Doping of the Emeraldine Form to the Metallic Regime. *Synth. Met.* **1986**, *13* (1–3), 193–205. [https://doi.org/10.1016/0379-6779\(86\)90070-6](https://doi.org/10.1016/0379-6779(86)90070-6).

(97) Huang, Y.; Gao, X.; Zhang, Z.; Batool, S.; Li, X.; Li, T. Porous Hollow Carbon Aerogel-Assembled Core@polypyrrole Nanoparticle Shell as an Efficient Sulfur Host through a Tunable Molecular Self-Assembly Method for Rechargeable Lithium/Sulfur Batteries. *ACS Sustain. Chem. Eng.* **2020**, *8* (42), 15822–15833. <https://doi.org/10.1021/acssuschemeng.0c02456>.

(98) Kim, J. Y.; Jang, H. J.; Bae, G. T.; Park, C.-S.; Jung, E. Y.; Tae, H.-S. Improvement of Nanostructured Polythiophene Film Uniformity Using a Cruciform Electrode and Substrate Rotation in Atmospheric Pressure Plasma Polymerization. *Nanomaterials* **2021**, *12* (1), 32. <https://doi.org/10.3390/nano12010032>.

(99) Pillalamarri, S. K.; Blum, F. D.; Tokuhito, A. T.; Story, J. G.; Bertino, M. F. Radiolytic Synthesis of Polyaniline Nanofibers: A New Templateless Pathway. *Chemistry of Materials* **2005**, *17* (2), 227–229. <https://doi.org/10.1021/cm0488478>.

- (100) Moriarty, P. Nanostructured Materials. *Reports on Progress in Physics* **2001**, *64* (3), 297–381. <https://doi.org/10.1088/0034-4885/64/3/201>.
- (101) Dan, L. I.; Huang, J.; Kaner, R. B. Polyaniline Nanofibers: A Unique Polymer Nanostructure for Versatile Applications. *Acc. Chem. Res.* **2009**, *42* (1), 135–145. <https://doi.org/10.1021/ar800080n>.
- (102) Zhao, F.; Shi, Y.; Pan, L.; Yu, G. Multifunctional Nanostructured Conductive Polymer Gels: Synthesis, Properties, and Applications. *Acc. Chem. Res.* **2017**, *50* (7), 1734–1743. <https://doi.org/10.1021/acs.accounts.7b00191>.
- (103) Ghosh, S.; Maiyalagan, T.; Basu, R. N. Nanostructured Conducting Polymers for Energy Applications: Towards a Sustainable Platform. *Nanoscale* **2016**, *8* (13), 6921–6947. <https://doi.org/10.1039/C5NR08803H>.
- (104) Xue, Y.; Chen, S.; Yu, J.; Bunes, B. R.; Xue, Z.; Xu, J.; Lu, B.; Zang, L. Nanostructured Conducting Polymers and Their Composites: Synthesis Methodologies, Morphologies and Applications. *J. Mater. Chem. C Mater.* **2020**, *8* (30), 10136–10159. <https://doi.org/10.1039/d0tc02152k>.
- (105) Nguyen, D. N.; Yoon, H. Recent Advances in Nanostructured Conducting Polymers: From Synthesis to Practical Applications. *Polymers*. **2016**. <https://doi.org/10.3390/polym8040118>.
- (106) Zhao, J.; Tan, D.; Chen, G. A Strategy to Improve the Thermoelectric Performance of Conducting Polymer Nanostructures. *J. Mater. Chem. C Mater.* **2017**, *5* (1), 47–53. <https://doi.org/10.1039/C6TC04613D>.
- (107) Alcaraz-Espinoza, J. J.; Ramos-Sánchez, G.; Sierra-Urbe, J. H.; González, I. Supramolecular Assembly of Nanostructured Conducting Polymer Hydrogels by Hydrotropic Agents for Outstanding Supercapacitive Energy Storage. *ACS Appl. Energy Mater.* **2021**, *4* (9), 9099–9110. <https://doi.org/10.1021/acsaem.1c01385>.
- (108) He, Y.; Bai, Y.; Yang, X.; Zhang, J.; Kang, L.; Xu, H.; Shi, F.; Lei, Z.; Liu, Z. H. Holey Graphene/Polypyrrole Nanoparticle Hybrid Aerogels with Three-Dimensional Hierarchical Porous Structure for High Performance Supercapacitor. *J. Power Sources* **2016**, *317*, 10–18. <https://doi.org/10.1016/j.jpowsour.2016.03.089>.
- (109) Huang, M.; Li, L.; Ai, Z.; Gao, X.; Qian, J.; Xu, H.; Su, X.; Wu, J.; Gao, Y. One-Step Fabrication of Ice-Templated Pure Polypyrrole Nanoparticle Hydrogels for High-Rate Supercapacitors. *ACS Appl. Nano Mater.* **2022**, *5* (8), 11940–11947. <https://doi.org/10.1021/acsanm.2c02957>.
- (110) Zhang, J.; Fan, X.; Meng, X.; Zhou, J.; Wang, M.; Chen, S.; Cao, Y.; Chen, Y.; Bielawski, C. W.; Geng, J. Ice-Templated Large-Scale Preparation of Two-Dimensional Sheets of Conjugated Polymers: Thickness-Independent Flexible Supercapacitance. *ACS Nano* **2021**, *15* (5), 8870–8882. <https://doi.org/10.1021/acsnano.1c01459>.

- (111) Shiu, B.-C.; Liu, Y.-L.; Yuan, Q.-Y.; Lou, C.-W.; Lin, J.-H. Preparation and Characterization of PEDOT:PSS/TiO₂ Micro/Nanofiber-Based Gas Sensors. *Polymers (Basel)* **2022**, *14* (9), 1780. <https://doi.org/10.3390/polym14091780>.
- (112) Yang, Y.; Li, S.; Yang, W.; Yuan, W.; Xu, J.; Jiang, Y. In Situ Polymerization Deposition of Porous Conducting Polymer on Reduced Graphene Oxide for Gas Sensor. *ACS Appl. Mater. Interfaces* **2014**, *6* (16), 13807–13814. <https://doi.org/10.1021/am5032456>.
- (113) Jiang, W.; Yu, D.; Zhang, Q.; Goh, K.; Wei, L.; Yong, Y.; Jiang, R.; Wei, J.; Chen, Y. Ternary Hybrids of Amorphous Nickel Hydroxide-Carbon Nanotube-Conducting Polymer for Supercapacitors with High Energy Density, Excellent Rate Capability, and Long Cycle Life. *Adv. Funct. Mater.* **2015**, *25* (7), 1063–1073. <https://doi.org/10.1002/adfm.201403354>.
- (114) Huang, H.; Abbas, S. C.; Deng, Q.; Ni, Y.; Cao, S.; Ma, X. An All-Paper, Scalable and Flexible Supercapacitor Based on Vertically Aligned Polyaniline (PANI) Nano-Dendrites@fibers. *J. Power Sources* **2021**, *498*, 229886. <https://doi.org/10.1016/j.jpowsour.2021.229886>.
- (115) Ding, H.; Zhong, M.; Wu, H.; Park, S.; Mohin, J. W.; Klosterman, L.; Yang, Z.; Yang, H.; Matyjaszewski, K.; Bettinger, C. J. Elastomeric Conducting Polyaniline Formed Through Topological Control of Molecular Templates. *ACS Nano* **2016**, *10* (6), 5991–5998. <https://doi.org/10.1021/acsnano.6b01520>.
- (116) Li, F.; Qin, T.; Sun, Y.; Jiang, R.; Yuan, J.; Liu, X.; O'Mullane, A. P. Preparation of a One-Dimensional Hierarchical MnO@CNT@Co-N/C Ternary Nanostructure as a High-Performance Bifunctional Electrocatalyst for Rechargeable Zn-Air Batteries. *J. Mater. Chem. A Mater.* **2021**, *9* (39), 22533–22543. <https://doi.org/10.1039/d1ta07259e>.
- (117) Han, J.; Li, L.; Fang, P.; Guo, R. Ultrathin MnO₂ Nanorods on Conducting Polymer Nanofibers as a New Class of Hierarchical Nanostructures for High-Performance Supercapacitors. *The Journal of Physical Chemistry C* **2012**, *116* (30), 15900–15907. <https://doi.org/10.1021/jp303324x>.
- (118) Bai, M.-H.; Bian, L.-J.; Song, Y.; Liu, X.-X. Electrochemical Codeposition of Vanadium Oxide and Polypyrrole for High-Performance Supercapacitor with High Working Voltage. *ACS Appl Mater Interfaces* **2014**, *6* (15), 12656–12664. <https://doi.org/10.1021/am502630g>.
- (119) Wang, J.-G.; Liu, H.; Liu, H.; Hua, W.; Shao, M. Interfacial Constructing Flexible V₂O₅@Polypyrrole Core-Shell Nanowire Membrane with Superior Supercapacitive Performance. *ACS Appl. Mater. Interfaces* **2018**, *10* (22), 18816–18823. <https://doi.org/10.1021/acsami.8b05660>.
- (120) Qu, Q.; Zhu, Y.; Gao, X.; Wu, Y. Core-Shell Structure of Polypyrrole Grown on V₂O₅ Nanoribbon as High Performance Anode Material for Supercapacitors. *Adv. Energy Mater.* **2012**, *2* (8), 950–955. <https://doi.org/10.1002/aenm.201200088>.

- (121) Liu, S.; Zhu, H.; Zhang, B.; Li, G.; Zhu, H.; Ren, Y.; Geng, H.; Yang, Y.; Liu, Q.; Li, C. C. Tuning the Kinetics of Zinc-Ion Insertion/Extraction in V₂O₅ by In Situ Polyaniline Intercalation Enables Improved Aqueous Zinc-Ion Storage Performance. *Advanced Materials* **2020**, 32 (26), 1–10. <https://doi.org/10.1002/adma.202001113>.
- (122) Zhou, K.; He, Y.; Xu, Q.; Zhang, Q.; Zhou, A.; Lu, Z.; Yang, L.-K.; Jiang, Y.; Ge, D.; Liu, X. Y.; Bai, H. A Hydrogel of Ultrathin Pure Polyaniline Nanofibers: Oxidant-Templating Preparation and Supercapacitor Application. *ACS Nano* **2018**, 12 (6), 5888–5894. <https://doi.org/10.1021/acsnano.8b02055>.
- (123) Xu, Z.; Teng, H.; Song, J.; Gao, F.; Ma, L.; Xu, G.; Luo, X. A Nanocomposite Consisting of MnO₂ Nanoflowers and the Conducting Polymer PEDOT for Highly Sensitive Amperometric Detection of Paracetamol. *Microchimica Acta* **2019**, 186 (8), 1–8. <https://doi.org/10.1007/s00604-019-3614-3>.
- (124) Hu, X.; Xiong, W.; Wang, W.; Qin, S.; Cheng, H.; Zeng, Y.; Wang, B.; Zhu, Z. Hierarchical Manganese Dioxide/Poly(3,4-Ethylenedioxythiophene) Core-Shell Nanoflakes on Ramie-Derived Carbon Fiber for High-Performance Flexible All-Solid-State Supercapacitor. *ACS Sustain. Chem. Eng.* **2016**, 4 (3), 1201–1211. <https://doi.org/10.1021/acssuschemeng.5b01263>.
- (125) Yoon, H.; Chang, M.; Jang, J. Formation of 1D Poly(3,4-Ethylenedioxythiophene) Nanomaterials in Reverse Microemulsions and Their Application to Chemical Sensors. *Adv. Funct. Mater.* **2007**, 17 (3), 431–436. <https://doi.org/10.1002/adfm.200600106>.
- (126) Kopanichuk, I. v.; Vedenchuk, E. A.; Koneva, A. S.; Vanin, A. A. Structural Properties of Span 80/Tween 80 Reverse Micelles by Molecular Dynamics Simulations. *J. Phys. Chem. B* **2018**, 122 (33), 8047–8055. <https://doi.org/10.1021/acs.jpcc.8b03945>.
- (127) Jun, C. S.; Kwon, S. H.; Choi, H. J.; Seo, Y. Polymeric Nanoparticle-Coated Pickering Emulsion-Synthesized Conducting Polyaniline Hybrid Particles and Their Electrorheological Study. *ACS Appl. Mater. Interfaces* **2017**, 9 (51), 44811–44819. <https://doi.org/10.1021/acsami.7b13808>.
- (128) Sydulu Singu, B.; Srinivasan, P.; Yoon, K. R. Emulsion Polymerization Method for Polyaniline-Multiwalled Carbon Nanotube Nanocomposites as Supercapacitor Materials. *Journal of Solid State Electrochemistry* **2016**, 20 (12), 3447–3457. <https://doi.org/10.1007/s10008-016-3309-1>.
- (129) Kolathodi, M. S.; Akbarinejad, A.; Tollemache, C.; Zhang, P.; Travas-Sejdic, J. Highly Stretchable and Flexible Supercapacitors Based on Electrospun PEDOT:SSEBS Electrodes. *J. Mater. Chem. A Mater.* **2022**, 10 (39), 21124–21134. <https://doi.org/10.1039/D2TA04476E>.
- (130) Li, Y.; Yu, H.; Zhang, Y.; Zhou, N.; Tan, Z. Kinetics and Characterization of Preparing Conductive Nanofibrous Membrane by In-Situ Polymerization of Polypyrrole on Electrospun Nanofibers. *Chemical Engineering Journal* **2022**, 433, 133531. <https://doi.org/10.1016/j.cej.2021.133531>.

- (131) Sanviti, M.; Mester, L.; Hillenbrand, R.; Alegría, A.; Martínez-Tong, D. E. Solvent-Structured PEDOT:PSS Surfaces: Fabrication Strategies and Nanoscale Properties. *Polymer (Guildf)* **2022**, *246*, 124723. <https://doi.org/10.1016/j.polymer.2022.124723>.
- (132) Huang, J.; Kaner, R. B. A General Chemical Route to Polyaniline Nanofibers. *J. Am. Chem. Soc.* **2004**, *126* (3), 851–855. <https://doi.org/10.1021/ja0371754>.
- (133) Konwar, G.; Sarma, S. Ch.; Mahanta, D.; Peter, S. C. Polyaniline Hybrid Nanofibers via Green Interfacial Polymerization for All-Solid-State Symmetric Supercapacitors. *ACS Omega* **2020**, *5* (24), 14494–14501. <https://doi.org/10.1021/acsomega.0c01158>.
- (134) Faivre, D. *Iron Oxides: From Nature to Applications*, 1st ed.; Faivre, D., Ed.; Wiley: Weinheim, 2016. <https://doi.org/10.1002/9783527691395>.
- (135) Post, J. E.; Heaney, P. J.; von Dreele, R. B.; Hanson, J. C. Neutron and Temperature-Resolved Synchrotron X-Ray Powder Diffraction Study of Akaganéite. *American Mineralogist* **2003**, *88* (5), 782–788. <https://doi.org/10.2138/am-2003-5-607>.
- (136) Birch, W. D.; Pring, A.; Reller, A.; Schmalte, H. W. Bernalite, Fe(OH)₃, a New Mineral from Broken Hill, New South Wales: Description and Structure. *American Mineralogist* **1993**, *78* (7–8), 827–834.
- (137) Verwey, E. J. W. The Crystal Structure of γ -Fe₂O₃ and γ -Al₂O₃. *Z Kristallogr. Cryst. Mater.* **1935**, *91* (1–6), 65–69. <https://doi.org/10.1524/zkri.1935.91.1.65>.
- (138) Tuček, J.; Zbořil, R.; Namai, A.; Ohkoshi, S. I. ϵ -Fe₂O₃: An Advanced Nanomaterial Exhibiting Giant Coercive Field, Millimeter-Wave Ferromagnetic Resonance, and Magnetoelectric Coupling. *Chemistry of Materials* **2010**, *22* (24), 6483–6505. <https://doi.org/10.1021/cm101967h>.
- (139) Lavina, B.; Dera, P.; Kim, E.; Meng, Y.; Downs, R. T.; Weck, P. F.; Sutton, S. R.; Zhao, Y. Discovery of the Recoverable High-Pressure Iron Oxide Fe₄O₅. *Proc. Natl. Acad. Sci. U.S.A.* **2011**, *108* (42), 17281–17285. <https://doi.org/10.1073/pnas.1107573108>.
- (140) Sestu, M.; Carta, D.; Casula, M. F.; Corrias, A.; Navarra, G. Novel Interpretation of the Mean Structure of Feroxyhyte. *J. Solid State Chem.* **2015**, *225*, 256–260. <https://doi.org/10.1016/j.jssc.2015.01.003>.
- (141) Khan, I.; Hashmi, A.; Farooq, M. U.; Hong, J. Two-Dimensional Magnetic Semiconductor in Feroxyhyte. *ACS Appl. Mater. Interfaces* **2017**, *9* (40), 35368–35375. <https://doi.org/10.1021/acsami.7b08499>.
- (142) Patrat, G.; de Bergevin, F.; Pernet, M.; Joubert, J. C. Structure Locale de Δ -FeOOH. *Acta Crystallographica Section B* **1983**, *39* (2), 165–170. <https://doi.org/10.1107/S0108768183002232>.

- (143) Trolard, F.; Bourrié, G.; Abdelmoula, M.; Refait, P.; Feder, F. Fougérite, a New Mineral of the Pyroaurite-Iowaite Group: Description and Crystal Structure. *Clays Clay Miner.* **2007**, *55* (3), 323–334. <https://doi.org/10.1346/CCMN.2007.0550308>.
- (144) Hazemann, J.-L.; Bérar, J. F.; Manceau, A. Rietveld Studies of the Aluminium-Iron Substitution in Synthetic Goethite. *Materials Science Forum* **1991**, 79–82, 821–826. <https://doi.org/10.4028/www.scientific.net/msf.79-82.821>.
- (145) Fabrykiewicz, P.; Stękiel, M.; Sosnowska, I.; Przeniosło, R. Deformations of the α -Fe₂O₃ Rhombohedral Lattice across the Néel Temperature. *Acta Crystallogr. B Struct. Sci. Cryst. Eng. Mater.* **2017**, *73* (1), 27–32. <https://doi.org/10.1107/S2052520616017935>.
- (146) Ewing, F. J. The Crystal Structure of Lepidocrocite. *J. Chem. Phys.* **1935**, *3* (7), 420–424. <https://doi.org/10.1063/1.1749692>.
- (147) Claassen, A. A. The Scattering Power of Oxygen and Iron for X-Rays. *Proceedings of the Physical Society of London* **1925**, *38* (1), 482–487. <https://doi.org/10.1088/1478-7814/38/1/348>.
- (148) Fernandez-Martinez, A.; Timon, V.; Romaman-Ross, G.; Cuello, G. J.; Daniels, J. E.; Ayora, C. The Structure of Schwertmannite, a Nanocrystalline Iron Oxyhydroxysulfate. *American Mineralogist* **2010**, *95* (8–9), 1312–1322. <https://doi.org/10.2138/am.2010.3446>.
- (149) Parise, J. B.; Marshall, W. G.; Smith, R. I.; Luiz, H. D.; Möller, H. The Nuclear and Magnetic Structure of “White Rust”-Fe(OH_{0.86}D_{0.14})₂. *American Mineralogist* **2000**, *85* (1), 189–193. <https://doi.org/10.2138/am-2000-0118>.
- (150) Fei, Y.; Mao, H. kwang; Shu, J.; Hu, J. P-V-T Equation of State of Magnesio-wüstite (Mg_{0.6}Fe_{0.4})O. *Phys. Chem. Miner.* **1992**, *18* (7), 416–422. <https://doi.org/10.1007/BF00200964>.
- (151) Pecharrromán, C.; González-Carreño, T.; Iglesias, J. E. The Infrared Dielectric Properties of Maghemite, γ -Fe₂O₃, from Reflectance Measurement on Pressed Powders. *Phys. Chem. Miner.* **1995**, *22* (1), 21–29. <https://doi.org/10.1007/BF00202677>.
- (152) Pauling, L.; Hendricks, S. B. The Crystal Structures of Hematite and Corundum. *J. Am. Chem. Soc.* **1925**, *47* (3), 781–790. <https://doi.org/10.1021/ja01680a027>.
- (153) Michel, F. M.; Ehm, L.; Antao, S. M.; Lee, P. L.; Chupas, P. J.; Liu, G.; Strongin, D. R.; Schoonen, M. A. A.; Phillips, B. L.; Parise, J. B. The Structure of Ferrihydrite, a Nanocrystalline Material. *Science (1979)* **2007**, *316* (5832), 1726–1729. <https://doi.org/10.1126/science.1142525>.
- (154) Enthaler, S.; Junge, K.; Beller, M. Sustainable Metal Catalysis with Iron: From Rust to a Rising Star? *Angewandte Chemie International Edition* **2008**, *47* (18), 3317–3321. <https://doi.org/10.1002/anie.200800012>.

- (155) Bora, D. K.; Braun, A.; Constable, E. C. “in Rust We Trust”. Hematite-the Prospective Inorganic Backbone for Artificial Photosynthesis. *Energy Environ. Sci.* **2013**, 6 (2), 407–425. <https://doi.org/10.1039/c2ee23668k>.
- (156) Salunkhe, T. T.; Varma, R. S.; Kadam, A. N.; Lee, S.-W.; Lee, Y.-C.; Hur, J.; Kim, I. T. Scraps to Superior Anodes for Li-Ion Batteries: Sustainable and Scalable Upgrading of Waste Rust. *J. Hazard. Mater.* **2021**, 410, 124571. <https://doi.org/10.1016/j.jhazmat.2020.124571>.
- (157) Gurav, R.; Surve, S. K.; Babar, S.; Choudhari, P.; Patil, D.; More, V.; Sankpal, S.; Hangirgekar, S. Rust-Derived Fe₂O₃ Nanoparticles as a Green Catalyst for the One-Pot Synthesis of Hydrazinyl Thiazole Derivatives. *Org. Biomol. Chem.* **2020**, 18 (24), 4575–4582. <https://doi.org/10.1039/D0OB00109K>.
- (158) Babar, S.; Gavade, N.; Shinde, H.; Mahajan, P.; Lee, K. H.; Mane, N.; Deshmukh, Ashish.; Garadkar, K.; Bhuse, V. Evolution of Waste Iron Rust into Magnetically Separable G-C₃N₄-Fe₂O₃ Photocatalyst: An Efficient and Economical Waste Management Approach. *ACS Appl. Nano Mater.* **2018**, 1 (9), 4682–4694. <https://doi.org/10.1021/acsanm.8b00936>.
- (159) Deganello, F.; Joshi, M.; Liotta, L. F.; La Parola, V.; Marci, G.; Pantaleo, G. Sustainable Recycling of Insoluble Rust Waste for the Synthesis of Iron-Containing Perovskite-Type Catalysts. *ACS Omega* **2019**, 4 (4), 6994–7004. <https://doi.org/10.1021/acsomega.8b03522>.
- (160) Mikucki, J. A.; Pearson, A.; Johnston, D. T.; Turchyn, A. V.; Farquhar, J.; Schrag, D. P.; Anbar, A. D.; Priscu, J. C.; Lee, P. A. A Contemporary Microbially Maintained Subglacial Ferrous “Ocean.” *Science* (1979) **209**, 324 (5925), 397–400. <https://doi.org/10.1126/science.1167350>.
- (161) Zhu, J.; Li, L.; Xiong, Z.; Hu, Y.; Jiang, J. Evolution of Useless Iron Rust into Uniform α -Fe₂O₃ Nanospheres: A Smart Way to Make Sustainable Anodes for Hybrid Ni-Fe Cell Devices. *ACS Sustain. Chem. Eng.* **2017**, 5 (1), 269–276. <https://doi.org/10.1021/acssuschemeng.6b01527>.
- (162) Mao, H.; Lu, X.; Chao, D.; Cui, L.; Li, Y.; Zhang, W. Preparation and Characterization of PEDOT/ β -Fe₃O₄(OH,Cl) Nanospindles with Controllable Sizes in Aqueous Solution. *Journal of Physical Chemistry C* **2008**, 112 (51), 20469–20480. <https://doi.org/10.1021/jp807988f>.
- (163) Mao, H.; Li, Y.; Liu, X.; Zhang, W.; Wang, C.; Al-Deyab, S. S.; El-Newehy, M. The Application of Novel Spindle-like Polypyrrole Hollow Nanocapsules Containing Pt Nanoparticles in Electrocatalysis Oxidation of Nicotinamide Adenine Dinucleotide (NADH). *J. Colloid Interface Sci.* **2011**, 356 (2), 757–762. <https://doi.org/10.1016/j.jcis.2011.01.004>.
- (164) Ebrahim, S.; Shokry, A.; Ibrahim, H.; Soliman, M. Polyaniline/Akaganéite Nanocomposite for Detoxification of Noxious Cr(VI) from Aquatic Environment. *Journal of Polymer Research* **2016**, 23 (4), 79. <https://doi.org/10.1007/s10965-016-0977-6>.
- (165) Wei, G.; Du, K.; Zhao, X.; Li, C.; Li, J.; Ren, K.; Huang, Y.; Wang, H.; Yao, S.; An, C. Integrated FeOOH Nanospindles with Conductive Polymer Layer for High-Performance

Supercapacitors. *J. Alloys Compd.* **2017**, 728, 631–639.
<https://doi.org/10.1016/j.jallcom.2017.09.002>.

(166) McNaught, A. D.; Wilkinson, A. Hydrolysis. In *IUPAC. Compendium of Chemical Terminology, 2nd ed. (the “Gold Book”)*; Blackwell Scientific Publications: Oxford, 1997; Vol. 1077, p 2902. <https://doi.org/10.1351/goldbook.H02902>.

(167) McNaught, A. D.; Wilkinson, A. Solvolysis. In *IUPAC. Compendium of Chemical Terminology, 2nd ed. (the “Gold Book”)*; Blackwell Scientific Publications: Oxford, 1997; Vol. 1077, p 5762. <https://doi.org/10.1351/goldbook.S05762>.

(168) Baes, C. F.; Messmer, R. E. *The Hydrolysis of Cations*; John Wiley & Sons Inc., 1976.

(169) Cornell, R. M.; Schwertmann, U. *The Iron Oxide Structure, Properties, Reactions, Occurrences and Uses*, 2nd ed.; WILEY-VCH Verlag GmbH & Co. KGaA: Weinheim, 2003. <https://doi.org/10.4324/9780203221815>.

(170) De Yoreo, J. J.; Gilbert, P. U. P. A.; Sommerdijk, N. A. J. M.; Penn, R. L.; Whitlam, S.; Joester, D.; Zhang, H.; Rimer, J. D.; Navrotsky, A.; Banfield, J. F.; Wallace, A. F.; Michel, F. M.; Meldrum, F. C.; Cölfen, H.; Dove, P. M. Crystallization by Particle Attachment in Synthetic, Biogenic, and Geologic Environments. *Science* (1979) **2015**, 349 (6247). <https://doi.org/10.1126/science.aaa6760>.

(171) Yuwono, V. M.; Burrows, N. D.; Soltis, J. A.; Lee Penn, R. Oriented Aggregation: Formation and Transformation of Mesocrystal. *J. Am. Chem. Soc.* **2010**, 132 (7), 2163–2165. <https://doi.org/10.1021/ja909769a>.

(172) Frandsen, C.; Legg, B. A.; Comolli, L. R.; Zhang, H.; Gilbert, B.; Johnson, E.; Banfield, J. F. Aggregation-Induced Growth and Transformation of β -FeOOH Nanorods to Micron-Sized α -Fe₂O₃ Spindles. *CrystEngComm* **2014**, 16 (8), 1451–1458. <https://doi.org/10.1039/c3ce40983j>.

(173) Tang, J.; Paul Alivisatos, A. Crystal Splitting in the Growth of Bi₂S₃. *Nano Lett.* **2006**, 6 (12), 2701–2706. <https://doi.org/10.1021/nl0615930>.

(174) Hu, Y.; Chen, K. Crystal Splitting in the Growth of β -FeO(OH). *J. Cryst. Growth* **2007**, 308 (1), 185–188. <https://doi.org/10.1016/j.jcrysgro.2007.07.035>.

(175) Papias, D.; Taxiarchou, M.; Paspaliaris, I.; Kontopoulos, A. Mechanisms of Dissolution of Iron Oxides in Aqueous Oxalic Acid Solutions. *Hydrometallurgy* **1996**, 42 (2), 257–265. [https://doi.org/10.1016/0304-386X\(95\)00104-O](https://doi.org/10.1016/0304-386X(95)00104-O).

(176) Schwertmann, U.; Cambier, P.; Murad, E. Properties of Goethites of Varying Crystallinity. *Clays Clay Miner.* **1985**, 33 (5), 369–378. <https://doi.org/10.1346/CCMN.1985.0330501>.

- (177) Stumm, W.; Furrer, G. The Dissolution of Oxides and Aluminum Silicates : Examples of Surface-Coordination-Controlled Kinetics. *Aquatic surface chemistry* **1987**, 197–219.
- (178) Stumm, W.; Furrer, G.; Wieland, E.; Zinder, B. The Effects of Complex-Forming Ligands on the Dissolution of Oxides and Aluminosilicates. In *The Chemistry of Weathering*; Drever, J. I., Ed.; Springer Netherlands: Dordrecht, 1985; pp 55–74. https://doi.org/10.1007/978-94-009-5333-8_4.
- (179) Schwertmann, U. Solubility and Dissolution of Iron Oxides. *Plant Soil* **1991**, 130 (1–2), 1–25. <https://doi.org/10.1007/BF00011851>.
- (180) Klyukin, K.; Rosso, K. M.; Alexandrov, V. Iron Dissolution from Goethite (α -FeOOH) Surfaces in Water by Ab Initio Enhanced Free-Energy Simulations. *Journal of Physical Chemistry C* **2018**, 122 (28), 16086–16091. <https://doi.org/10.1021/acs.jpcc.8b03743>.
- (181) Diao, Y.; Chen, H.; Lu, Y.; Santino, L. M.; Wang, H.; D’Arcy, J. M. Converting Rust to PEDOT Nanofibers for Supercapacitors. *ACS Appl. Energy Mater.* **2019**, 2 (5), 3435–3444. <https://doi.org/10.1021/acsaem.9b00244>.

Chapter 2: Rust-based Vapor-phase Polymerization of Nanofibrillar Poly(3,4-ethylenedioxythiophene)/Polypyrrole Composite on Flexible Substrates

At the end of Chapter 1, I introduced a synthetic strategy that produces nanostructured conducting polymers. Previous publications from the D'Arcy lab applied this technique to the synthesis of poly(3,4-ethylenedioxythiophene) (PEDOT). In this chapter, I utilize rust-based vapor-phase polymerization in the synthesis of polypyrrole (PPy), demonstrating the versatility of this technique. I also present my work on the synthesis of a PEDOT/PPy composite on a flexible substrate that enables the fabrication of a flexible, stretchable supercapacitor and a wearable humidity dosimeter.

2.1 Introduction

Flexible and wearable electronics are gaining much research interest in recent years due to the increasing demand of biocompatible sensors and electronic skins in real-time health monitoring, as well as foldable capacitive touch screens in novel smart devices.¹⁻⁶ Conducting polymer rises as a promising material for electrodes in wearable electronics due to its stability under ambient conditions, mechanical flexibility, light weight, and ease of synthesis.⁷⁻¹² Polypyrrole (PPy) and poly(3,4-ethylenedioxythiophene) (PEDOT) are two most widely studied polymers for wearable electronics fabrication. As a single material, both PEDOT and PPy are suitable for electrodes of flexible energy storage devices. Creating a polymer composite takes advantage of the electrochemical properties of both polymers and introduce synergy between the two components.

Here, we present a synthetic strategy that combines clean room techniques and chemical synthesis in laboratory to fabricate flexible PEDOT/PPy composite electrodes for supercapacitors. A homogenous coating of polymer is deposited on a flexible substrate through rust-based vapor-phase polymerization (RVPP). The difference in mechanism between PEDOT and PPy in an acid-catalyzed polymerization is examined via stoichiometric studies. These experiments assist our understanding of the mixed mechanistic pathways that take place in RVPP.

Stretchability is an essential mechanical property of wearable electronics, and vapor-phase synthesized conducting polymers are often flexible but lack stretchability due to their crystallinity.^{13–15} Therefore, an alternative approach to deposition on stretchable substrate is needed for fabrication of wearable electronics. Kirigami, the art of paper cutting, is an emerging approach to constructing stretchable 3D architectures out of simply cutting planar sheets. Under external strain, cuts made in thin films undergo in-plane rotation and out-of-plane buckling that result in expanded 3D structures.^{16,17} Combining Kirigami with electrode material deposition enables simultaneous achievement of macroscopic robustness, mechanical strength, and high stretchability alongside high electronic performance.^{2,18} These properties are ideally suited to a variety of flexible devices including chemoresistive sensors and supercapacitors. Precise control over conducting polymer nanofibers deposition on pre-patterned substrates is achieved for humidity dosimeter and supercapacitor electrode fabrication. We combine the engineering of Kirigami techniques with chemistry in vapor-phase polymer synthesis. Our synthetic strategy affords multi-layer deposition for developing bilayer PEDOT/PPy nanofibrillar composite supercapacitors. This composite supercapacitor exhibits a synergistic effect that elicits a state-of-

the-art energy density of 115 $\mu\text{Wh}/\text{cm}^2$ at 1 mA/cm^2 and an extended cycle stability when stretched (85% capacitance after 100% elongation over 300 cycles). Assembling the supercapacitor into a planar configuration enables it to light up LEDs at various open voltages and demonstrates its potential as a power supply for wearable electronics. A flexible and stretchable nanofibrillar PEDOT humidity dosimeter exhibits significant sensitivity, showing a 40% resistance change within seconds when exposed to a new humidity level under 200% stretch, making it an ideal mask accessory for detecting the presence of droplets from coughs or sneezes.

This chapter is adapted from a previous publication.¹⁹ The research was led by Dr. Yifan Diao, and I was responsible for vapor-phase synthesis and electrochemical characterizations of PEDOT, PPy, and their composite. The introduction, results and discussion, and the conclusion sections in this chapter are rewritten based on the published data with an emphasis on mechanisms during polymer synthesis.

2.2 Materials and Methods

Materials

Pyrrole, 3,4-ethylenedioxythiophene (EDOT, 97%), chlorobenzene (99%), sulfuric acid (98%), hydrochloric acid (37%), lithium perchlorate (99.9%), acetonitrile (99.8%), aqueous ammonia (25%) and hydrazine hydrate (50%) were purchased from Sigma Aldrich and used as received.

Deposition of nanofibrillar Kirigami electrodes

- 1) Kirigami cuts were generated via CO_2 laser cutting following a pattern designed in AutoCAD.
- 2) A solid-oxidant precursor, $\alpha\text{-Fe}_2\text{O}_3$ (hematite), was sputtered over polyethylene terephthalate

(PET) films via physical vapor deposition (Kurt J. Lesker PVD 75 RF and DC). 3) For single polymer electrodes, all syntheses were performed at 140 °C for 1.5 h in glass reactors, each containing a hematite coated PET film, a reservoir for concentrated hydrochloric acid (HCl), and a reservoir for 1.56 M monomer (pyrrole or EDOT) solution in chlorobenzene. Various volume combinations of liquid reactants were tested (10~200 μ L HCl, 100~200 μ L monomer solution) to achieve conformal coating of polymer on the substrate and to obtain optimal electrochemical performance. After 1.5 h, the electrodes were immediately removed from the reactors, cooled to room temperature, and purified with 6 M HCl. 4) For a PEDOT/PPy composite electrode, another layer of α -Fe₂O₃ was deposited on a purified PEDOT electrode. The same synthetic procedure was performed again using concentrated HCl and pyrrole/chlorobenzene solution. A composite electrode was purified with 6 M HCl to remove all iron impurities.

Kirigami electrode characterizations

Optical micrographs were obtained from a Nikon Eclipse LV100ND microscope. Scanning electron micrographs and energy-dispersive X-ray spectra were collected using a JEOL 7001LVF FE-SEM. Raman spectra were obtained using a Renishaw inVia confocal Raman spectrometer mounted on a Leica microscope with a 20 \times objective and 785 nm wavelength diode laser serving as an illumination source. A low power was necessary to mitigate heating of conducting polymer samples. Current-voltage (I-V) curves were obtained with a built-in-house 3D-printed probe station using two gold needles 1.24 mm apart. Four-point probe sheet resistance measurements were carried out using a Keithley 2450 SourceMeter with a Signatone SP4 four-point probe head. Stress-strain curves were characterized via INSTRON 5583.

Preparation of gel electrolyte

Both 1 M H_2SO_4 and LiClO_4 aqueous electrolyte required degassing of milli-Q water (18 M Ω) for 15 min. A 1 M LiClO_4 /polyvinyl alcohol gel electrolyte was prepared by adding 1 g of concentrated LiClO_4 to 10 mL of deionized water, followed by addition of 1 g of polyvinyl alcohol powder. The whole mixture was heated to 85 °C while stirring until a clear solution was obtained.

Fabrication of PEDOT nanofibrillar Kirigami humidity dosimeter

Platinum current leads were connected to a PEDOT-coated film using polyimide tape and attached onto the surgical mask via Scotch tape.

Humidity characterizations

PEDOT nanofibrillar film and PEDOT:PSS granular film were tested in a humidity chamber. Utilizing N_2 gas flow to decrease the humidity and water vapor to increase the humidity.

Fabrication of PPy/PEDOT nanofibrillar Kirigami supercapacitor

Platinum current leads were connected to a PEDOT/PPy composite film and 100 μL of a 1 M LiClO_4 gel electrolyte was added by drop-casting, followed by drying at 55 °C for 2 h.

Electrochemical characterizations

All electrochemical tests were performed on a BioLogic VMP3 multi-potentiostat and the data were averaged over 5 devices. Cyclic voltammetry was carried out from 25 mV/s to 1000 mV/s between -0.2 V and 0.8 V. Electrochemical impedance spectroscopy was carried out at the

electrode's open circuit potential after obtaining a reversible cyclic voltammogram. Impedance values were recorded using a 10 mV sinusoidal disturbance at frequencies ranging from 100 kHz to 100 MHz. For 3-electrode tests, various electrolytes (aqueous 1 M H₂SO₄, aqueous and acetonitrile 1 M LiClO₄) were tested against a Ag/AgCl reference electrode at room temperature (25 °C). Galvanostatic charging/discharging (GCD) was carried out from 0.1 mA/cm² to 2 mA/cm² between 0 to 1 V.

2.3 Results and Discussion

Deposition of hematite and vapor-phase synthesis of polymers

A conformal oxidant precursor coating is produced by sputtering hematite (α -Fe₂O₃) onto a laser cut polyethylene terephthalate (PET) film (Figure 2.1a). The uniformity of the solid-state precursor ensures homogenous polymer deposition, and synthesis on a pre-cut substrate instead of laser cutting after polymer deposition prevents polymer damage from CO₂ laser heating. α -Fe₂O₃ is dissolved by HCl vapor at 140 °C, releasing ferric ions (Fe³⁺) that oxidize EDOT and initiate polymerization (Figure 2.1b).^{20,21} Hydrolysis of Fe³⁺ produces β -FeOOH spindles in situ; these spindles serve as nucleation sites for PEDOT and template one-dimensional nanofiber formation (Figure 2.1b). Polypyrrole is synthesized via a similar vapor-phase technique because the oxidation potential of a ferric ion is adequate for initiating both EDOT and pyrrole polymerization (Figure 2.1b).²² Scanning electron micrographs (SEM) in Figure 2.1c-d show homogeneous PEDOT (blue) and PPy (black) thin films consist of nanofibers with an aspect ratio of 50. Polymer nanofibers deposit with a high packing density, resulting in a polymer film that possesses a high surface area.

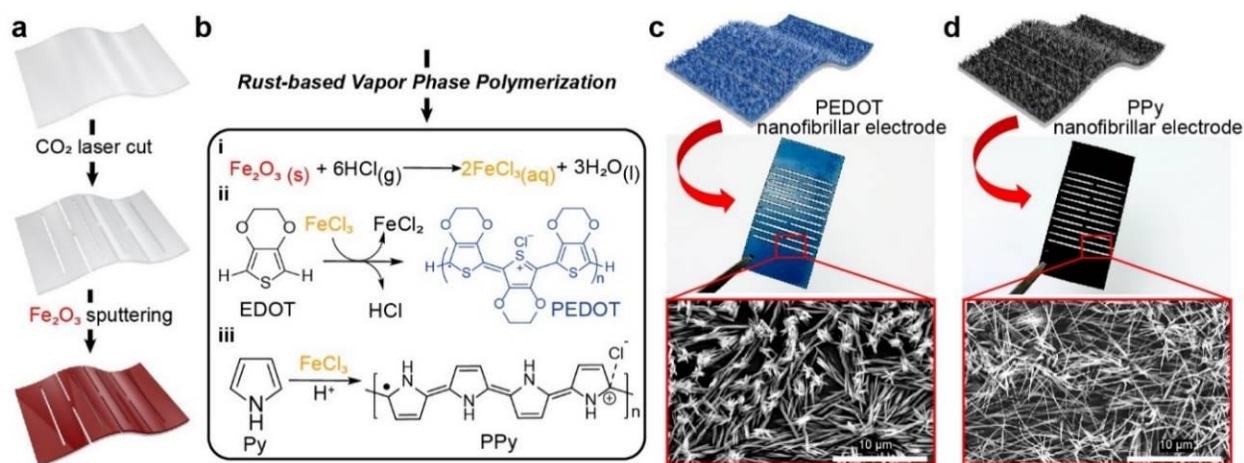


Figure 2.1 Schematic diagram for vapor-phase deposition of conducting polymer nanofibers on Kirigami sheets. a) PET sheet is laser-cut and subsequently sputtered with a 60 nm layer of $\alpha\text{-Fe}_2\text{O}_3$. b) PEDOT and PPy nanofibers are deposited via rust-based vapor-phase polymerization, and the synthesis consists of i) dissolution of Fe_2O_3 into Fe^{3+} and oxidative polymerization of ii) EDOT and iii) pyrrole. The resulting nanofibrillar coatings are homogeneous as shown by c) blue PEDOT and d) black PPy.

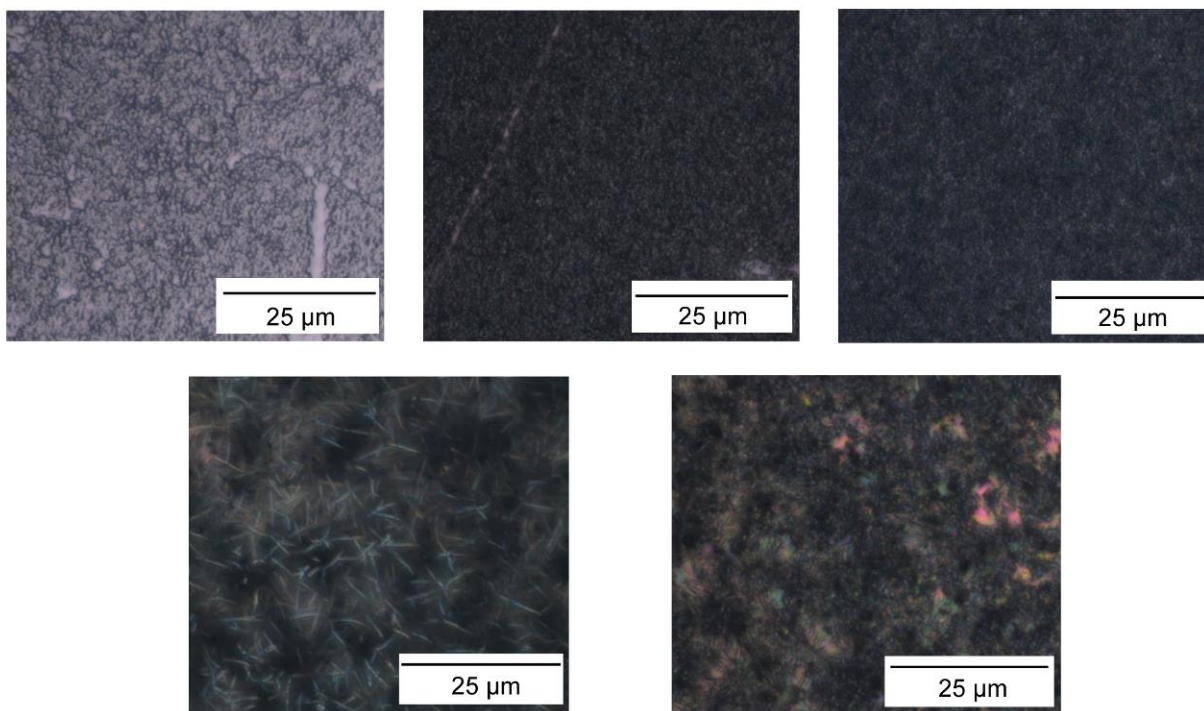


Figure 2.2 Optical micrographs of polypyrrole synthesized under various HCl concentration. a) 20 μL , b) 60 μL , c) 90 μL , d) 120 μL , and e) 150 μL . Fibrillar PPy causes refraction and is lighter in color under the optical microscope compared to granular PPy. The structure is obtained when 120 μL HCl is used during synthesis.

Acid-catalyzed polymerization of EDOT and pyrrole

Comparing the optical micrographs of polypyrrole films synthesized under different HCl concentration reveals a correlation between the stoichiometry of reactants and the morphology of the films (Figure 2.2). The nanostructure of a PPy film changes from granular (stage one) to fibrillar (stage two) then to granular (stage three) as the HCl concentration in the reactor increases. The morphology change from stage two to stage three (fibrillar to granular) is also observed in PEDOT vapor-phase synthesis and is attributed to excess HCl dissolving the structure-directing iron oxides and oxyhydroxides. The consequent lack of nucleation sites and templates for nanofiber growth results in an undesirable granular morphology (Figure 2.3). The structural change between stage one and stage two (granular to fibrillar) is unique to polypyrrole synthesis. Based on the evidence from both microscopy and the acid-catalyzed polymerization mechanisms reported in the literature, a mechanism is proposed to explain the evolution of morphologies during polypyrrole synthesis.

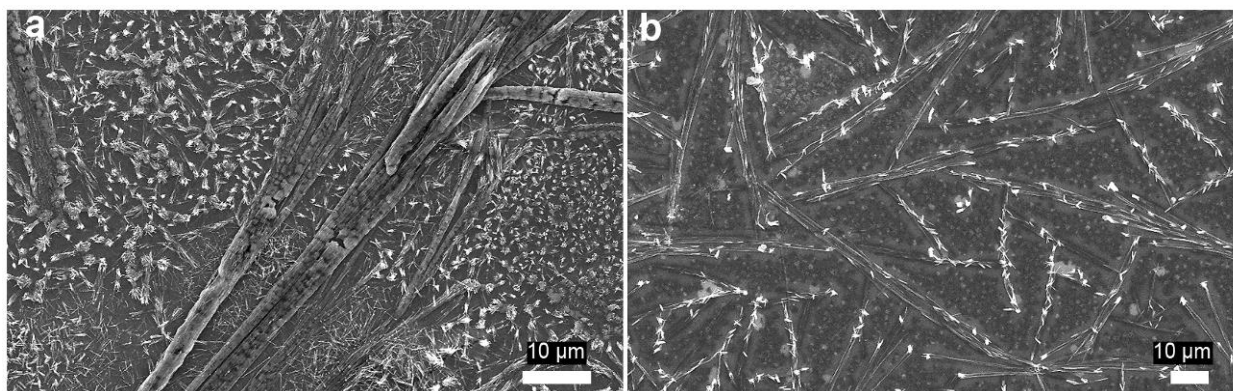


Figure 2.3 SEM images of β -FeOOH crystals and granular morphology of PEDOT.

Both EDOT and pyrrole monomers protonate and undergo acid-catalyzed polymerization in the presence of low pH.^{23,24} Figure 2.4 depicts the proposed mechanisms of acid catalyzed

polymerization of EDOT and pyrrole. The reaction is initiated by the protonation of monomer and propagates via coupling between a protonated monomer cation and a neutral monomer. The dimer cation either terminates the reaction by deprotonating into a neutral dimer, or couple with other neutral monomer/oligomers. The polymer backbone formed in acid-catalyzed polymerization does not contain the alternating double-single bond structure. Therefore, π -electrons do not delocalize over the entire polymer backbone, resulting in poor electrical conductivity. Spectroscopic evidence from the literature suggests that EDOT forms oligomeric chains through this mechanism (average degree of polymerization is 11.3), while pyrrole forms polymeric chains that consist of a mixture of pyrrole and pyrrolidine.^{23–28} Pyrrole is susceptible to reduction in acidic environment, resulting in the formation of pyrrolidine.^{29,30} Pyrrolidine and pyrrole form a trimer in a ratio of one pyrrolidine to two pyrroles. In a reaction that consists of both oxidative and acid-catalyzed polymerization, the ratio between pyrrole monomer and pyrrole/pyrrolidine trimer influences the conjugation and electrical conductivity of the polymer product.^{24–26} During vapor-phase synthesis, high acidity triggers the acid-catalyzed polymerization, and this mechanism competes with iron oxide dissolution for HCl. Polypyrrole synthesis requires higher acid concentration than PEDOT synthesis because pyrrole forms conjugated backbone via both oxidative polymerization and acid-catalyzed polymerization, whereas conjugated PEDOT forms exclusively via oxidative polymerization. Thus, greater volumes of HCl are required to account for protonation and for the Fe^{3+} liberated by dissolution to generate a nanofibrillar morphology during PPy synthesis.

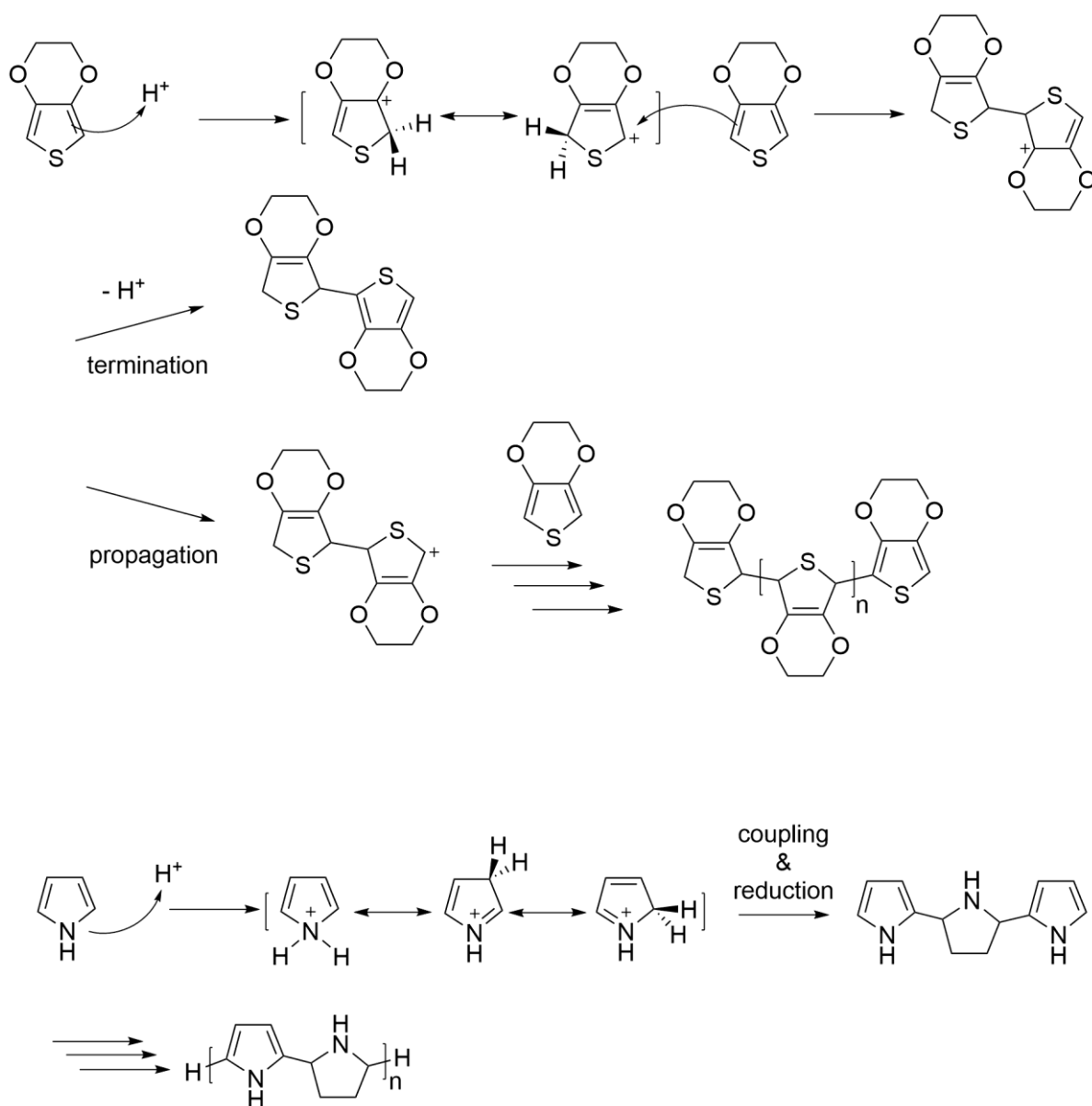


Figure 2.4 Acid-catalyzed polymerization of EDOT and pyrrole.

Spectroscopic analysis of PEDOT and PPy films

Characterizing the bonding in a nanofibrillar conducting polymer film is necessary to deepen understanding of their physical and chemical properties. Raman spectroscopy provides insight into the impact of doping on chemical bonding within the materials. Raman peaks of PEDOT

(Figure 2.5a) at 1261 and 1357 cm^{-1} correspond to $\text{C}_\alpha\text{-C}_\alpha'$ and $\text{C}_\beta\text{-C}_\beta'$ bonds, respectively. Peaks at 1437 and 1510 cm^{-1} correspond to symmetric and asymmetric $\text{C}_\alpha=\text{C}_\beta$ stretching.³¹ The symmetric $\text{C}_\alpha=\text{C}_\beta$ stretching peak shifts towards 1426 cm^{-1} after doping with HCl vapor. This shift towards higher wavenumbers corresponds to greater doping levels due to an increased ratio of quinoid vs. benzenoid structure in PEDOT and is consistent with previously reported behavior of electrochemically synthesized PEDOT samples.^{32,33} Similar information is derived from the Raman analysis of PPy that shows peaks at 1345 and 1573 cm^{-1} associated with $\text{C}_\alpha=\text{C}_\beta$ bonds at higher intensity (Figure 2.6). The behavior of the PEDOT and PPy samples indicates that Cl^- is an efficient dopant due to its small size and single negative charge as a counter anion.³⁴

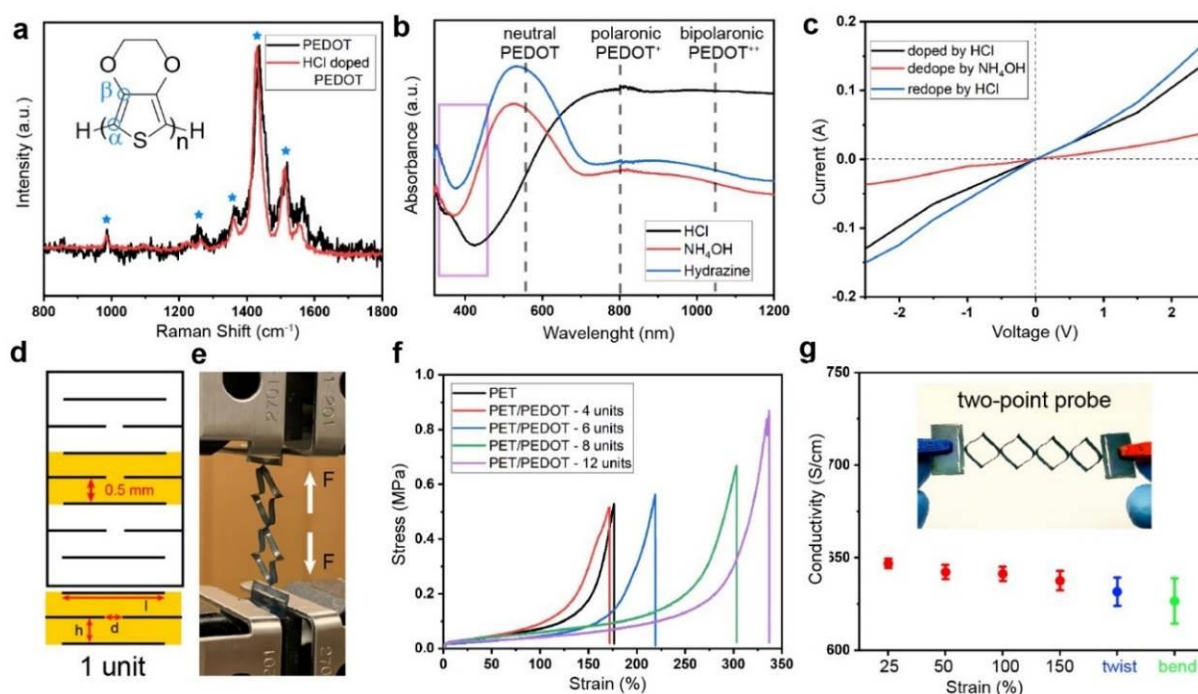


Figure 2.5 Spectroscopic and mechanical characterization of conducting polymer coatings. a) Raman spectra shows PEDOT possesses an oxidized conjugated backbone. b) UV-vis spectra prove that both reducing agent and base partially convert conductive polaronic and bipolaronic PEDOT to its non-conductive neutral state. c) I-V curves for a PEDOT-coated film demonstrate ohmic behavior that stems from a homogenous percolation network of conductive polymer backbone. d) Schematic diagram of a Kirigami unit cell. e) Tensile tests of PEDOT-coated

Kirigami sheet. f) Stress-strain curves show the increase of ultimate elongation is proportional to the increase in the number of unit cells. g) Electric conductivity remains stable throughout the stretching process.

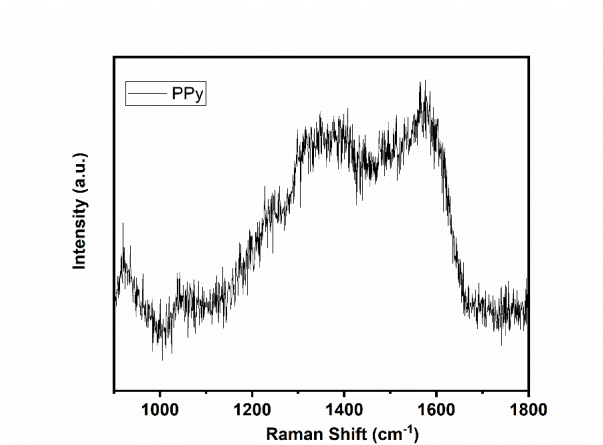


Figure 2.6 Raman spectrum of a HCl-doped PPy film.

Ultraviolet-Visible-near-IR spectroscopy (UV-Vis-NIR) is utilized to assess charge carrier density in polymer films and determine changes in molecular structures due to doping and dedoping. The UV-Vis-NIR spectra of PEDOT (Figure 2.5b) is divided into three regimes: neutral, polaronic, and bipolaronic.³⁵ A larger absorbance in the polaronic and bipolaronic regimes is observed for the HCl-doped PEDOT sample, compared to an aqueous-ammonia- ($\text{NH}_3 \cdot \text{H}_2\text{O}$) or a hydrazine-dedoped sample. Doping increases the charge carrier density in the polymer chain, resulting in formation of conductive polaron and bipolaron structures that enhance electrical conductivity. This behavior is also present in the UV-Vis-NIR spectra of HCl-doped PPy (Figure 2.7a).³⁶ Notably, the doping/dedoping process is reversible and controlled by charge carrier concentration as evidenced by Figure 2.7b. Electrical conductivity of a PEDOT film is probed via current vs. voltage measurement and shows ohmic behavior (straight line) with low resistance (large slope) (Figure 2.5c). This signifies a homogeneous and continuous percolation network of conductive polymer chains within the film that facilitate charge

transport.³⁷ The line slope decreases when the sample is dedoped with $\text{NH}_3 \cdot \text{H}_2\text{O}$ due to loss of charge carriers, and this is consistent with the reversibility demonstrated by UV-Vis spectra.

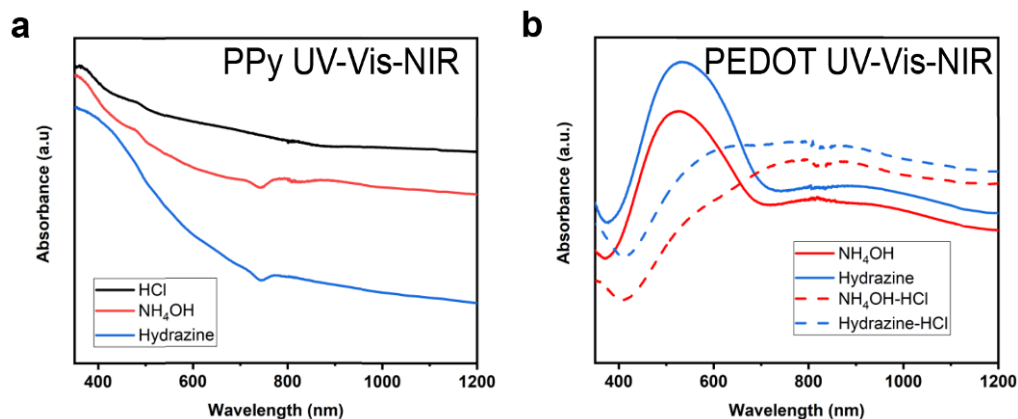


Figure 2.7 UV-Vis-NIR characterization of conducting polymers. (a) UV-Vis-NIR spectra of doped and dedoped PPy films. (b) UV-Vis-NIR spectra of dedoped and HCl-redoped PEDOT.

Electrochemical Characterizations of PEDOT, PPy, and composite polymer films

Layer-by-layer deposition of nanofibers with high packing density is achieved via the combination of hematite sputtering and vapor-phase synthesis. A composite polymer film is synthesized by polymerizing pyrrole directly on the surface of a PEDOT layer (Figure 2.8a). SEM images show that the composite film surface is comprised of a carpet of PEDOT/PPy nanofibers. This hierarchical structure suggests that the existing PEDOT layer acts as a barrier to the diffusion of HCl vapor. Pyrrole polymerization occurs on PEDOT nanofibers instead of on the PET substrate due to preferential nucleation.^{22,38} This novel synthetic approach for depositing electroactive polymer composites results in sequential deposition of conducting polymer layers that grafts PPy to PEDOT (Figure 2.8b).

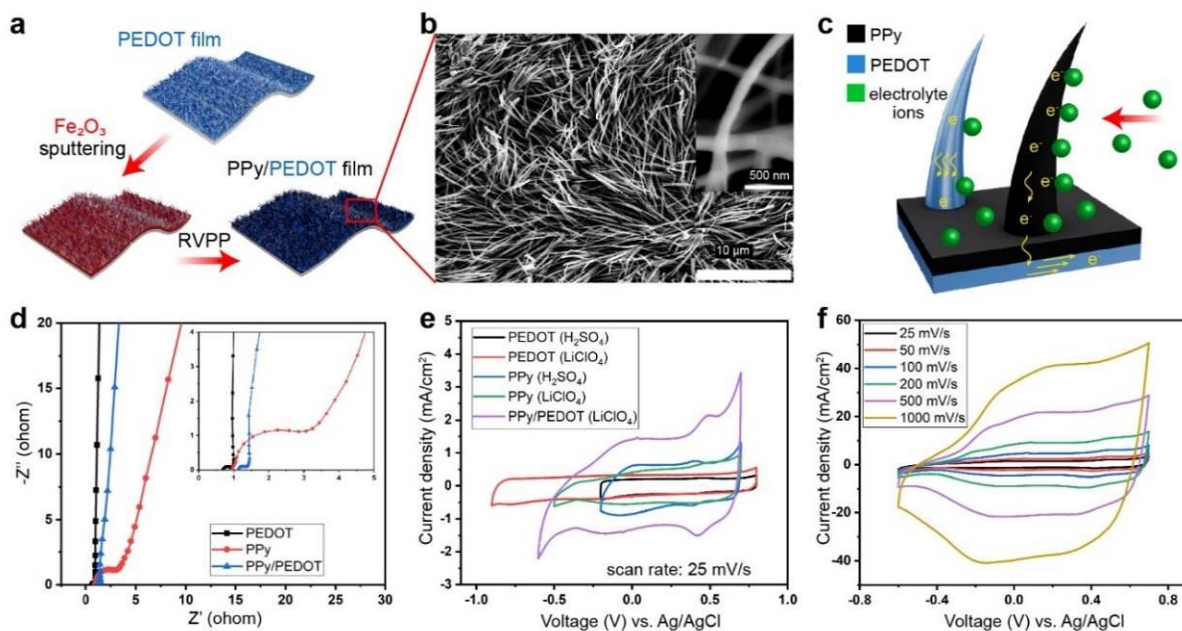


Figure 2.8 Nanofibrillar PEDOT/PPy composite as Kirigami electrodes. a) A schematic diagram shows the deposition strategy: a nanofibrillar PEDOT-coated PET film is sputtered with α -Fe₂O₃ and undergoes vapor-phase synthesis, resulting in a nanofibrillar PPy film on top of the PEDOT nanofibers. b) This bilayer PEDOT/PPy Kirigami electrode possesses a high packing density of nanofibers with a 150 nm diameter (inset). c) A schematic diagram shows a PEDOT/PPy composite electrode charging in the electrolyte. PPy serves as a highly capacitive material with active redox sites and PEDOT serves as a conductive layer that facilitates facile charge transfer. d) EIS of PEDOT, PPy, and PEDOT/PPy electrodes show that the composite possesses the lowest ESR due to the conductive PEDOT layer and low ion transfer resistance. e) Cyclic voltammograms of PEDOT, PPy, and PEDOT/PPy composite electrodes at 25 mV/s show the curve of the composite envelops the largest area, indicating a high capacitance. f) The PEDOT/PPy composite electrode is stable under various scan rates from 25 to 1000 mV/s in an aqueous LiClO₄ electrolyte.

The composite polymer film possess a bilayer architecture that capitalizes on the high conductivity of PEDOT (1000 S/cm) through intimate contact and chemical bonding at the electrode/current collector interface. The PPy layer (nanofibers) possesses high pseudo-capacitance and is more sensitive to ion adsorption at the electrode/electrolyte interface than PEDOT (Figure 2.8c). Electrochemical impedance spectroscopy is utilized to compare the electron and ion transfer resistance of the single electrode against the composite electrode (Figure 2.8d). Nyquist plots for PEDOT and PPy films reveal that PEDOT possesses a lower equivalent series resistance (intercept of x axis), lower ion diffusion resistance (small semicircle

radius) than PPy.²¹ In comparison, Nyquist plot of the composite polymer film possesses a smaller semicircle radius than a PEDOT film, indicating reduced contact resistance between electrolyte and electrode as well as low diffusion resistance for adsorption/desorption of electrolyte ions.³⁹ The enhanced electrical conductivity and adsorption/desorption of ions demonstrates synergy between two polymers inside the composite as a result of grafting during synthesis.

Three-electrode cyclic voltammetry (CV) provides fundamental understanding of electrochemical processes that occur during charging and discharging of the composite electrode. Figure 2.8e shows the CV curves for PEDOT, PPy and PEDOT/PPy electrodes immersed in 1 M aqueous solutions of various electrolytes. Unlike PEDOT that prefers acidic electrolyte, the most rectangular and reversible curve for PPy is achieved using a neutral LiClO₄ electrolyte (Figure 2.9). The composite electrode demonstrate the highest capacitance in LiClO₄ which typically weakens the charge storage performance of PEDOT. The loss in capacitance from PEDOT is offset by the high capacitance of PPy, and the synergy between the polymers enhances charge storage, resulting in a greater capacitance compared to single polymer electrodes. Cyclic voltammograms remain mostly undistorted at high scan rates (1000 mV/s) as the nanofibrillar architecture creates free volume and accessible electroactive sites; fast redox reactions in the devices enable high-rate charging that is ideal for supercapacitors (Figure 2.8f). The synergy between PEDOT's high electrical conductivity and PPy's pseudocapacitance enhances the overall electrochemical performance in a composite polymer electrode.

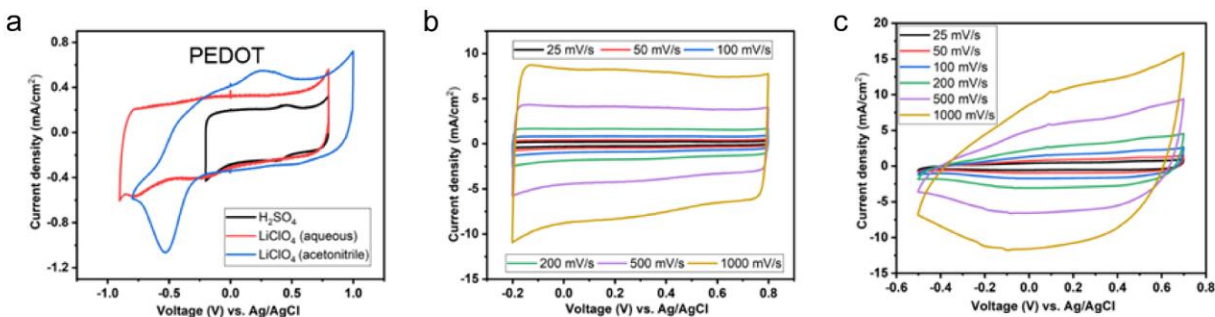


Figure 2.9 Electrochemical characterizations of PEDOT and PPy films. (a) Cyclic voltammograms of PEDOT in 1 M H₂SO₄, 1 M aqueous LiClO₄ and 1 M LiClO₄ in acetonitrile. (b) Rectangular cyclic voltammogram of PEDOT in 1 M H₂SO₄ electrolyte under various scan rates from 25 to 1000 mV/s. (c) Cyclic voltammograms of PPy in an aqueous 1 M LiClO₄ electrolyte under various scan rates from 25 to 1000 mV/s.

Flexibility and stretchability of conducting polymers

Conducting polymers such as PEDOT and PPy possess good flexibility but poor stretchability owing to their molecular structure: the single bonds in the polymer backbone afford rotational degree of freedom, and the delocalized π -orbitals enables polymer chains to slide against each other without breaking conjugation.^{13,14,40} The structure of a polymer consists of both crystalline and amorphous domains, and the stretchability of a polymer originates from straightening of coiled polymer chains in the amorphous domain.^{15,41,42} PEDOT and PPy synthesized from the vapor phase possess high crystallinity and few polymer chains in the amorphous domain, resulting in poor stretchability. Another challenge is the difference in mechanical properties between substrate material (PET) and active materials (PEDOT and PPy). The mismatch of strength (tensile, torsional, and flexural), ultimate elongation, Young's modulus, toughness, and viscoelasticity between materials often leads to delamination from substrate or break in the percolation network formed by the conductive polymer chains.^{42,43} Therefore, enhancing the

stretchability of conducting polymers while matching the mechanical properties between substrate and active material are crucial for fabricating electrodes in wearable electronics.

Kirigami is an engineering solution to a chemistry problem that overcomes the intrinsic stretch limits of conducting polymers by redirecting applied strain onto the macroscopic structure of the electrode instead. Strain-stress analysis and resistance measurement demonstrate the relationship between mechanical deformation and electrical conductivity. Unit cells are patterned with a cut geometry of length l (18 mm), horizontal spacing d (0.2 mm), and vertical spacing h (0.5 mm), resulting in PET-based films that stretch up to 350% strain before rupture (Figure 2.5d). As a mechanical strain is applied, the cuts open and redirect the stress into structural change, enhancing the in-plane stretching capacity of the substrate. Additional strain causes the initial planar structure to deform, and the unit cells begin bending out-of-plane to redistribute the stress to the vertices of the cuts (Figure 2.5e).⁴⁴ This structural response allows the substrate to accommodate increased stretching while maintaining low stress growth by on a PEDOT or PPy film. Conducting polymers exhibit strong interfacial adhesion to the PET substrate due to covalent bonding facilitated by Friedel-Crafts alkylation that grafts PEDOT onto aromatic functional groups of PET.⁴⁵ During polymer synthesis, dissolved ferric ions functions as both oxidants to EDOT monomer and a Lewis acid that catalyzes Friedel-Crafts alkylation between PEDOT and PET. PEDOT and PET exhibit strong adhesion and minimal delamination during bending, scotch tape test and bath sonication (Figure 2.10). In comparison, pristine a PPy electrode exhibits weak adhesion with PET, and the polymer film cracks and delaminate when bent due to a lack of covalent bonding (Figure 2.11).⁴⁵

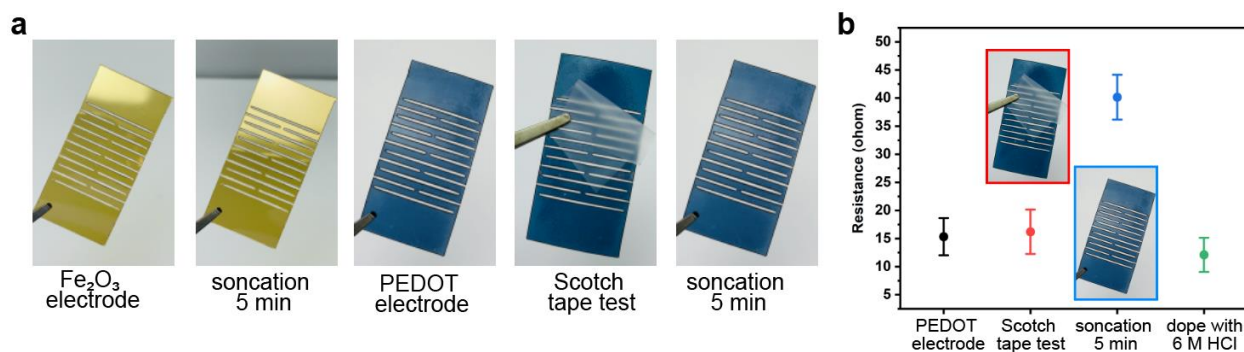


Figure 2.10 Adhesion tests of PEDOT to a PET substrate. (a) Adhesion of PEDOT to a PET substrate is examined via sonication, scotch tape test. (b) The electrical resistance is measured before and after each test.



Figure 2.11 PPy film delaminates from a PET substrate after scotch tape test.

Increasing the number of Kirigami unit cells further extends the maximum elongation of the film (Figure 2.12). Additional unit cells delay the point of fracture as demonstrated by the gradual decoupling of the stress-strain curves in Figure 2.5f. Similar stress-strain curves obtained for a PET film and a PEDOT-coated PET film indicate that a PEDOT-coated electrode retains the original mechanical properties of the substrate. Yielding initiates from the innermost cut and propagates outwards until the peripheral cuts reach their maximum stress load and the electrode ruptures.⁴⁶ Besides buffering the transmission of strain to outer regions of the film, extra unit cells also lessen the overall load distributed to individual cut, significantly enhancing the fracture limit.^{4,47} The nanofibrillar electrodes demonstrate excellent electrical stability stemming from their ability to withstand complex deformation without rupturing the conductive polymer layer.

Conductivity-strain curves (Figure 2.5g and Figure 2.13) confirm that electrode conductivity is not significantly affected by increasing strain. Localization of strain on the corners of the cuts allows the substrate to stretch without disrupting the homogeneity of nanofibrillar film.⁴⁸ Preservation of conducting pathways allows the electrode to retain a high degree of electrical conductivity (95%) under different mechanical tensile strains (0-150%). Other modes of mechanical deformation, such as bending and twisting, exert low stress on the film, and the structural and electrical properties of the active material layer also remain unchanged.⁴⁹

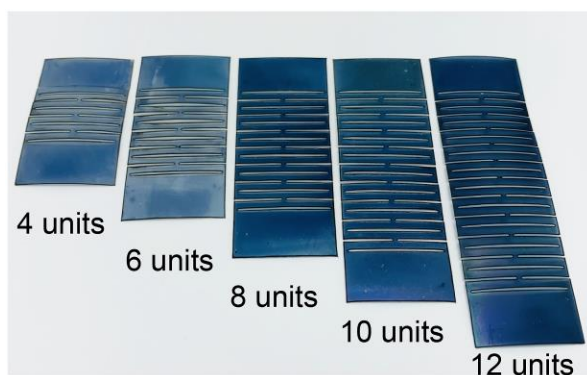


Figure 2.12 Nanofibrillar PEDOT Kirigami sheets with increasing numbers of unit cells.

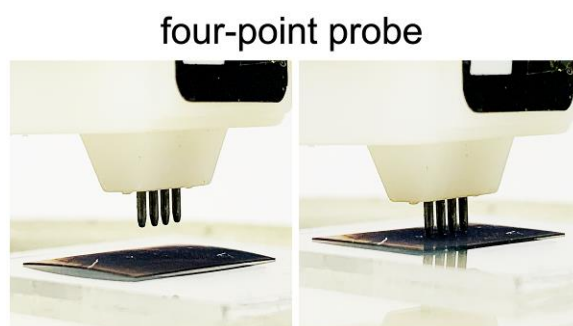


Figure 2.13 Conductivity measurement via a four-point probe.

Fabrication of flexible and stretchable supercapacitor

Both sandwich-type and planar supercapacitors are fabricated from stretchable PEDOT/PPy composite electrodes and characterized by two-electrode cyclic voltammetry (CV) as well as

galvanostatic charging/discharging (GCD) technique. The sandwich-type supercapacitor is comprised of two electrodes and 1M LiClO₄ gel electrolyte (Figure 2.14a). GCD curves (Figure 2.14b) for the composite electrode exhibit symmetric triangular shapes from 0-1 V under various current densities, indicating a reversible redox charge storage mechanism.⁵⁰ The linearity of the GCD curves together with minimized IR-drop at a fast discharge rate stems from a low internal resistance that promotes capacitive behavior.⁵¹ Cyclic voltammograms exhibit a rectangular shape proportional to the reversibility of doping/dedoping by electrolyte ions. The PEDOT/PPy composite electrode generates symmetric rectangular cyclic voltammograms under scan rates ranging from 5 mV/s to 50 mV/s and is capable of fast charging/discharging. The CV of a composite electrode envelops a larger area compared with pristine PEDOT and PPy electrodes (Figure 2.15). Areal capacitance calculations from CV curves are summarized in Figure 2.14c. The PEDOT/PPy composite supercapacitor possesses state-of-the art areal capacitance of 378 F/g due to its bilayer nanofibrillar morphology and the synergy between PEDOT and polypyrrole. PPy excels at charge storage due to its redox reactions during cycling and the high electrical conductivity of PEDOT facilitates charge transfer.⁵²

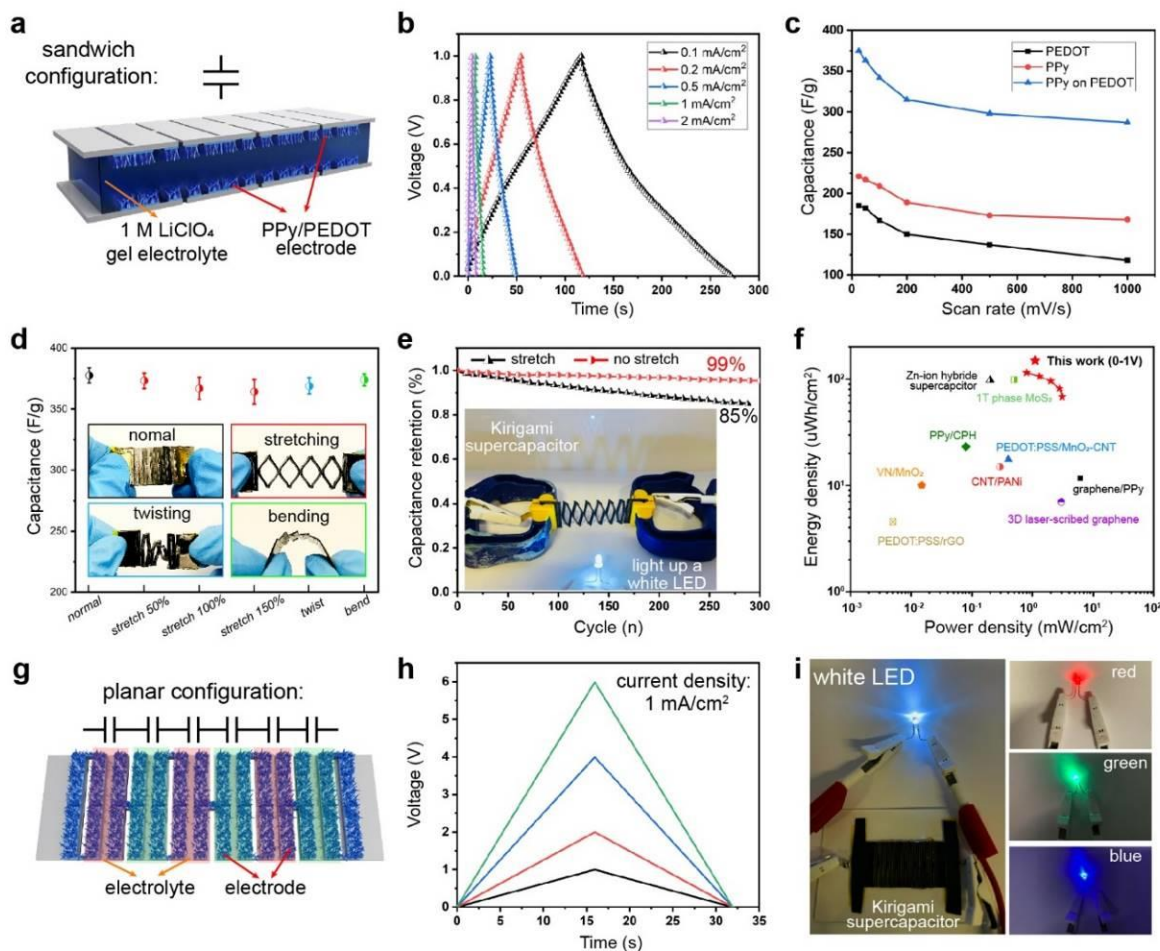


Figure 2.14 Nanofibrillar PEDOT/PPy Kirigami supercapacitors. a) A schematic diagram of a sandwich-type supercapacitor that consists of two composite electrodes and 1 M LiClO_4 gel electrolyte. b) Symmetric triangular charge/discharge curves at various current densities from 0.1 mA/cm^2 to 2 mA/cm^2 demonstrate reversible storage and release of charges. c) The PEDOT/PPy composite possesses higher capacitance than pristine PEDOT or PPy across all scan rates due to the synergistic interaction between capacitive PPy and conductive PEDOT. d) The capacitance remains stable during mechanical deformation such as stretching, twisting, and bending. e) Comparison of capacitance retention without stretching versus with stretching. An 85% capacitance retention is achieved after 300 stretching cycles. Inset shows an LED is powered using 3 stretched supercapacitors connected in series. f) A Ragone plot normalized by area compares this work against graphene/PPy, CNT/PANI, PEDOT:PSS/ MnO_2 /CNT, RuO_2 /PEDOT:PSS, PPy/CPH, 10%rGO-PEDOT:PSS, and PEDOT/rGO thin-film supercapacitors. g) A schematic diagram of a planar configuration that connects multiple supercapacitors in series to extend the voltage window. h) Charge/discharge curves collected at 1 mA/cm^2 demonstrates that reversible storage and release of charges when the number of unit cells is increased. 1 V (black), 2 V (red), 4 V (blue) and 6 V (green). i) Photographs that shows a planar PEDOT/PPy Kirigami supercapacitor powering up LEDs with various colors.

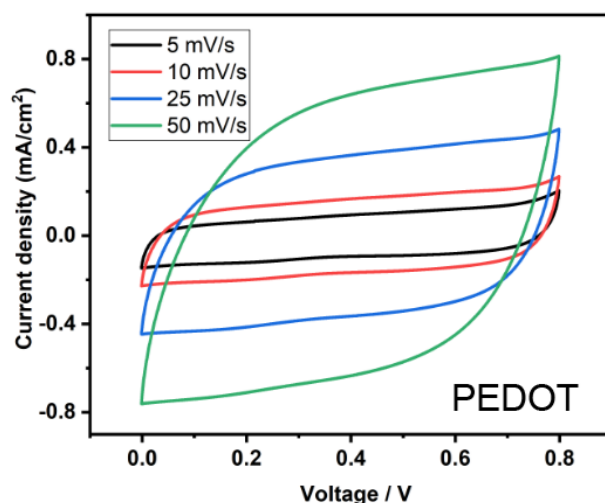


Figure 2.15 Cyclic voltammograms of PEDOT in 1 M LiClO₄ electrolyte under various scan rates.

Maintaining electrical performance under mechanical deformation is a crucial parameter for stretchable power sources. A planar PEDOT/PPy nanofibrillar supercapacitor shows minimal change in capacitance during stretching (378 F/g at 0% stretch, 373 F/g at 50% stretch, 368 F/g at 100% stretch, 363 F/g at 50% stretch), twisting (369 F/g at 50% stretch), and bending (372 F/g at 50% stretch) (Figure 2.14d) and demonstrates superior energy storage performance under mechanical strain. A composite supercapacitor exhibits 99% and 85% capacitance retention after 300 cycles (100% stretch), respectively (Figure 2.14e). An Ragone plot normalized by area graphs the relationship between power density and energy density and shows the state-of-the-art performance among supercapacitors fabricated from carbon allotropes and metal oxides, metal-organic framework (MOF), MXene, and transition metal dichalcogenide (Figure 2.14f).^{53–57} Among these, the PEDOT/PPy composite supercapacitor exhibits the highest areal energy density of 115 $\mu\text{Wh}/\text{cm}^2$.

Supercapacitor units are assembled both in series and in parallel to meet specific energy needs or open circuit voltages for various applications. Figure 2.14g and Figure 2.16 illustrate the details of the planar configuration comprised of 6 units of PEDOT/PPy supercapacitors (labeled in red and green) connected in parallel. The capacitance performance is confirmed via GCD curves collected at 1 mA/cm^2 for 1 V (black), 2 V (red), 4 V (blue) and 6 V (green). This functional device lights up LEDs of different colors, demonstrating the advantage of a planar configuration and highlighting its potential for stretchable electronics.

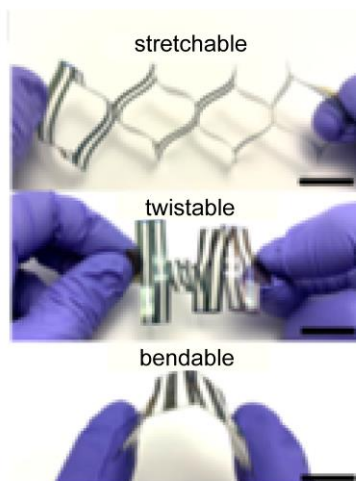


Figure 2.16 The supercapacitor withstands various modes of deformation, including stretching, twisting, and bending.

Fabrication of wearable humidity dosimeter

The global outbreak of COVID-19 significantly affected economy and human health in the past few years. Recent studies demonstrate that surgical masks efficiently prevent virus transmission from airborne aerosols.^{58,59} The ability to detect exposure to respiratory droplets from coughing or sneezing on the outer surface of a mask is of considerable importance, since a mask will lose its functionality once it experiences extreme humidity. Additionally, touching or handling a

contaminated mask carries the risk of transmitting bacteria or viruses (Figure 2.17a).⁶⁰ A flexible nanofibrillar PEDOT-coated film serves as a flexible chemoresistive dosimeter by monitoring the relative humidity change on the mask to detect droplet attachment. The stretchable 2D film is easily integrated onto the 2D mask via platinum lead, polyimide tape, and a multimeter (Figure 2.17b). A PEDOT-coated film shows clear compatibility with the mechanical requirements of wearing surgical masks due to the 3D tunable mechanical properties generated by Kirigami. Notably, the electrode is only 0.5 mm thick and weighs only 0.16 g, making it easy to assemble onto the mask (Figure 2.17c).

To explore the relationship between sensitivity and electrode morphology, a nanofibrillar PEDOT electrode and compare it against PEDOT:PSS thin film electrodes for testing humidity levels. Figure 2.17d shows that the resistance decreases with increasing humidity for both electrodes due to 1) polymer swelling-induced electron transfer through conjugation length and 2) formation of a water layer that induces electron hopping that facilitates electron transfer. Nanofibrillar PEDOT film exhibits remarkable decrease in resistance at the initial humidity range (around 40% relative humidity) and exhibits faster response (<2 s) in comparison to the PEDOT:PSS thin film (Figure 2.17e).⁶¹ The heightened response of the electrode is a consequence of the larger surface area generated by high aspect ratio nanofibers that provides more accessible pathways for water vapor to traverse.⁶² This is congruent with the porous nature of nanofiber films, in which gas molecules or aerosol droplets rapidly diffuse in and out of the nanofibers (Figure 2.17f).⁶³ A PEDOT nanofibrillar humidity dosimeter exhibits better performance in both sensitivity and response time than a conventional PEDOT:PSS film or other

commercial humidity sensors, demonstrating it as an ideal humidity-sensing dosimeter accessory for surgical masks.

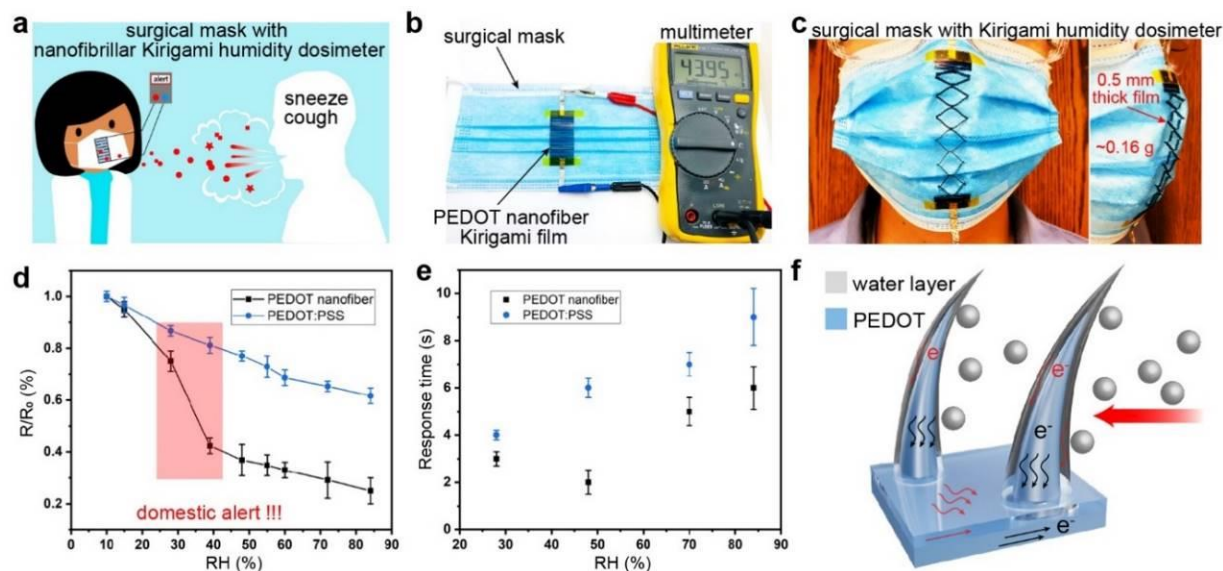


Figure 2.17 Nanofibrillar PEDOT Kirigami electrodes for wearable humidity dosimeters. a) A schematic diagram demonstrating the humidity dosimeter detects droplets that originate from sneezes and coughs. b) A photograph of humidity dosimeter in its 2D state attached to a surgical mask. c) Front and side view of the dosimeter stretching to accommodate 3D deformation from surgical mask. d) Resistance change and e) response time in a dosimeter comprised of PEDOT nanofibers vs. PEDOT:PSS as a function of relative humidity. f) A schematic diagram that demonstrates water droplets spreading on PEDOT nanofibers and enhancing charge transfer.

2.4 Conclusions

In this chapter, a synthetic strategy that combines cleanroom techniques and rust-based vapor-phase polymerization of conducting polymers is presented. The acid-catalyzed polymerization mechanism, a side reaction during polymer synthesis, is studied via stoichiometric experiments. The synthetic strategy presented enables fabrication of a flexible PEDOT/PPy composite electrode and advances the research in stretchable electrodes by combining Kirigami-based engineering techniques with vapor-phase polymer synthesis. The grafting between PEDOT and PET substrate enhances the stability of a polymer electrode and is facilitated by Friedel-Crafts alkylation. The interaction between PPy and PEDOT creates synergy that enhances the

electrochemical properties of the composite, enabling the fabrication of a supercapacitor that possesses state-of-the-art energy density ($115 \mu\text{Wh}/\text{cm}^2$ at $1 \text{ mA}/\text{cm}^2$) and capacitance (85% capacitance retention after 300 stretching cycles). A Kirigami humidity dosimeter is fabricated using PEDOT nanofibers that exhibits superior performance in both sensitivity (40% change) and response time ($<2 \text{ s}$).

2.5 References

- (1) Huang, Z.; Hao, Y.; Li, Y.; Hu, H.; Wang, C.; Nomoto, A.; Pan, T.; Gu, Y.; Chen, Y.; Zhang, T.; Li, W.; Lei, Y.; Kim, N.; Wang, C.; Zhang, L.; Ward, J. W.; Maralani, A.; Li, X.; Durstock, M. F.; Pisano, A.; Lin, Y.; Xu, S. Three-Dimensional Integrated Stretchable Electronics. *Nat. Electron.* **2018**, *1* (8), 473–480. <https://doi.org/10.1038/s41928-018-0116-y>.
- (2) Yang, C.; Zhang, H.; Liu, Y.; Yu, Z.; Wei, X.; Hu, Y. Kirigami-Inspired Deformable 3D Structures Conformable to Curved Biological Surface. *Advanced Science* **2018**, *5* (12), 1801070. <https://doi.org/10.1002/advs.201801070>.
- (3) Song, Z.; Wang, X.; Lv, C.; An, Y.; Liang, M.; Ma, T.; He, D.; Zheng, Y. J.; Huang, S. Q.; Yu, H.; Jiang, H. Kirigami-Based Stretchable Lithium-Ion Batteries. *Sci. Rep.* **2015**, *5* (1), 10988. <https://doi.org/10.1038/srep10988>.
- (4) Guan, Y. S.; Li, H.; Ren, F.; Ren, S. Kirigami-Inspired Conducting Polymer Thermoelectrics from Electrostatic Recognition Driven Assembly. *ACS Nano* **2018**, *12* (8), 7967–7973. <https://doi.org/10.1021/acsnano.8b02489>.
- (5) Guo, H.; Yeh, M. H.; Lai, Y. C.; Zi, Y.; Wu, C.; Wen, Z.; Hu, C.; Wang, Z. L. All-in-One Shape-Adaptive Self-Charging Power Package for Wearable Electronics. *ACS Nano* **2016**, *10* (11), 10580–10588. <https://doi.org/10.1021/acsnano.6b06621>.
- (6) Song, Y.; Kim, D.; Kang, S.; Ko, Y.; Ko, J.; Huh, J.; Ko, Y.; Lee, S. W.; Cho, J. Room-Temperature Metallic Fusion-Induced Layer-by-Layer Assembly for Highly Flexible Electrode Applications. *Adv. Funct. Mater.* **2019**, *29* (30), 1806584. <https://doi.org/10.1002/adfm.201806584>.
- (7) *Handbook of Conducting Polymers, Fourth Edition - 2 Volume Set*, 4th ed.; Reynolds, J. R., Thompson, B. C., Skotheim, T. A., Eds.; CRC Press, 2019. <https://doi.org/10.1201/b22233>.
- (8) Huang, M.; Li, L.; Ai, Z.; Gao, X.; Qian, J.; Xu, H.; Su, X.; Wu, J.; Gao, Y. One-Step Fabrication of Ice-Templated Pure Polypyrrole Nanoparticle Hydrogels for High-Rate Supercapacitors. *ACS Appl. Nano Mater.* **2022**, *5* (8), 11940–11947. <https://doi.org/10.1021/acsanm.2c02957>.
- (9) Cao, G.; Cai, S.; Chen, Y.; Zhou, D.; Zhang, H.; Tian, Y. Facile Synthesis of Highly Conductive and Dispersible PEDOT Particles. *Polymer (Guildf)* **2022**, *252*. <https://doi.org/10.1016/j.polymer.2022.124952>.
- (10) Mohanadas, D.; Sulaiman, Y. Recent Advances in Development of Electroactive Composite Materials for Electrochromic and Supercapacitor Applications. *J. Power Sources* **2022**, *523* (September 2021), 231029. <https://doi.org/10.1016/j.jpowsour.2022.231029>.
- (11) Shen, Z.-M.; Luo, X.-J.; Zhu, Y.-Y.; Liu, Y.-S. Facile Co-Deposition of NiO-CoO-PPy Composite for Asymmetric Supercapacitors. *J. Energy Storage* **2022**, *51* (December 2021), 104475. <https://doi.org/10.1016/j.est.2022.104475>.

- (12) Dhandapani, E.; Thangarasu, S.; Ramesh, S.; Ramesh, K.; Vasudevan, R.; Duraisamy, N. Recent Development and Prospective of Carbonaceous Material, Conducting Polymer and Their Composite Electrode Materials for Supercapacitor — A Review. *J. Energy Storage* **2022**, 52 (PC), 104937. <https://doi.org/10.1016/j.est.2022.104937>.
- (13) Flexibility of Polymer Chains and Its Origin. In *Fundamentals of Polymer Science for Engineers*; Wiley-VCH Verlag GmbH & Co. KGaA: Weinheim, Germany, 2017; pp 43–58. <https://doi.org/10.1002/9783527802180.ch2>.
- (14) Tsvetkov, V. N. Flexibility and Shape of Macromolecules. *Rubber Chemistry and Technology* **1963**, 36 (2), 337–350. <https://doi.org/10.5254/1.3539562>.
- (15) Chen, A. X.; Kleinschmidt, A. T.; Choudhary, K.; Lipomi, D. J. Beyond Stretchability: Strength, Toughness, and Elastic Range in Semiconducting Polymers. *Chemistry of Materials* **2020**, 32 (18), 7582–7601. <https://doi.org/10.1021/acs.chemmater.0c03019>.
- (16) Zhao, R.; Lin, S.; Yuk, H.; Zhao, X. Kirigami Enhances Film Adhesion. *Soft Matter* **2018**, 14 (13), 2515–2525. <https://doi.org/10.1039/C7SM02338C>.
- (17) Tang, Y.; Li, Y.; Hong, Y.; Yang, S.; Yin, J. Programmable Active Kirigami Metasheets with More Freedom of Actuation. *Proceedings of the National Academy of Sciences* **2019**, 116 (52), 26407–26413. <https://doi.org/10.1073/pnas.1906435116>.
- (18) Guan, Y.; Zhang, Z.; Tang, Y.; Yin, J.; Ren, S. Kirigami-Inspired Nanoconfined Polymer Conducting Nanosheets with 2000% Stretchability. *Advanced Materials* **2018**, 30 (20), 1706390. <https://doi.org/10.1002/adma.201706390>.
- (19) Diao, Y.; Woon, R.; Yang, H.; Chow, A.; Wang, H.; Lu, Y.; D’Arcy, J. M. Kirigami Electrodes of Conducting Polymer Nanofibers for Wearable Humidity Dosimeters and Stretchable Supercapacitors. *J. Mater. Chem. A Mater.* **2021**, 9 (15), 9849–9857. <https://doi.org/10.1039/d0ta11335b>.
- (20) Diao, Y.; Chen, H.; Lu, Y.; Santino, L. M.; Wang, H.; D’Arcy, J. M. Converting Rust to PEDOT Nanofibers for Supercapacitors. *ACS Appl. Energy Mater.* **2019**, 2 (5), 3435–3444. <https://doi.org/10.1021/acsaem.9b00244>.
- (21) Diao, Y.; Lu, Y.; Yang, H.; Wang, H.; Chen, H.; D’Arcy, J. M. Direct Conversion of Fe₂O₃ to 3D Nanofibrillar PEDOT Microsupercapacitors. *Adv. Funct. Mater.* **2020**, 30 (32), 2003394. <https://doi.org/10.1002/adfm.202003394>.
- (22) Santino, L. M.; Acharya, S.; D’Arcy, J. M. Low-Temperature Vapour Phase Polymerized Polypyrrole Nanobrushes for Supercapacitors. *J. Mater. Chem. A Mater.* **2017**, 5 (23), 11772–11780. <https://doi.org/10.1039/C7TA00369B>.
- (23) Zhang, S.; Zhang, W.; Zhang, G.; Bai, Y.; Chen, S.; Xu, J.; Yu, Z.; Sun, K. P-Toluenesulfonic Acid Catalytic Polymerization of EDOT without Oxidants. *Mater. Lett.* **2018**, 222, 105–108. <https://doi.org/10.1016/j.matlet.2018.03.135>.

- (24) Zhou, M.; Heinze, J. Electropolymerization of Pyrrole and Electrochemical Study of Polypyrrole. 2. Influence of Acidity on the Formation of Polypyrrole and the Multipathway Mechanism. *Journal of Physical Chemistry B* **1999**, *103* (40), 8443–8450. <https://doi.org/10.1021/jp990161t>.
- (25) Teare, G. C.; Ratcliffe, N. M. Electrorheological Properties of Polypyrrole Prepared by the Action of Mineral Acids on Pyrrole. *J. Mater. Chem.* **1996**, *6* (3), 301. <https://doi.org/10.1039/jm9960600301>.
- (26) Hawkins, S. J.; Ratcliffe, N. M. A Study of the Effects of Acid on the Polymerisation of Pyrrole, on the Oxidative Polymerisation of Pyrrole and on Polypyrrole. *J. Mater. Chem.* **2000**, *10* (9), 2057–2062. <https://doi.org/10.1039/b001912g>.
- (27) Bendrea, A.-D.; Cianga, L.; Ailiesei, G.-L.; Ursu, E.-L.; Göen Colak, D.; Cianga, I. 3,4-Ethylenedioxythiophene (EDOT) End-Group Functionalized Poly- ϵ -Caprolactone (PCL): Self-Assembly in Organic Solvents and Its Coincidentally Observed Peculiar Behavior in Thin Film and Protonated Media. *Polymers (Basel)* **2021**, *13* (16), 2720. <https://doi.org/10.3390/polym13162720>.
- (28) Tomšík, E.; Ivanko, I.; Svoboda, J.; Šeděnková, I.; Zhigunov, A.; Hromádková, J.; Pánek, J.; Lukešová, M.; Velychkivska, N.; Janisová, L. Method of Preparation of Soluble PEDOT: Self-Polymerization of EDOT without Oxidant at Room Temperature. *Macromol. Chem. Phys.* **2020**, *221* (18), 2000219. <https://doi.org/10.1002/macp.202000219>.
- (29) Oxidation and Reduction of the Pyrrole Ring; 1977; pp 209–247. <https://doi.org/10.1016/B978-0-12-389840-1.50010-3>.
- (30) Akiyama, T.; Mori, K. Stronger Brønsted Acids: Recent Progress. *Chem. Rev.* **2015**, *115* (17), 9277–9306. <https://doi.org/10.1021/acs.chemrev.5b00041>.
- (31) Pistillo, B. R.; Menguelti, K.; Desbenoit, N.; Arl, D.; Leturcq, R.; Ishchenko, O. M.; Kunat, M.; Baumann, P. K.; Lenoble, D. One Step Deposition of PEDOT Films by Plasma Radicals Assisted Polymerization via Chemical Vapour Deposition. *J. Mater. Chem. C Mater.* **2016**, *4* (24), 5617–5625. <https://doi.org/10.1039/C6TC00181E>.
- (32) Yang, J.; Zeng, F.; Wang, Z. S.; Chen, C.; Wang, G. Y.; Lin, Y. S.; Pan, F. Modulating Resistive Switching by Diluted Additive of Poly(Vinylpyrrolidone) in Poly(3,4-Ethylenedioxythiophene):Poly(Styrenesulfonate). *J. Appl. Phys.* **2011**, *110* (11), 114518. <https://doi.org/10.1063/1.3666057>.
- (33) Wang, Y.; Zhu, C.; Pfattner, R.; Yan, H.; Jin, L.; Chen, S.; Molina-Lopez, F.; Lissel, F.; Liu, J.; Rabiah, N. I.; Chen, Z.; Chung, J. W.; Linder, C.; Toney, M. F.; Murmann, B.; Bao, Z. A Highly Stretchable, Transparent, and Conductive Polymer. *Sci. Adv.* **2017**, *3* (3). <https://doi.org/10.1126/sciadv.1602076>.

- (34) Šetka, M.; Calavia, R.; Vojkůvka, L.; Llobet, E.; Drbohlavová, J.; Vallejos, S. Raman and XPS Studies of Ammonia Sensitive Polypyrrole Nanorods and Nanoparticles. *Sci. Rep.* **2019**, *9* (1), 8465. <https://doi.org/10.1038/s41598-019-44900-1>.
- (35) Yemata, T. A.; Zheng, Y.; Kyaw, A. K. K.; Wang, X.; Song, J.; Chin, W. S.; Xu, J. Modulation of the Doping Level of PEDOT:PSS Film by Treatment with Hydrazine to Improve the Seebeck Coefficient. *RSC Adv.* **2020**, *10* (3), 1786–1792. <https://doi.org/10.1039/C9RA07648D>.
- (36) Zhao, W.; Wang, Y.; Wang, A. Nonlinear Optical Properties of Novel Polypyrrole Derivatives Bearing Different Aromatic Segments. *Materials Sciences and Applications* **2017**, *08* (11), 774–783. <https://doi.org/10.4236/msa.2017.811056>.
- (37) Huang, P.; Lethien, C.; Pinaud, S.; Brousse, K.; Laloo, R.; Turq, V.; Respaud, M.; Demortière, A.; Daffos, B.; Taberna, P. L.; Chaudret, B.; Gogotsi, Y.; Simon, P. On-Chip and Freestanding Elastic Carbon Films for Micro-Supercapacitors. *Science (1979)* **2016**, *351* (6274), 691–695. <https://doi.org/10.1126/science.aad3345>.
- (38) Wang, H.; Diao, Y.; Rubin, M.; Santino, L. M.; Lu, Y.; D'Arcy, J. M. Metal Oxide-Assisted PEDOT Nanostructures via Hydrolysis-Assisted Vapor-Phase Polymerization for Energy Storage. *ACS Appl. Nano Mater.* **2018**, *1* (3), 1219–1227. <https://doi.org/10.1021/acsanm.7b00382>.
- (39) Jiao, S.; Zhou, A.; Wu, M.; Hu, H. Kirigami Patterning of MXene/Bacterial Cellulose Composite Paper for All-Solid-State Stretchable Micro-Supercapacitor Arrays. *Advanced Science* **2019**, *6* (12), 1900529. <https://doi.org/10.1002/advs.201900529>.
- (40) Root, S. E.; Savagatrup, S.; Printz, A. D.; Rodriguez, D.; Lipomi, D. J. Mechanical Properties of Organic Semiconductors for Stretchable, Highly Flexible, and Mechanically Robust Electronics. *Chem. Rev.* **2017**, *117* (9), 6467–6499. <https://doi.org/10.1021/acs.chemrev.7b00003>.
- (41) Panyukov, S. Theory of Flexible Polymer Networks: Elasticity and Heterogeneities. *Polymers (Basel)* **2020**, *12* (4), 767. <https://doi.org/10.3390/polym12040767>.
- (42) Balani, K.; Verma, V.; Agarwal, A.; Narayan, R. Physical, Thermal, and Mechanical Properties of Polymers. In *Biosurfaces*; John Wiley & Sons, Inc: Hoboken, NJ, USA, 2015; pp 329–344. <https://doi.org/10.1002/9781118950623.app1>.
- (43) Qu, J.; Ouyang, L.; Kuo, C.; Martin, D. C. Stiffness, Strength and Adhesion Characterization of Electrochemically Deposited Conjugated Polymer Films. *Acta Biomater.* **2016**, *31*, 114–121. <https://doi.org/10.1016/j.actbio.2015.11.018>.
- (44) van Manen, T.; Janbaz, S.; Ganjian, M.; Zadpoor, A. A. Kirigami-Enabled Self-Folding Origami. *Materials Today* **2020**, *32*, 59–67. <https://doi.org/10.1016/j.mattod.2019.08.001>.

- (45) Im, S. G.; Yoo, P. J.; Hammond, P. T.; Gleason, K. K. Grafted Conducting Polymer Films for Nano-Patterning onto Various Organic and Inorganic Substrates by Oxidative Chemical Vapor Deposition. *Advanced Materials* **2007**, *19* (19), 2863–2867. <https://doi.org/10.1002/adma.200701170>.
- (46) Tang, Y.; Lin, G.; Han, L.; Qiu, S.; Yang, S.; Yin, J. Design of Hierarchically Cut Hinges for Highly Stretchable and Reconfigurable Metamaterials with Enhanced Strength. *Advanced Materials* **2015**, *27* (44), 7181–7190. <https://doi.org/10.1002/adma.201502559>.
- (47) Wu, C.; Wang, X.; Lin, L.; Guo, H.; Wang, Z. L. Paper-Based Triboelectric Nanogenerators Made of Stretchable Interlocking Kirigami Patterns. *ACS Nano* **2016**, *10* (4), 4652–4659. <https://doi.org/10.1021/acsnano.6b00949>.
- (48) Kim, J.; Park, H.; Jeong, S.-H. A Kirigami Concept for Transparent and Stretchable Nanofiber Networks-Based Conductors and UV Photodetectors. *Journal of Industrial and Engineering Chemistry* **2020**, *82*, 144–152. <https://doi.org/10.1016/j.jiec.2019.10.006>.
- (49) Li, H.; Wang, W.; Yang, Y.; Wang, Y.; Li, P.; Huang, J.; Li, J.; Lu, Y.; Li, Z.; Wang, Z.; Fan, B.; Fang, J.; Song, W. Kirigami-Based Highly Stretchable Thin Film Solar Cells That Are Mechanically Stable for More than 1000 Cycles. *ACS Nano* **2020**, *14* (2), 1560–1568. <https://doi.org/10.1021/acsnano.9b06562>.
- (50) Lee, J.-S. M.; Briggs, M. E.; Hu, C.-C.; Cooper, A. I. Controlling Electric Double-Layer Capacitance and Pseudocapacitance in Heteroatom-Doped Carbons Derived from Hypercrosslinked Microporous Polymers. *Nano Energy* **2018**, *46*, 277–289. <https://doi.org/10.1016/j.nanoen.2018.01.042>.
- (51) Dong, K.; Wang, Y.-C.; Deng, J.; Dai, Y.; Zhang, S. L.; Zou, H.; Gu, B.; Sun, B.; Wang, Z. L. A Highly Stretchable and Washable All-Yarn-Based Self-Charging Knitting Power Textile Composed of Fiber Triboelectric Nanogenerators and Supercapacitors. *ACS Nano* **2017**, *11* (9), 9490–9499. <https://doi.org/10.1021/acsnano.7b05317>.
- (52) Khan, S.; Majid, A.; Raza, R. Synthesis of PEDOT: PPy/AC Composite as an Electrode for Supercapacitor. *Journal of Materials Science: Materials in Electronics* **2020**, *31* (16), 13597–13609. <https://doi.org/10.1007/s10854-020-03916-4>.
- (53) Wang, Y.; Ding, Y.; Guo, X.; Yu, G. Conductive Polymers for Stretchable Supercapacitors. *Nano Res.* **2019**, *12* (9), 1978–1987. <https://doi.org/10.1007/s12274-019-2296-9>.
- (54) Zhu, H.; Li, M.; Wang, D.; Zhou, S.; Peng, C. Interfacial Synthesis of Free-Standing Asymmetrical PPY-PEDOT Copolymer Film with 3D Network Structure for Supercapacitors. *J. Electrochem. Soc.* **2017**, *164* (9), A1820–A1825. <https://doi.org/10.1149/2.1401707jes>.
- (55) Ma, Y.; Wang, Q.; Liang, X.; Zhang, D.; Miao, M. Wearable Supercapacitors Based on Conductive Cotton Yarns. *J. Mater. Sci.* **2018**, *53* (20), 14586–14597. <https://doi.org/10.1007/s10853-018-2655-z>.

- (56) Zhou, H.; Han, G. One-Step Fabrication of Heterogeneous Conducting Polymers-Coated Graphene Oxide/Carbon Nanotubes Composite Films for High-Performance Supercapacitors. *Electrochim. Acta* **2016**, *192*, 448–455. <https://doi.org/10.1016/j.electacta.2016.02.015>.
- (57) Wang, N.; Wang, X.; Zhang, Y.; Hou, W.; Chang, Y.; Song, H.; Zhao, Y.; Han, G. All-in-One Flexible Asymmetric Supercapacitor Based on Composite of Polypyrrole-Graphene Oxide and Poly(3,4-Ethylenedioxythiophene). *J. Alloys Compd.* **2020**, *835*, 155299. <https://doi.org/10.1016/j.jallcom.2020.155299>.
- (58) Sohrabi, C.; Alsafi, Z.; O'Neill, N.; Khan, M.; Kerwan, A.; Al-Jabir, A.; Iosifidis, C.; Agha, R. World Health Organization Declares Global Emergency: A Review of the 2019 Novel Coronavirus (COVID-19). *International Journal of Surgery* **2020**, *76*, 71–76. <https://doi.org/10.1016/j.ijsu.2020.02.034>.
- (59) Leung, N. H. L.; Chu, D. K. W.; Shiu, E. Y. C.; Chan, K. H.; McDevitt, J. J.; Hau, B. J. P.; Yen, H. L.; Li, Y.; Ip, D. K. M.; Peiris, J. S. M.; Seto, W. H.; Leung, G. M.; Milton, D. K.; Cowling, B. J. Respiratory Virus Shedding in Exhaled Breath and Efficacy of Face Masks. *Nat. Med.* **2020**, *26* (5), 676–680. <https://doi.org/10.1038/s41591-020-0843-2>.
- (60) Huang, L.; Xu, S.; Wang, Z.; Xue, K.; Su, J.; Song, Y.; Chen, S.; Zhu, C.; Tang, B. Z.; Ye, R. Self-Reporting and Photothermally Enhanced Rapid Bacterial Killing on a Laser-Induced Graphene Mask. *ACS Nano* **2020**, *14* (9), 12045–12053. <https://doi.org/10.1021/acsnano.0c05330>.
- (61) Françon, H.; Wang, Z.; Marais, A.; Mystek, K.; Piper, A.; Granberg, H.; Malti, A.; Gatenholm, P.; Larsson, P. A.; Wågberg, L. Ambient-Dried, 3D-Printable and Electrically Conducting Cellulose Nanofiber Aerogels by Inclusion of Functional Polymers. *Adv. Funct. Mater.* **2020**, *30* (12), 1909383. <https://doi.org/10.1002/adfm.201909383>.
- (62) Panapoy, M.; Singsang, W.; Ksapabutr, B. Electrically Conductive Poly(3,4-Ethylenedioxythiophene)–Poly(Styrene Sulfonate)/Polyacrylonitrile Fabrics for Humidity Sensors. *Phys. Scr.* **2010**, *T139*, 014056. <https://doi.org/10.1088/0031-8949/2010/T139/014056>.
- (63) Huang, J.; Virji, S.; Weiller, B. H.; Kaner, R. B. Polyaniline Nanofibers: Facile Synthesis and Chemical Sensors. *J. Am. Chem. Soc.* **2003**, *125* (2), 314–315. <https://doi.org/10.1021/ja028371y>.

Chapter 3: Covalently Bonding

Nanostructured Poly(3,4-ethylenedioxythiophene) to Functionalized

Glass

In Chapter 2, I briefly discussed the Friedel-Crafts alkylation between poly(3,4-ethylenedioxythiophene) (PEDOT) and polyethylene terephthalate (PET). This reaction inspired further investigation on covalently bonding PEDOT to other surfaces containing phenyl functional groups. In this chapter, I present my work on covalently bonding nanostructured PEDOT to a glass surface functionalized by phenyl silane. This novel synthetic strategy enables the fabrication of a transparent supercapacitor electrode on glass.

3.1 Introduction

Transparent energy storage devices draw much attention in recent years due to the emergence of smart windows and the rapid development of solar cells and touchscreen electronics.¹⁻⁶ Among all energy storage devices, supercapacitors show much promise due to their fast-charging ability and cycling stability. Supercapacitors also bridge the gap between electrolytic capacitors and batteries in terms of energy and power densities.⁷⁻¹⁴ Various factors are evaluated for a transparent supercapacitor, including transparency, energy and power densities, specific capacitance, and cycle stability.^{4-6,15,16} Among materials for energy storage, poly(3,4-ethylenedioxythiophene) (PEDOT) rises as one of the most promising supercapacitor electrode materials due to high conductivity, stability under ambient conditions, light weight, and ease of synthesis.^{6,17} A major challenge for depositing this conducting polymer on a glass substrate is the

lack of molecular interactions between organic and inorganic moieties resulting in poor adhesion and low cycle stability of the electrode.^{1,17,18} Many studies overcome this challenge by embedding polymers in a framework, utilizing a sacrificial layer, or creating polymer/metal oxide composites.^{3,17–20} However, these studies rely on glass with conductive coatings, such as fluorine-doped tin oxide or indium-doped tin oxide, that are both susceptible to dissolution in acidic environment and potentially costly for large scale implementation.

Here, we present an alternative strategy for depositing conducting polymers on a glass substrate by covalently linking polymer and glass through a self-assembled diphenyldimethoxysilane monolayer. The synthetic strategy is inspired by silanization and Friedel-Crafts alkylation mechanisms (briefly discussed in the previous chapter)^{1,21–23}. This method is superior because it obviates the need for a conductive metal oxide coating, enabling the fabrication of current collector-free supercapacitor electrodes on any glass surface. In previous studies, transparent electrode fabrication often involves a tradeoff between transparency and functionality.^{5,6,24–26} This issue is circumvented by localizing a PEDOT coating to the edge of a glass substrate, enabling the assembly a proof-of-concept tandem supercapacitor. This approach retains electrochemical performance of a PEDOT electrode without compromising transparency of glass.

This chapter is adapted from a previous publication.²⁷

3.2 Materials and Methods

Chlorobenzene (99%), 3,4-ethylenedioxythiophene (97%), hydrochloric acid (37%), hydrogen peroxide (30%), poly(vinyl alcohol) (Mw 89,000–98,000, 99+% hydrolyzed), ethanol (200

proof), and toluene were purchased from Sigma-Aldrich; sulfuric acid (98%) was purchased from Macron. Diphenyldimethoxysilane (98%) was purchased from Gelest. All chemicals were used without further purification. Corning glass slides were purchased from Ted Pella, Inc. (product #265005). Hematite particles (α -Fe₂O₃) produced by NewLook Inc. were purchased at The Home Depot Inc. Platinum foil (0.025 mm thick, 99.9%) was purchased from Alfa Aesar for current leads.

Electrochemical Characterization, Microscopy, and Spectroscopy

Optical microscopy was performed on a Nikon Eclipse LV100ND microscope. Scanning electron microscopy with energy dispersive X-ray analysis was performed with a Thermo Fisher Scientific Quattro S environmental scanning electron microscope. Cyclic voltammetry and electrochemical impedance spectroscopy were performed using a Biologic VMP3 multichannel potentiostat. A platinum mesh counter electrode and an Ag/AgCl reference electrode were used in 3-electrode cyclic voltammetry. For electrochemical impedance spectroscopy, the sinusoidal disturbance was 10 mV with frequencies scanned between 100 kHz and 0.1 Hz. 2-point resistance and 4-point conductivity measurements were made using a Keithley 2450 SourceMeter with 1 mm distance between probes. Dimensions of the film used for conductivity measurements were 1 cm \times 2 cm \times 10 μ m, and sheet resistivity was calculated using equation $\rho = (V/I) * C$ (V is voltage measured, I is current applied, and C is a geometric correction factor).

UV-Vis-NIR spectroscopy was conducted from 300 nm to 1300 nm on a Cary 5000 UV-Vis-NIR spectrophotometer. Raman spectroscopy was performed using a Renishaw inVia™ confocal

Raman microscope under green light excitation at 514 nm. Thermogravimetric analysis was conducted on a Discovery TGA (TA Instruments).

Glass Silanization

Microscope glass slides were cut into 1 cm by 2.5 cm pieces then washed in piranha solution (3:1 mixture of 98% sulfuric acid and 30% hydrogen peroxide) for 30 min and rinsed thrice with deionized water. After drying in air, a slide was immersed in 0.1 M diphenyldimethoxysilane/toluene solution with 0.05 M ethanol for 30 h at room temperature (20 °C). Excess silane was rinsed off with toluene, and the slide was dried and annealed in a 50 °C oven for 2 h.

Hematite Deposition

Hematite particles were sieved using a 1.58 mm pore size steel mesh to remove large agglomerates and bath sonicated in deionized water. A 0.1 g/mL aqueous dispersion was produced under constant stirring (900 rpm) and 1 mL aliquots were utilized for air-brushing. A silanized glass slide was oxygen plasma-treated for 5 min prior to hematite deposition; the slide was positioned vertically with respect to the air brush and 1 cm by 2 cm area was coated. The slide was air-brushed five times with the hematite dispersion at 40 psi and a nozzle distance of 50 cm. Each layer was fully dried in between each deposition.

PEDOT Synthesis and Purification

A PEDOT coating was produced via rust-based vapor-phase polymerization (130 °C / 5 h). A 300 mL Teflon-lined hydrothermal reactor was loaded with a hematite-coated glass slide, a half-

dram vial containing 200 μL of 1.56 M EDOT/chlorobenzene solution, and 10 μL of concentrated hydrochloric acid (injected at the bottom of the Teflon liner). PEDOT/glass composite was purified by immersing in 6 M hydrochloric acid overnight and dried on a 50 $^{\circ}\text{C}$ hotplate.

Preparation of poly(vinyl alcohol)/H₂SO₄ gel electrolyte

A 1 M sulfuric acid gel electrolyte was formulated using 1 g of poly(vinyl alcohol) powder dissolved in 10 mL deionized water under 500 rpm magnetic stirring at 90 $^{\circ}\text{C}$. 0.6 mL of concentrated H₂SO₄ was added dropwise to prevent carbonization of poly(vinyl alcohol). Stirring continued for 1 h until the mixture was homogeneous, translucent, and colorless.

Planar Supercapacitor Fabrication

Polyimide tape was used to mask and pattern a glass slide prior to hematite deposition. The mask was removed after synthesis and two parallel electrodes (0.45 cm x 2 cm) with 1 mm gap were produced and purified in hydrochloric acid. A symmetric supercapacitor was assembled by attaching platinum current leads to each electrode and sealing with polyimide tape; 200 μL of gel electrolyte were injected at the gap of electrodes.

Sandwich-type Supercapacitor Fabrication

A 7.5 cm by 5 cm silanized glass slide was air-brushed on one of its short edges (0.1 cm by 5 cm) with hematite particles. Polymer synthesis (130 $^{\circ}\text{C}$ / 24 h) was carried out in a 500 mL glass jar loaded with a hematite-coated-edge glass slide and two half-dram vials separately containing 100 μL of concentrated hydrochloric acid and 200 μL of 1.56 M EDOT/chlorobenzene solution.

A PEDOT/glass composite was purified and dried, and a small piece ($0.3\text{ cm} \times 0.5\text{ cm}$) of carbon tape was used as current collector. A platinum current lead was attached to the carbon tape and sealed with polyimide tape (edge-coated electrode). A sandwich-type supercapacitor was assembled by fitting two edge-coated electrodes in an FDM-printed frame. The gap between electrodes was approximately 0.2 mm, and 100 μL of gel electrolyte were injected between the edge-coated electrodes.

Fabrication of a Tandem Supercapacitor

A tandem supercapacitor was fabricated using edge-coated electrodes by connecting three sandwich-type supercapacitors in series. The supercapacitors were stacked to mimic a window and charged with 3 V to light up a blue LED.

3.3 Results and Discussion

Glass Silanization

Glass is silanized with molecules of general formula $\text{R}_n\text{SiX}_{4-n}$ (X is a methoxy, ethoxy, or halogen group) where substitution of X with hydroxyl groups leads to covalent bond formation.^{28,29} To produce a high density of hydroxyl groups, glass is pretreated with piranha solution. Depending on the number of X groups, a silane molecule forms either bipodal (two covalent bonds) or monopodal (one covalent bond) “anchoring” on glass. Unreacted X groups crosslink both vertically and horizontally with adjacent silanes, resulting in a disordered multilayered structure. Previous studies report that alkoxysilane avoids crosslinking and forms a highly ordered and well-packed monolayer.^{1,28} To obviate crosslinking, a bipodal-anchoring alkoxysilane (diphenyldimethoxysilane) is utilized here (Figure 3.1a).

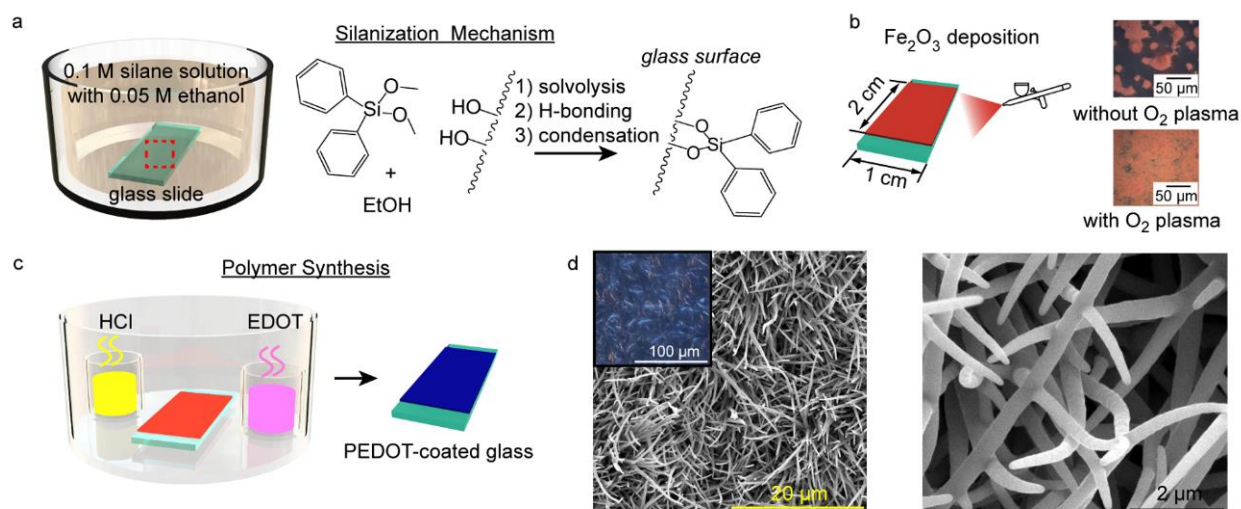


Figure 3.1 Glass silanization and polymer synthesis. a) A microscope glass slide is treated in piranha solution prior to silanization in 1 M diphenyldimethoxysilane/toluene solution with 0.05 M ethanol. Silanization substitutes -OH groups on the glass surface with methoxy groups and deposits a monolayer of diphenyldimethoxysilane. b) Hematite ($\alpha\text{-Fe}_2\text{O}_3$) particles are airbrushed from an aqueous dispersion on a silanized glass slide. The slide is oxygen plasma-treated prior to airbrushing for homogeneous deposition. c) Vapor-phase polymer synthesis is carried out in a hydrothermal reactor loaded with a hematite-coated slide and reservoirs containing concentrated hydrochloric acid and EDOT/chlorobenzene solutions, respectively. d) Scanning electron micrographs demonstrate that a PEDOT coating is comprised of nanofibers; optical micrograph is shown on the inset. The diameter and length of nanofibers ranges between 0.5 to 0.8 μm and between 15 to 18 μm , respectively.

Hematite Deposition and Rust-based Vapor-phase Polymerization (RVPP)

Hematite ($\alpha\text{-Fe}_2\text{O}_3$) nanoparticles possesses trivalent ferric ions necessary for initiating polymerization and is deposited as a thin film on a silanized glass by air brushing from an aqueous medium. The surface of silanized glass lacks hydrophilicity, resulting in islands of agglomerates (Figure 3.1b). Oxygen plasma treatment prior to air brushing restores hydrophilicity and ensures a homogenous coating (Figure 3.1b).

Nanofibrillar PEDOT synthesis follows rust-based vapor-phase polymerization (RVPP) mechanism reported in a previous work (Figure 3.1c).³⁰ Synthesis starts with diffusion of hydrochloric acid (HCl) vapor that initiates hematite particle dissolution. Hematite dissolution

occurs by detachment of Fe^{3+} from bulk oxide and is catalyzed by the formation of dative bond between chloride (Cl^-) and ferric (Fe^{3+}) ions (Figure 3.2a).^{31–33} Hygroscopic ferric ions absorb water and forms an aqueous oxidant layer. EDOT monomer is oxidized by dissolved Fe^{3+} in the aqueous layer and creates a cationic radical that undergoes oxidative radical polymerization (ORP). Polymerization propagates by coupling of two radicals and deprotonation of an intermediate di-cation. Water molecules or chloride ions scavenge the released protons and stabilize the dimer. The oxidation and propagation steps release Fe^{2+} and HCl as side products that accelerate hematite dissolution, creating an autocatalytic cycle of dissolution, oxidation, coupling, and deprotonation (Figure 3.2b).^{34–38} Excess ferric ions oxidatively dope PEDOT into conductive polaronic and bipolaronic forms (Figure 3.2c).^{36,39}

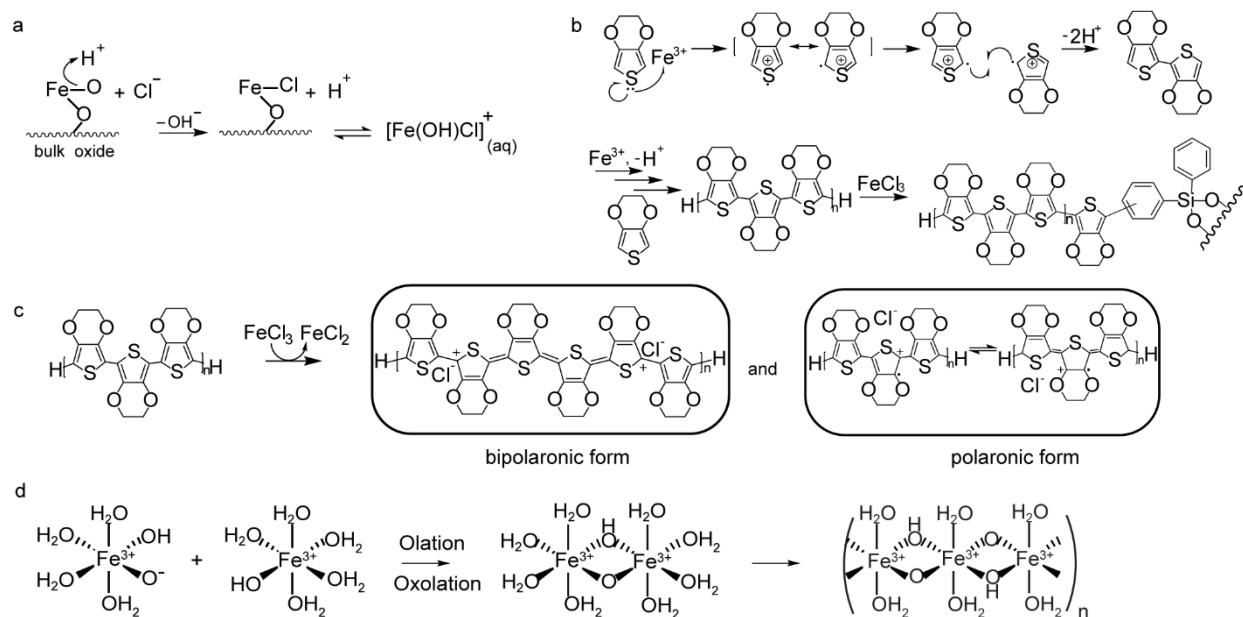


Figure 3.2 Mechanisms in rust-based vapor-phase polymerization. a) Dissolution of hematite in hydrochloric acid forms complexes with ferric and chloride ions on the surface of bulk oxide, facilitating its detachment. b) Oxidative radical polymerization of EDOT molecule is initiated by Fe^{3+} , resulting in a resonantly stabilized cationic radical. The reaction propagates via a cycle of oxidation, coupling of radical cations, and deprotonation to form PEDOT. A polymer chain covalently bonds to a phenyl group on a silanized glass via Friedel Crafts alkylation (detail in Figure 3.7). c) Oxidative doping of PEDOT using FeCl_3 generates bipolaronic and polaronic forms of the polymer while

chloride ions are incorporated as charge carriers. Polaronic PEDOT exists in resonance forms between benzoid and quinoid structures. d) Forced hydrolysis of ferric ion forms an octahedral complex with hydroxyl and aqua groups in an aqueous medium. In forced hydrolysis, a Fe(III) complex forms oxo- and hydroxo-bonds with other complexes via ololation and oxolation reactions, generating iron oxyhydroxide.

Elevated temperature during polymer synthesis leads to forced hydrolysis of ferric ions that directs the formation of PEDOT nanofibers. Iron hydrolysis reaction produces various crystal structures and sizes depending on concentration, temperature, pH, solvent, and spectator ions.^{40–}

⁴⁵ Hydrolysis begins with ferric ions forming complexes consisting aqua and hydroxo groups via dative bonding; ololation and oxolation reactions link octahedral Fe^{3+} complexes via hydroxo- and oxo-bonds (Figure 3.2d).^{42,46–48} Spectator ion concentration influences the structure of unit cell formed during hydrolysis, and a high chloride ion concentration (from HCl) facilitates the formation of monoclinic akageneite ($\beta\text{-FeOOH}$).^{40,43,49} Columbic interaction and Lewis acid/base interaction drive oriented attachment during $\beta\text{-FeOOH}$ crystallization.⁵⁰ Oversaturation results in splitting growth of spindle-like $\beta\text{-FeOOH}$ crystals that elongate and merge into one-dimensional templates for directing PEDOT nanofiber formation (Figure 3.1d and Figure 3.3).^{51–53} Akageneite crystallization and EDOT polymerization occur simultaneously, resulting in development of a core/shell structure. Optical micrographs of quenched syntheses show formation of smooth PEDOT coatings after 0.5 h of reaction and development of fibrillar morphology after 1.5 h (Figure 3.4). Reaction time for nanofiber growth is thrice the formation of smooth PEDOT because deprotonation during EDOT polymerization generates an acidic pH and stifles the kinetics of hydrolysis.

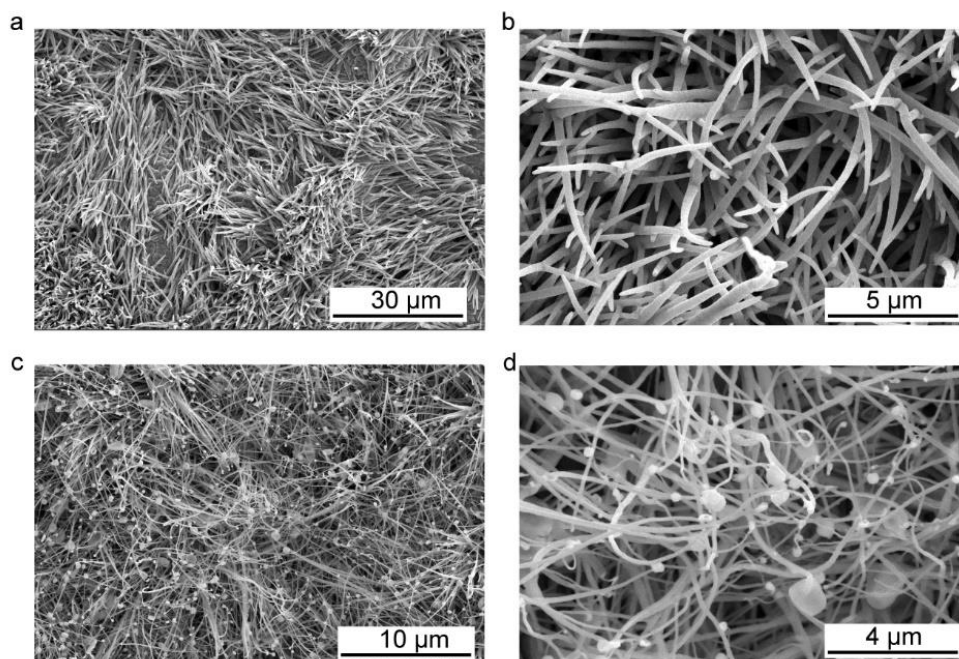


Figure 3.3 Scanning electron micrographs of washed (a and b) and unwashed (c and d) PEDOT nanofibers.

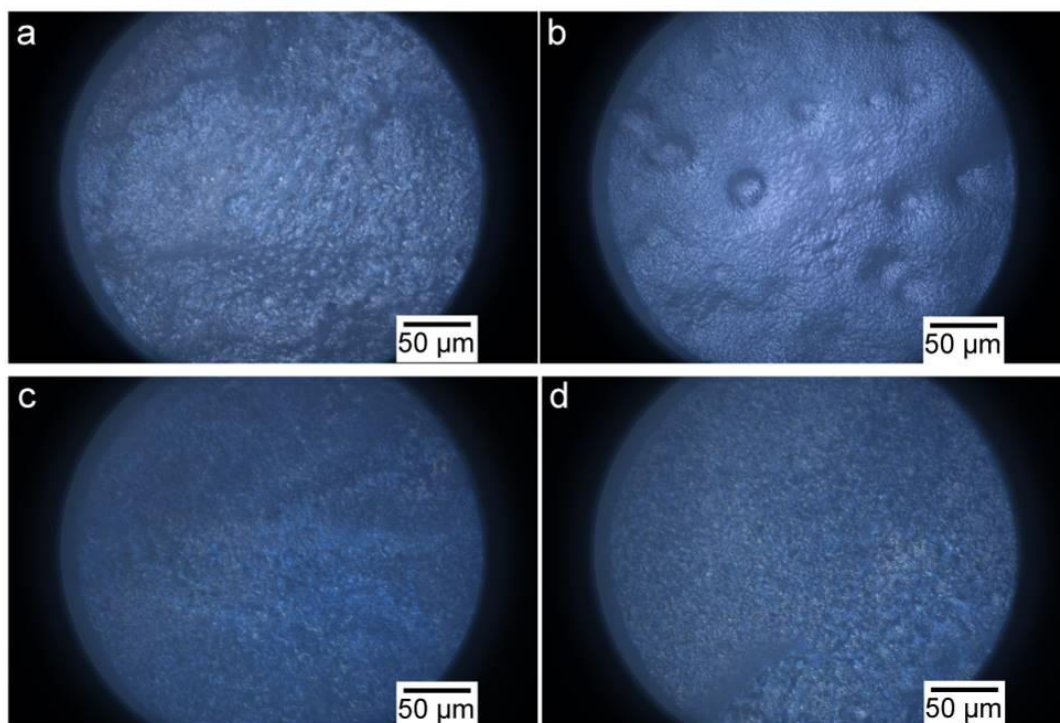


Figure 3.4 Rust-based vapor-phase polymerization of PEDOT on silanized glass is quenched at various times. Quenching times are a) 30 min. b) 60 min. c) 90 min. and d) 120 min., respectively.

Effects of post-synthetic doping and oxidative doping during polymerization are compared via electronic conductivity measurements, UV-Visible spectroscopy, and Raman spectroscopy on as-synthesized (partially doped), HCl-doped and hydrazine-dedoped samples. Current vs. voltage curves (Figure 3.5a) are generated via a linear voltage sweep from -2 V to 2 V. The sheet resistance of a doped PEDOT film is $2.1 \Omega/\square$, and the conductivity is calculated to be 473.8 S/cm ($\sim 10 \mu\text{m}$ thickness). Conductivity drops substantially (almost 0 slope) in a dedoped sample, and the partially doped sample shows a non-linear curve (capacitive) as voltage passes beyond 1 V or -1 V. An electrically conductive material requires both mobile charge carriers and a conductive pathway.⁵⁴ Doped PEDOT possesses delocalized π -electrons on its backbone (pathway) and chloride counter anions (charge carrier). Hydrazine treatment reduces (dedopes) the polymer, localizing π -electrons into double bonds and stripping chloride dopants from PEDOT.^{55,56} UV-vis-NIR spectroscopy is utilized to assess charge carrier density and to characterize changes in molecular structure caused by doping. A UV-vis-NIR spectrum of PEDOT (Figure 3.5b) is divided into neutral (550 nm), polaronic (780 nm) and bipolaronic (1020 nm) regions.⁵⁷ Spectrum of dedoped PEDOT possesses high intensity in neutral region and low intensities in polaronic and bipolaronic regions. In comparison, partially doped and HCl-doped samples show an intensity drop in neutral region and enhanced signals in polaronic and bipolaronic regions, suggesting large concentration of conjugated double bonds with delocalized π -electrons present. The spectra also show slightly higher concentration of bipolaronic PEDOT in the HCl-doped sample (compared to partially-doped). Bipolaronic PEDOT is reported to have higher conductivity than polaronic PEDOT, resulting in higher conductivity in the HCl-doped sample.⁵⁸

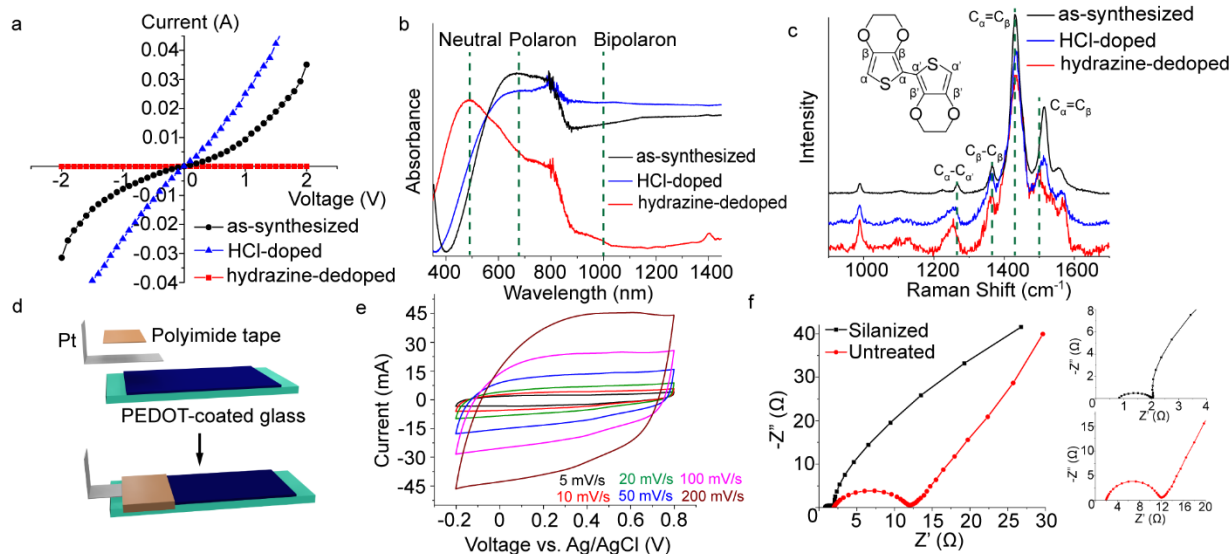


Figure 3.5 Characterization of a PEDOT-coated silanized glass electrode. a) Current-voltage curves, b) UV-Visible spectra, and c) Raman spectra of as-synthesized (black), HCl-doped (blue), and hydrazine-dedoped (red) samples. d) A PEDOT-coated glass is utilized as a working electrode in a 3-electrode electrochemical cell with platinum strip as current lead and polyimide tape seal to minimize contact resistance. e) Cyclic voltammogram in 1 M sulfuric acid at various scan rates of a PEDOT-coated electrode. A platinum mesh counter electrode and a Ag/AgCl reference electrode are used to complete the 3-electrode cell. The cyclic voltammograms are quasi-rectangular at low scan rates (5 to 50 mV/s) and gradually shift to fusiform at high scan rates (100 and 200 mV/s). f) Electrochemical impedance spectroscopy results are shown in Nyquist plots. A PEDOT-coated silanized glass electrode (black) possesses lower internal resistance and charge transfer resistance than a PEDOT-coated untreated glass electrode (red).

Raman spectroscopy aids in investigating changes in bonding during doping process (Figure 3.5c). Peaks at 1260 and 1365 cm^{-1} correspond to $\text{C}_\alpha\text{-C}_{\alpha'}$ and $\text{C}_\beta\text{-C}_\beta$ bonds, respectively. $\text{C}_\alpha=\text{C}_\beta$ double bond corresponds to peaks at 1440 and 1500 cm^{-1} , while peaks near 990 cm^{-1} represent oxyethylene ring in each repeating unit of PEDOT.^{55,59-61} Comparing partially doped and doped to the dedoped spectra demonstrates rising oxidation levels lead to red shifting of $\text{C}_\alpha=\text{C}_\beta$ peak near 1420 cm^{-1} and enhanced intensity of $\text{C}_\alpha=\text{C}_\beta$ peak near 1500 cm^{-1} .^{59,60,62} In comparison, spectrum of a partially doped PEDOT on glass without silanization shows less significant red shift of the 1500 cm^{-1} $\text{C}_\alpha=\text{C}_\beta$ peak (Figure 3.6a). Doping process (oxidation) delocalizes π -electrons from the polymer, and the structure of PEDOT becomes more planar as it shifts from

benzoid to quinoid form. The latter structure possesses a higher concentration of double bonds, creating a more linear conformation. This conformation generates strong interactions between PEDOT chains and enhances conductivity.⁵⁹

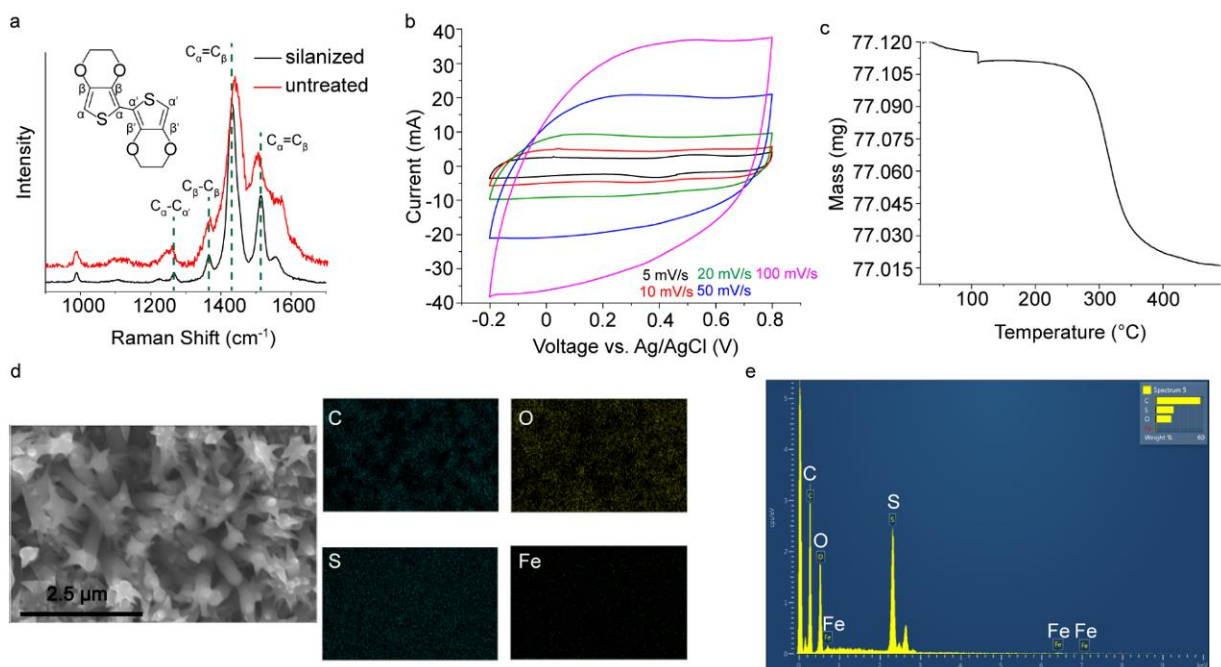


Figure 3.6 Additional characterization of PEDOT on silanized glass and untreated glass. a) Raman spectra of PEDOT on silanized glass and untreated glass. b) 3-electrode cyclic voltammograms of PEDOT on untreated glass. c) Thermalgravimetric analysis from 25 to 490 °C of PEDOT coating on 0.25 cm² of silanized glass. d) Elemental mapping via EDX of washed PEDOT nanofibers. e) Spectrum of washed PEDOT nanofibers obtained from EDX.

Friedel-Crafts Alkylation of PEDOT

Polymerization on a silanized surface enables chemical anchoring and enhances electrochemical performance of a PEDOT coating. Friedel-Crafts alkylation attaches PEDOT to aromatic functional groups and is documented in many previous studies.^{22,23,63} Ferric chloride forms a [FeCl₄]⁻ intermediate in the presence of excess chloride ions and catalyzes the reaction between the conjugated backbone of PEDOT and phenyl functional groups of a silane molecule (Figure

3.7). Covalent bonds are generated between PEDOT and a glass substrate, resulting in a mechanically robust coating that withstand delamination of scotch tape test. In comparison, PEDOT coating on untreated glass peels off easily as a thin film. The mechanism in Figure 3.7 shows alkylation is catalyzed by ferric chloride (Lewis acid), resulting in competing mechanisms between polymerization, forced hydrolysis, and alkylation for Fe^{3+} . Extending reaction time from 3 h to 5 h enhances adhesion between PEDOT and glass as a function of time. (Figure 3.8).

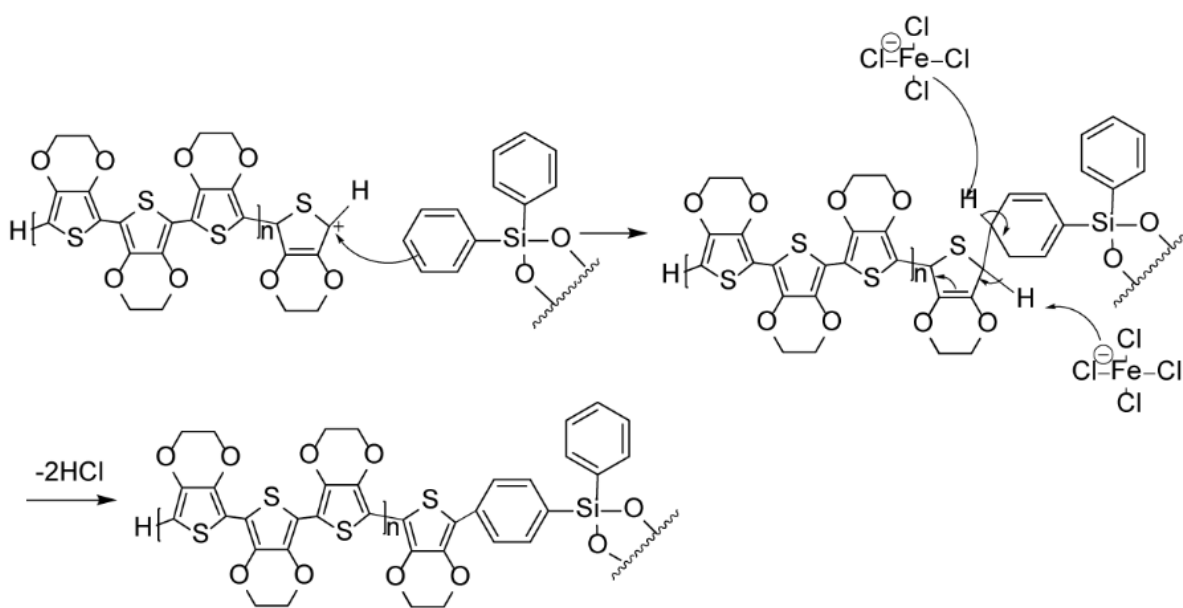


Figure 3.7 Proposed mechanism of a PEDOT chain covalently bonding to the phenyl group of a silanized glass surface via Friedel-Crafts alkylation.

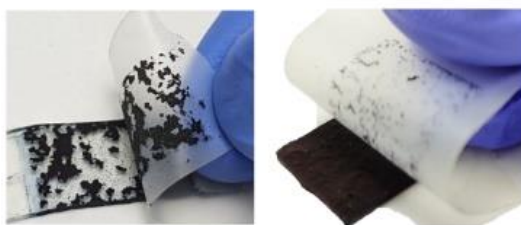


Figure 3.8 Scotch tape test of PEDOT coating on silanized glass after 3 h of synthesis (left) and 5 h of synthesis (right).

A PEDOT-coated silanized glass is purified in hydrochloric acid and characterized with 3-electrode cyclic voltammetry and electrochemical impedance spectroscopy. Elemental mapping from energy dispersive X-ray analysis (EDX) demonstrate purification removes excess iron chloride (Figure 3.6d and e). The working electrode for electrochemical characterization is fabricated by attaching a platinum current lead to PEDOT coating and sealing with polyimide tape to ensure good electrical contact (Figure 3.5d). PEDOT coating is highly conductive, enabling the fabrication of a current collector-free working electrode. The electrode is cycled at different scan rates in 1 M sulfuric acid with an Ag/AgCl reference electrode and a platinum mesh counter electrode (Figure 3.5e). Current vs. voltage curve remains quasi-rectangular at low scan rates and gradually shifts to fusiform as scan rate increases beyond 100 mV/s. Gravimetric capacitance of an electrode is ~200 F/g based on thermogravimetric analysis (TGA) result (Figure 3.6c, plotted from 25 to 490 °C). The difference between the first (starting at 100 °C) and second (starting at 450 °C) plateaus represents the mass of a PEDOT-coating. The polymer coating on silanized glass is mechanically robust and remains attached to the substrate. Cyclic voltammograms of a PEDOT on untreated glass electrode shifts to fusiform at a much lower scan rate (50 mV/s, Figure 3.6b). Additionally, polymer coating on untreated glass suffers from poor adhesion and delaminates from substrate during cycling.

In a cyclic voltammetry experiment, sulfate ions diffuse in and out of PEDOT during oxidation and reduction sweeps, respectively. The rate of sulfate ion diffusion is driven by scan rate and limited by electronic conductivity and surface structure of a working electrode. At a low scan rate, sulfate ions have ample time to diffuse, resulting in a quasi-rectangular curve. As scan rate increases, diffusion is stifled due to the ionic radii of sulfate ions, leading to a shift from quasi-

rectangular to fusiform. The electronic conductivity of PEDOT on silanized and untreated glass is investigated by electrochemical impedance spectroscopy (EIS). Impedance spectroscopy perturbs an electrochemical system using alternating current and measures the effective resistance of that system. Each EIS spectrum of a PEDOT electrode, shown as Nyquist plot (Figure 3.5f), consists of a semicircle and a straight line at an angle (typically 45°). The x-intercept represents equivalent series resistance and diameter of semicircle represents charge transfer resistance. The impedance spectrum of PEDOT on silanized glass possesses both smaller x-intercept and semicircle diameter than PEDOT on untreated glass, corresponding to the results obtained from 4-point conductivity measurements. Diffusional Warburg impedance affects the arc at which the semicircle transitions into the straight line.^{64,65} Nyquist plots of both electrodes transition into a 45° line at identical arcs, suggesting both samples possess similar Warburg impedance. The slope of the line in a Nyquist plot is influenced by both electric double layer (EDL) formation near the electrode and ion diffusion in the electrolyte. Small slope indicates ion diffusion limited charge transfer, whereas steep slope indicates EDL formation-controlled charge transfer process.⁶⁵ PEDOT on silanized glass electrode exhibits superior conductivity and more facile charge transfer, resulting in a smaller x-intercept and semicircle radius than an untreated glass electrode. The interaction between PEDOT and glass surface dictates the structure of polymer chains and influences the measured electronic conductivity. Each phenyl group on a tightly packed diphenyldimethoxysilane monolayer functions as a chemical “anchor” for PEDOT deposition. Covalent bonding between PEDOT and phenyl group results in mechanically robust coating possessing enhanced adhesion. At the molecular level, high density of phenyl groups increases packing density of PEDOT chains, enhances interactions between molecules. The

conducting polymer structure consists of crystalline and amorphous domains, and charge transport is achieved in the crystalline domain due to the ordered overlapping and constructive interference of p orbitals. Charge transport is more efficient within the plane of a polymer backbone and less efficient via interchain hopping.⁶⁶ We propose that the PEDOT chains covalently bonded to phenyl groups are close-packed with overlapping of polymer backbones, resulting in improved efficiency of interchain hopping and enhanced electrical. Additionally, the close proximity between PEDOT chains forces the polymer to adopt the more conductive linear (quinoid) configuration. Raman spectrum demonstrates PEDOT chains on untreated glass are more likely to adopt a coiled (benzoid, Figure 3.9) configuration due to the lack of phenyl groups. Linear molecular configuration and enhanced interaction between polymer chains of PEDOT coating on silanized glass results in higher conductivity.⁵⁹

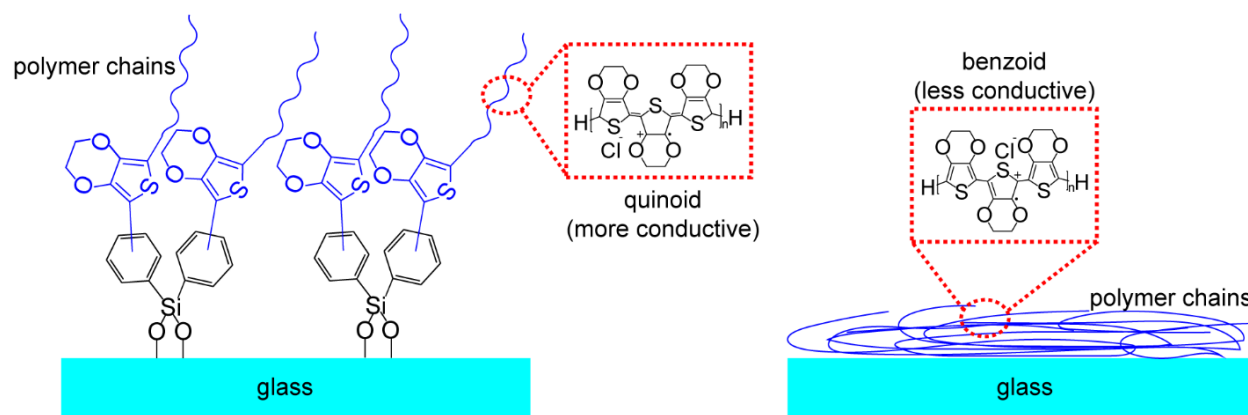


Figure 3.9 Proposed structures of PEDOT polymer chains on silanized glass (left) and untreated glass (right).

Planar PEDOT Supercapacitor

Electrochemical capacitors (or supercapacitors) are a type of energy storage device that stores charges via surface adsorption and redox reactions of the electrodes. Supercapacitors are categorized into planar and sandwich-type, depending on the geometry of the device. To

fabricate a planar PEDOT supercapacitor, silanized glass slide is masked with polyimide tape prior to polymer synthesis and removing the mask results in a symmetric planar supercapacitor with 1 mm gap (Figure 3.10a). A 1 M sulfuric acid in 0.1 g/L poly(vinyl alcohol) gel electrolyte is used instead of aqueous electrolyte to minimize the influence of electrolyte evaporation.

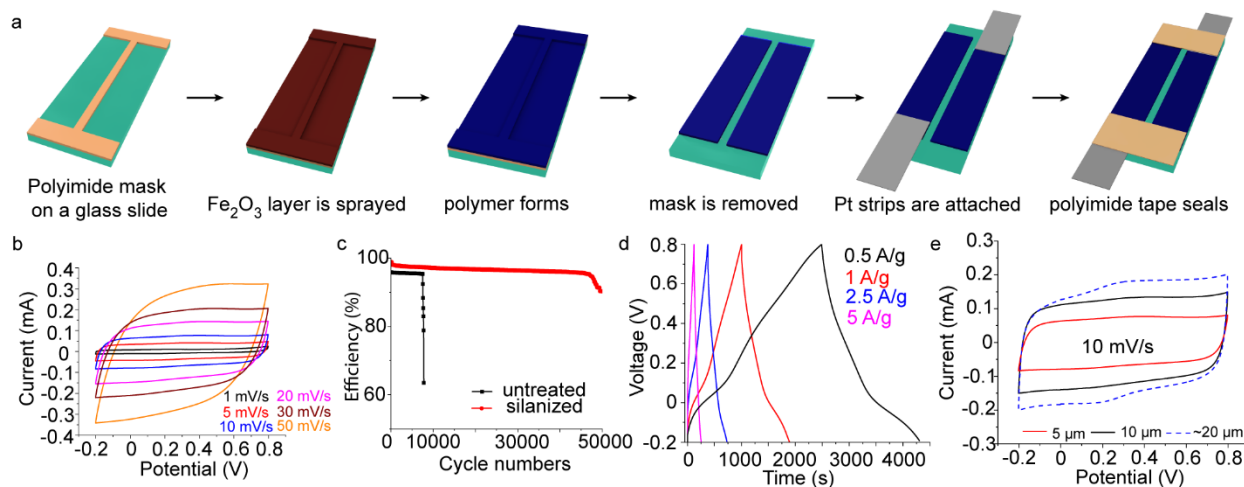


Figure 3.10 Fabrication and performance of a planar supercapacitor. a) Schematic diagram of device. The mask is removed after synthesis, creating a 1 mm gap between electrodes. 200 μL of sulfuric acid in poly(vinyl alcohol) gel are used as electrolyte. b) Cyclic voltammogram of a planar supercapacitor at various scan rates. The shape remains quasi-rectangular up to 50 mV/s. c) Supercapacitor fabricated from PEDOT on silanized glass possesses superior cycle stability (50000 cycles) to PEDOT on untreated glass (less than 10,000 cycles). d) Coulombic charge/discharge curves of a device at various current densities. e) Thickness of a nanofibrillar PEDOT coating is controlled by varying the thickness of the precursor layer of hematite. Increasing PEDOT coating thickness enhances the capacitance of a planar device; however, polymer delaminates during cycling when coating thickness is greater than 10 μm (blue dashed).

The charge storage mechanisms occur predominately at the interface between electrolyte and the surface of an electrode.^{67,68} In a cyclic voltammetry experiment, a layer of solvated anions in the electrolyte move adjacent to the surface of working electrode, creating a narrow area with positive charges on the polymer called the Helmholtz double layer (EDLC).⁶⁸ Some sulfate ions are specifically adsorbed to positively charged sites on the polymer backbone (inner Helmholtz plane), resulting in pseudocapacitive behavior of a PEDOT electrode.⁶⁹ The performance of a

supercapacitor remains stable as long as the interface between its two electrodes remain untouched.^{67–69} Cyclic voltammetry is conducted on planar devices with different coating area. A standard sample consists of two identical parallel electrodes ($4.5 \text{ mm} \times 20 \text{ mm}$) separated by a gap distance of 1 mm (100% coating area). Gel electrolyte is injected and covers the entire polymer coating; a portion of PEDOT coating is partially removed from each electrode after 10 cycles at 10 mV/s (Figure 3.11). A device is cycled again at the same scan rate, and removal procedure is repeated, creating cyclic voltammograms of 75%, 50%, 25%, and 10% coating areas, respectively (Figure 3.11). Cyclic voltammograms remain quasirectangular from 100% to 25% coating area and slightly shifts to fusiform when only 10% coating remains on each electrode.

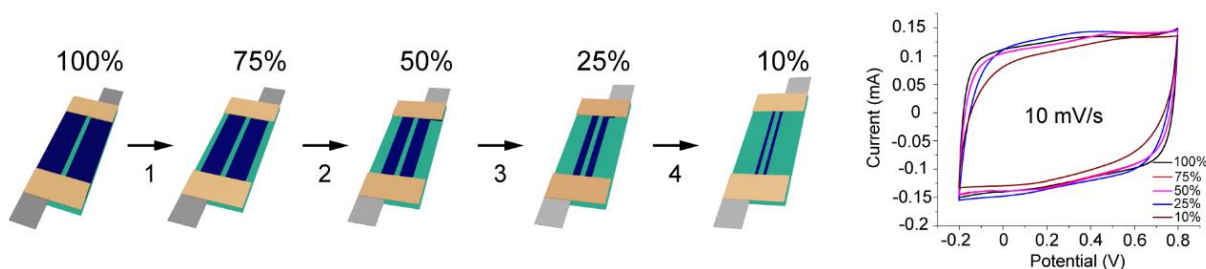


Figure 3.11 PEDOT coating is removed sequentially from a planar supercapacitor. After each removal, the device is characterized via cyclic voltammetry for 10 cycles. The capacitance of a planar supercapacitor remains stable as long as the interface between electrode and electrolyte is unaltered.

A planar PEDOT supercapacitor is cycled at various scan rates, and its cyclic voltammograms remain quasi-rectangular from 1 to 50 mV/s (Figure 3.10b). A planar supercapacitor possesses a gravimetric capacitance of 130.7 F/g and an outstanding cycle stability, retaining 86% of its capacitance after 50000 cycles at 2.5 A/g (Figure 3.10c and Figure 3.12). This cycle limit the PEDOT electrode is determined based on charge/discharge efficiency ($\geq 85\%$). Galvanostatic charge/discharge experiments shows minimal IR drop at various current densities in a 1 V

voltage window (Figure 3.10c). Cross-sectional electron microscopy is used to investigate the structure of PEDOT films on a glass slide and shows a polymer coating is comprised of a bilayer structure with nanofibrillar polymer on top of a smooth film (Figure 3.13). The thickness of PEDOT coating is controlled by the amount of hematite deposited from air-brushing. Optical micrographs in Figure 3.13 represent silanized glass slides with 0.19 and 0.38 milligrams of deposited hematite. A glass with 0.19 milligrams of air-brushed hematite results in average polymer coating thickness of $\sim 5\ \mu\text{m}$. Increasing the amount of air-brushed hematite to 0.38 or 0.76 milligrams results in average polymer thickness of 10 and 20 (approximated) μm , respectively. Gravimetric capacitance of a planar supercapacitor is proportional to the thickness of fibrillar section of a polymer coating (Figure 3.10d). A PEDOT electrode with higher average thickness also possesses a thicker fibrillar section, enhancing its interaction with charge carriers in the electrolyte and increasing its gravimetric capacitance. The 10 μm thick sample produces a planar supercapacitor with the best overall performance, combining high capacitance and no delamination during testing.

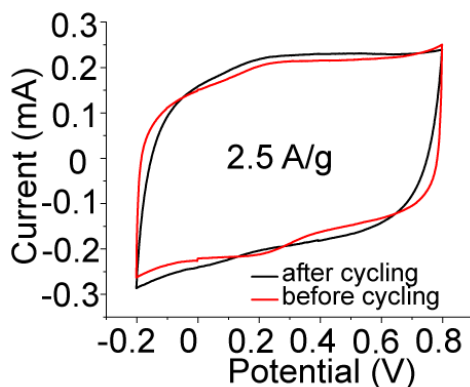


Figure 3.12 A planar supercapacitor is repeatedly charged/discharged at 2.5 A/g and retains its capacitance after 50000 cycles.

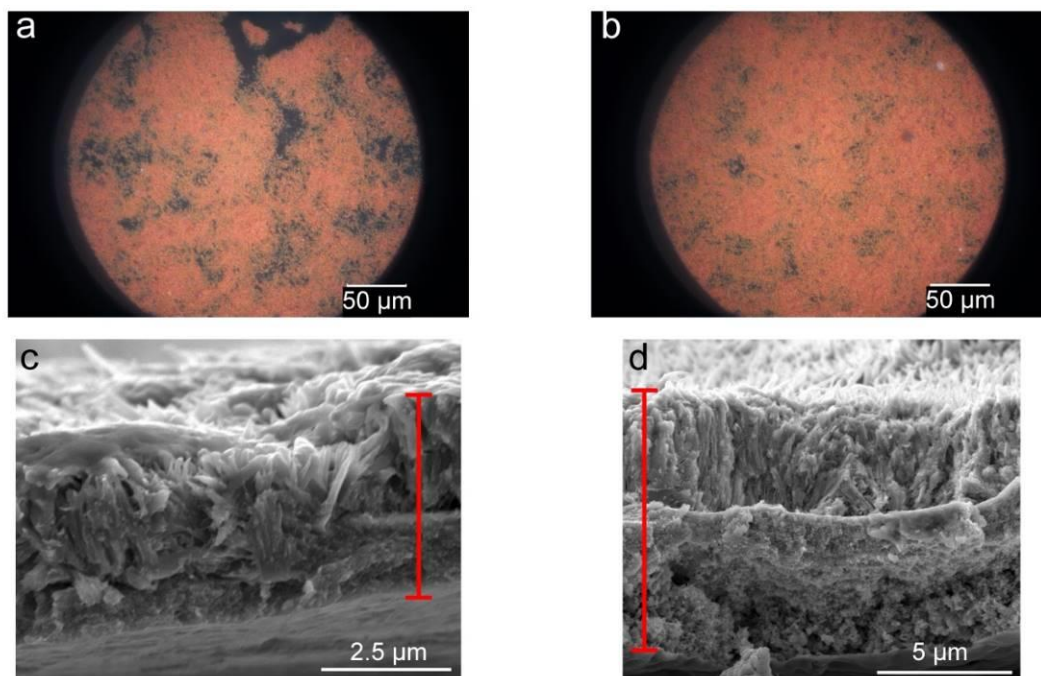


Figure 3.13 Optical micrographs of silanized glass after a) 0.19 mg and b) 0.38 mg of hematite deposition. Cross-sectional electron micrographs in c) and d) demonstrate PEDOT coating thickness increases as the mass of deposited hematite particles increases.

Transparent Sandwich-type PEDOT Supercapacitor

A sandwich-type device consists of two edge-coated electrodes, platinum leads, and gel electrolyte. The edge of a glass slide (0.1 cm by 5 cm) is coated by PEDOT (0.5 cm²). Electrodes are separated by gel electrolyte and held together by a 3D-printed frame that maintains the electrode/electrolyte interface (estimated gap of 0.5 mm, Figure 3.14a). A sandwich-type device possesses similar electrochemical performance as a planar device, resulting in quasi-rectangular cyclic voltammogram at various scan rates (Figure 3.14b). Silanization treatment enables deposition of diphenyldimethoxysilane on all six surfaces of a glass slide. PEDOT coating is localized on the edge (narrow surface) and presents minimal influence on the transparency of glass (Figure 3.14c, broad surface of a glass slide remains transparent). Edge-coated electrodes

completely circumvent the tradeoff between functionality and transparency often seen in previous transparent supercapacitors.

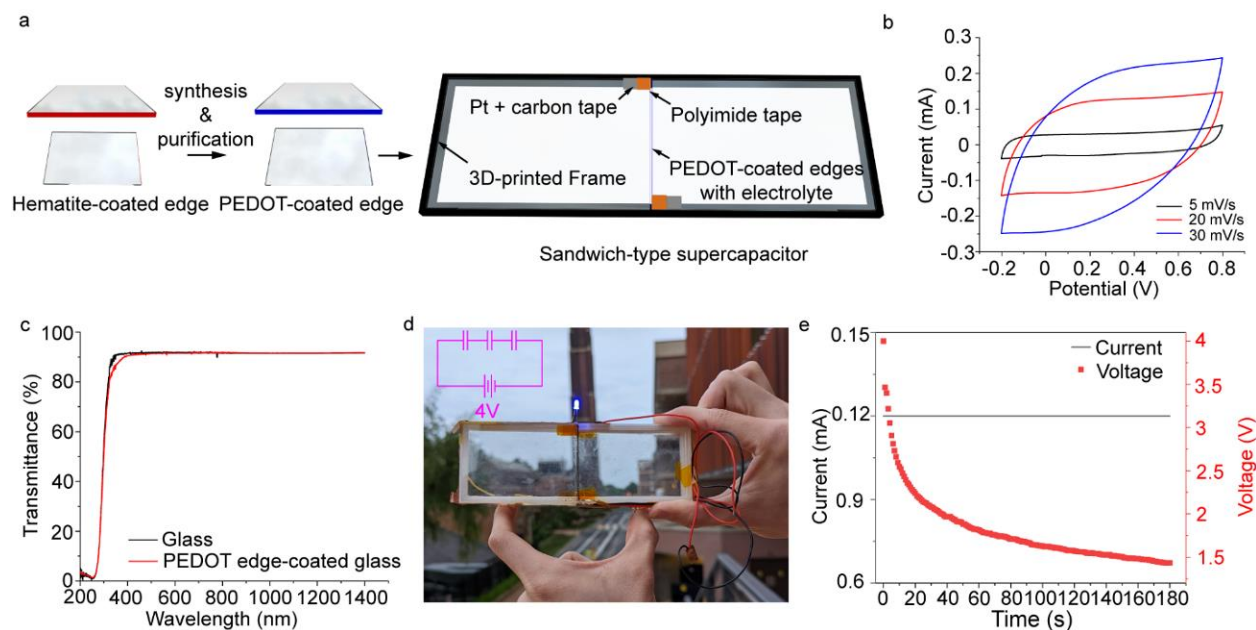


Figure 3.14 Characterization of an edge-coated electrode and fabrication of a transparent supercapacitor. a) A sandwich-type supercapacitor is fabricated by assembling two PEDOT edge-coated electrodes in a 3D-printed frame. The gap between two electrodes is ~ 0.5 mm and filled with gel electrolyte. b) Cyclic voltammograms of a sandwich-type device at various scan rates. c) A PEDOT coating is localized to the edge of a glass slide unhampering transparency. d) A tandem supercapacitor consists of three sandwich-type devices connected in series, and it lights up a blue LED (forward voltage 3.0 V) for ~ 10 s after charging for 1 min. Inset shows the circuit diagram of a charging tandem supercapacitor. e) A tandem supercapacitor outputs a constant current during discharge.

A tandem supercapacitor is fabricated by stacking three sandwich devices and connecting them in series (assembly procedure of sandwich-type supercapacitor is in Figure 3.15). The tandem device possesses excellent transparency and lights up a blue LED with a 3.0 V forward voltage for 10 s after 1 min of charging (Figure 3.14c and d). A device is fully charged to 4 V in 2.5 min and lights up the blue LED for ~ 3 min (fully lit to dim) while maintaining a stable 0.12 mA current until its voltage output drops below 1.5 V (Figure 3.14e).

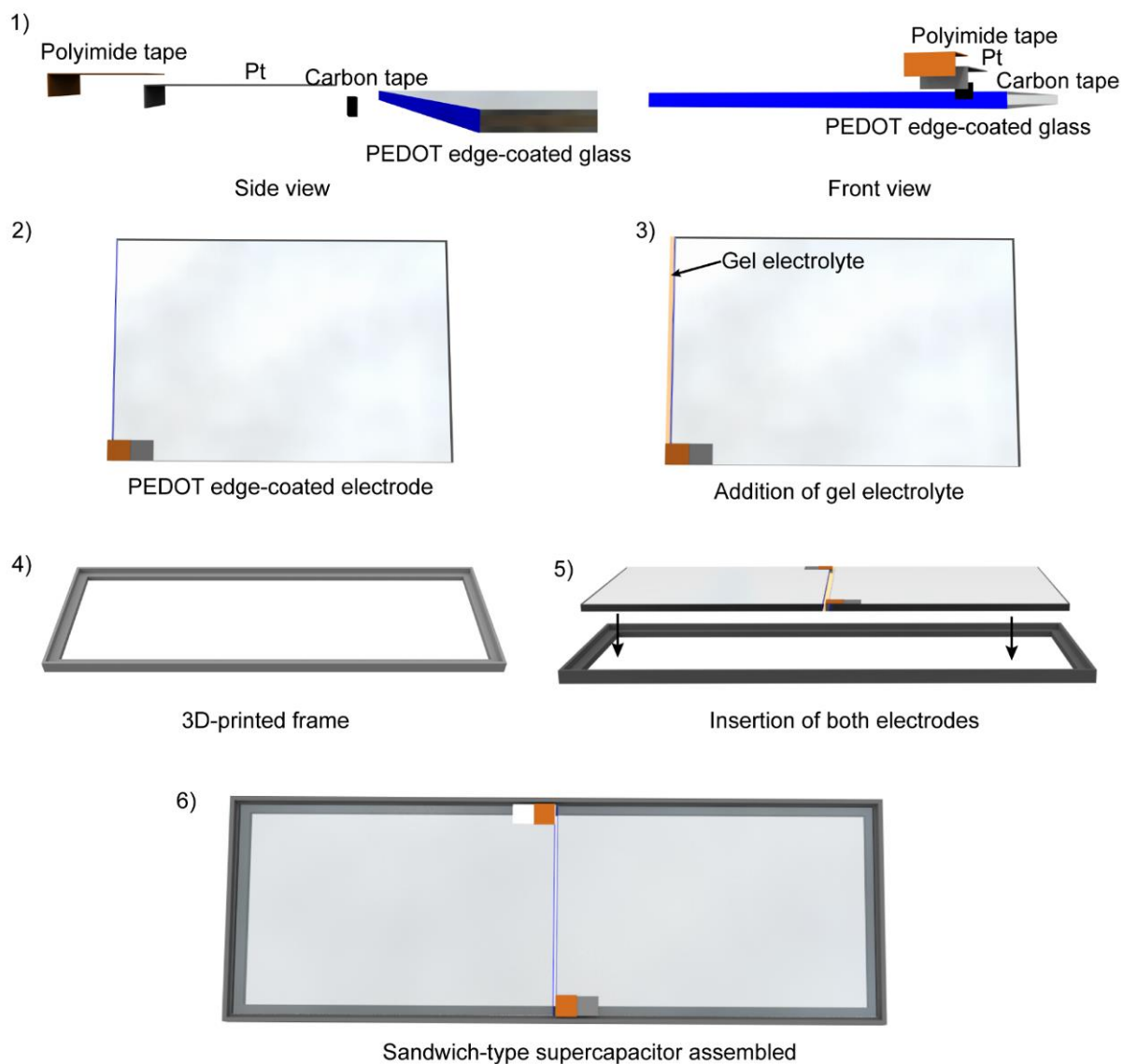


Figure 3.15 Assembly procedure of a sandwich-type supercapacitor.

3.4 Conclusions

The development of conducting polymer-based transparent energy storage devices requires strong adhesion between organic polymer and inorganic glass substrate. This chapter presents a chemical solution to this problem by vapor-phase synthesis of a PEDOT coating and covalently bonding it to a silanized glass through Friedel Crafts alkylation. Phenyl functional groups on the

silane monolayer influences the molecular configuration of polymer chains, enhancing the performance of a PEDOT-coated silanized glass electrode. The strong adhesion between polymer coating and glass also results in high cycle stability of a planar PEDOT supercapacitor. Transparent electrode fabrication often involves a tradeoff between functionality and transparency. This challenge is resolved by localizing the polymer to the edge of a substrate, creating a proof-of-concept transparent tandem supercapacitor that charges to 4 V and outputs a stable current to light up an LED. Future experiments for optimizing this synthesis include standardizing the scotch tape test that examines the adhesion between polymer and substrate. The pressure applied on the scotch tape, the duration of applying the scotch tape, and the peel-off speed need to be quantitative. Additionally, the deposition of silane require spectroscopic characterization (FTIR or Raman) to ensure the formation of a homogeneous silane monolayer and bonding between PEDOT and phenyl groups.

3.5 References

- (1) Carli, S.; Casarin, L.; Bergamini, G.; Caramori, S.; Bignozzi, C. A. Conductive PEDOT Covalently Bound to Transparent FTO Electrodes. *Journal of Physical Chemistry C* **2014**, *118* (30), 16782–16790. <https://doi.org/10.1021/jp412758g>.
- (2) Devarayan, K.; Lei, D.; Kim, H. Y.; Kim, B. S. Flexible Transparent Electrode Based on PANi Nanowire/Nylon Nanofiber Reinforced Cellulose Acetate Thin Film as Supercapacitor. *Chemical Engineering Journal* **2015**, *273*, 603–609. <https://doi.org/10.1016/j.cej.2015.03.115>.
- (3) Singh, S. B.; Kshetri, T.; Singh, T. I.; Kim, N. H.; Lee, J. H. Embedded PEDOT:PSS/AgNFs Network Flexible Transparent Electrode for Solid-State Supercapacitor. *Chemical Engineering Journal* **2019**, *359* (September 2018), 197–207. <https://doi.org/10.1016/j.cej.2018.11.160>.
- (4) Mondal, S.; Yoshida, T.; Maji, S.; Ariga, K.; Higuchi, M. Transparent Supercapacitor Display with Redox-Active Metallo-Supramolecular Polymer Films. *ACS Appl. Mater. Interfaces* **2020**, *12* (14), 16342–16349. <https://doi.org/10.1021/acsami.9b23123>.
- (5) Liu, T.; Yan, R.; Huang, H.; Pan, L.; Cao, X.; DeMello, A.; Niederberger, M. A Micromolding Method for Transparent and Flexible Thin-Film Supercapacitors and Hybrid Supercapacitors. *Adv. Funct. Mater.* **2020**, *30* (46), 2004410. <https://doi.org/10.1002/adfm.202004410>.
- (6) Zhu, W. C.; He, P. Q.; Tien, H. C.; Liu, H. L.; Chen, W. C.; Lv, W.; Lee, W. Y. Solvent-Enhanced Transparent Stretchable Polymer Nanocomposite Electrode for Supercapacitors. *ACS Appl. Energy Mater.* **2021**, *4* (3), 2266–2274. <https://doi.org/10.1021/acsam.0c02781>.
- (7) Chen, C.; Feng, J.; Li, J.; Guo, Y.; Shi, X.; Peng, H. Functional Fiber Materials to Smart Fiber Devices. *Chem. Rev.* **2022**. <https://doi.org/10.1021/acs.chemrev.2c00192>.
- (8) Chen, Y.; Yang, H.; Han, Z.; Bo, Z.; Yan, J.; Cen, K.; Ostrikov, K. K. MXene-Based Electrodes for Supercapacitor Energy Storage. *Energy and Fuels* **2022**, *36* (5), 2390–2406. <https://doi.org/10.1021/acs.energyfuels.1c04104>.
- (9) Xing, F.; Bi, Z.; Su, F.; Liu, F.; Wu, Z. S. Unraveling the Design Principles of Battery-Supercapacitor Hybrid Devices: From Fundamental Mechanisms to Microstructure Engineering and Challenging Perspectives. *Adv. Energy Mater.* **2022**, *12* (26), 2200594. <https://doi.org/10.1002/aenm.202200594>.
- (10) Iqbal, M. Z.; Aziz, U. Supercapattery: Merging of Battery-Supercapacitor Electrodes for Hybrid Energy Storage Devices. *J. Energy Storage* **2022**, *46* (December 2021), 103823. <https://doi.org/10.1016/j.est.2021.103823>.
- (11) Mohanadas, D.; Sulaiman, Y. Recent Advances in Development of Electroactive Composite Materials for Electrochromic and Supercapacitor Applications. *J. Power Sources* **2022**, *523* (September 2021), 231029. <https://doi.org/10.1016/j.jpowsour.2022.231029>.

- (12) Yan, L.; Li, D.; Yan, T.; Chen, G.; Shi, L.; An, Z.; Zhang, D. Confining Redox Electrolytes in Functionalized Porous Carbon with Improved Energy Density for Supercapacitors. *ACS Appl. Mater. Interfaces* **2018**, *10* (49), 42494–42502. <https://doi.org/10.1021/acsami.8b16642>.
- (13) Yan, L.; Li, D.; Yan, T.; Chen, G.; Shi, L.; An, Z.; Zhang, D. N,P,S-Codoped Hierarchically Porous Carbon Spheres with Well-Balanced Gravimetric/Volumetric Capacitance for Supercapacitors. *ACS Sustain. Chem. Eng.* **2018**, *6* (4), 5265–5272. <https://doi.org/10.1021/acssuschemeng.7b04922>.
- (14) Duan, H.; Yan, T.; Li, Z.; Chen, G.; Zhang, J.; Shi, L.; Zhang, D. Rapid Synthesis of Self-Supported Three-Dimensional Bubble-like Graphene Frameworks as High-Performance Electrodes for Supercapacitors. *Sustain. Energy Fuels* **2017**, *1* (7), 1557–1567. <https://doi.org/10.1039/C7SE00178A>.
- (15) Zhang, C. (John); Nicolosi, V. Graphene and MXene-Based Transparent Conductive Electrodes and Supercapacitors. *Energy Storage Mater.* **2019**, *16* (April 2018), 102–125. <https://doi.org/10.1016/j.ensm.2018.05.003>.
- (16) Chen, S.; Shi, B.; He, W.; Wu, X.; Zhang, X.; Zhu, Y.; He, S.; Peng, H.; Jiang, Y.; Gao, X.; Fan, Z.; Zhou, G.; Liu, J.; Kempa, K.; Gao, J. Quasifractal Networks as Current Collectors for Transparent Flexible Supercapacitors. *Adv. Funct. Mater.* **2019**, *29* (48), 1906618. <https://doi.org/10.1002/adfm.201906618>.
- (17) Huang, Q.; Chen, J.; Yan, S.; Shao, X.; Dong, Y.; Liu, J.; Li, W.; Zhang, C. New Donor-Acceptor-Donor Conjugated Polymer with Twisted Donor-Acceptor Configuration for High-Capacitance Electrochromic Supercapacitor Application. *ACS Sustain. Chem. Eng.* **2021**, *9* (41), 13807–13817. <https://doi.org/10.1021/acssuschemeng.1c04498>.
- (18) Wei, B.; Liu, J.; Ouyang, L.; Kuo, C. C.; Martin, D. C. Significant Enhancement of PEDOT Thin Film Adhesion to Inorganic Solid Substrates with EDOT-Acid. *ACS Appl. Mater. Interfaces* **2015**, *7* (28), 15388–15394. <https://doi.org/10.1021/acsami.5b03350>.
- (19) Inamdar, A. I.; Chavan, H. S.; Kim, H.; Im, H. Mesoporous Ni-PANI Composite Electrode for Electrochromic Energy Storage Applications. *Solar Energy Materials and Solar Cells* **2019**, *201* (August), 110121. <https://doi.org/10.1016/j.solmat.2019.110121>.
- (20) Ouyang, L.; Wei, B.; Kuo, C.; Pathak, S.; Farrell, B.; Martin, D. C. Enhanced PEDOT Adhesion on Solid Substrates with Electrografted P(EDOT-NH₂). *Sci. Adv.* **2017**, *3* (3), 1–12. <https://doi.org/10.1126/sciadv.1600448>.
- (21) Arkles B. Tailoring Surfaces with Silanes. *Chemtech* **1977**, *7* (12), 766.
- (22) Im, S. G.; Yoo, P. J.; Hammond, P. T.; Gleason, K. K. Grafted Conducting Polymer Films for Nano-Patterning onto Various Organic and Inorganic Substrates by Oxidative Chemical Vapor Deposition. *Advanced Materials* **2007**, *19* (19), 2863–2867. <https://doi.org/10.1002/adma.200701170>.

- (23) Robinson, M. T.; Simons, C. E.; Cliffler, D. E.; Jennings, G. K. Photocatalytic Photosystem I/PEDOT Composite Films Prepared by Vapor-Phase Polymerization. *Nanoscale* **2017**, 9 (18), 6158–6166. <https://doi.org/10.1039/c7nr01158j>.
- (24) Lee, Y.; Chae, S.; Park, H.; Kim, J.; Jeong, S. H. Stretchable and Transparent Supercapacitors Based on Extremely Long MnO₂/Au Nanofiber Networks. *Chemical Engineering Journal* **2020**, 382 (September 2019). <https://doi.org/10.1016/j.cej.2019.122798>.
- (25) Soram, B. S.; Dai, J.; Kshetri, T.; Kim, N. H.; Lee, J. H. Vertically Grown and Intertwined Co(OH)₂ Nanosheet@Ni-Mesh Network for Transparent Flexible Supercapacitor. *Chemical Engineering Journal* **2020**, 391 (September 2019), 123540. <https://doi.org/10.1016/j.cej.2019.123540>.
- (26) Soram, B. S.; Thangjam, I. S.; Dai, J. Y.; Kshetri, T.; Kim, N. H.; Lee, J. H. Flexible Transparent Supercapacitor with Core-Shell Cu@Ni@NiCoS Nanofibers Network Electrode. *Chemical Engineering Journal* **2020**, 395 (January), 125019. <https://doi.org/10.1016/j.cej.2020.125019>.
- (27) Yang, H.; Chow, B.; Awoyomi, A.; D'Arcy, J. M. Nanostructured Poly(3,4-Ethylenedioxythiophene) Coatings on Functionalized Glass for Energy Storage. *ACS Appl. Mater. Interfaces* **2023**, 15 (2), 3235–3243. <https://doi.org/10.1021/acsami.2c20328>.
- (28) Fadeev, A. Y.; McCarthy, T. J. Self-Assembly Is Not the Only Reaction Possible between Alkyltrichlorosilanes and Surfaces: Monomolecular and Oligomeric Covalently Attached Layers of Dichloro- and Trichloroalkylsilanes on Silicon. *Langmuir* **2000**, 16 (18), 7268–7274. <https://doi.org/10.1021/la000471z>.
- (29) Haensch, C.; Hoeppener, S.; Schubert, U. S. Chemical Modification of Self-Assembled Silane Based Monolayers by Surface Reactions. *Chem Soc Rev* **2010**, 39 (6), 2323–2334. <https://doi.org/10.1039/b920491a>.
- (30) Diao, Y.; Chen, H.; Lu, Y.; Santino, L. M.; Wang, H.; D'Arcy, J. M. Converting Rust to PEDOT Nanofibers for Supercapacitors. *ACS Appl. Energy Mater.* **2019**, 2 (5), 3435–3444. <https://doi.org/10.1021/acsam.9b00244>.
- (31) Stumm, W.; Furrer, G.; Wieland, E.; Zinder, B. The Effects of Complex-Forming Ligands on the Dissolution of Oxides and Aluminosilicates. In *The Chemistry of Weathering*; Drever, J. I., Ed.; Springer Netherlands: Dordrecht, 1985; pp 55–74. https://doi.org/10.1007/978-94-009-5333-8_4.
- (32) Chastukhin, A. E.; Izotov, A. D.; Gorichev, I. G.; Kutepov, A. M. Analysis of the Kinetics of Iron(II, III) Oxide Dissolution in Hydrochloric Acid Using a Generalized Delmon Model. *Theoretical Foundations of Chemical Engineering* **2004**, 38 (1), 81–85. <https://doi.org/10.1023/B:TFCE.0000014393.78680.a7>.
- (33) Schwertmann, U. Solubility and Dissolution of Iron Oxides. *Plant Soil* **1991**, 130 (1–2), 1–25. <https://doi.org/10.1007/BF00011851>.

- (34) *Handbook of Conducting Polymers, Fourth Edition - 2 Volume Set*, 4th ed.; Reynolds, J. R., Thompson, B. C., Skotheim, T. A., Eds.; CRC Press, 2019. <https://doi.org/10.1201/b22233>.
- (35) Mueller, M.; Fabretto, M.; Evans, D.; Hojati-Talemi, P.; Gruber, C.; Murphy, P. Vacuum Vapour Phase Polymerization of High Conductivity PEDOT: Role of PEG-PPG-PEG, the Origin of Water, and Choice of Oxidant. *Polymer (Guildf)* **2012**, *53* (11), 2146–2151. <https://doi.org/10.1016/j.polymer.2012.03.028>.
- (36) Im, S. G.; Gleason, K. K. Systematic Control of the Electrical Conductivity of Poly(3,4-Ethylenedioxythiophene) via Oxidative Chemical Vapor Deposition. *Macromolecules* **2007**, *40* (18), 6552–6556. <https://doi.org/10.1021/ma0628477>.
- (37) Fabretto, M.; Zuber, K.; Hall, C.; Murphy, P.; Griesser, H. J. The Role of Water in the Synthesis and Performance of Vapour Phase Polymerised PEDOT Electrochromic Devices. *J. Mater. Chem.* **2009**, *19* (42), 7871–7878. <https://doi.org/10.1039/b912324e>.
- (38) Panias, D.; Taxiarchou, M.; Paspaliaris, I.; Kontopoulos, A. Mechanisms of Dissolution of Iron Oxides in Aqueous Oxalic Acid Solutions. *Hydrometallurgy* **1996**, *42* (2), 257–265. [https://doi.org/10.1016/0304-386X\(95\)00104-O](https://doi.org/10.1016/0304-386X(95)00104-O).
- (39) Evans, D. R. Understanding PEDOT Doped with Tosylate. *Chemical Communications* **2022**, *58* (29), 4553–4560. <https://doi.org/10.1039/d2cc01100j>.
- (40) Faivre, D. *Iron Oxides: From Nature to Applications*, 1st ed.; Faivre, D., Ed.; Wiley: Weinheim, 2016. <https://doi.org/10.1002/9783527691395>.
- (41) Pu, Z.; Cao, M.; Yang, J.; Huang, K.; Hu, C. Controlled Synthesis and Growth Mechanism of Hematite Nanorhomboheda, Nanorods and Nanocubes. *Nanotechnology* **2006**, *17* (3), 799–804. <https://doi.org/10.1088/0957-4484/17/3/031>.
- (42) Chaudhari, N. K.; Yu, J. S. Size Control Synthesis of Uniform β -FeOOH to High Coercive Field Porous Magnetic α -Fe₂O₃ Nanorods. *Journal of Physical Chemistry C* **2008**, *112* (50), 19957–19962. <https://doi.org/10.1021/jp808589y>.
- (43) Wang, W.; Howe, J. Y.; Gu, B. Structure and Morphology Evolution of Hematite (α -Fe₂O₃) Nanoparticles in Forced Hydrolysis of Ferric Chloride. *Journal of Physical Chemistry C* **2008**, *112* (25), 9203–9208. <https://doi.org/10.1021/jp800683j>.
- (44) Guo, P.; Wei, Z.; Wang, B.; Ding, Y.; Li, H.; Zhang, G.; Zhao, X. S. Controlled Synthesis, Magnetic and Sensing Properties of Hematite Nanorods and Microcapsules. *Colloids Surf. A Physicochem. Eng. Asp.* **2011**, *380* (1–3), 234–240. <https://doi.org/10.1016/j.colsurfa.2011.02.026>.
- (45) Chiu, C. A.; Hristovski, K. D.; Dockery, R.; Doudrick, K.; Westerhoff, P. Modeling Temperature and Reaction Time Impacts on Hematite Nanoparticle Size during Forced Hydrolysis of Ferric Chloride. *Chemical Engineering Journal* **2012**, *210*, 357–362. <https://doi.org/10.1016/j.cej.2012.08.093>.

- (46) Jolivet, J.-P.; Tronc, E.; Chanéac, C. Iron Oxides: From Molecular Clusters to Solid. A Nice Example of Chemical Versatility. *Comptes Rendus Geoscience* **2006**, 338 (6–7), 488–497. <https://doi.org/10.1016/j.crte.2006.04.014>.
- (47) Scheck, J.; Wu, B.; Drechsler, M.; Rosenberg, R.; Van Driessche, A. E. S.; Stawski, T. M.; Gebauer, D. The Molecular Mechanism of Iron(III) Oxide Nucleation. *Journal of Physical Chemistry Letters* **2016**, 7 (16), 3123–3130. <https://doi.org/10.1021/acs.jpclett.6b01237>.
- (48) Flynn, C. M. Hydrolysis of Inorganic Iron(III) Salts. *Chem. Rev.* **1984**, 84 (1), 31–41. <https://doi.org/10.1021/cr00059a003>.
- (49) Bottero, J. Y.; Manceau, A.; Villieras, F.; Tchoubar, D. Structure and Mechanisms of Formation of FeOOH(Cl) Polymers. *Langmuir* **1994**, 10 (1), 316–319. <https://doi.org/10.1021/la00013a046>.
- (50) De Yoreo, J. J.; Gilbert, P. U. P. A.; Sommerdijk, N. A. J. M.; Penn, R. L.; Whitlam, S.; Joester, D.; Zhang, H.; Rimer, J. D.; Navrotsky, A.; Banfield, J. F.; Wallace, A. F.; Michel, F. M.; Meldrum, F. C.; Cölfen, H.; Dove, P. M. Crystallization by Particle Attachment in Synthetic, Biogenic, and Geologic Environments. *Science* (1979) **2015**, 349 (6247). <https://doi.org/10.1126/science.aaa6760>.
- (51) Tang, J.; Paul Alivisatos, A. Crystal Splitting in the Growth of Bi₂S₃. *Nano Lett.* **2006**, 6 (12), 2701–2706. <https://doi.org/10.1021/nl0615930>.
- (52) Hu, Y.; Chen, K. Crystal Splitting in the Growth of β -FeO(OH). *J. Cryst. Growth* **2007**, 308 (1), 185–188. <https://doi.org/10.1016/j.jcrysgr.2007.07.035>.
- (53) Grigor'ev, D. P. *Ontogeny of Minerals*; Israel Program for Scientific Translations Jerusalem, 1965.
- (54) Dongmin Kang, S.; Jeffrey Snyder, G. Charge-Transport Model for Conducting Polymers. *Nat Mater* **2017**, 16 (2), 252–257. <https://doi.org/10.1038/nmat4784>.
- (55) Stavytska-Barba, M.; Kelley, A. M. Surface-Enhanced Raman Study of the Interaction of PEDOT: PSS with Plasmonically Active Nanoparticles. *Journal of Physical Chemistry C* **2010**, 114 (14), 6822–6830. <https://doi.org/10.1021/jp100135x>.
- (56) Park, H.; Lee, S. H.; Kim, F. S.; Choi, H. H.; Cheong, I. W.; Kim, J. H. Enhanced Thermoelectric Properties of PEDOT:PSS Nanofilms by a Chemical Dedoping Process. *J Mater. Chem. A Mater.* **2014**, 2 (18), 6532–6539. <https://doi.org/10.1039/C3TA14960A>.
- (57) Zozoulenko, I.; Singh, A.; Singh, S. K.; Gueskine, V.; Crispin, X.; Berggren, M. Polarons, Bipolarons, and Absorption Spectroscopy of PEDOT. *ACS Appl. Polym. Mater.* **2019**, 1 (1), 83–94. <https://doi.org/10.1021/acsapm.8b00061>.
- (58) Bredas, J. L.; Street, G. B. Polarons, Bipolarons, and Solitons in Conducting Polymers. *Acc. Chem. Res.* **1985**, 18 (10), 309–315. <https://doi.org/10.1021/ar00118a005>.

- (59) Ouyang, J.; Xu, Q.; Chu, C. W.; Yang, Y.; Li, G.; Shinar, J. On the Mechanism of Conductivity Enhancement in Poly(3,4- Ethylenedioxythiophene):Poly(Styrene Sulfonate) Film through Solvent Treatment. *Polymer (Guildf)* **2004**, 45 (25), 8443–8450. <https://doi.org/10.1016/j.polymer.2004.10.001>.
- (60) Shi, W.; Yao, Q.; Qu, S.; Chen, H.; Zhang, T.; Chen, L. Micron-Thick Highly Conductive Pedot Films Synthesized via Self-Inhibited Polymerization: Roles of Anions. *NPG Asia Mater.* **2017**, 9 (7), e405–e405. <https://doi.org/10.1038/am.2017.107>.
- (61) Bora, P. J.; Anil, A. G.; Vinoy, K. J.; Ramamurthy, P. C. Outstanding Absolute Electromagnetic Interference Shielding Effectiveness of Cross-Linked PEDOT:PSS Film. *Adv. Mater. Interfaces* **2019**, 6 (22), 1–5. <https://doi.org/10.1002/admi.201901353>.
- (62) Culebras, M.; Serrano-Claumarchirant, J. F.; Sanchis, M. J.; Landfester, K.; Cantarero, A.; Gómez, C. M.; Munoz-Espí, R. Conducting PEDOT Nanoparticles: Controlling Colloidal Stability and Electrical Properties. *Journal of Physical Chemistry C* **2018**, 122 (33), 19197–19203. <https://doi.org/10.1021/acs.jpcc.8b04981>.
- (63) Acharya, S.; Santino, L. M.; Lu, Y.; Anandarajah, H.; Wayne, A.; D’Arcy, J. M. Ultrahigh Stability of High-Power Nanofibrillar PEDOT Supercapacitors. *Sustain. Energy Fuels* **2017**, 1 (3), 482–491. <https://doi.org/10.1039/c7se00057j>.
- (64) Wang, S.; Zhang, J.; Gharbi, O.; Vivier, V.; Gao, M.; Orazem, M. E. Electrochemical Impedance Spectroscopy. *Nature Reviews Methods Primers* **2021**, 1 (1), 41. <https://doi.org/10.1038/s43586-021-00039-w>.
- (65) Mei, B. A.; Munteshari, O.; Lau, J.; Dunn, B.; Pilon, L. Physical Interpretations of Nyquist Plots for EDLC Electrodes and Devices. *Journal of Physical Chemistry C* **2018**, 122 (1), 194–206. <https://doi.org/10.1021/acs.jpcc.7b10582>.
- (66) Salleo, A. Charge Transport in Polymeric Transistors. *Materials Today* **2007**, 10 (3), 38–45. [https://doi.org/10.1016/S1369-7021\(07\)70018-4](https://doi.org/10.1016/S1369-7021(07)70018-4).
- (67) Sardana, S.; Gupta, A.; Singh, K.; Maan, A. S.; Ohlan, A. Conducting Polymer Hydrogel Based Electrode Materials for Supercapacitor Applications. *J. Energy Storage* **2022**, 45 (November 2021), 103510. <https://doi.org/10.1016/j.est.2021.103510>.
- (68) Meng, Q.; Cai, K.; Chen, Y.; Chen, L. Research Progress on Conducting Polymer Based Supercapacitor Electrode Materials. *Nano Energy* **2017**, 36, 268–285. <https://doi.org/10.1016/j.nanoen.2017.04.040>.
- (69) Fleischmann, S.; Mitchell, J. B.; Wang, R.; Zhan, C.; Jiang, D. E.; Presser, V.; Augustyn, V. Pseudocapacitance: From Fundamental Understanding to High Power Energy Storage Materials. *Chem. Rev.* **2020**, 120 (14), 6738–6782. <https://doi.org/10.1021/acs.chemrev.0c00170>.

Chapter 4: Poly(3,4-ethylenedioxythiophene)- integrated Masonry Material via Vapor- phase Polymerization

In Chapter 3, I presented a novel approach that covalently bonds PEDOT to glass, a material commonly used in construction. The integration between conducting polymers and construction materials inspires further research of combining a construction material that contains Fe^{3+} and conducting polymers. In this chapter, I present my work on integrating vapor-phase synthesized PEDOT with masonry materials, such as bricks and tiles. This project is unfinished, but the synthesis and mechanisms involved deserve more investigation.

4.1 Introduction

Masonry construction is ubiquitous across cultures and widely utilized through history for its versatility and durability.^{1,2} In the past, architects develop various designs to cope with different climates across the globe.³⁻⁷ For example, in the Middle East mashrabiya window contains built-in spaces for water jars and utilizes evaporation for passive cooling, in northern China sky well (an enclosed courtyard) orients towards south to maximize sunlight intake and blocks cold northern winds.^{8,9} In modern architecture, the rapid development in automated and energy efficient buildings requires real time temperature sensing to minimize ecological footprint in the long term.^{10,11} Monitoring and regulating temperature in a masonry structure is essential for reducing building energy consumption and creating energy efficient architecture.¹²⁻¹⁶ The current solution to temperature monitoring often involves embedding wired or wireless sensors into

walls, however these sensors suffer from low response time and limited battery life.^{13,15} Alternatively, embedded resistive temperature sensors with fast response time and long term sensing capability overcomes these stifling limitations. Recently, the chemoresistive and thermoresistive properties of conducting polymers has attracted much interest in sensor research,^{17–23} and among these materials PEDOT stands out due to its stability under ambient conditions. Unfortunately, current PEDOT-based temperature sensors suffer from a narrow temperature sensing window and poor linearity.^{20–22,24} Here, we present a novel strategy for developing a temperature sensor by integrating nanofibrillar PEDOT within the inorganic microstructure of common masonry materials. The synthetic strategy is inspired by a previously published work using rust-based vapor phase synthesis (RVPP) and fired bricks.²⁵ The electrical conductivity of PEDOT-integrated brick is enhanced by introducing organic solvents during vapor-phase synthesis, resulting in improved linearity and widened temperature sensing range. Mechanisms that lead to enhanced electrical conductivity is presented and discussed. Our unique synthetic approach combines the semiconducting properties of PEDOT and the structural integrity of masonry materials. The homogeneous integration between PEDOT and brick/tile results in a superior composite material for long term real-time sensing. A device possesses excellent sensitivity of $0.50\text{ }^{\circ}\text{C}^{-1}$ (normalized resistance per Celsius, $\Delta R/(R_0 \cdot \Delta T)$) and exhibits approximate linear behavior to temperature change within a wide temperature window ($-20\text{ }^{\circ}\text{C}$ to $60\text{ }^{\circ}\text{C}$), demonstrating potential for new integrated electronic functionality in load bearing construction materials.

4.2 Materials and Methods

Chlorobenzene (99%), 3,4-ethylenedioxythiophene (97%) methanol ($\geq 99.8\%$), and hydrochloric acid (37%) were purchased from Sigma-Aldrich. Fired bricks were purchased from local hardware stores: The Home Depot Inc. (type 1 brick, <https://www.homedepot.com>, Internet #100323015, Model #RED0126MCO, Store SKU #393134), Lowe's Inc. Floor tiles were purchased from local hardware stores: Internet #305322621, Model #NRETBLA3X6INBEV, Store SKU #1003235709, Store SO SKU #1003190599. All chemicals were used without further purification.

Microscopy and Spectroscopy

Optical microscopy was performed on a Nikon Eclipse LV100ND microscope. Scanning electron microscopy was performed with a Thermo Fisher Scientific Quattro S environmental scanning electron microscope. Raman spectroscopy was performed using a Renishaw inVia™ confocal Raman microscope, and samples were under green light excitation at 514 nm.

PEDOT Synthesis and RVPP with Organic Solvents

In a standard synthesis, a tile or brick was cut into 1.5 cm by 1.5 cm by 0.6 cm cubes and placed in a sealed glass jar reactor with two vials containing concentrated HCl (tile synthesis: 150 μL , brick synthesis: 300 μL) and 1.56 M EDOT/chlorobenzene solution (tile synthesis: 200 μL , brick synthesis: 400 μL) respectively. For tile synthesis, 300 μL ethanol was drop-casted on top before the reactor was sealed and heated in a 140 °C oven over 1.5 h. For brick synthesis, no additional solvent was used, and the reactor was sealed and heated under 140 °C over 3 h.

Experiment comparing the effect of sample size utilized tiles cut into 1.5 cm x 5.5 cm x 0.6 cm for synthesis. Reaction time was increased to 2 h, and reactant amounts were scaled to 300 μ L concentrated HCl and 400 μ L 1.56 M monomer solution, respectively.

Experiment comparing the effect of incorporating different solvents followed a similar procedure as a standard synthesis on tiles. 300 μ L of isopropanol, t-butanol, or nitromethane were drop-casted on a tile instead of ethanol. Experiment comparing the effect of varying ethanol volumes were prepared with 50 μ L, 100 μ L, 300 μ L, and 1000 μ L, respectively.

Temperature Sensor Fabrication and Testing

Samples were soaked in methanol overnight to remove any excess iron ions from the reaction, then dried at room temperature for sensor fabrication. Two pieces of copper tape 2 mm in width were placed 1 mm apart on a washed and dried sample as current leads. All surfaces of the sample were covered with polyimide tape to prevent dopant leakage. The current leads were connected via alligator clips to a Fluke 177 True-RMS multimeter for resistance measurement, and a thermocouple was attached to the tile to monitor temperature. T_0 and R_0 were set as room temperature at the time of measurement and the resistance at that temperature. Temperature was varied via heating on a hot plate or cooling with dry ice, and a calibration curve was created by plotting and fitting the sensor's normalized resistance $((R-R_0)/R_0)$ against temperature. In an experiment exploring the effect of distances between leads, 1 mm, 3 mm, and 6 mm gaps were tested. All current vs. voltage curves were generated using a Keithley 2450 SourceMeter.

4.3 Results and Discussions

Rust-based Vapor-phase Polymerization (RVPP) of PEDOT on Tiles

A brick/tile is placed in a glass jar reactor along with two reservoirs that contain concentrated hydrochloric acid (HCl) and EDOT in chlorobenzene solution respectively (Figure 4.1a). All liquid phase reactants evaporate, and the synthesis occurs in vapor phase under a temperature of 140 °C. HCl vapor arrives at the tile surface to dissolve hematite ($\alpha\text{-Fe}_2\text{O}_3$) and liberate ferric ions. The presence of chloride ion facilitates the dissolution of hematite, complexing with a ferric ion that accelerates its detachment from the bulk oxide (Figure 4.2).^{26,27} The liberated ferric ions are hygroscopic and forms a thin aqueous layer at the tile surface. Figure 4.3 shows EDOT monomer is oxidized by Fe^{3+} and forms a cationic radical (initiation). Two cationic radicals undergo coupling and deprotonation, forming a neutral dimer (propagation). The initiation and propagation steps are cyclic until steric hinderance eventually terminates polymerization. As the cross-sectional photo shows, polymerization occurs both at the surface and inside the brick/tile (Figure 4.1b). Ferric ions both initiate oxidative radical polymerization and undergo forced hydrolysis. At molecular scale, free ferric ions first form complexes consisting aqua and hydroxo groups, olation and oxolation reactions then link Fe^{3+} complexes via hydroxo- and oxo-bonding (Figure 4.4). During hydrolysis, chloride ion is a spectator ion and influence crystal structure formation when present at high concentration, facilitating the formation of monoclinic akageneite ($\beta\text{-FeOOH}$).^{28,29} Columbic interaction and Lewis acid/base interaction drive the oriented attachment during $\beta\text{-FeOOH}$ crystallization.^{30,31} Smaller spindle-like $\beta\text{-FeOOH}$ crystals elongate and merge to template the formation of highly conductive PEDOT with nanofibrillar morphology (Figure 4.1c). A sample is washed and dried after synthesis and fabricated into a resistive temperature sensor for testing (Figure 4.1d).

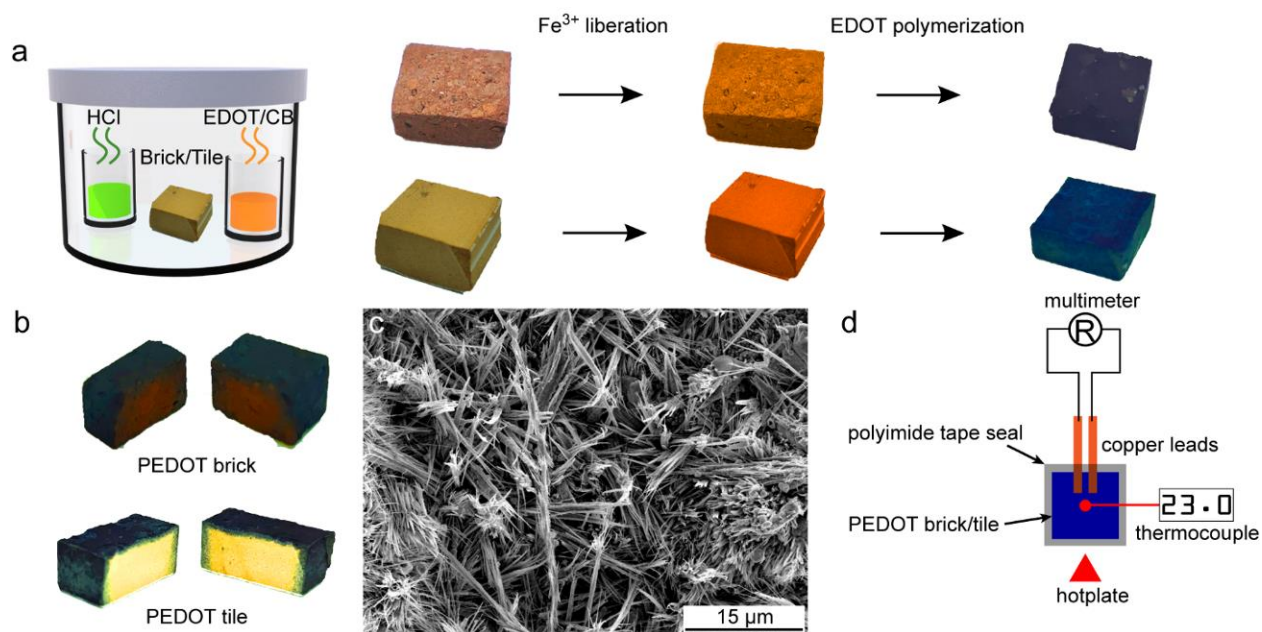


Figure 4.1 Schematic diagrams of synthetic approach and temperature sensing device. a) Rust-based vapor phase polymerization on a brick/tile occurs when ferric ions liberated by HCl oxidize EDOT molecules and initiate polymerization. This results in the integration of PEDOT nanofibers within the inorganic matrix. b) Cross-sectional photos of PEDOT-coated brick and tile. c) Electron micrograph of a nanofibrillar PEDOT coating. d) A temperature sensor contains two copper leads attached to a PEDOT-coated sample and a polyimide tape seal; temperature is monitored via changes in electrical resistance.

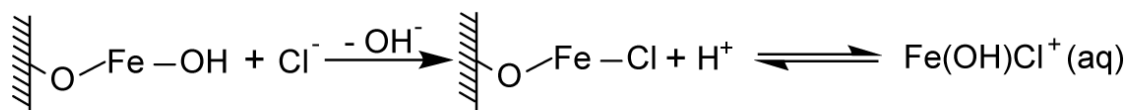


Figure 4.2 Dissolution of ferric oxyhydroxide in hydrochloric acid.

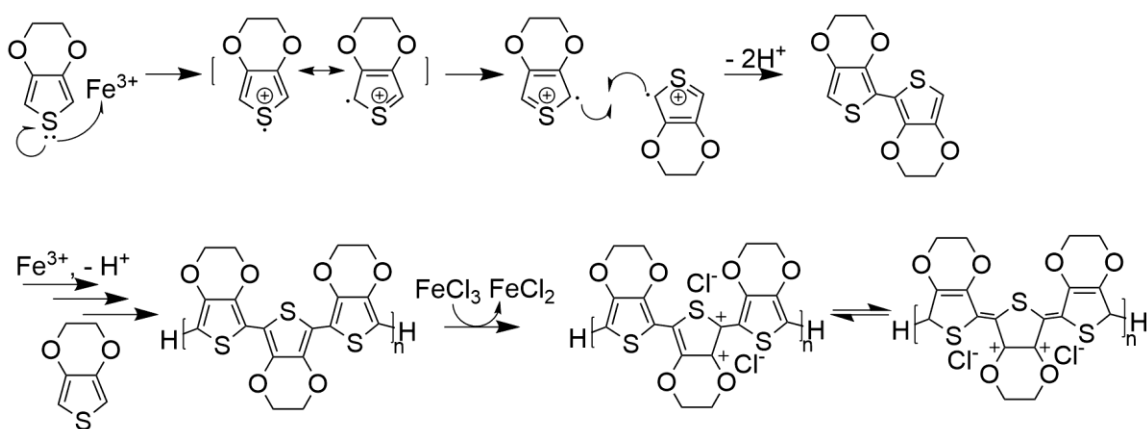


Figure 4.3 Oxidative radical polymerization of EDOT.

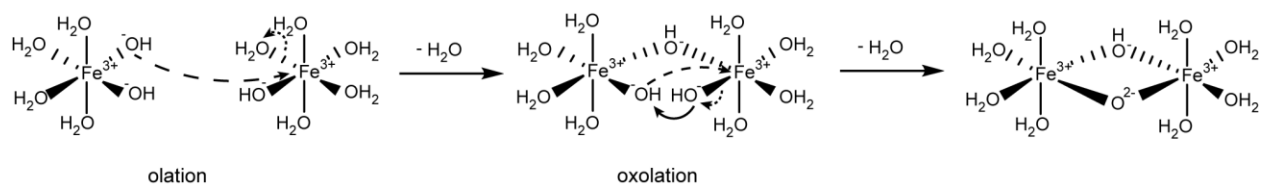


Figure 4.4 Olation and oxolation of ferric ions.

Effect of Organic Solvents

Four organic solvents are added individually (ethanol, isopropanol, t-butanol, and nitromethane) via drop-casting on tiles prior to polymer synthesis. The polymer produced from these syntheses are named Et-PEDOT, iPr-PEDOT, tBu-PEDOT, and NM-PEDOT, respectively. The electrical resistance of PEDOT is measured at several spots on a coated tile and averaged. Et-PEDOT is the most conductive coating (16 Ω), and NM-PEDOT is the least conductive (34 Ω). For comparison, synthesis without organic solvents produces a PEDOT-coated tile (water-PEDOT) with an average electrical resistance of 38 Ω (Table 4.1). Optical microscopy and back-scattering scanning electron microscopy (SEM) are utilized to measure PEDOT coating thickness from each synthesis. The detector in back-scattering SEM picks up electrons deflected back by the nucleus of an atom, and heavier atoms back-scatter more electrons and appears brighter in a micrograph. The boundary between polymer and tile is distinct in a micrograph (Figure 4.5) because PEDOT consists of lighter elements, such as carbon, hydrogen, and oxygen, whereas tile is comprised of heavier elements, such as iron, titanium, and silicon. Et-PEDOT possesses the thickest coating (~ 100 μm) while the coating of NM-PEDOT is the thinnest, similar to the water-PEDOT (~ 50 μm). Raman spectra is used to investigate the effect of adding organic solvent at molecular scale and examine changes in oxidative doping (Figure 4.6a). Raman peaks at 1260 and 1365 cm^{-1} correspond to $\text{C}_\alpha\text{-C}_\alpha'$ and $\text{C}_\beta\text{-C}_\beta$ bonds, respectively. The $\text{C}_\alpha\text{=C}_\beta$ double bond is

shown through the peaks at 1440 and 1500 cm^{-1} , while the peaks near 990 cm^{-1} indicate oxyethylene ring in each repeating unit of PEDOT.^{32–35} Comparing spectra of different samples shows the $\text{C}_\alpha=\text{C}_\beta$ peak near 1440 cm^{-1} blue shifts with the decrease in solvent surface tension while another peak near 1570 cm^{-1} becomes prominent, revealing an increase in PEDOT conjugation.³⁵

Table 4.1 Average two-point electrical resistance of PEDOT from RVPP with organic solvents.

<i>Solvent</i>	<i>Average Two-point Resistance (Ω)</i>
<i>Water (reference)</i>	38
<i>Nitromethane</i>	34
<i>Ethanol</i>	16
<i>Isopropanol</i>	28
<i>t-Butanol</i>	30

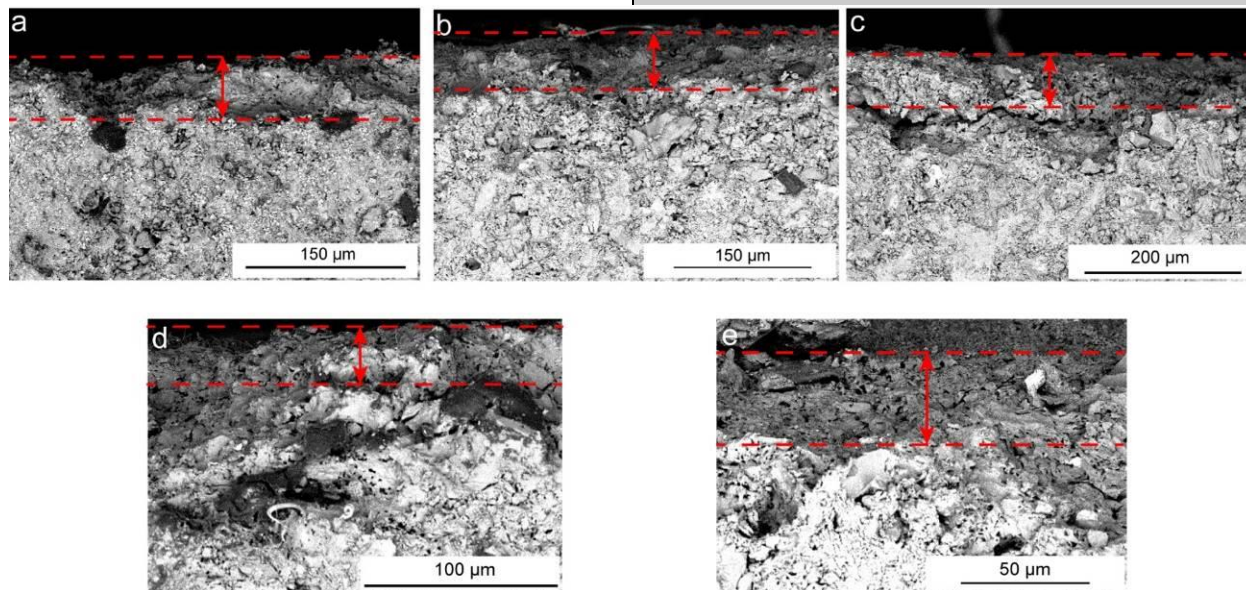


Figure 4.5 Back-scattering electron micrographs of PEDOT-coated tiles. Samples are synthesized from tiles pretreated with a) ethanol, b) isopropanol, c) t-butanol, d) nitromethane and e) Millipore water. PEDOT consists of

lighter elements than a tile, therefore deflecting less electrons to the detector and appearing lower in brightness. Note that sample placement is not perfectly perpendicular to the detector.

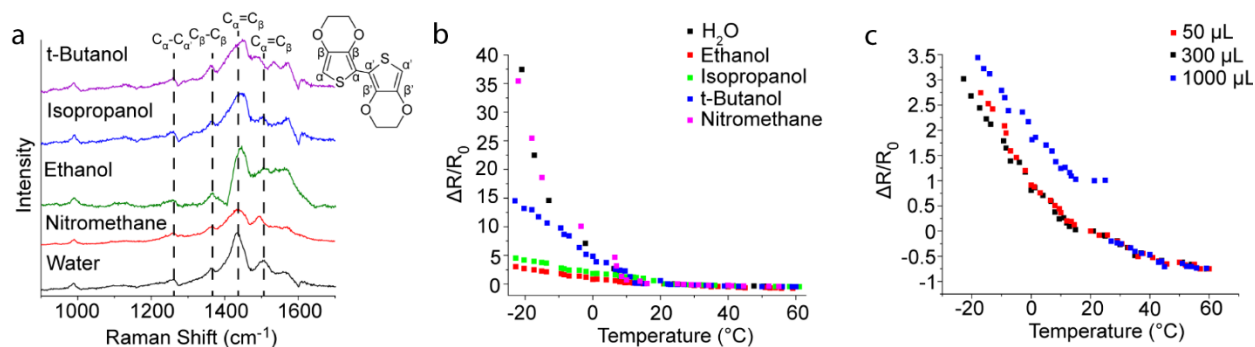


Figure 4.6 Characterization of PEDOT synthesized with organic solvents. a) PEDOT Raman spectra show an increase in oxidative doping when a tile is pretreated with an alcohol. b) Plot of normalized resistance vs. temperature shows a device possesses less linear response when solvent surface tension is high. c) 300 μL of ethanol results in a device with optimal performance (enhanced linear response).

Electrical resistance measurements, microscopy, and spectroscopic characterization demonstrate little to no difference between the water-PEDOT sample and NM-PEDOT. However, syntheses with alcohols result in PEDOT coatings with some variations in molecular structure. Based on experimental evidence and literature search, we propose two side-reactions that occur during synthesis that used alcohols that lead to the changes in polymer structure: 1) Friedel-Crafts alkylation between alcohols and chlorobenzene and 2) reaction between HCl and alcohols that forms alkyl chlorides. Previous studies report that PEDOT catalyze Friedel-Crafts alkylation between alcohols and aromatic compounds, such as benzene or toluene.³⁶ We propose that PEDOT catalyzes a similar reaction between the chlorobenzene solvent and alcohols in our synthesis, resulting in the formation of 1-chloro-2-alkylbenzene and water (Figure 4.7). The relative humidity inside the reactor is crucial for vapor-phase polymerization of EDOT because water molecules are proton scavengers that remove excess charges during the deprotonation step and stabilize newly formed oligomer and polymer chains.^{37–39} High concentration of proton scavengers results in formation of a highly conjugated PEDOT backbone that possesses

enhanced electrical conductivity. The optimal relative humidity for PEDOT synthesis reported in the literature is around 35%, and any deviation (too high or too low) from this relative humidity leads to decrease in electrical conductivity of the polymer.³⁹ During our synthesis, the side reaction between alcohols and chlorobenzene produces proton scavenging water molecules that leads to the formation of PEDOT with longer conjugation.

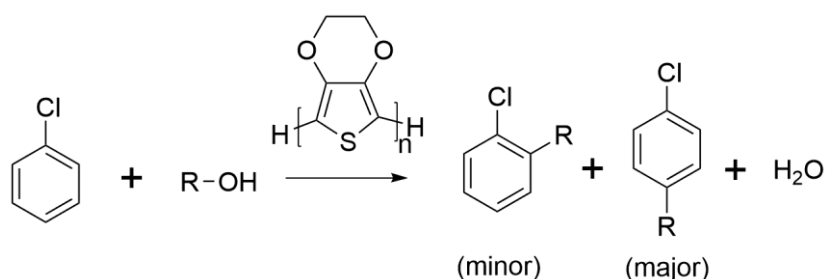


Figure 4.7 Friedel-Crafts alkylation between alcohol and chlorobenzene catalyzed by PEDOT. R is an ethyl, isopropyl, or t-butyl functional groups.

The second side reaction is the formation of alkyl chloride from the reaction between alcohols and HCl (Figure 4.8).⁴⁰ This reaction competes with the dissolution of hematite for HCl, resulting in resulting in less Fe^{3+} available for the oxidation of EDOT that initiates polymerization. Additionally, lack of ferric ions leads to insufficient oxidative doping, resulting in low concentration of conductive polaronic or bipolaronic structures in the polymer backbone. The reactivity between alcohols and HCl is tertiary (t-butanol) > secondary (isopropanol) > primary (ethanol).⁴⁰ The competing side reaction is least likely to occur during the synthesis with ethanol, resulting in Et-PEDOT possessing an oxidatively doped polymer backbone and the highest electrical conductivity.

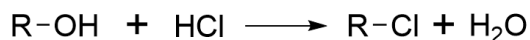


Figure 4.8 Reaction between alcohol and concentrated HCl. R is an ethyl, isopropyl, or t-butyl functional group.

PEDOT Tile and Brick Temperature Sensors

A material needs both charge carrier and conductive pathways to conduct electricity; conductors and semiconductors behave differently in resistance under changes of temperature. Conductors like metal shows an increase in electrical resistance when its temperature is increased because increased lattice vibration in a metal under heat generates more phonons that scatter electrons. Macroscopically, the scattering is reflected through increase of electrical resistance.⁴¹ Unlike metals, semiconductors such as PEDOT exhibit the opposite behavior in electrical resistance when heated. The conducting mechanism in semiconductors does not originate from movements of free electrons, but through the promotion of its charge carriers from the valence band to the conduction band. When heated, the valence band charge carriers possess more internal energy and are more readily promoted to conduction band, therefore as temperature increases the electrical resistance of semiconductor decreases.⁴² The change in electrical resistance under different temperatures is governed by the equation $R = R_{\text{ref}}(1 + \alpha(T - T_{\text{ref}}))$, where α is the temperature coefficient of the material; this coefficient is positive for metals and negative for semiconductors.⁴³ T_{ref} and R_{ref} are arbitrary reference temperature and the resistance measured at that temperature. The equation indicates that theoretically the resistance of any electrically conducting material responds linearly to changes in temperature. A resistive temperature sensor sometimes shows non-linear curve due to bad electrical contact or errors in measurements. Increasing the conductivity of a sensing material improves the electrical contact in a sensor and enhances linearity.

Figure 4.6b shows the normalized resistance vs. temperature of sensors fabricated from syntheses with organic solvents. Comparing data from Table 4.1 and Figure 4.6b reveals linearity of a

device and conductivity of PEDOT are also positively correlated. Et-PEDOT possesses the lowest electrical resistance, resulting in the highest linearity in temperature sensing. Figure 4.6c compares the result of varying the volume of ethanol in a reaction and demonstrates high concentration of ethanol during synthesis negatively affects the performance of a temperature sensor. This is likely due to excess water molecules formed from the side reaction between ethanol and chlorobenzene, resulting in the relative humidity inside the reactor deviating far from the optimal 35% and impeding the formation of conjugated polymer backbone.

The current vs. voltage curve in Figure 4.9 shows linear behavior when PEDOT coating is exposed to acidic, neutral, and basic pH. This demonstrates the coating is chemically stable under various acidity/basicity and is ideal for temperature sensing. The testing temperature range is set from -20 °C to 60 °C to mimic the environment an actual masonry structure experiences throughout the year. Instead of relying on an absolute resistance value, we utilize normalized resistance ($\Delta R/R_0$) to eliminate any error associated with electrical contact and minor difference between batches, where R_0 equals to the resistance measured under an arbitrary temperature (21 °C) and ΔR is the difference between a resistance measured and R_0 . The calibration curve has a good fit with a reduced χ^2 of 0.01039 and an R^2 of 0.99171. The overall trend is close to linear, demonstrating constant sensitivity of 0.46 °C⁻¹ (normalized resistance divided by temperature), and the sensor shows little margin of error across the temperature scale we measured (Figure 4.10a). With proper sealing, PEDOT tile also exhibits stability in temperature sensing performance and fast response time of 1.1 s (Figure 4.10b and c). Figure 4.10d compares response to temperature from PEDOT-coated tiles with different sizes (1.5 cm x 1.5 cm x 0.6 cm and 5.5 cm x 1.5 cm x 0.6 cm), and a small tile shows a steeper change in normalized resistance

(higher sensitivity) than a large tile. Heat takes less time to transport through a small volume, resulting in steep change in normalized resistance. This also demonstrates only a small PEDOT-coated area is needed for an accurate and highly sensitive temperature sensor. Figure 4.10e shows the absolute resistance measured from various gap distances (1mm, 3 mm, and 6 mm). We find changes in absolute resistance do not affect the sensitivity or linearity because resistance is always normalized.

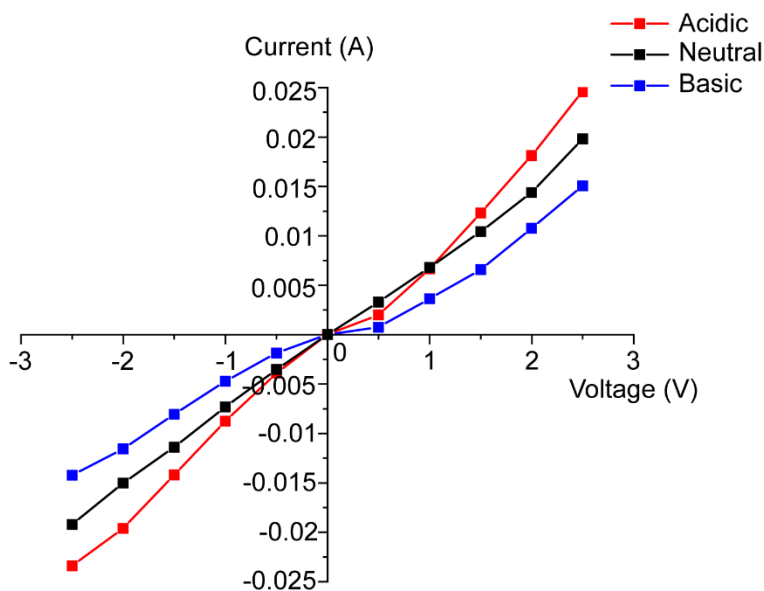


Figure 4.9 Current vs. voltage curves of PEDOT show linear behavior even when exposed to various pH.

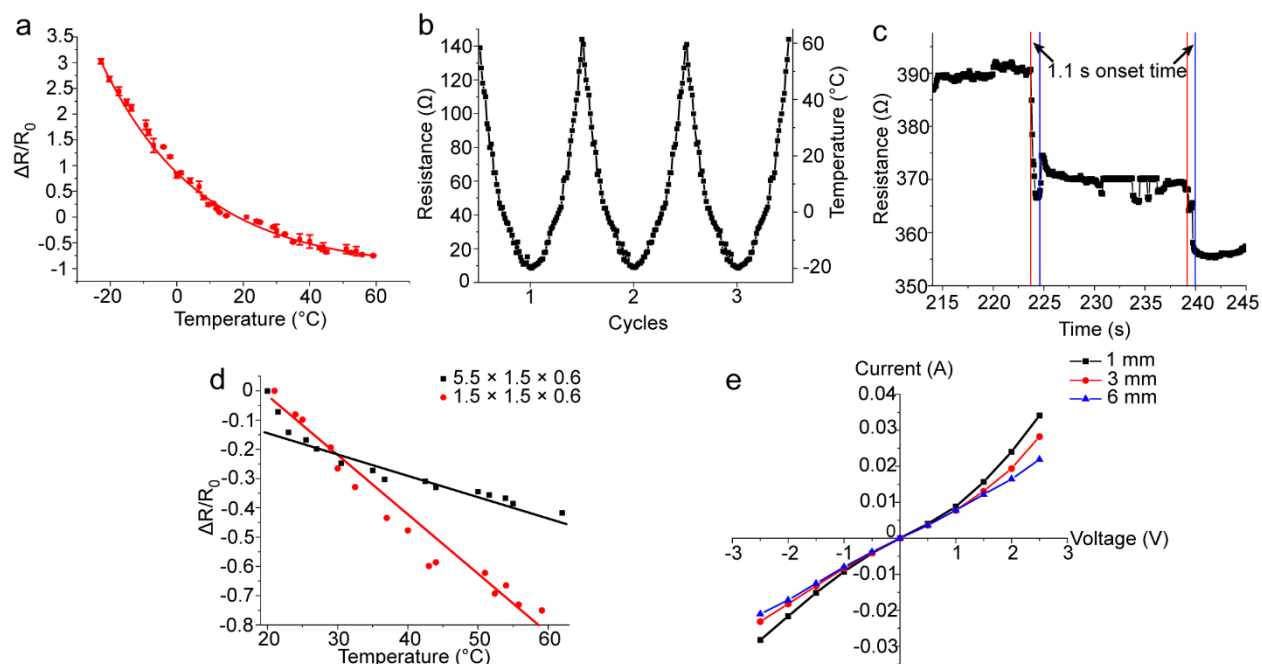


Figure 4.10 Performance of a PEDOT tile temperature sensor. a) Normalized resistance ($\Delta R/R_0$) plotted against temperature generates a calibration curve of PEDOT tile temperature sensor. The sensor demonstrates close to linear response to temperature over a wide range (-20 to 60 °C) and possesses an excellent sensitivity (0.46 °C⁻¹). b) The sensor is stable after repeated cycling and c) exhibits fast response time to temperature change. d) A small PEDOT tile demonstrates steeper response to changes in temperature because its temperature changes more rapidly. e) Sensitivity and linearity remain unaffected by gap distance between current leads, only absolute resistance changes.

Figure 4.11a plots the normalized resistance vs. temperature (-20 to 60 °C), and the fitted curve of a brick sensor has reduced χ^2 of 0.01245 and an R^2 of 0.99414 with little margin of error at each point. A brick sensor is also stable under repeated heating and cooling and demonstrates similar response time to a tile sensor (Figure 4.11b). A device fabricated from PEDOT brick possesses similar sensitivity (0.50 °C⁻¹) and linearity to a tile sensor. We prove the synthetic technique versatile and accessible for integration with masonry structures such as a brick wall (Figure 4.11c).

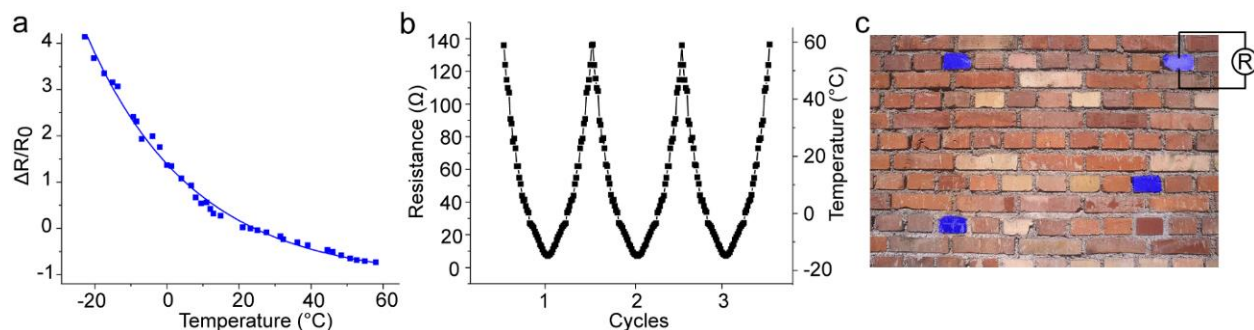


Figure 4.11 Performance of a PEDOT brick temperature sensor and a concept of integrated sensing in masonry construction. a) Calibration curve of a PEDOT brick sensor also exhibits high linearity and sensitivity (0.50 °C⁻¹). b) The device is stable during repeated cycling between -20 and 60 °C. c) Schematic diagram of a wall utilizing PEDOT bricks for integrated temperature sensing.

4.4 Conclusions

This chapter presents a proof-of-concept demonstration of integrating PEDOT and common masonry materials for a long term, real-time monitoring temperature sensor used in construction. The vapor-phase synthesis of PEDOT is modified by adding an organic solvent prior to synthesis. Enhanced electrical conductivity is observed when ethanol is introduced in polymer synthesis. We propose an increase in proton scavenger concentration, as a result of side reactions of alcohol molecules, is responsible for the enhanced electrical conductivity. Further experimentation is needed to deconvolute the roles of organic solvents and the optimal relative humidity for rust-based vapor-phase polymerization. Proof-of-concept temperature sensors based on both tile and brick are fabricated; the sensors possess good linearity, high sensitivity, and fast response time. The synthetic technique is versatile and presents new avenue to integrate electronic functionality for load bearing construction materials.

4.5 References

- (1) Young, H. D.; Freedman, R. A.; Ford, A. L. *Sears and Zemansky's University Physics: With Modern Physics*, 12th ed.; Black, A., Otway, M., Eds.; Pearson Education, Inc.: San Francisco, 2004.
- (2) TL, J. *History of Masonry*. New York. <https://www.masoncontractors.org/history/>.
- (3) Cowan, H. J. A History of Masonry and Concrete Domes in Building Construction. *Build. Environ.* **1977**, *12* (1), 1–24. [https://doi.org/10.1016/0360-1323\(77\)90002-6](https://doi.org/10.1016/0360-1323(77)90002-6).
- (4) Tobriner, S. History of Reinforced Masonry Construction Designed To Resist Earthquakes: 1755-1907. *Earthquake Spectra.* 1984, pp 125–149. <https://doi.org/10.1193/1.1585260>.
- (5) Foce, F. On the Safety of the Masonry Arch. Different Formulations from the History of Structural Mechanics.
- (6) Como, M. *Statics of Historic Masonry Constructions: An Essay*; 2015. https://doi.org/10.1007/978-3-319-13003-3_3.
- (7) Ionescu, C.; Baracu, T.; Vlad, G. E.; Necula, H.; Badea, A. The Historical Evolution of the Energy Efficient Buildings. *Renewable and Sustainable Energy Reviews* **2015**, *49*, 243–253. <https://doi.org/10.1016/j.rser.2015.04.062>.
- (8) Fathy, H. *Natural Energy and Vernacular Architecture: Principles and Examples with Reference to Hot Arid Climates*; Shearer, W., Sultan, A. A., Eds.; United Nations University, 1986.
- (9) Knapp, R. G.; Spence, J.; Ong, A. C. *Chinese Houses: The Architectural Heritage of a Nation*; Tuttle Publishing, 2006.
- (10) Gubbi, J.; Buyya, R.; Marusic, S.; Palaniswami, M. Internet of Things (IoT): A Vision, Architectural Elements, and Future Directions. *Future Generation Computer Systems* **2013**, *29* (7), 1645–1660. <https://doi.org/10.1016/j.future.2013.01.010>.
- (11) Perera, C.; Zaslavsky, A.; Christen, P.; Georgakopoulos, D. Sensing as a Service Model for Smart Cities Supported by Internet of Things. *Transactions on Emerging Telecommunications Technologies* **2014**, *25* (1), 81–93. <https://doi.org/10.1002/ett.2704>.
- (12) Maurenbrecher, A. H. P.; Chidiac, S. E. Temperature Measurements on Brick Veneer. *Symposium A Quarterly Journal In Modern Foreign Literatures* **1995**, *1* (June), 238–251.
- (13) Ueno, K. *Analysis of Joist Masonry Moisture Content Monitoring*; 2015.
- (14) Hruby, D.; Kajnar, T.; Kepak, S.; Jaros, J.; Nedoma, J.; Fajkus, M.; Perecar, F.; Vasinek, V. Masonry Moisture Measurement Using the Distributed Temperature Sensing System. *Fiber*

Optic Sensors and Applications XIV **2017**, 10208 (April 2017), 1020814. <https://doi.org/10.1117/12.2262511>.

(15) Chang, C. Y. Study on the Correlation between Humidity and Material Strains in Separable Micro Humidity Sensor Design. *Sensors (Switzerland)* **2017**, 17 (5). <https://doi.org/10.3390/s17051066>.

(16) Agliata, R.; Bogaard, T. A.; Greco, R.; Minardo, A.; Mollo, L.; Steele-Dunne, S. C. Non-Invasive Water Content Estimation in a Tuff Wall by DTS. *Constr. Build. Mater.* **2019**, 197, 821–829. <https://doi.org/10.1016/j.conbuildmat.2018.11.250>.

(17) Jung, M.; Kim, K.; Kim, B.; Cheong, H.; Shin, K.; Kwon, O. S.; Park, J. J.; Jeon, S. Paper-Based Bimodal Sensor for Electronic Skin Applications. *ACS Appl. Mater. Interfaces* **2017**, 9 (32), 26974–26982. <https://doi.org/10.1021/acsami.7b05672>.

(18) He, T.; Shi, Q.; Wang, H.; Wen, F.; Chen, T.; Ouyang, J.; Lee, C. Beyond Energy Harvesting - Multi-Functional Triboelectric Nanosensors on a Textile. *Nano Energy* **2019**, 57, 338–352. <https://doi.org/https://doi.org/10.1016/j.nanoen.2018.12.032>.

(19) Zhang, Y.; Cui, Y. A Flexible Calligraphy-Integrated in Situ Humidity Sensor. *Measurement (Lond.)* **2019**, 147, 106853. <https://doi.org/10.1016/j.measurement.2019.106853>.

(20) Yu, Y.; Peng, S.; Blanloeuil, P.; Wu, S.; Wang, C. H. Wearable Temperature Sensors with Enhanced Sensitivity by Engineering Microcrack Morphology in PEDOT:PSS-PDMS Sensors. *ACS Appl. Mater. Interfaces* **2020**, 12 (32), 36578–36588. <https://doi.org/10.1021/acsami.0c07649>.

(21) Vuorinen, T.; Niittynen, J.; Kankkunen, T.; Kraft, T. M.; Mäntysalo, M. Inkjet-Printed Graphene/PEDOT:PSS Temperature Sensors on a Skin-Conformable Polyurethane Substrate. *Sci. Rep.* **2016**, 6 (October), 1–8. <https://doi.org/10.1038/srep35289>.

(22) Rivadeneyra, A.; Bobinger, M.; Albrecht, A.; Becherer, M.; Lugli, P.; Falco, A.; Salmerón, J. F. Cost-Effective PEDOT : PSS Temperature Sensors Inkjetted on a Bendable Substrate by a Consumer Printer. *Polymers (Basel)* **2019**, 11 (5). <https://doi.org/10.3390/polym11050824>.

(23) Kaushik, A.; Kumar, R.; Arya, S. K.; Nair, M.; Malhotra, B. D.; Bhansali, S. Organic-Inorganic Hybrid Nanocomposite-Based Gas Sensors for Environmental Monitoring. *Chem. Rev.* **2015**, 115 (11), 4571–4606. <https://doi.org/10.1021/cr400659h>.

(24) Miao, J.; Chen, Y.; Li, Y.; Cheng, J.; Wu, Q.; Ng, K. W.; Cheng, X.; Chen, R.; Cheng, C.; Tang, Z. Proton Conducting Polyoxometalate/Polypyrrole Films and Their Humidity Sensing Performance. *ACS Appl. Nano Mater.* **2018**, 1 (2), 564–571. <https://doi.org/10.1021/acsanm.7b00072>.

- (25) Wang, H.; Diao, Y.; Lu, Y.; Yang, H.; Zhou, Q.; Chrulski, K.; D'Arcy, J. M. Energy Storing Bricks for Stationary PEDOT Supercapacitors. *Nat. Commun.* **2020**, *11* (1), 1–9. <https://doi.org/10.1038/s41467-020-17708-1>.
- (26) Cornell, R. M.; Posner, A. M.; Quirk, J. P. Kinetics and Mechanisms of the Acid Dissolution of Goethite (α -FeOOH). *Journal of Inorganic and Nuclear Chemistry* **1976**, *38* (3), 563–567. [https://doi.org/10.1016/0022-1902\(76\)80305-3](https://doi.org/10.1016/0022-1902(76)80305-3).
- (27) Sidhu, P. S.; Gilkes, R. J.; Cornell, R. M.; Posner, A. M.; Quirk, J. P. Dissolution of Iron Oxides and Oxyhydroxides in Hydrochloric and Perchloric Acids. *Clays Clay Miner.* **1981**, *29* (4), 269–276. <https://doi.org/10.1346/CCMN.1981.0290404>.
- (28) Cornell, R. M.; Schwertmann, U. *The Iron Oxide Structure, Properties, Reactions, Occurrences and Uses*, 2nd ed.; WILEY-VCH Verlag GmbH & Co. KGaA: Weinheim, 2003. <https://doi.org/10.4324/9780203221815>.
- (29) Baes, C. F.; Messmer, R. E. *The Hydrolysis of Cations*; John Wiley & Sons Inc., 1976.
- (30) De Yoreo, J. J.; Gilbert, P. U. P. A.; Sommerdijk, N. A. J. M.; Penn, R. L.; Whitlam, S.; Joester, D.; Zhang, H.; Rimer, J. D.; Navrotsky, A.; Banfield, J. F.; Wallace, A. F.; Michel, F. M.; Meldrum, F. C.; Cölfen, H.; Dove, P. M. Crystallization by Particle Attachment in Synthetic, Biogenic, and Geologic Environments. *Science* (1979) **2015**, *349* (6247). <https://doi.org/10.1126/science.aaa6760>.
- (31) Frandsen, C.; Legg, B. A.; Comolli, L. R.; Zhang, H.; Gilbert, B.; Johnson, E.; Banfield, J. F. Aggregation-Induced Growth and Transformation of β -FeOOH Nanorods to Micron-Sized α -Fe₂O₃ Spindles. *CrystEngComm* **2014**, *16* (8), 1451–1458. <https://doi.org/10.1039/c3ce40983j>.
- (32) Ouyang, J.; Xu, Q.; Chu, C. W.; Yang, Y.; Li, G.; Shinar, J. On the Mechanism of Conductivity Enhancement in Poly(3,4- Ethylenedioxythiophene):Poly(Styrene Sulfonate) Film through Solvent Treatment. *Polymer (Guildf)* **2004**, *45* (25), 8443–8450. <https://doi.org/10.1016/j.polymer.2004.10.001>.
- (33) Stavytska-Barba, M.; Kelley, A. M. Surface-Enhanced Raman Study of the Interaction of PEDOT: PSS with Plasmonically Active Nanoparticles. *Journal of Physical Chemistry C* **2010**, *114* (14), 6822–6830. <https://doi.org/10.1021/jp100135x>.
- (34) Wang, Y.; Zhu, C.; Pfattner, R.; Yan, H.; Jin, L.; Chen, S.; Molina-Lopez, F.; Lissel, F.; Liu, J.; Rabiah, N. I.; Chen, Z.; Chung, J. W.; Linder, C.; Toney, M. F.; Murmann, B.; Bao, Z. A Highly Stretchable, Transparent, and Conductive Polymer. *Sci. Adv.* **2017**, *3* (3), 1–11. <https://doi.org/10.1126/sciadv.1602076>.
- (35) Dunst, K. J.; Trzciński, K.; Scheibe, B.; Sawczak, M.; Jasiński, P. Study of the NO₂ Sensing Mechanism of PEDOT-RGO Film Using in Situ Raman Spectroscopy. *Sens. Actuators B Chem.* **2018**, *260* (2), 1025–1033. <https://doi.org/10.1016/j.snb.2018.01.089>.

- (36) D'Angelo, J. G.; Kumar, A.; Onorato, A.; Delude, C. J.; Sotzing, G. A.; Smith, M. B. Chemical Stability of Conducting Polymers: Friedel-Crafts Reactions of Alcohols with Poly(3,4-Ethylenedioxythiophene) (PEDOT). *Polymer (Guildf)* **2007**, *48* (15), 4328–4336. <https://doi.org/10.1016/j.polymer.2007.05.051>.
- (37) Goktas, H.; Wang, X.; Ugur, A.; Gleason, K. K. Water-Assisted Vapor Deposition of PEDOT Thin Film. *Macromol. Rapid Commun.* **2015**, *36* (13), 1283–1289. <https://doi.org/10.1002/marc.201500069>.
- (38) Mueller, M.; Fabretto, M.; Evans, D.; Hojati-Talemi, P.; Gruber, C.; Murphy, P. Vacuum Vapour Phase Polymerization of High Conductivity PEDOT: Role of PEG-PPG-PEG, the Origin of Water, and Choice of Oxidant. *Polymer (Guildf)* **2012**, *53* (11), 2146–2151. <https://doi.org/10.1016/j.polymer.2012.03.028>.
- (39) Fabretto, M.; Zuber, K.; Hall, C.; Murphy, P.; Griesser, H. J. The Role of Water in the Synthesis and Performance of Vapour Phase Polymerised PEDOT Electrochromic Devices. *J. Mater. Chem.* **2009**, *19* (42), 7871–7878. <https://doi.org/10.1039/b912324e>.
- (40) Kjonaas, R. A.; Riedford, B. A. A Study of the Lucas Test. *J. Chem. Educ.* **1991**, *68* (8), 704–706. <https://doi.org/10.1021/ed068p704>.
- (41) Ziman, J. M. *Electrons and Phonons: The Theory of Transport Phenomena in Solids*; Mott, N. F., Bullard, E. C., Wilkinson, D. H., Eds.; Clarendon Press: Oxford, 1960.
- (42) Kittel, C. *Introduction to Solid State Physics*, 8th ed.; Johnson, S., Ed.; John Wiley & Sons, Inc.: New York, 1953.
- (43) Ward, M. R. *Electrical Engineering Science*; McGraw-Hill: New York, 1971; pp 36–40.

Chapter 5: Solution Processing of Sub-micron Poly(3,4-ethylenedioxythiophene) Particles

Previous chapters extensively discussed the rust-based vapor-phase polymerization of conducting polymers and applying the synthetic strategy to various substrates. However, a major limitation of this technique is the mass transport of reactants through diffusion (passive transport). In this chapter, I present an aerosol-based vapor-phase synthesis that actively transports reactant by pushing the vapors and droplets with a carrier gas. I also present my work on overcoming challenges in solution processing of nanostructured conducting polymer particles.

5.1 Introduction

Conducting polymers possess unique electronic, ionic, and optical properties with potential for advancing the next generation of bioelectronics,^{1,2} energy harvesting/storage electrodes³⁻⁵ and electrochemical catalysts.⁶⁻⁸ Unfortunately, the recalcitrant insolubility for the vast majority of conducting polymers remains a challenge stifling the development of current and future applications. Among conducting polymers, poly(3,4-ethylenedioxythiophene) polystyrene sulfonate (PEDOT:PSS) is a solution processable exception commonly purchased as a water-based formulation⁹ suitable for ink-jet printing¹⁰, drop casting and spin coating.^{11,12} A major limitation for PEDOT:PSS stems from its incompatibility with organic solvents leading to coatings that readily delaminate from untreated hydrophobic substrates such as 3D-printed thermoplastics. An alternative to processing a solution-based formulation is found by dispersing conducting polymer particles as colloids;¹³ however, few reports in the literature discuss the

synthesis and optimization of solution processable conductive PEDOT particles.^{14–16} Here, we present a continuous aerosol synthesis that produces submicron PEDOT particles of low electrical resistance ($4.2 \pm 0.5 \Omega$). Particles synthesized via this method is processable in organic solvents, resulting in a stable dispersion (surfactant is unnecessary) that conformally coats untreated 3D-printed thermoplastics. A particle-based coating is robust, electrically conductive (1 k Ω /cm) and enables engineering of stretchable resistive sensors. Moreover, PEDOT coatings are highly photothermally active because PEDOT's charge carriers absorb light in the near-infrared (NIR) region. Exposing a coating to a 5 second laser pulse (808 nm, 0.8 mW/cm²) raises its temperature to 194.5 °C, the highest reported among PEDOT coatings,^{17,18} with the potential for light-induced surface sterilization applications.

This chapter is adapted from a previous publication and was coauthored with Dr. Yang Lu.¹⁹

5.2 Materials and Methods

Iron(III) chloride (reagent grade, 97%), ethanol (200 proof, anhydrous) and 3,4-ethylenedioxythiophene (EDOT, 97%) were purchased from Sigma Aldrich and used without further purification. Ultrapure water was obtained from a Millipore filter (18.2 M Ω). 3D printing filaments were purchased from eSUN (PLA and PETG, brand name: Inland) and Ninjiatek (TPU, brand name: NinjaFlex). Conductive PLA filaments were purchased from Proto-Pasta.

Particle Synthesis and Purification

A straight Vigreux tube with 60 cm in length and 2.54 cm in diameter was held vertically as the reactor and heated to 130 °C; the finger indentations inside the glass reactor disturbed the gas streams for a better reactant mixing. Iron(III) chloride aerosol generated via a 1.7 MHz ultrasonic

transducer was carried by a 125 sccm (standard cubic centimeter) N₂ flow, and 3,4-ethylenedioxythiophene (EDOT) vapor generated via bubbling the liquid was carried by a 75 sccm N₂ flow. Liquid EDOT was in a 50 mL three-neck flask so that addition of reactant was continuous. The reactor was heated to 130 °C while the EDOT monomer temperature was 50 °C. Particles were collected as dispersion by directing aerosol flow through three ethanol-filled scrubbing bottles connected in series.

Solvent removal of collected PEDOT in ethanol dispersion was carried out in a rotary evaporator at 50 mL aliquots. The remaining dispersion was subsequently purified by centrifuging in 50% 1 M hydrochloric acid and 50% ethanol until the supernatant became colorless or light blue. Hydrochloric acid removed any iron from particles and doped the polymer. The purified dispersion was lyophilized resulting in a blue colored powder.

Spectroscopic Characterization

Scanning electron microscopy and energy-dispersive X-ray spectroscopy data were collected using a JEOL 7001LVF FESEM and a Thermo Fisher Quattro S ESEM, respectively. Samples were prepared via dispersing PEDOT particles in water and drop-casting on gold-coated polyimide tape. Optical microscopy images were collected using a Nikon microscope (NIKON Eclipse, LV100ND) fitted with a Nikon Ds-Ri2 camera. Powder X-ray diffraction spectra were collected using a Bruker d8 advance X-ray diffractometer at room temperature, with a Cu K α radiation source ($\lambda = 1.5406 \text{ \AA}$) and LynxEyeXE detector, operating at 40 kV and 40 mA. Dry sample powders were cast onto a zero-intensity silicon wafer and the sample holder was rotated at 30 rpm/min with a scan step of 0.02°. Ultraviolet-visible-near infrared spectra were collected

on a Cary 5000 UV-Vis-NIR spectrophotometer using a parallel liquid cell. Solid powders were dispersed in 1 M HCl aqueous solutions via bath sonication and the spectra were immediately collected to minimize the effect of particle precipitation; data was collected in a quartz cuvette. Each measurement requires a small amount of sample (< 1 mg) allowing for batch processing.

Electrochemical and Thermogravimetric Characterizations of PEDOT Particle Electrodes

The electrochemical set-up consisted of a PEDOT particle working electrode, an Ag/AgCl reference electrode, a platinum mesh counter electrode, and aqueous 1 M H₂SO₄ electrolyte. Cyclic voltammograms were collected using a BioLogic VMP3 multipotentiostat. The active mass of the working electrode was determined via thermogravimetric analysis using a Discovery TGA (TA Instruments). The cycled electrode was rinsed thrice using water and dried in air at 25 °C before loading onto the sample pans (high temperature Pt pans). The ramping recipe consisted of two steps 1) 50 °C to 110 °C at 20 °C/min then maintained at 110 °C for 5 min to evaporate free water and 2) 110 °C to 500 °C at 15 °C/min then maintained at 500 °C for 30 min to burn off all the active materials (Figure 5.1a). Total mass loss of the second step were the total mass of PEDOT and PLA because both PEDOT and PLA were fully degraded before temperature reaches 500 °C, while the mass loss of carbon paper was negligible (Figure 5.1b). Air was required to fully burn off all active materials on the carbon paper; if N₂ was used, residual active materials would remain in the electrode resulting in inaccurate mass determination (Figure 5.1c-f).

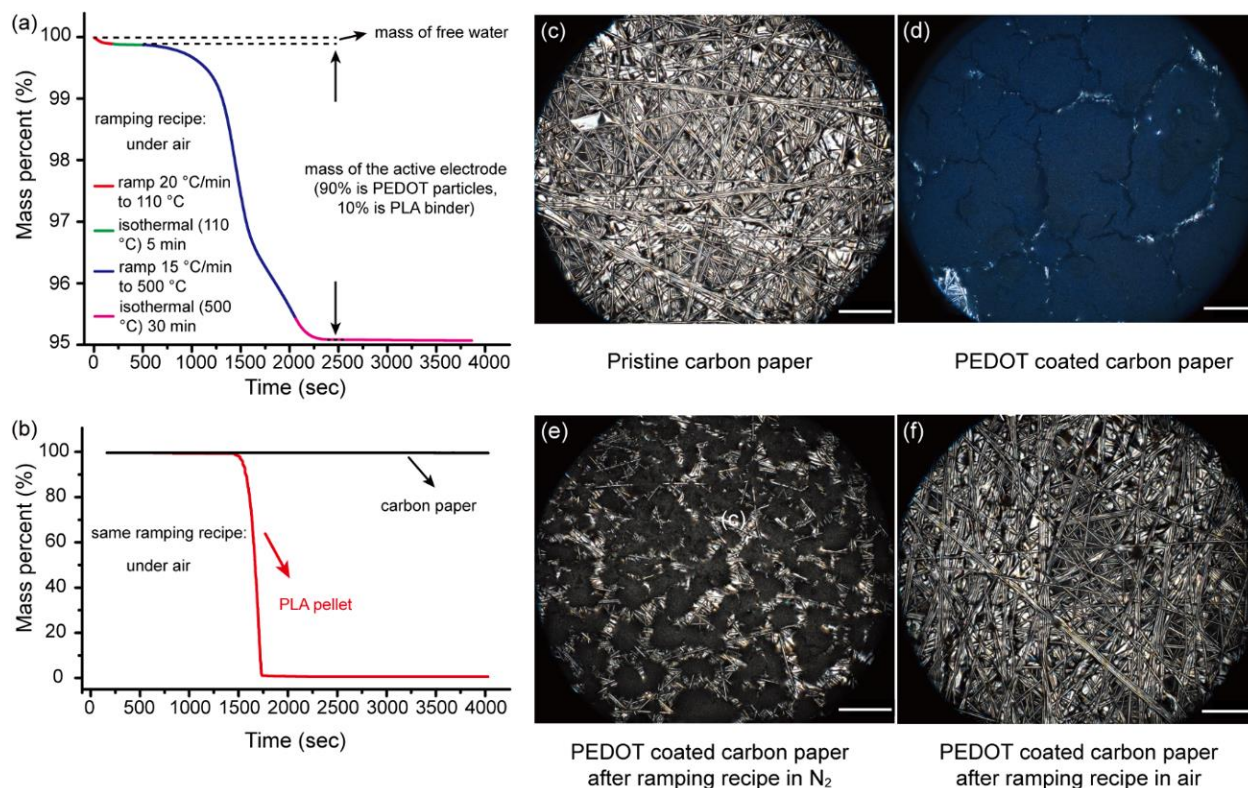


Figure 5.1 Thermogravimetric analysis of PEDOT particle electrode. a) A typical thermogravimetric analysis of PEDOT-PLA-coated carbon paper electrode. The ramping recipe consisted of four steps where the first two removed the mass of free water and the rest two steps removed the mass of PEDOT and PLA. The active PEDOT mass was 90% of this overall mass due to the electrode preparation formulation. b) Thermogravimetric analysis of pure carbon paper and PLA pellets using the same ramping recipe. Carbon Paper exhibits a negligible mass change because degrading temperature of carbon was higher than 700 °C in air and PLA were burnt off completely at temperature ~ 350 °C, similar to the PEDOT degradation temperature. Air was needed to conduct the thermogravimetric analysis otherwise there will be residue mass of PEDOT leading to error in mass determination. c) –f) were optical micrographs showing that when ramping the thermogravimetric analysis with only N₂, PEDOT particles were incomplete leading to residues on the carbon paper while running the same recipe under air resulted in a cleaned-up carbon paper.

Paint Formulations and Functionalized 3D-printed Objects

Organic paint formulation for thermoplastics consisted of 33 wt% PEDOT particles, 67 wt% polycaprolactone and 1 mL trifluoroethanol (per 100 mg solids). All components were mixed using bath sonication for 1 h and were brush painted onto 3D prints to form the coating. Organic paint formulation for carbon paper electrode consisted of 90 wt% PEDOT particles, 10 wt%

polylactic acid and 1 mL chloroform. All components were thoroughly mixed using bath sonication for 1h, and a PEDOT particle electrode was fabricated by drop-casting 50 μ L of the dispersion onto a piece of carbon paper (1.5 cm \times 1 cm). 3D-printed objects were designed in Rhino or downloaded from the open-source website www.thingiverse.com and were sliced using the software Simplify 3D. Makergear M2 was used as the FDM based 3D printer.

An 808 nm laser was used as the NIR source, and an IR camera (ICI 7320 USB camera) was used to monitor temperature. An aluminum foil was placed under the samples as background due to its low infrared light absorbance.

5.3 Results and Discussion

PEDOT Particles of High Electrical Conductivity

PEDOT particles are synthesized when a stream of aerosolized aqueous FeCl_3 droplets reacts with EDOT vapor inside a flow reactor (Figure 5.2a). The reactor is optimized from a previous publication to achieve continuous polymerization (details in materials and methods) within 1 min of residence time.^{20,21} Particles are collected in ethanol-filled scrubbing bottles, then purified and dried, resulting in a powder (Figure 5.2b) comprised of spherical particles (Figure 5.2c and Figure 5.3) readily dispersible in water (Figure 5.2c inset). Electrical resistance, measured by pressing particles over a 1 mm gap electrode (Figure 5.4), is the lowest reported among PEDOT particles ($4.2 \pm 0.5 \Omega$). A pressed pellet enhances probe contact facilitating I-V measurements that result in linear curves with ohmic window ranging between -2 V and 2 V. The slope increases upon exposure to HCl vapor (Figure 5.2d).

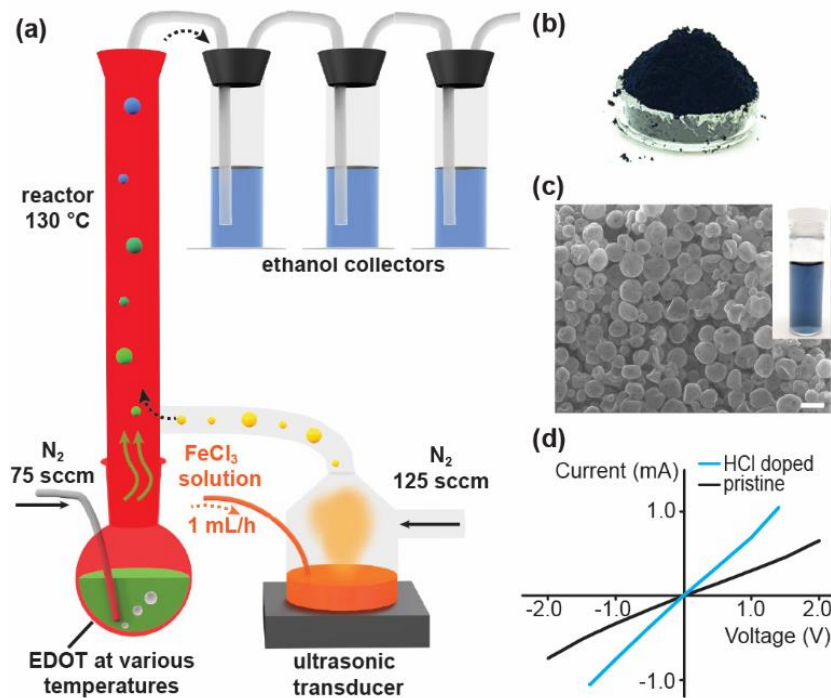


Figure 5.2 (a) Flow process diagram of aerosol vapor-phase polymerization reactor. (b) Purified and lyophilized particles are collected as a powder. (c) Scanning electron micrograph of spherical and discrete PEDOT particles (scale bar is 1 μm); inset shows particles dispersed in water. (d) Current-voltage curves demonstrate ohmic behavior and a steeper slope (blue curve) for HCl vapor doped particles.

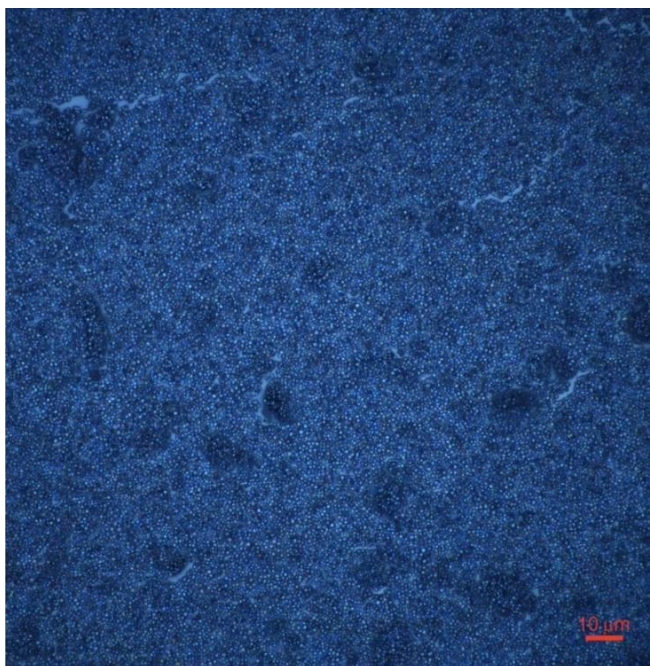


Figure 5.3 An optical micrograph of PEDOT particles (drop-casted on a glass slide) showing spherical shape.

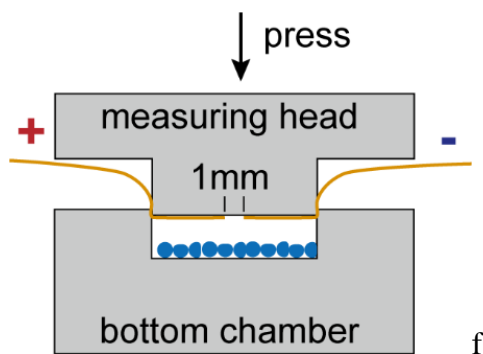


Figure 5.4 Schematic diagram of a 3D-printed gap electrode for measuring electrical resistance. In each measurement, 10 mg PEDOT particles are weighed and casted into the bottom chamber, where the measuring head was pressed against using a certain weight. The electrodes were two copper tapes with a separation of 1 mm and a multimeter was used to measure the resistance.

During synthesis, oxidative doping imparts electrical conductivity to the polymer chains by introducing mobile charge carriers (polarons, bipolarons).²² According to the Drude model ($\sigma = qn\mu$),²³ high electrical conductivity is achieved when charge carrier concentration (n) and mobility (μ) are maximized (q is a unit charge). In order to achieve high electrical conductivity, a polymer's molecular structure must possess 1) long conjugation length to accommodate a high concentration of charge carriers (doping level)^{24,25} and 2) ordered chain packing (crystallinity) enabling high mobility of charge carriers.²⁶ The oxidative radical polymerization of conducting polymers follows a step-growth mechanism,^{25,27} and concomitant oxidative doping takes place after each chain coupling.²⁵ Therefore, synthetic conditions are of paramount importance for controlling a polymer's molecular structure and its electrical properties. Our synthesis requires 1) aerosolization of oxidant (FeCl_3 solution) and 2) vaporization of liquid monomer (EDOT), the former is achieved using an ultrasonic transducer and the latter by heating a nitrogen pushed bubbler.²⁰ The product that flows out of the aerosol reactor is comprised of a mixture of PEDOT particles, unreacted liquid oxidant droplets, monomer vapor and byproducts (reduced oxidant or EDOT oligomers).

Particles collected in the ethanol dispersion show a blue color, characteristic of doped PEDOT. The color of ethanol also changes due to excess oxidant (yellow) or excess monomer (purple) (Figure 5.5). The morphology of washed particles also varies as the ratio between EDOT and Fe^{3+} changes. The synthesized particles are perforated spheres when the reactor contains a much higher concentration of EDOT than Fe^{3+} . Shriveled/walnut-shape particles form when excess Fe^{3+} is present in the reactor (Figure 5.6). The crystallinity, doping levels and electrical resistance of PEDOT particles is studied as a function of stoichiometry by varying the EDOT to Fe^{3+} ratio (0.25, 1, 5, 9, 20) using samples labeled PEDOT (1:4), PEDOT (1:1), PEDOT (5:1), PEDOT (9:1) and PEDOT (20:1), respectively. Polymer crystallinity is examined via powder X-ray diffraction (XRD), a fast and nondestructive technique.^{28,29} All XRD patterns exhibit three peaks (characteristic of PEDOT)³⁰ where the first two ($2\theta = 6.5^\circ$ and $2\theta = 12.8^\circ$) represent edge-on packing for (100) and (200) planes, respectively (interplanar distance = 1.32 nm). The third peak ($2\theta = 25.9^\circ$), due to face-on π - π stacking of (020) plane, exhibits a d-spacing (0.41 nm) smaller than that of a single crystalline PEDOT nanowire.²⁶ This short π - π distance facilitates high charge mobility²³ leading to high electrical conductivity in the particles. The packing of polymer chains is independent of stoichiometry as demonstrated by negligible difference in the number and position of XRD peaks (Figure 5.7a). PEDOT particles possess higher crystallinity than those synthesized from solution phase^{21,31,32} due to size-constrained polymerization at the micron-sized aerosol droplet's surface facilitating π - π stacking.²⁶

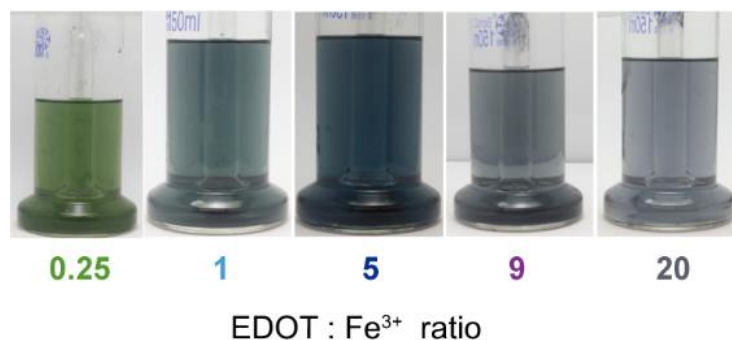


Figure 5.5 Photos of collected liquid dispersion from various EDOT: Fe³⁺ ratios during synthesis. A light blue color indicated the optimized synthesis with an equal concentration of both reactants. Greenish or yellowish color indicated excess oxidant while purplish color indicated excess monomer.

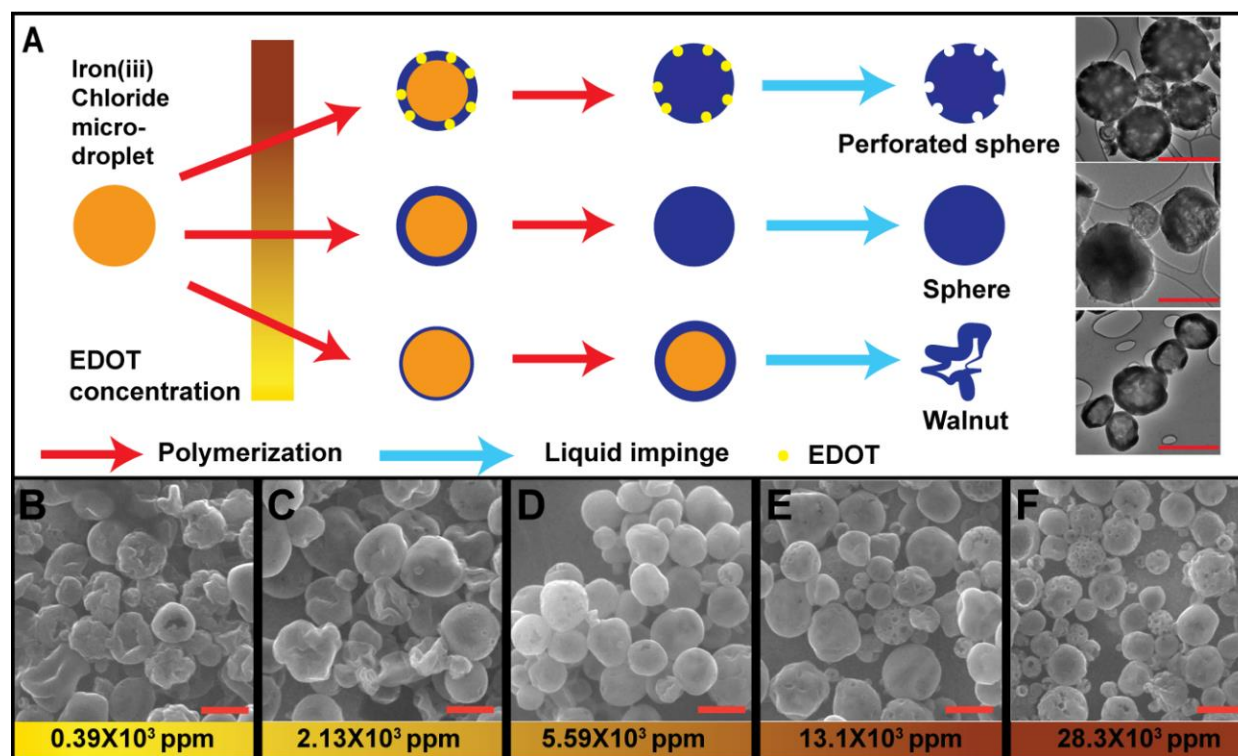


Figure 5.6 Morphology evolution of PEDOT particles with different EDOT to Fe³⁺ ratios. a) iron(III) chloride microdroplets, when react with different concentration of EDOT vapor, undergo different routes of morphology evolution, resulting in different morphologies. A TEM image is present in accordance with each route. All scale bars are 1 μ m. (b-f), representative scanning electron micrographs of PEDOT with different EDOT to Fe³⁺ ratio synthesis. All scale bars are 1 μ m.

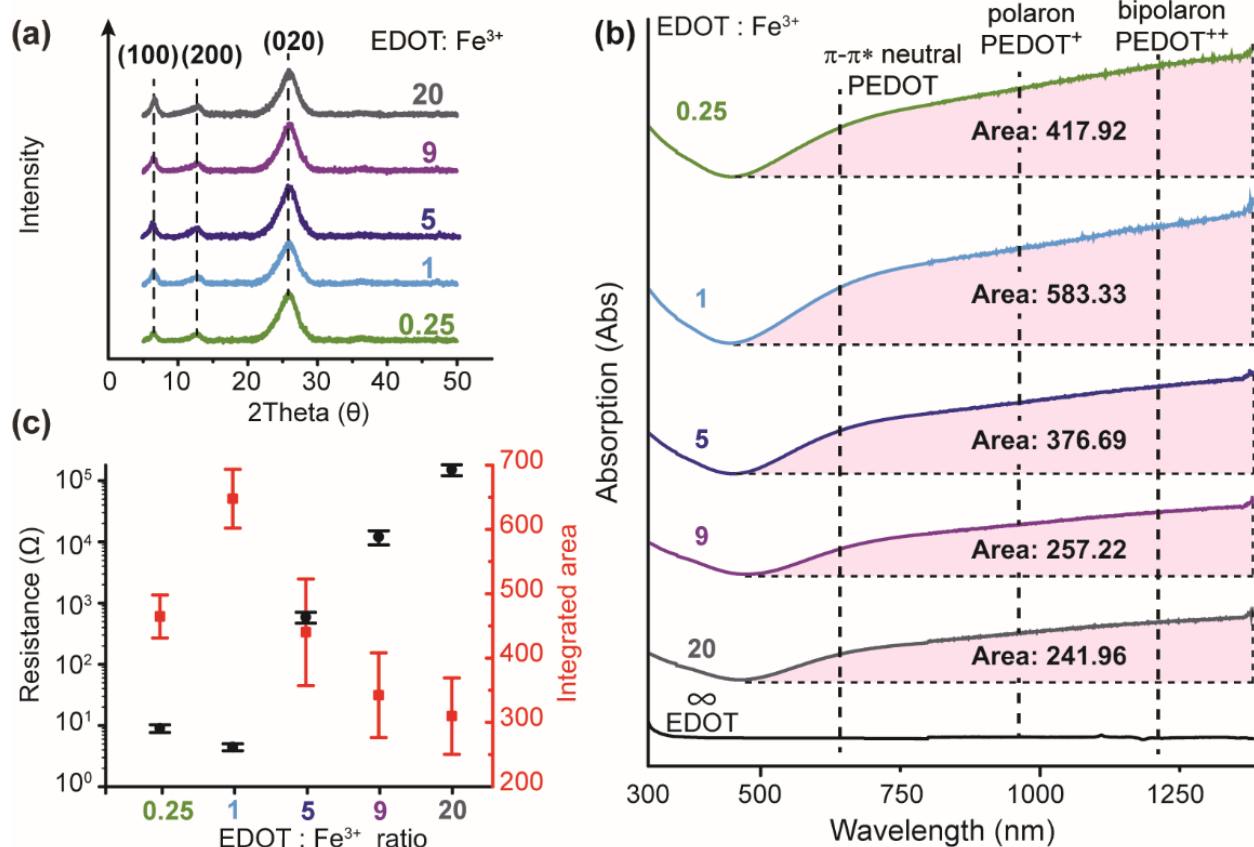


Figure 5.7 (a) Powder X-ray diffraction patterns for PEDOT particles synthesized under varying EDOT to Fe³⁺ ratios. (b) UV-Vis-NIR spectra for PEDOT particles synthesized under varying EDOT to Fe³⁺ ratios and EDOT monomer. (c) Plot shows electrical resistance is inversely proportional to the UV-Vis-NIR integrated area under the curve (450 nm – 1370 nm).

The doping level of PEDOT particles is quantitatively probed via UV-Vis-NIR absorption spectroscopy. Particles are doped in a 1 M HCl solution (0.1 mg/mL) to eliminate variations in the spectra due to unlevelled protonic doping.²⁰ Results show that EDOT to Fe³⁺ ratio controls the area-under-the-curve in the free charge carrier region (450 nm – 1370 nm) (Figure 5.7b). This region is chosen because it maximizes the signal-to-noise ratio. The integrated area-under-the-curve (baseline against lowest point on a spectrum) exhibits an inverse and proportional relationship with PEDOT's electrical resistance (measured using a 1 mm gap-electrode) (Figure 5.7c) due to polaronic and bipolaronic charge carriers. A larger area corresponds to a greater

charge carrier concentration based on Beer-Lambert law³³ resulting in lower electrical resistance. Neutral π - π^* is not considered a charge carrier in PEDOT chains,²² but it aids in determining the extent of conjugation because the spectrum for EDOT lacks π - π^* transitions, as well as polarons and bipolarons (Figure 5.7b bottom curve). Therefore, a magnitude of 500 for the integrated area-under-the-curve in the free charge carrier region serves as an indicative test for selecting PEDOT batches of high conductivity.

PEDOT Particle-based Coatings on Carbon Fiber Paper

Carbon fiber paper is an ideal substrate for electrochemical applications and PEDOT particles produce robust coatings on carbon substrates when formulated using chloroform (solvent) and polylactic acid (ion-permeable binder).⁵⁰ An electroactive and mechanically robust particle-based coating on carbon fiber paper is comprised of 10 wt% particle loading, and the working electrode is fabricated via drop-casting. A three-electrode configuration is employed for measuring the gravimetric capacitance (details in materials and methods), and a quasi-rectangular cyclic voltammogram (25 mV/s) reveals the capacitive behavior of PEDOT particles with negligible contribution from carbon paper (Figure 5.8a).^{51,52} Redox peaks at 0.4V (vs. Ag/AgCl) likely stemming from residual iron species diminish as the scan rate increases to 1000 mV/s because faradaic processes occur faster in PEDOT than in iron species.⁵² PEDOT (1:1) sample possesses the highest gravimetric capacitance (80 F/g at 25 mV/s) and the lowest electrical resistance among all samples (Figure 5.8b) and represents the state-of-the-art among reported PEDOT particle-based electrodes.^{53,54}

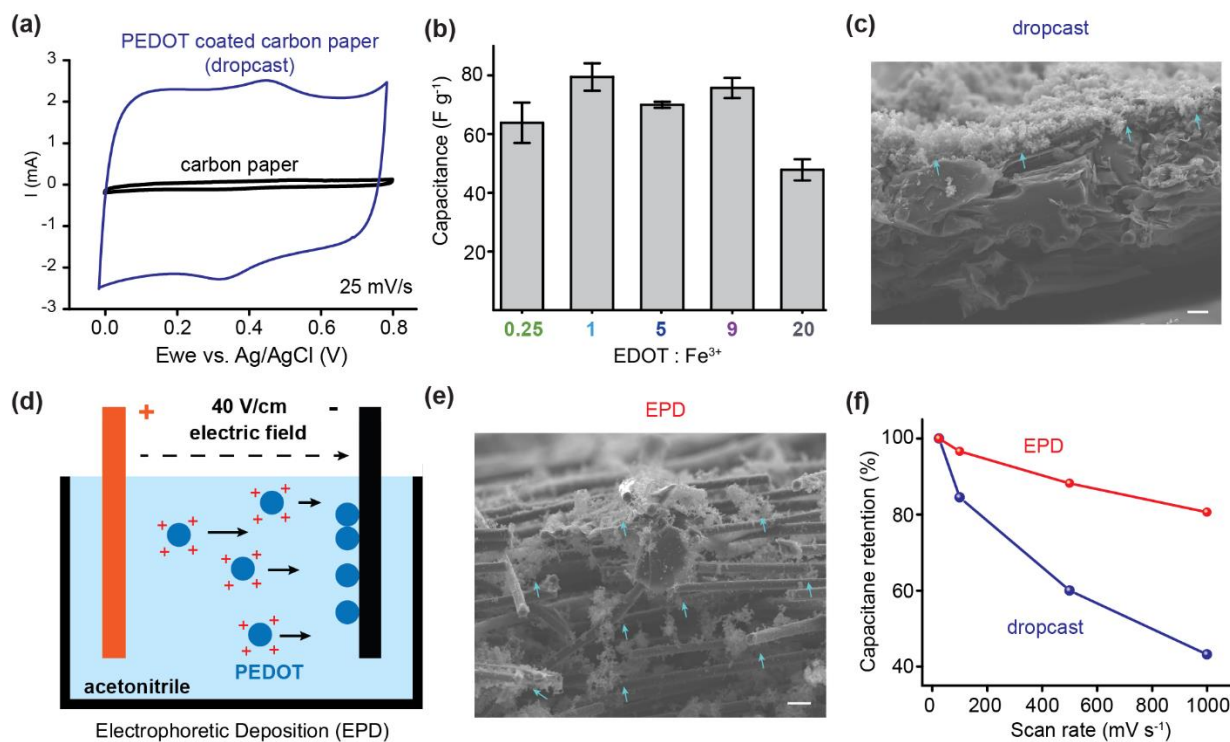


Figure 5.8 (a) Cyclic voltammograms of carbon paper and PEDOT particle-coated carbon paper produced via drop-casting (electrode). (b) Specific capacitance plot for electrodes produced using particles synthesized from various EDOT to Fe³⁺ ratios (calculated from cyclic voltammograms at 25 mV/s). (c) Cross-sectional scanning electron micrograph for an electrode fabricated via drop-casting (blue arrows indicate particles, scale bar = 10 μm). (d) Illustration of electrophoretic deposition. (e) Cross-sectional scanning electron micrograph for an electrode fabricated via electrophoretic deposition shows particles integrated within carbon fibers (blue arrows indicate particles, scale bar = 10 μm). (f) Capacitance retention plot compares electrodes fabricated via electrophoretic deposition versus drop-casting.

Fabricating electrodes via drop-casting presents two drawbacks: 1) particles aggregate on the carbon paper surface (Figure 5.8c) and 2) an insulating binder is required for immobilizing particles. Both stifling features are detrimental to charge transport between the polymer and current collector,⁵⁵ causing the cyclic voltammogram to shrink to a fusiform shape with a 55% capacitance loss when the cycling rate increases to 1000 mV/s (Figure 5.9a and b). Electrophoresis is a deposition technique that overcomes the challenges in drop-casting by obviating the need for insulating binders. In electrophoretic deposition, an electrical field is applied across a colloidal dispersion allowing positively charged particles to migrate to the

negative substrate. As a result, a stable coating is formed and able to undergo repeated electrochemical cycling.⁵⁵ Electrophoretic deposition at 40 V/cm is utilized to deposit positively charged particles to fabricate a working electrode, and a porous carbon paper serves as current collector (PEDOT (1:1) sample, dispersed in acetonitrile, 1 mg/mL) (Figure 5.8d). A homogeneous particle coating is deposited throughout the porous carbon current collector (Figure 5.8e) facilitating facile charge transport at the interface. Moreover, small capacitance loss (<20%) (Figure 5.8f), with a quasi-rectangular cyclic voltammogram (collected from 25 mV/s to 1000 mV/s) (Figure 5.9c), indicates a high rate performing electrode.

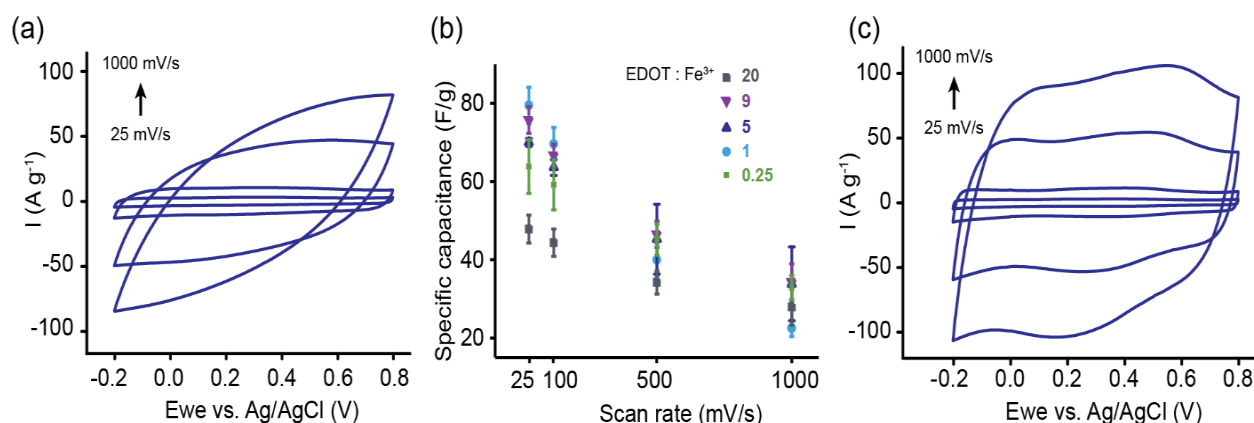


Figure 5.9 Electrochemical performance comparison between a drop-casted electrode and an electrophoretic deposited electrode. a) Representative cyclic voltammogram of electrodes fabricated by drop-casting at different scan rate. b) Specific capacitance with respect to scan rate of different EDOT to Fe³⁺ ratio. c) Representative cyclic voltammogram of electrodes fabricated by EPD at different scan rate.

Challenges in Fabricating Electrically Conductive 3D-printed Objects

Expanding the functionalities of 3D-printed objects beyond their basic structural functions gains importance as 3D printing becomes a popular method of manufacturing.³⁴ A common form of 3D printing, fused deposition modeling (FDM), is inexpensive and works with varying levels of resources, as it can be implemented at the household level.³⁵ FDM's accessibility means it has

the capacity to make societal impacts across disciplines, especially with the production of 3D-printed objects with high electrical conductivity. The exploration of electronic and thermal capabilities in 3D-printed materials is of paramount importance for developing applications ranging from energy storage to biotechnologies. Notably, 3D printing is used to create custom, patient-specific medical constructs, such as hearing aids and prosthetics, and to fabricate electrochemical energy storage devices such as batteries and capacitors.^{36,37} However, 3D printing objects from commercially conductive filaments has limitations. Conductive filaments typically consist of carbon, which can be tough on the typically soft nozzles used in FDM printers.³⁸ Aside from FDM, other methods for 3D printing electronics have their own limitations. For example, the use of surface direct write techniques to print with conductive filaments can require expensive equipment, the printers can get clogged, and the 3D printing capacity of the technology that tries to circumvent those clogging issues is often limited.³⁹ Freeform 3D printing techniques using conductive metal filaments and inks necessitate high-temperature sintering; or exist in a liquid form which limits their practicality in application.³⁹ Conformally coating untreated 3D-printed thermoplastics with functional and robust film or paint is needed to impart electrically conductivity and provide a viable alternative to conductive commercial filaments.

PEDOT Particle-based Coatings on Untreated Thermoplastics

To produce a homogeneous conductive coating on untreated 3D-printed thermoplastics (Figure 5.10a), such as polylactic acid (PLA), polyethylene terephthalate glycol (PETG) and thermoplastic polyurethane (TPU), a paint formulation comprised of PEDOT particles, trifluoroethanol (solvent) and polycaprolactone (thickener) is developed. The formulation

obviates the need for a primer because trifluoroethanol partially dissolves the thermoplastic resulting in strong particle adhesion to a 3D-printed object.⁴⁰ Trifluoroethanol's moderate evaporation rate (vapor pressure of 7 kPa at 20 °C)⁴¹ facilitates deposition of PEDOT and prevents particles from agglomerating during drying (Figure 5.10b).⁴² PEDOT coating is conformal (Figure 5.10c), and particles remain adhered after repeated scotch tape tests (Figure 5.10d) whereas a PEDOT:PSS produces a non-conformal coating that readily delaminates from the surface of a 3D-printed object after drying (Figure 5.11). At 20 wt% particle loading a percolation network is achieved and the coating becomes conductive,⁴³ while a 30 wt% particle loading (PEDOT:polycaprolactone volume ratio of 1:2), produces a 1 k Ω electrical resistance (measured via two-point technique with a 1 cm gap) (Figure 5.10e). Increasing the loading beyond 30 wt% induces cracks during drying and results in a partially insulating coating. The electrical resistance measured is lower than that of a 3D-printed object produced from a commercial conductive 3D printing filament (1.8 k Ω). Moreover, applying an organic particle paint obviates the issues of nozzle cracking and low printing fidelity that often accompany 3D printing with a conductive filament laden with carbon particles.^{44,45}

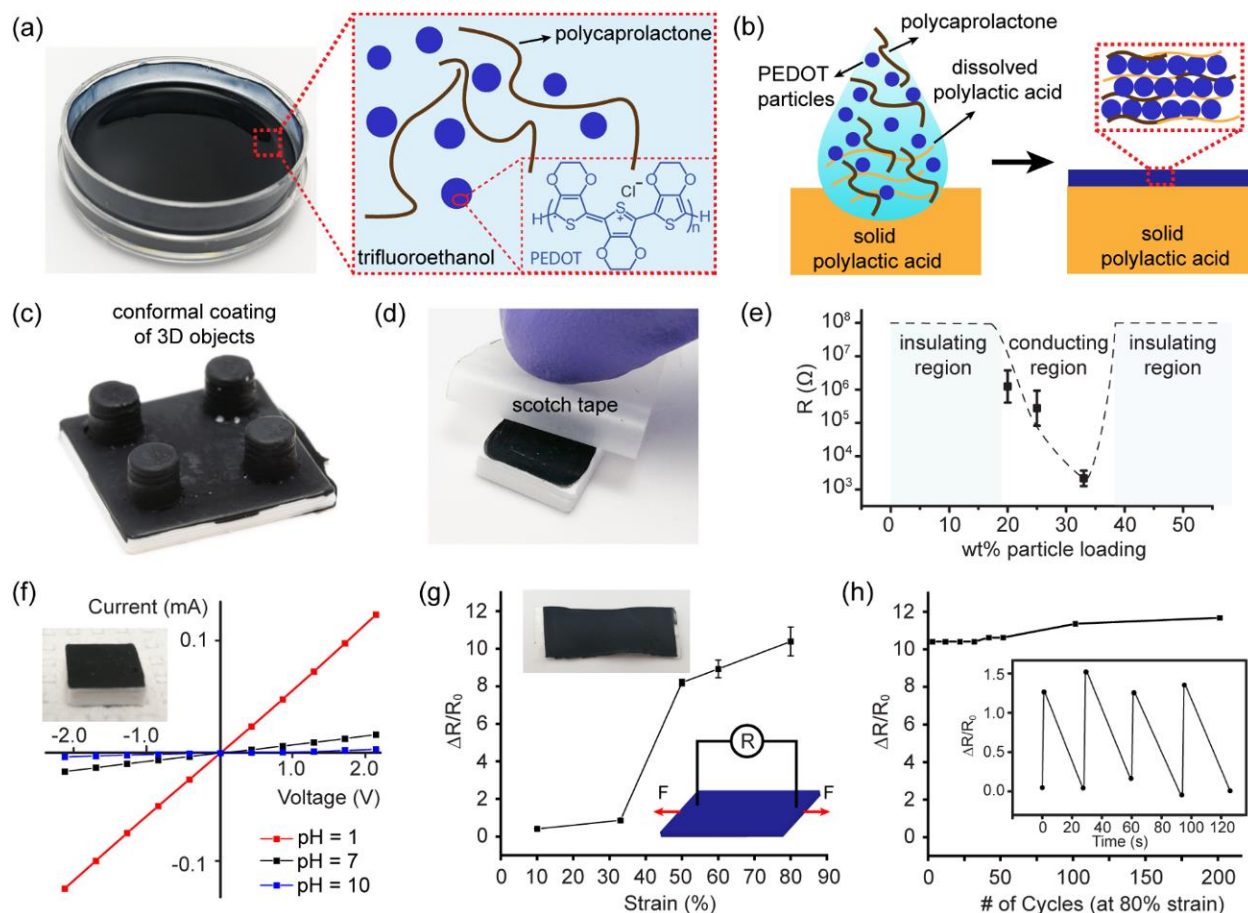


Figure 5.10 (a) Photo of a PEDOT particle-based dispersion and illustration of its composition. (b) Diagram shows dissolution of polylactic acid surface and formation of a coating. (c) Conformal coating on a 3D-printed object is (d) impervious to delamination after repeated Scotch tape tests. (e) Plot of a coating's two-point electrical resistance versus particle mass loading. (f) Particle-coated thermoplastic poly(lactic acid) block (inset) exhibits linear I-V curves after exposure to vapors of different pH. (g) Resistance versus strain plot for a particle-coated thermoplastic polyurethane film (top inset) serving as a strain sensor (bottom inset). (h) Strain sensor is stable over 200 cycles (inset shows hysteresis profile).

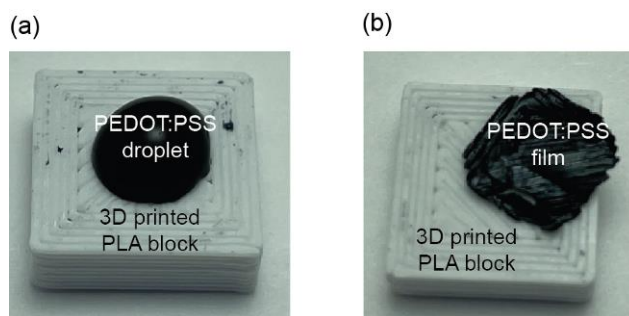


Figure 5.11 Photos of PEDOT:PSS paint on 3D-printed thermoplastics. a) A droplet of PEDOT:PSS beaded up on the hydrophobic surfaces. b) The PEDOT:PSS coating delaminated after drying.

Coating a 3D-printed object with PEDOT particle paint enables engineering of a chemically resistive pH sensor. PEDOT particles are sensitive to pH changes, acidic pH lower PEDOT's resistance due to protonic doping⁴⁶ while bases increase its resistance due to dedoping.⁴⁷ Changes in electrical resistance are measured using a two-point current-voltage technique after exposure to acid (HCl) or base (NH₄OH) vapors (Figure 5.10f inset); a linear correlation with the steepest slope corresponding to the lowest electrical resistance is obtained from exposure to HCl vapor (pH = 1) (Figure 5.10f).

A particle-based formulation also enables engineering of a strain sensor when applied as a coating to an untreated 3D-printed stretchable polyurethane substrate (Figure 5.10g top left inset). Electrical resistance is measured during repeated stretch-release cycles using a multimeter (Figure 5.10g bottom right inset). The relative resistance change ($\Delta R/R_0$) is highly reproducible within a wide strain range (0%-80%) and comparable to that of a strain sensor fabricated from silver nanowires, reduced graphene oxide and polyurethane.⁴⁸ $\Delta R/R_0$ follows an approximately linear trend that increases with greater strain (Figure 5.10g). A sharp jump in slope is observed when strain rises from 33% to 50% due to the formation of cracks (Figure 5.12) that disrupt the conductive percolation network. The measurement is reproducible because PEDOT particles strongly adhere to polyurethane surfaces and the conductive percolation network is restored once the polyurethane returns to its original shape.⁴⁹ The strain sensor is stable for up to 200 cycles (at 80% strain) (Figure 5.10h). Interestingly, the coating also enables monitoring of strain sensor hysteresis exhibiting a ~20 second delay when returning to its original shape after experiencing 33% strain (Figure 5.10h inset).

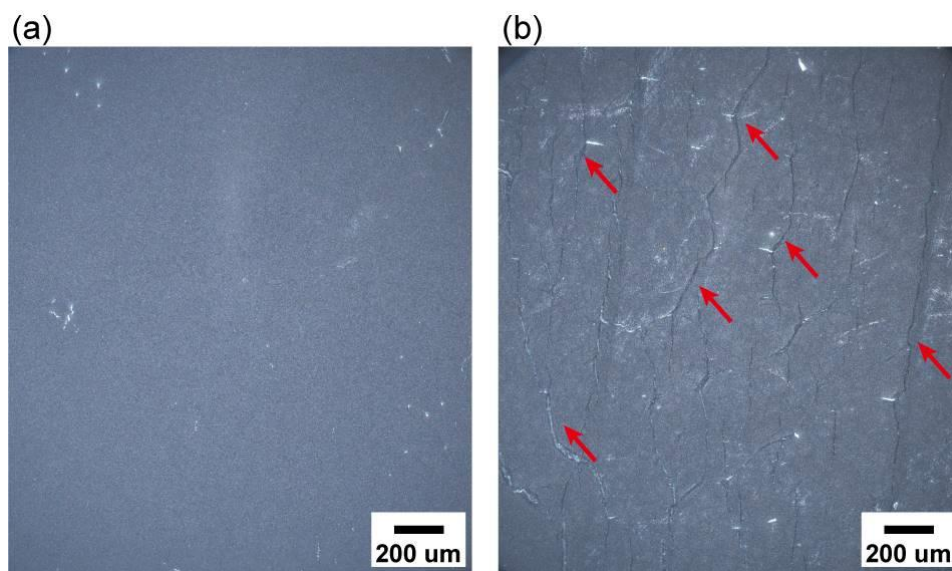


Figure 5.12 Optical micrographs of PEDOT particle coated TPU strain sensor. a) PEDOT particles were homogenous on TPU film before stretch-releasing test. b) After stretch-release tests, a lot of cracks (pointed by red arrows) were observed on the film. Note that measurements were still reproducible because particles were well adhered to base TPU.

Particle Coatings with High Photothermal Activity

A PEDOT particle-based coating is photothermally active in the near-infrared region. After a 5-second laser exposure (808 nm laser, 0.8 W/cm^2 power density) (Figure 5.13a), a free-standing PEDOT particle-polycaprolactone composite film (24°C) heats up to 218.5°C . This temperature rise (194.5°C) is higher than that of a Norit carbon/polycaprolactone composite film (124°C) or PEDOT:PSS film (9.7°C). PEDOT particles are the major contributor to the temperature rise, and a pure polycaprolactone film shows $< 5^\circ\text{C}$ increase after the same exposure (Figure 5.13b). Our coating's temperature rise is also higher than other reported PEDOT films^{17,18} because particle boundaries lower the heat dissipation rate, creating a heat confinement effect.⁵⁶ We also observed that the light from a camera flash ignites a cotton ball impregnated with PEDOT particles.

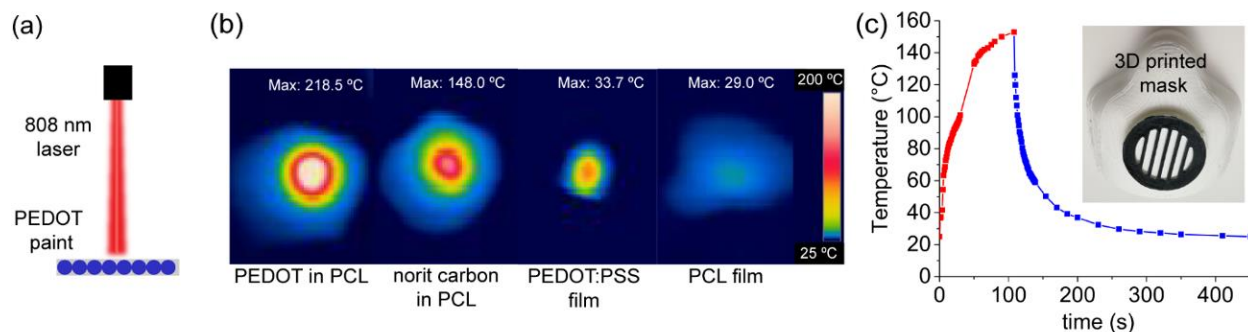


Figure 5.13 (a) Illustration of photothermal experiment (808 nm laser). (b) Temperature distribution for films comprised of PEDOT-polycaprolactone, Norit carbon-polycaprolactone, PEDOT:PSS on glass, and pristine polycaprolactone after a 5 second laser exposure (power density 0.8 W/cm^2). (c) Temperature profile for a PEDOT-coated 3D-printed polyethylene terephthalate glycol mask during and after laser exposure (inset shows a photograph of the mask).

The spread of COVID-19 since 2020 affects human life profoundly and masks are an effective prevention against the spreading of the virus. Unfortunately, increased use of disposable masks also generates large amount of plastic waste and is forcing us to look for alternatives. 3D printing is a promising technique for fast prototyping of reusable masks. However, masks are reusable only if the surface is effectively disinfected after each use. Utilizing the photothermal property of PEDOT coatings as a fast, non-destructive microbial ablation method, a proof-of-concept reusable mask is proposed.⁵⁷ Brushing the PEDOT particle-based formulation on the air filter cap of a 3D-printed polyethylene terephthalate glycol mask (Figure 5.13c inset) and exposing it to a laser for 100 s (808 nm , 0.8 W/cm^2) increases the surface temperature to $150 \text{ }^\circ\text{C}$, a temperature demonstrated sufficient for inactivating COVID-19.⁵⁸ The temperature rise is lower than that of a freestanding PEDOT particle-polycaprolactone composite film because the 3D-printed polyethylene terephthalate glycol mask absorbs heat. The surface temperature drops after the laser is turned off (Figure 5.13c) and the mask structure and particle coating remain intact.

5.4 Conclusions

This chapter introduces a continuous aerosol synthesis of PEDOT particles with an optimized low resistance of $4.2 \pm 0.5 \, \Omega$ measured by 1 mm-gap electrodes. Tuning EDOT to Fe^{3+} ratio reveals that stoichiometry affects PEDOT's crystallinity, doping level, electrical and electrochemical properties. Results show that a balanced EDOT to Fe^{3+} ratio (1:1) results in PEDOT particles with the highest charge carrier concentration and the lowest electrical resistance among all samples. A highly stable electrode is fabricated via electrophoretic deposition of PEDOT particles on carbon fiber paper. The electrode is characterized by cyclic voltammetry and possesses state-of-the-art gravimetric capacitance for PEDOT particles. Particles are readily processable as a colloidal dispersion, and an organic paint is formulated to conformally coat 3D-printed thermoplastic objects resulting in a low electrical resistance (1 k Ω /cm), comparable to prints produced from commercial conductive filaments. The particle-based paint enables the fabrication of 3D-printed pH sensors, strain sensors, and affords a light-induced method for triggering rapid heating of a PEDOT-coated surface. Future work of aerosol synthesis may include optimizing the synthesis condition for scaling up of polymer particle production and controlling of particle sizes. This include altering the frequency of the ultrasonic nebulizer to control the sizes FeCl_3 droplets that template PEDOT particle synthesis and establishing a continuous feed for the reactants. Additionally, the formulation of PEDOT particle paint require optimization for coating large surfaces without delamination of particles or defect in the coating. Potential experiments include quantitative rheological characterization to study the shearing of paint during deposition and adopting other coating techniques, such as spin-coating or spray-coating.

5.5 References

- (1) Someya, T.; Bao, Z.; Malliaras, G. G. The Rise of Plastic Bioelectronics. *Nature* **2016**, *540* (7633), 379–385. <https://doi.org/10.1038/nature21004>.
- (2) Rivnay, J.; Inal, S.; Salleo, A.; Owens, R. M.; Berggren, M.; Malliaras, G. G. Organic Electrochemical Transistors. *Nat. Rev. Mater.* **2018**, *3* (2), 17086. <https://doi.org/10.1038/natrevmats.2017.86>.
- (3) Bubnova, O.; Khan, Z. U.; Malti, A.; Braun, S.; Fahlman, M.; Berggren, M.; Crispin, X. Optimization of the Thermoelectric Figure of Merit in the Conducting Polymer Poly(3,4-Ethylenedioxythiophene). *Nat. Mater.* **2011**, *10* (6), 429–433. <https://doi.org/10.1038/nmat3012>.
- (4) Berggren, M.; Malliaras, G. G. How Conducting Polymer Electrodes Operate. *Science* (1979) **2019**, *364* (6437), 233–234. <https://doi.org/10.1126/science.aaw9295>.
- (5) Guo, X.; Facchetti, A. The Journey of Conducting Polymers from Discovery to Application. *Nat. Mater.* **2020**, *19* (9), 922–928. <https://doi.org/10.1038/s41563-020-0778-5>.
- (6) Mitraka, E.; Gryszel, M.; Vagin, M.; Jafari, M. J.; Singh, A.; Warczak, M.; Mitrakas, M.; Berggren, M.; Ederth, T.; Zozoulenko, I.; Crispin, X.; Głowacki, E. D. Electrocatalytic Production of Hydrogen Peroxide with Poly(3,4-Ethylenedioxythiophene) Electrodes. *Adv. Sustain. Syst.* **2019**, *3* (2), 1800110. <https://doi.org/10.1002/adsu.201800110>.
- (7) Ghosh, S.; Kouame, N. A.; Remita, S.; Ramos, L.; Goubard, F.; Aubert, P. H.; Dazzi, A.; Deniset-Besseau, A.; Remita, H. Visible-Light Active Conducting Polymer Nanostructures with Superior Photocatalytic Activity. *Sci. Rep.* **2015**, *5*. <https://doi.org/10.1038/srep18002>.
- (8) Valiollahi, R.; Vagin, M.; Gueskine, V.; Singh, A.; Grigoriev, S. A.; Pushkarev, A. S.; Pushkareva, I. v.; Fahlman, M.; Liu, X.; Khan, Z.; Berggren, M.; Zozoulenko, I.; Crispin, X. Electrochemical Hydrogen Production on a Metal-Free Polymer. *Sustain. Energy Fuels* **2019**, *3* (12), 3387–3398. <https://doi.org/10.1039/c9se00687g>.
- (9) Horii, T.; Li, Y.; Mori, Y.; Okuzaki, H. Correlation between the Hierarchical Structure and Electrical Conductivity of PEDOT/PSS. *Polym. J.* **2015**, *47* (10), 695–699. <https://doi.org/10.1038/pj.2015.48>.
- (10) Seekaew, Y.; Lokavee, S.; Phokharatkul, D.; Wisitsoraat, A.; Kerdcharoen, T.; Wongchoosuk, C. Low-Cost and Flexible Printed Graphene-PEDOT:PSS Gas Sensor for Ammonia Detection. *Org. Electron.* **2014**, *15* (11), 2971–2981. <https://doi.org/10.1016/j.orgel.2014.08.044>.
- (11) Yuk, H.; Lu, B.; Lin, S.; Qu, K.; Xu, J.; Luo, J.; Zhao, X. 3D Printing of Conducting Polymers. *Nat. Commun.* **2020**, *11* (1). <https://doi.org/10.1038/s41467-020-15316-7>.
- (12) Jordan, R. S.; Wang, Y. 3D Printing of Conjugated Polymers. *J. Polym. Sci. B Polym. Phys.* **2019**, *57* (23), 1592–1605. <https://doi.org/10.1002/polb.24893>.

- (13) Xia, Y.; Ouyang, J. PEDOT:PSS Films with Significantly Enhanced Conductivities Induced by Preferential Solvation with Cosolvents and Their Application in Polymer Photovoltaic Cells. *J. Mater. Chem.* **2011**, *21* (13), 4927–4936. <https://doi.org/10.1039/c0jm04177g>.
- (14) Lei, Y.; Oohata, H.; Kuroda, S. I.; Sasaki, S.; Yamamoto, T. Highly Electrically Conductive Poly(3,4-Ethylenedioxythiophene) Prepared via High-Concentration Emulsion Polymerization. *Synth. Met.* **2005**, *149* (2–3), 211–217. <https://doi.org/10.1016/j.synthmet.2005.01.004>.
- (15) Pang, R.; Hu, X.; Zhou, S.; Sun, C.; Yan, J.; Sun, X.; Xiao, S.; Chen, P. Preparation of Multi-Shelled Conductive Polymer Hollow Microspheres by Using Fe₃O₄ Hollow Spheres as Sacrificial Templates. *Chemical Communications* **2014**, *50* (83), 12493–12496. <https://doi.org/10.1039/c4cc05469e>.
- (16) Zhang, X.; MacDiarmid, A. G.; Manohar, S. K. Chemical Synthesis of PEDOT Nanofibers. *Chemical Communications* **2005**, No. 42, 5328–5330. <https://doi.org/10.1039/b511290g>.
- (17) Kim, B.; Han, M.; Kim, E. Photothermally Powered Conductive Films for Absorber-Free Solar Thermoelectric Harvesting. *J. Mater. Chem. A Mater.* **2019**, *7* (5), 2066–2074. <https://doi.org/10.1039/c8ta10399b>.
- (18) Lim, H.; Park, T.; Na, J.; Park, C.; Kim, B.; Kim, E. Construction of a Photothermal Venus Flytrap from Conductive Polymer Bimorphs. *NPG Asia Mater.* **2017**, *9* (7). <https://doi.org/10.1038/am.2017.101>.
- (19) Lu, Y.; Yang, H.; Diao, Y.; Wang, H.; Izima, C.; Jones, I.; Woon, R.; Chrulski, K.; D’Arcy, J. M. Solution-Processable PEDOT Particles for Coatings of Untreated 3D-Printed Thermoplastics. *ACS Appl. Mater. Interfaces* **2023**, *15* (2), 3433–3441. <https://doi.org/10.1021/acsami.2c18328>.
- (20) Lu, Y.; Kacica, C.; Bansal, S.; Santino, L. M.; Acharya, S.; Hu, J.; Izima, C.; Chrulski, K.; Diao, Y.; Wang, H.; Yang, H.; Biswas, P.; Schaefer, J.; D’Arcy, J. M. Synthesis of Submicron PEDOT Particles of High Electrical Conductivity via Continuous Aerosol Vapor Polymerization. *ACS Appl. Mater. Interfaces* **2019**, *11* (50), 47320–47329. <https://doi.org/10.1021/acsami.9b15625>.
- (21) Zhang, Y.; Suslick, K. S. Synthesis of Poly(3,4-Ethylenedioxythiophene) Microspheres by Ultrasonic Spray Polymerization (USPo). *Chemistry of Materials* **2015**, *27* (22), 7559–7563. <https://doi.org/10.1021/acs.chemmater.5b03423>.
- (22) Zozoulenko, I.; Singh, A.; Singh, S. K.; Gueskine, V.; Crispin, X.; Berggren, M. Polarons, Bipolarons, and Absorption Spectroscopy of PEDOT. *ACS Appl. Polym. Mater.* **2019**, *1* (1), 83–94. <https://doi.org/10.1021/acsapm.8b00061>.

- (23) Heydari Gharahcheshmeh, M.; Tavakoli, M. M.; Gleason, E. F.; Robinson, M. T.; Kong, J.; Gleason, K. K. Tuning, Optimization, and Perovskite Solar Cell Device Integration of Ultrathin Poly(3,4-Ethylene Dioxythiophene) Films via a Single-Step All-Dry Process. *Sci. Adv.* **2019**, 5 (11). <https://doi.org/10.1126/sciadv.aay0414>.
- (24) Lock, J. P.; Im, S. G.; Gleason, K. K. Oxidative Chemical Vapor Deposition of Electrically Conducting Poly(3,4-Ethylenedioxythiophene) Films. *Macromolecules* **2006**, 39 (16), 5326–5329. <https://doi.org/10.1021/ma060113o>.
- (25) Kim, D.; Zozoulenko, I. Why Is Pristine PEDOT Oxidized to 33%? A Density Functional Theory Study of Oxidative Polymerization Mechanism. *Journal of Physical Chemistry B* **2019**, 123 (24), 5160–5167. <https://doi.org/10.1021/acs.jpcc.9b01745>.
- (26) Cho, B.; Park, K. S.; Baek, J.; Oh, H. S.; Koo Lee, Y. E.; Sung, M. M. Single-Crystal Poly(3,4-Ethylenedioxythiophene) Nanowires with Ultrahigh Conductivity. *Nano Lett.* **2014**, 14 (6), 3321–3327. <https://doi.org/10.1021/nl500748y>.
- (27) Aplan, M. P.; Gomez, E. D. Recent Developments in Chain-Growth Polymerizations of Conjugated Polymers. *Industrial and Engineering Chemistry Research*. American Chemical Society July 19, 2017, pp 7888–7901. <https://doi.org/10.1021/acs.iecr.7b01030>.
- (28) Patel, A. K.; Bajpai, R.; Keller, J. M. On the Crystallinity of PVA/Palm Leaf Biocomposite Using DSC and XRD Techniques. *Microsystem Technologies* **2014**, 20 (1), 41–49. <https://doi.org/10.1007/s00542-013-1882-0>.
- (29) Sami, A.; David, E.; Fréchette, M. Procedure for Evaluating the Crystallinity from X-Ray Diffraction Scans of High and Low Density Polyethylene/SiO₂ Composites. *2010 Annual Report Conference on Electrical Insulation and Dielectric Phenomena* **2010**, 1–4. <https://doi.org/10.1109/CEIDP.2010.5724069>.
- (30) Wang, H.; Santino, L. M.; Rubin, M.; Diao, Y.; Lu, Y.; D'Arcy, J. M. Self-Woven Nanofibrillar PEDOT Mats for Impact-Resistant Supercapacitors. *Sustain. Energy Fuels* **2019**, 3 (5), 1154–1162. <https://doi.org/10.1039/c8se00591e>.
- (31) Paradee, N.; Sirivat, A. Synthesis of Poly(3,4-Ethylenedioxythiophene) Nanoparticles via Chemical Oxidation Polymerization. *Polym. Int.* **2014**, 63 (1), 106–113. <https://doi.org/10.1002/pi.4538>.
- (32) Zheng, H.; Jiang, Y.; Xu, J.; Yang, Y. The Characteristic Properties of PEDOT Nano-Particle Based on Reversed Micelle Method. *Sci. China Technol. Sci.* **2010**, 53 (9), 2355–2362. <https://doi.org/10.1007/s11431-010-4052-y>.
- (33) Lee, H.; Kim, Y.; Cho, H.; Lee, J. G.; Kim, J. H. Improvement of PEDOT:PSS Linearity: Via Controlled Addition Process. *RSC Adv.* **2019**, 9 (30), 17318–17324. <https://doi.org/10.1039/c9ra03040a>.

- (34) Billah, K. M. M.; Coronel, J. L.; Halbig, M. C.; Wicker, R. B.; Espalin, D. Electrical and Thermal Characterization of 3D Printed Thermoplastic Parts with Embedded Wires for High Current-Carrying Applications. *IEEE Access* **2019**, *7*, 18799–18810. <https://doi.org/10.1109/ACCESS.2019.2895620>.
- (35) Alafaghani, A.; Qattawi, A.; Ablat, M. A. Design Consideration for Additive Manufacturing: Fused Deposition Modelling. *Open Journal of Applied Sciences* **2017**, *07* (06), 291–318. <https://doi.org/10.4236/ojapps.2017.76024>.
- (36) Liaw, C. Y.; Guvendiren, M. Current and Emerging Applications of 3D Printing in Medicine. *Biofabrication* **2017**, *9*, 024102. <https://doi.org/10.1088/1758-5090/aa7279>.
- (37) Gulzar, U.; Glynn, C.; O'Dwyer, C. Additive Manufacturing for Energy Storage: Methods, Designs and Material Selection for Customizable 3D Printed Batteries and Supercapacitors. *Curr. Opin. Electrochem.* **2020**, *20*, 46–53. <https://doi.org/10.1016/j.coelec.2020.02.009>.
- (38) Griffey, Jason. *3-D Printers for Libraries*; 2014; Vol. 50.
- (39) Flowers, P. F.; Reyes, C.; Ye, S.; Kim, M. J.; Wiley, B. J. 3D Printing Electronic Components and Circuits with Conductive Thermoplastic Filament. *Addit. Manuf.* **2017**, *18*, 156–163. <https://doi.org/10.1016/j.addma.2017.10.002>.
- (40) Mamatha, S.; Biswas, P.; Das, D.; Johnson, R. Fabrication of Complex Shaped Ceramic Articles from 3D Printed Polylactic Acid Templates by Replication Process. *Ceram. Int.* **2019**, *45* (15), 19577–19580. <https://doi.org/10.1016/j.ceramint.2019.06.203>.
- (41) Chaudhari, S. K.; Patil, K. R.; Allepús, J.; Coronas, A. Measurement of the Vapor Pressure of 2,2,2-Trifluoroethanol and Tetraethylene Glycol Dimethyl Ether by Static Method. *Fluid Phase Equilib.* **1995**, *108* (1–2), 159–165. [https://doi.org/10.1016/0378-3812\(95\)02683-6](https://doi.org/10.1016/0378-3812(95)02683-6).
- (42) Munekata, T.; Suzuki, T.; Yamakawa, S.; Asahi, R. Effects of Viscosity, Surface Tension, and Evaporation Rate of Solvent on Dry Colloidal Structures: A Lattice Boltzmann Study. *Phys. Rev. E. Stat. Nonlin. Soft Matter Phys.* **2013**, *88* (5). <https://doi.org/10.1103/PhysRevE.88.052314>.
- (43) Chen, J.; Yu, Q.; Cui, X.; Dong, M.; Zhang, J.; Wang, C.; Fan, J.; Zhu, Y.; Guo, Z. An Overview of Stretchable Strain Sensors from Conductive Polymer Nanocomposites. *J. Mater. Chem. C Mater.* **2019**, *38*, 11710–11730. <https://doi.org/10.1039/c9tc03655e>.
- (44) Olsson, A.; Hellsing, M. S.; Rennie, A. R. New Possibilities Using Additive Manufacturing with Materials That Are Difficult to Process and with Complex Structures. *Phys. Scr.* **2017**, *92* (5). <https://doi.org/10.1088/1402-4896/aa694e>.
- (45) Gnanasekaran, K.; Heijmans, T.; van Bennekom, S.; Woldhuis, H.; Wijnia, S.; de With, G.; Friedrich, H. 3D Printing of CNT- and Graphene-Based Conductive Polymer

Nanocomposites by Fused Deposition Modeling. *Appl. Mater. Today*. **2017**, *9*, 21–28. <https://doi.org/10.1016/j.apmt.2017.04.003>.

(46) He, S.; Mukaida, M.; Kirihaara, K.; Lyu, L.; Wei, Q. Reversible Protonic Doping in Poly(3,4-Ethylenedioxythiophene). *Polymers (Basel)* **2018**, *10* (10). <https://doi.org/10.3390/polym10101065>.

(47) Sethumadhavan, V.; Zuber, K.; Bassell, C.; Teasdale, P. R.; Evans, D. Hydrolysis of Doped Conducting Polymers. *Commun. Chem.* **2020**, *3* (1). <https://doi.org/10.1038/s42004-020-00404-y>.

(48) Li, Y.; Wang, S.; Xiao, Z. C.; Yang, Y.; Deng, B. W.; Yin, B.; Ke, K.; Yang, M. B. Flexible TPU Strain Sensors with Tunable Sensitivity and Stretchability by Coupling AgNWs with RGO. *J. Mater. Chem. C Mater.* **2020**, *8* (12), 4040–4048. <https://doi.org/10.1039/d0tc00029a>.

(49) Tolvanen, J.; Hannu, J.; Jantunen, H. Stretchable and Washable Strain Sensor Based on Cracking Structure for Human Motion Monitoring. *Sci. Rep.* **2018**, *8* (1). <https://doi.org/10.1038/s41598-018-31628-7>.

(50) Santino, L. M.; Lu, Y.; Acharya, S.; Bloom, L.; Cotton, D.; Wayne, A.; D’Arcy, J. M. Enhancing Cycling Stability of Aqueous Polyaniline Electrochemical Capacitors. *ACS Appl. Mater. Interfaces* **2016**, *8* (43), 29452–29460. <https://doi.org/10.1021/acsami.6b09779>.

(51) Diao, Y.; Chen, H.; Lu, Y.; Santino, L. M.; Wang, H.; D’Arcy, J. M. Converting Rust to PEDOT Nanofibers for Supercapacitors. *ACS Appl. Energy Mater.* **2019**, *2* (5), 3435–3444. <https://doi.org/10.1021/acsaem.9b00244>.

(52) Wang, H.; Diao, Y.; Lu, Y.; Yang, H.; Zhou, Q.; Chrulski, K.; D’Arcy, J. M. Energy Storing Bricks for Stationary PEDOT Supercapacitors. *Nat. Commun.* **2020**, *11* (1). <https://doi.org/10.1038/s41467-020-17708-1>.

(53) Kelly, T. L.; Yano, K.; Wolf, M. O. Supercapacitive Properties of PEDOT and Carbon Colloidal Microspheres. *ACS Appl. Mater. Interfaces* **2009**, *1* (11), 2536–2543. <https://doi.org/10.1021/am900575v>.

(54) Liu, Y.; Turner, A. P. F.; Zhao, M.; Mak, W. C. Facile Synthesis of Highly Processable and Water Dispersible Polypyrrole and Poly(3,4-Ethylenedioxythiophene) Microspheres for Enhanced Supercapacitive Performance. *Eur. Polym. J.* **2018**, *99*, 332–339. <https://doi.org/10.1016/j.eurpolymj.2017.12.013>.

(55) Li, G.; Martinez, C.; Semancik, S. Controlled Electrophoretic Patterning of Polyaniline from a Colloidal Suspension. *J. Am. Chem. Soc.* **2005**, *127* (13), 4903–4909. <https://doi.org/10.1021/ja0441763>.

- (56) Ajayan, P. M.; Terrones, M.; de la Guardia, A.; Huc, V.; Grobert, N.; Wei, B. Q.; Lezec, H.; Ramanath, G.; Ebbesen, T. W. Nanotubes in a Flash - Ignition and Reconstruction. *Science* (1979) **2002**, 296 (5568), 705. <https://doi.org/10.1126/science.296.5568.705>.
- (57) Huang, L.; Xu, S.; Wang, Z.; Xue, K.; Su, J.; Song, Y.; Chen, S.; Zhu, C.; Tang, B. Z.; Ye, R. Self-Reporting and Photothermally Enhanced Rapid Bacterial Killing on a Laser-Induced Graphene Mask. *ACS Nano* **2020**, 14 (9), 12045–12053. <https://doi.org/10.1021/acsnano.0c05330>.
- (58) Pastorino, B.; Touret, F.; Gilles, M.; Luciani, L.; de Lamballerie, X.; Charrel, R. N. Evaluation of Chemical Protocols for Inactivating SARS-CoV-2 Infectious Samples. *Viruses* **2020**, 12 (6). <https://doi.org/10.3390/v12060624>.

Chapter 6: One Eye on the Past, the Other on the Future

In this chapter, I will present some ideas for future projects, both based on interesting phenomena observed during my experiments and inspirations from the literature.

6.1 Effect of Relative Humidity and Additional Organic Solvents in Rust-based Vapor-phase Polymerization

The reaction mechanisms discussed in Chapter 4 involves potential reaction between organic solvents (ethanol, isopropanol, and t-butanol) and chlorobenzene catalyzed by PEDOT. Chlorobenzene is often used as a solvent for monomer solution because it increases the vapor pressure of the less volatile EDOT and enhances mass transport during polymer synthesis. The mechanism I presented in Chapter 4 propose that a side reaction between chlorobenzene and ethanol changes the relative humidity in the reactor, resulting in the increase in electrical conductivity of PEDOT. The results also suggest an optimal relative humidity exists, and the electrical conductivity of PEDOT decreases when relative humidity is out of the optimal range. Water molecules are proton scavengers that deprotonate oligomer cations and facilitates the formation of highly conjugated polymer backbone. Various studies demonstrate an optimal relative humidity exists in vapor-phase synthesis but varies based on the synthetic technique.¹⁻³ Obtaining an optimal humidity for RVPP is crucial for enhancing the electrical conductivity of a polymer product.

One of the previous works from D'Arcy lab discussed the effect of solvent polarity on nanostructure formation in a hydrolysis-assisted vapor-phase polymerization technique (HVPP).

A 2D nanoflower structure is obtained by using a ferric chloride/ethanol solution as oxidant (Figure 6.1). This work also demonstrate that the 2D morphology only forms under high ethanol concentration.⁴ The synthetic protocol in RVPP exclusively produces 1D nanofibrillar due to hydrolysis mechanism between ferric ions and water (from concentrated hydrochloric acid) in the reactor. Substituting the solvent water in concentrated HCl with other solvents alters the hydrolysis of ferric ions to solvolysis and generates 2D nanoflowers or other nanostructures. Additionally, substituting HCl with other acids introduces different spectator ions and coordinating ions that influence the crystal structure of hydrolysis/solvolysis product. These experiments enhance the versatility of the synthetic technique and create an opportunity to study the structural-property relationship in conducting polymers synthesized from the vapor phase.

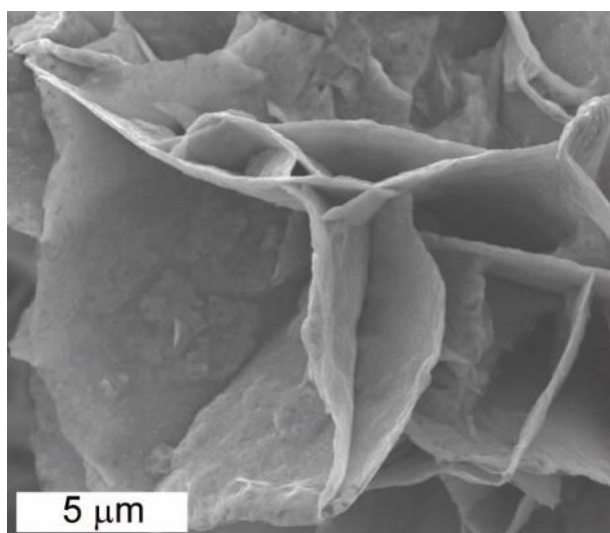


Figure 6.1 2D PEDOT nanoflower synthesized under high concentration of ethanol. Adapted with permission from Reference 4. Copyright 2018, American Chemical Society.

6.2 Spectroelectrochemical Characterization of Reaction Intermediates

The mechanism of rust-based vapor-phase polymerization (RVPP) and the mechanisms proposed in Chapters 2 and 3 consist of a variety of organic and inorganic intermediate species. The mechanisms are proposed based on indirect evidence from spectroscopy, microscopy, and electrochemical characterizations. Capturing and characterizing these reaction intermediates directly validates the proposed mechanisms in the mixed-mechanistic pathways of RVPP. Developing fundamental understanding of this synthetic technique unlocks new chemical handles to control the electrochemical properties of the conducting polymer product. Additionally, in situ spectroelectrochemical technique is useful for calculating and controlling degree of polymerization.^{5,6} A 3D-printed spectroelectrochemical cell was previously designed by Dr. Santino in the appendix of his dissertation, and concomitant spectroscopic and electrochemical characterization is achievable via a portable UV-Vis spectrometer and the Biologic potentiostat.

6.3 Conducting Polymer-filled 3D Printing Filaments

Fabrication of conductive filaments is challenging for 3D printing, especially fused deposition model (FDM) printing. Formation of an electrically conductive percolation network requires the concentration of the conductive filler above a certain threshold. However, high filler concentration often results in poor mechanical strength of the filament.^{7,8} In Chapter 5, I presented a solution that involves coating a 3D-printed object with a conducting polymer particle-based paint. This method circumvent the trade-off between mechanical strength and electrical conductivity, but it also limits the coating to the surface of a 3D-printed object. A

conducting polymer-filled filament is required to generate electrically conductive pathways throughout a 3D-printed object.

Recent reports from the literature demonstrate methods that combines polymerization or other chemical reactions with extrusion during 3D printing.^{9,10} The extrusion temperature for printing polylactic acid and polycaprolactone commonly used in our group is between 170 and 210 °C, sufficient for polymerizing both EDOT and pyrrole. A modified extruder in the 3D printer that possesses inlet for monomer, oxidant, and filament combines the function of a traditional 3D printing extruder and a polymerization reactor (Figure 6.2). The filament extrusion speed is programmable, providing sufficient reaction time between monomer and the oxidant. Pretreatment by impregnating a filament with either monomer or oxidant enhances the mixing between reactants. This method demonstrates potential for controlling the isotropy of a functional 3D-printed object.

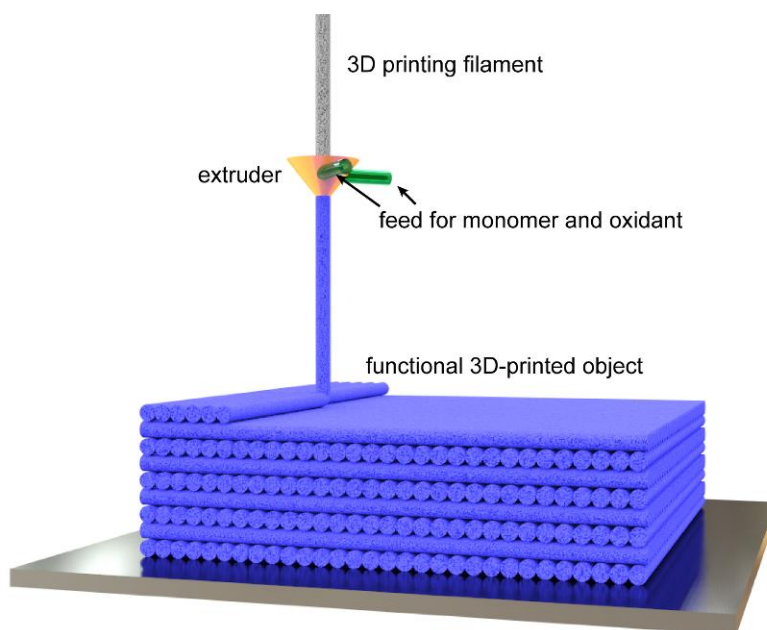


Figure 6.2 Schematic diagram of a modified 3D printing extruder that combines extrusion and polymerization.

6.4 Enhancing the Energy Density of Conducting Polymer-based Supercapacitors

Many groups have utilized metal oxide/conducting polymer core/shell composites as electrode materials for energy storage devices and showed promising results. This type of composite takes advantage of the electrical conductivity of the polymer shells and the large pseudocapacitance of metal oxide cores, such as V_2O_5 , MnO_2 , NiO , and CoO .^{11–13} Ions such as V^{5+} and Mn^{4+} possesses similar oxidative properties to Fe^{3+} for initiating polymerization of pyrrole and EDOT. Incorporating these ions into vapor-phase synthesis of conducting polymer produce chemical bonding between polymer and metal oxides, which potentially generates synergy between the two components in a composite material. The dissolution of metal oxides and the hydrolysis of ions need to be examined in detail prior to combining metal oxides (V_2O_5 , MnO_2 , NiO , and CoO) with PEDOT and PPy as polymer composites. Additionally, the selection of electrolyte is crucial for taking advantage of the strength of both polymer and metal oxide. Polymer-based electrodes typically exhibit high capacitance in acidic or neutral electrolytes, whereas metal oxide-based electrodes prefer basic or neutral electrolytes.

6.5 References

- (1) Goktas, H.; Wang, X.; Ugur, A.; Gleason, K. K. Water-Assisted Vapor Deposition of PEDOT Thin Film. *Macromol. Rapid Commun.* **2015**, *36* (13), 1283–1289. <https://doi.org/10.1002/marc.201500069>.
- (2) Mueller, M.; Fabretto, M.; Evans, D.; Hojati-Talemi, P.; Gruber, C.; Murphy, P. Vacuum Vapour Phase Polymerization of High Conductivity PEDOT: Role of PEG-PPG-PEG, the Origin of Water, and Choice of Oxidant. *Polymer (Guildf)* **2012**, *53* (11), 2146–2151. <https://doi.org/10.1016/j.polymer.2012.03.028>.
- (3) Fabretto, M.; Zuber, K.; Hall, C.; Murphy, P.; Griesser, H. J. The Role of Water in the Synthesis and Performance of Vapour Phase Polymerised PEDOT Electrochromic Devices. *J. Mater. Chem.* **2009**, *19* (42), 7871–7878. <https://doi.org/10.1039/b912324e>.
- (4) Wang, H.; Diao, Y.; Rubin, M.; Santino, L. M.; Lu, Y.; D'Arcy, J. M. Metal Oxide-Assisted PEDOT Nanostructures via Hydrolysis-Assisted Vapor-Phase Polymerization for Energy Storage. *ACS Appl. Nano Mater.* **2018**, *1* (3), 1219–1227. <https://doi.org/10.1021/acsanm.7b00382>.
- (5) Genies, E. M.; Lapkowski, M. Spectroelectrochemical Evidence for an Intermediate in the Electropolymerization of Aniline. *J. Electroanal. Chem. Interfacial Electrochem.* **1987**, *236* (1–2), 189–197. [https://doi.org/10.1016/0022-0728\(87\)88026-9](https://doi.org/10.1016/0022-0728(87)88026-9).
- (6) Zhou, M.; Heinze, J. Electropolymerization of Pyrrole and Electrochemical Study of Polypyrrole. 2. Influence of Acidity on the Formation of Polypyrrole and the Multipathway Mechanism. *Journal of Physical Chemistry B* **1999**, *103* (40), 8443–8450. <https://doi.org/10.1021/jp990161t>.
- (7) Chen, J.; Yu, Q.; Cui, X.; Dong, M.; Zhang, J.; Wang, C.; Fan, J.; Zhu, Y.; Guo, Z. An Overview of Stretchable Strain Sensors from Conductive Polymer Nanocomposites. *J. Mater. Chem. C Mater.* **2019**, *7* (38), 11710–11730. <https://doi.org/10.1039/C9TC03655E>.
- (8) Gnanasekaran, K.; Heijmans, T.; van Bennekom, S.; Woldhuis, H.; Wijnia, S.; de With, G.; Friedrich, H. 3D Printing of CNT- and Graphene-Based Conductive Polymer Nanocomposites by Fused Deposition Modeling. *Appl. Mater. Today* **2017**, *9*, 21–28. <https://doi.org/10.1016/j.apmt.2017.04.003>.
- (9) Gastaldi, M.; Cardano, F.; Zanetti, M.; Viscardi, G.; Barolo, C.; Bordiga, S.; Magdassi, S.; Fin, A.; Roppolo, I. Functional Dyes in Polymeric 3D Printing: Applications and Perspectives. *ACS Mater. Lett.* **2021**, *3* (1), 1–17. <https://doi.org/10.1021/acsmaterialslett.0c00455>.
- (10) Schaffner, M.; Rühs, P. A.; Coulter, F.; Kilcher, S.; Studart, A. R. 3D Printing of Bacteria into Functional Complex Materials. *Sci. Adv.* **2017**, *3* (12). <https://doi.org/10.1126/sciadv.aao6804>.

- (11) Wang, J.-G.; Liu, H.; Liu, H.; Hua, W.; Shao, M. Interfacial Constructing Flexible V₂O₅@Polypyrrole Core–Shell Nanowire Membrane with Superior Supercapacitive Performance. *ACS Appl. Mater. Interfaces* **2018**, *10* (22), 18816–18823. <https://doi.org/10.1021/acsami.8b05660>.
- (12) Lee, H. U.; Park, C.; Jin, J.-H.; Kim, S. W. A Stretchable Vertically Stacked Microsupercapacitor with Kirigami-Bridged Island Structure: MnO₂/Graphene/Poly(3,4-Ethylenedioxythiophene) Nanocomposite Electrode through Pen Lithography. *J. Power Sources* **2020**, *453*, 227898. <https://doi.org/10.1016/j.jpowsour.2020.227898>.
- (13) Shen, Z.-M.; Luo, X.-J.; Zhu, Y.-Y.; Liu, Y.-S. Facile Co-Deposition of NiO-CoO-PPy Composite for Asymmetric Supercapacitors. *J. Energy Storage* **2022**, *51* (December 2021), 104475. <https://doi.org/10.1016/j.est.2022.104475>.

Appendix

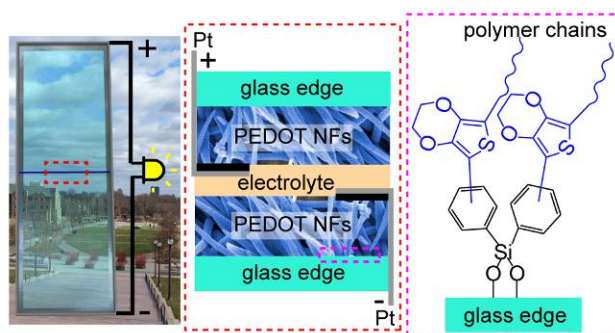


Figure A1 Graphical abstract of publication, “Nanostructured Poly(3,4-Ethylenedioxythiophene) (PEDOT) Coatings on Functionalized Glass for Energy Storage.”

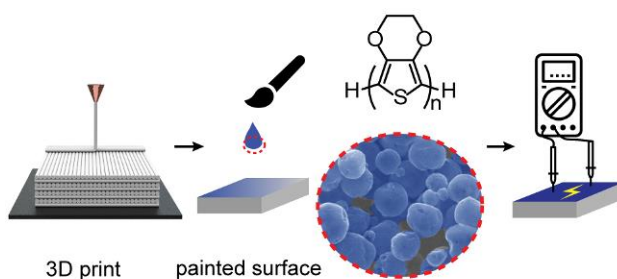


Figure A2 Graphical abstract of publication, “Solution Processable Poly(3,4-Ethylenedioxythiophene) Nanoparticles.”

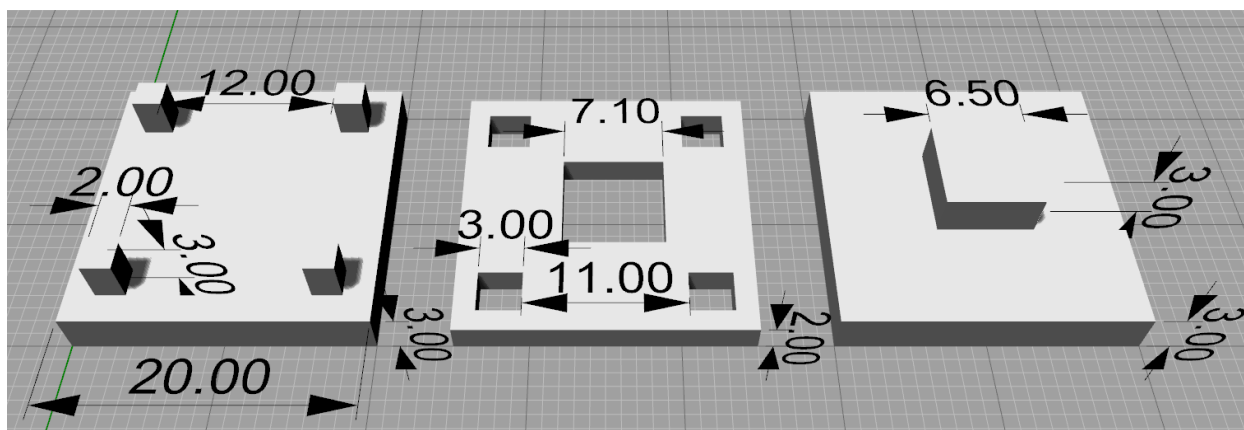


Figure A3 Model of a 3D-printed pellet press for measuring electrical conductivity of powders. The dimensions are measured in millimeters.

Curriculum Vitae

Haoru Yang
(314) 606-7547, yanghaoru@wustl.edu

EDUCATION

Washington University in St. Louis

Ph.D. in Chemistry May 2023
School of Arts & Sciences Advisor: Julio D'Arcy, Ph.D.
GPA: 3.77 / 4.0

Bachelor of Arts in Chemistry, Minor in Linguistics May 2018
School of Arts & Sciences Advisor: Beth Martin
GPA: 3.44 / 4.0

TECHNICAL SKILLS

Experiment

Expertise in oxidative polymerization, surface functionalization, and deposition of conducting polymer thin films from both vapor phase and solution phase. Expertise in hydrothermal and continuous flow synthesis, Schlenk line and reflux techniques. Expertise in designing, fabricating, and testing of electrochemical capacitors.

Instrument

Proficiency in electrochemical analysis of conducting polymers (cyclic and linear sweep voltammetry, chronopotentiometry, four-point probe), spectroscopy (electrochemical impedance, UV-vis-NIR, Raman, energy dispersive x-ray), microscopy (optical, electron, atomic force), and thermalgravimetric analysis. Expertise in working with tube furnace, probe sonicator, low pressure oxygen plasma system, and UV ozone cleaner. Proficiency with 3D printer and laser cutter.

Software

Proficiency in ChemDraw(3D), OriginLab, Adobe Illustrator, Rhino 5, Flamingo nXt, Microsoft Word, PowerPoint, and Excel. Skillfully use Adobe Photoshop and After effects, ImageJ, CrystalMaker, CrystalDiffract, and Blender video editor.

RESEARCH EXPERIENCE

Covalently bonding conducting polymers to silanized surfaces from the vapor phase

Deposited silane monolayers that obviates crosslinking on substrates via solution treatment. Developed a synthesis that covalently bonds a homogenous conducting polymer coating to a silanized surface via vapor phase polymerization.

Grafting conducting polymers to flexible substrates via Friedel-Crafts alkylation

Synthesized composites of polypyrrole and poly(3,4-ethylenedioxythiophene) from the vapor phase. Grafted conducting polymer films to a flexible substrate via Friedel-Crafts alkylation.

Vapor phase synthesis of conducting polymer composites on masonry materials

Synthesized composites of conducting polymers and iron-containing masonry materials from the vapor phase. Investigated correlations between polymer nanostructure and humidity during synthesis.

Aerosol-based synthesis of submicron conducting polymer particles

Developed a scalable continuous batch-processing synthesis that produces spherical submicron-sized conducting polymer particles with high electrical conductivity. Developed solution processing techniques that homogenously disperse polymer particles in both water and organic solvents.

PUBLICATIONS

- 1) **Yang, H.**; Chow, B.; Awoyomi, A.; D'Arcy, J. M. Nanostructured Poly(3,4-Ethylenedioxythiophene) (PEDOT) Coatings on Functionalized Glass for Energy Storage. *ACS Appl. Mater. Int.*, 2023, 15 (2), 3235–3243.
- 2) **Yang, H.**; Lu, Y.; Izima, C.; Diao, Y.; Wang, H.; D'Arcy, J. M. Solution Processable Poly(3,4-Ethylenedioxythiophene) Nanoparticles. *ACS Appl. Mater. Int.*, 2023, 15 (2), 3433–3441.
- 3) **Yang, H.**; Diao, Y.; Lu, Y.; Wang, H.; Chow, A.; Izima, C.; Woon, R.; Chow, B.; D'Arcy, J. M. Converting Iron Corrosion Product to Nanostructured Conducting Polymers: Synthetic Strategies and Applications. *Accounts of Materials Research*, submitted (invited review).
- 4) Wang, H.; **Yang, H.**; Diao, Y.; Lu, Y.; Chrulski, K.; D'Arcy, J. M. Solid-State Precursor Impregnation for Enhanced Capacitance in Hierarchical Flexible Poly(3,4-Ethylenedioxythiophene) Supercapacitors. *ACS Nano* 2021, 15 (4), 7799–7810. <https://doi.org/10.1021/acsnano.1c01887>.
- 5) Wang, H.; **Yang, H.**; Woon, R.; Lu, Y.; Diao, Y.; D'Arcy, J. M. Microtubular PEDOT-Coated Bricks for Atmospheric Water Harvesting. *ACS Applied Materials & Interfaces*, 2021, 13 (29), 34671–34678. <https://doi.org/10.1021/acsaami.1c04631>.
- 6) Santino, L. M.; Diao, Y.; **Yang, H.**; Lu, Y.; Wang, H.; Hwang, E.; D'Arcy, J. M. Vapor/Liquid Polymerization of Ultraporous Transparent and Capacitive Polypyrrole Nanonets. *Nanoscale*, 2019, 11 (25), 12358–12369. <https://doi.org/10.1039/c9nr02771h>.
- 7) Diao, Y.; Lu, Y.; **Yang, H.**; Wang, H.; Chen, H.; D'Arcy, J. M. Direct Conversion of Fe₂O₃ to 3D Nanofibrillar PEDOT Microsupercapacitors. *Advanced Functional Materials*, 2020, 30 (32), 2003394. <https://doi.org/10.1002/adfm.202003394>.
- 8) Diao, Y.; Woon, R.; **Yang, H.**; Chow, A.; Wang, H.; Lu, Y.; D'Arcy, J. M. Kirigami Electrodes of Conducting Polymer Nanofibers for Wearable Humidity Dosimeters and Stretchable Supercapacitors. *Journal of Materials Chemistry A*, 2021, 9 (15), 9849–9857. <https://doi.org/10.1039/d0ta11335b>.
- 9) Wang, H.; Diao, Y.; Lu, Y.; **Yang, H.**; Zhou, Q.; Chrulski, K.; D'Arcy, J. M. Energy Storing Bricks for Stationary PEDOT Supercapacitors. *Nature Communications*, 2020, 11 (1), 3882. <https://doi.org/10.1038/s41467-020-17708-1>.

10) Diao, Y.; Jung, S.; Kouhnavard, M.; Woon, R.; **Yang, H.**; Biswas, P.; D'Arcy, J. M. Single PEDOT Catalyst Boosts CO₂ Photoreduction Efficiency. *ACS Central Science*, 2021, 7 (10), 1668–1675. <https://doi.org/10.1021/acscentsci.1c00712>.

11) Lu, Y.; Kacica, C.; Bansal, S.; Santino, L. M.; Acharya, S.; Hu, J.; Izima, C.; Chrulski, K.; Diao, Y.; Wang, H.; **Yang, H.**; Biswas P.; Schaefer J.; D'Arcy, J. M. Synthesis of Submicron PEDOT Particles of High Electrical Conductivity via Continuous Aerosol Vapor Polymerization. *ACS Applied Materials & Interfaces*, 2019, 11 (50), 47320–47329. <https://doi.org/10.1021/acsami.9b15625>.

AWARD & LEADERSHIP

Chemistry Department Teaching Award

August 2020

Chinese Students and Scholars Association (WUCSSA)

Vice President

Fall 2021-Summer 2022

Deputy Secretary of Project & Event Committee

Fall 2020-Summer 2021

Explore Program for International Students

Volunteer Student Leader

August 2015 and 2017

Asian Music Association

Executive Board Member

September 2016-May 2018

OTHER SKILLS

Basic life support (CPR and AED). Bilingual proficiency in Mandarin and English, professional working German.